



**Universidade do Minho**

I3Bs - Instituto de Investigação em Biomateriais,  
Biodegradáveis e Biomiméticos

João Pedro Bebiano e Costa

**Advanced engineering strategies for bioprinting  
of patient-specific cartilage tissues**

Advanced engineering strategies for bioprinting  
of patient-specific cartilage tissues

João Pedro Bebiano e Costa

**FCT**  
Fundação para a Ciência e a Tecnologia  
MINISTÉRIO DA EDUCAÇÃO E CIÊNCIA

**PO PH**  
QUALIFICAR É CRESCER.

**QREN**  
QUADRO DE REFERÊNCIA ESTRATÉGICO NACIONAL  
PORTUGAL 2007.2013

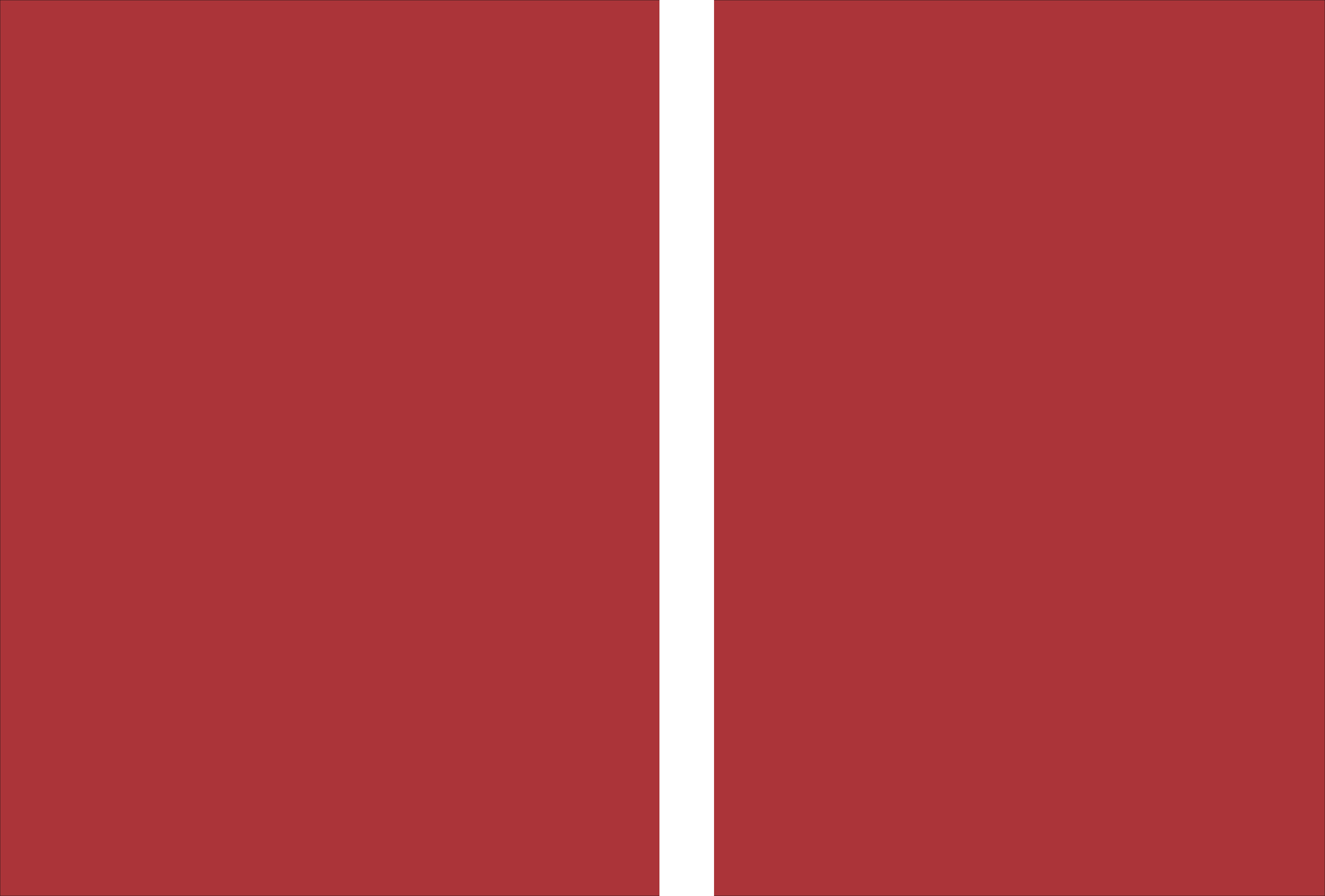
**PD+ F**  
PROGRAMAS DE DOUTORAMENTO FCT

Governo da República Portuguesa

UNIÃO EUROPEIA  
Fundo Social Europeu

UMinho | 2019

julho de 2019





**Universidade do Minho**

I3Bs - Instituto de Investigação em Biomateriais,  
Biodegradáveis e Biomiméticos

João Pedro Bebiano e Costa

## **Advanced engineering strategies for bioprinting of patient-specific cartilage tissues**

Tese de Doutoramento

Doutoramento em Engenharia de Tecidos, Medicina Regenerativa  
e Células Estaminais

Trabalho efetuado sob a orientação do

**Professor Doutor Rui Luís Gonçalves dos Reis**

e do

**Doutor Joaquim Miguel Antunes Correia de Oliveira**

## DIREITOS DE AUTOR E CONDIÇÕES DE UTILIZAÇÃO DO TRABALHO POR TERCEIROS

Este é um trabalho académico que pode ser utilizado por terceiros desde que respeitadas as regras e boas práticas internacionalmente aceites, no que concerne aos direitos de autor e direitos conexos.

Assim, o presente trabalho pode ser utilizado nos termos previstos na licença abaixo indicada.

Caso o utilizador necessite de permissão para poder fazer um uso do trabalho em condições não previstas no licenciamento indicado, deverá contactar o autor, através do RepositóriUM da Universidade do Minho.

*Licença concedida aos utilizadores deste trabalho*



Atribuição

CC BY

<https://creativecommons.org/licenses/by/4.0/>



## ACKNOWLEDGMENTS

I would like to start by expressing my gratitude to my formal PhD supervisor and director of the 3Bs Research group, Prof. Rui Reis. In these four years, you inspired me with your leadership and ambition, preparing me to the competitive scientific world.

To my supervisor Dr. Miguel Oliveira and Dra. Joana Silva-Correia, I express a really special recognition for the support during these 4 years. It is difficult to put in words how thankful I am for the patience, availability and inspiration during these last years. This would not be possible without all your knowledge and capability to supervise me.

I would also like to express my gratitude to Professor Anthony Atala, Professor James Yoo and Dr. Sang Jin Lee for receiving me in the Wake Forest Institute for Regenerative Medicine, Winston-Salem, USA.

I would like to thank my forever friends José Miguel, João Santos, Daniela Rego and Joana Rua, for all the emotional support and most importantly, for their special visit to USA. I would like also to thank to my 3B's friends, colleagues and co-workers.

Finally, I would like to thank my beautiful family for all the unconditional love and support. I consider myself the luckiest person in the world to have this wonderful family. This thesis is dedicated to each one of them: Mom, Dad, Grandparents, Uncles, my little brothers João and Luis, and to my deceased Grandparents. I believe that this accomplishment would make them proud and happy. To my Mom and to my Dad, it is difficult to put in words how much I love you and how much I appreciate to be your son. The person that I am today is due to the way that you raised me and to all the principals that you transmitted to me. Last but not the least, I am really thankful for the fact that during this journey my family has grown. I gained a sister for life. Mariana Carvalho, thank you for all the support, patient and for being there when I needed the most. You are family now. Besides a sister for life, most importantly I won a partner for life, my everything, the love of my life Cristiana Carvalho. All the pressure, all the bad moments, all the stress, all the late night work seems a blessing when I realize that this journey brought you to my side making me the happiest person ever. I'm deeply grateful to be part of your life now and I would like to say thank you for all the support, patient, and love and for staying by my side in the best and hardest moments. Thank you for being who you are!

I would like to acknowledge the Foundation for Science and Technology (FCT) for my PhD scholarship (PD/BD/113803/2015).

## **STATEMENT OF INTEGRITY**

I hereby declare having conducted this academic work with integrity. I confirm that I have not used plagiarism or any form of undue use of information or falsification of results along the process leading to its elaboration.

I further declare that I have fully acknowledged the Code of Ethical Conduct of the University of Minho.

## ABSTRACT

Organ shortage and transplantation needs have led to congestion in healthcare systems resulting in a huge socioeconomic impact. Tissue Engineering has been revolutionizing the engineering of functional tissues, making them great alternatives to achieve a better, faster and effective worldwide patient care. Fibrocartilage is an avascular and aneural tissue characterized by the reduced number of cells and can be found in different tissues, such as intervertebral disc (IVD) and meniscus. These tissues own poor regenerative properties where a massive number of individuals have been affected by their degeneration. The current available treatments have shown poor clinical outcomes and none of them can be consensually designated as the “gold” standard treatment. Tissue engineers have been trying to overcome all the current challenges by developing novel approaches where different biomaterials have been explored to achieve a suitable implant (**Chap. I and II**). However, the pursuit for the “perfect” biomimetic implant is still a big challenge. Therefore, the combination of high-resolution imaging techniques (magnetic resonance imaging and micro-computed tomography) with 3D printing can be a powerful tool to closely mimic the fibrocartilaginous native tissue. This approach can provide reproducibility of the produced scaffolds and allows the production of patient-specific implants, helping to improve patient recovery time and biofunctionality reestablishment (**Chap. III**). The concept of patient-specificity is explored in this thesis using natural-based materials, where silk fibroin (SF) plays the central role due to its high processing versatility and remarkable mechanical properties. In the first work, indirect printed patient-specific hierarchical scaffolds were produced combining SF with ionic-doped  $\beta$ -tricalcium phosphates (**Chap. V**). Furthermore, using a 3D printing extrusion-based technology, an innovative SF-based bioink was developed (**Chap. VI**). Using the previously developed horseradish peroxidase-mediated crosslinking system, 3D patient-specific memory-shape implants were produced (**Chap. VII**). As third work, a step forward in terms of mimicking the IVD native tissue was given, where the previously developed SF bioink was combined with elastin (**Chap. VIII**). Finally, an extrusion-based 3D printing hybrid system comprising a gellan gum/fibrinogen cell-laden bioink and a SF methacrylated bioink was developed to produce cell-laden patient-specific implants (**Chap. IX**). In summary, the proposed novel 3D printing approaches revealed to be promising alternatives for the production of patient-specific implants for fibrocartilage regeneration.

**Keywords:** Bioprinting, Bioinks, Cartilage, Patient-specific, Personalized

## RESUMO

A escassez de órgãos e a necessidade de transplantação levaram ao congestionamento dos sistemas de saúde, resultando num enorme impacto socioeconómico. Engenharia de Tecidos tem revolucionado a fabricação de tecidos, tornando-se uma ótima alternativa para criar um melhor atendimento ao paciente. Fibrocartilagem é um tecido avascular e aneural caracterizado pelo reduzido número de células e pode ser encontrado em diferentes tecidos, como o disco intervertebral (DIV) e o menisco. Estes tecidos possuem fracas propriedades regenerativas, contribuindo para um elevado número de indivíduos afetado pela sua degeneração. Os tratamentos atualmente disponíveis revelam resultados inadequados e nenhum é consensualmente designado como o tratamento padrão. Engenheiros têm tentado superar os desafios encontrados, utilizando diferentes biomateriais para desenvolver novas estratégias para produzir implantes adequados (**Cap. I e II**). No entanto, a procura por um implante biomimético “perfeito” permanece um grande desafio. A combinação de técnicas de imagem de alta resolução (ressonância magnética e tomografia micro-computadorizada) com a impressão 3D pode ser uma ferramenta poderosa para mimetizar o tecido fibrocartilagenoso. Esta abordagem promove a produção de implantes reprodutíveis e específicos para cada paciente, ajudando a melhorar o tempo de recuperação e o restabelecimento da biofuncionalidade do tecido (**Cap. III**). O conceito de implantes específicos para cada paciente é explorado nesta tese usando materiais de origem natural, onde a fibroína de seda (SF) desempenha um papel central devido à sua elevada versatilidade de processamento e notáveis propriedades mecânicas. No primeiro trabalho, foram produzidos implantes hierárquicos específicos para cada paciente, impressos indiretamente, combinando SF com fosfatos de  $\beta$ -tricálcio dopados com iões (**Cap. V**). Para além disso, usando uma tecnologia de impressão 3D, desenvolveu-se uma “bioink” de SF usando um processamento rápido (**Cap. VI**). Utilizando um sistema de reticulação com base na enzima peroxidase, foram produzidos implantes 3D específicos para cada paciente (**Cap. VII**). No terceiro trabalho, foi feita uma melhoria em termos de mimetização do DIV cojugando elastina com a “bioink” de SF (**Cap. VIII**). Finalmente, foi desenvolvido um sistema híbrido de impressão 3D baseado em extrusão usando uma “bioink” de goma gelatina/fibrinogénio com células encapsuladas e uma “bioink” de SF metacrilada (**Cap. IX**). Em resumo, estas novas abordagens de impressão 3D revelaram ser alternativas promissoras para a produção de implantes específicos para cada paciente visando a regeneração de fibrocartilagem.

**Palavras-chave:** Bioimpressão, “Biotintas”, Cartilagem, Específico de paciente, Personalizado

## TABLE OF CONTENTS

ACKNOWLEDGMENTS _____	III
STATEMENT OF INTEGRITY _____	IV
ABSTRACT _____	V
RESUMO _____	VI
TABLE OF CONTENTS _____	VII
LIST OF ABBREVIATIONS _____	XI
LIST OF EQUATIONS _____	XXI
LIST OF FIGURES _____	XXII
LIST OF SUPPLEMENTARY FIGURES _____	XXXII
LIST OF TABLES _____	XXXIII
LIST OF SUPPLEMENTARY TABLES _____	XXXIV
SHORT <i>CURRICULUM VITAE</i> _____	XXXV
LIST OF PUBLICATIONS _____	XXXVI
INTRODUCTION TO THE THESIS FORMAT _____	XLI
SECTION 1 _____	1
GENERAL INTRODUCTION _____	1
CHAPTER I - BIOMATERIALS IN MENISCUS TISSUE ENGINEERING _____	3
Abstract _____	3
I-1. Introduction _____	4
I-2. Non-resorbable polymers _____	5
I-3. Resorbable polymers _____	10
I-4. Conclusions and future perspectives _____	21
I-5. References _____	21
CHAPTER II - BIOMATERIALS IN INTERVERTEBRAL DISC TISSUE ENGINEERING _____	29
Abstract _____	29

II-1.	Introduction	30
II-2.	Natural-based Biomaterials	31
II-3.	Synthetic-based Biomaterials	42
II-4.	Final considerations	48
II-5.	References	49
CHAPTER III - RECENT ADVANCES ON 3D PRINTING OF PATIENT-SPECIFIC IMPLANTS FOR FIBROCARILAGE TISSUE REGENERATION		58
Abstract		58
III-1.	Introduction	59
III-2.	3D Printing in Tissue Engineering Approaches	60
III-3.	3D Printing for Fibrocartilage Tissue Regeneration	65
III-4.	Conclusions and future perspectives	72
III-5.	References	73
SECTION 2		77
EXPERIMENTAL DESIGN		77
CHAPTER IV - MATERIALS AND METHODS		79
Overview		79
IV-1.	Materials	80
IV-2.	Reagents	86
IV-3.	Production of patient-specific implants	86
IV-4.	Physico-chemical characterization	94
IV-5.	<i>In vitro</i> biological characterization	104
IV-6.	<i>In vivo</i> studies	113
IV-7.	Statistical analysis	117
IV-8.	References	118
SECTION 3		124
EXPERIMENTAL STUDIES		124
CHAPTER V - INDIRECT PRINTING OF HIERARCHICAL PATIENT- SPECIFIC SCAFFOLDS FOR MENISCUS TISSUE ENGINEERING		126

Abstract	126
V-1. Introduction	127
V-2. Materials and Methods	130
V-3. Results	138
V-4. Discussion	148
V-5. Conclusions	153
V-6. Acknowledgments	153
V-7. References	153
V-8. Supplementary material	158
 CHAPTER VI - PATENT - INKS FOR 3D PRINTING, METHODS OF PRODUCTION AND USES THEREOF	 161
Abstract	161
VI-1. Description	162
VI-2. Claims	169
VI-3. Drawings	171
VI-4. References	175
 CHAPTER VII - FAST SETTING SILK FIBROIN BIOINK FOR BIOPRINTING OF PATIENT-SPECIFIC MEMORY-SHAPE IMPLANTS	 177
Abstract	177
VII-1. Introduction	178
VII-2. Materials and Methods	179
VII-3. Results and Discussion	185
VII-4. Conclusions	192
VII-5. Acknowledgments	192
VII-6. References	192
VII-7. Supplementary material	195
 CHAPTER VIII - ENGINEERING PATIENT-SPECIFIC BIOPRINTED CONSTRUCTS FOR TREATMENT OF DEGENERATED INTERVERTEBRAL DISC	 198
Abstract	198
VIII-1. Introduction	199
VIII-2. Materials and Methods	201

VIII-3.	Results and Discussion _____	206
VIII-4.	Conclusions _____	211
VIII-5.	Acknowledgments _____	212
VIII-6.	References _____	212
VIII-7.	Supplementary material _____	214
CHAPTER IX - 3D BIOPRINTING OF A MECHANICALLY REINFORCED HYBRID TISSUE CONSTRUCT FOR ADVANCED FIBROCARILAGINOUS REGENERATION _____		216
Abstract _____		216
IX-1.	Introduction _____	217
IX-2.	Materials and Methods _____	220
IX-3.	Results _____	230
IX-4.	Discussion _____	242
IX-5.	Conclusions _____	243
IX-6.	References _____	244
IX-7.	Supplementary material _____	249
SECTION 4 _____		253
GENERAL CONCLUSIONS _____		253
CHAPTER X - GENERAL CONCLUSIONS AND FUTURE PERSPECTIVES. _____		255
X-1.	General conclusions _____	255
X-2.	Future Perspectives _____	259



## LIST OF ABBREVIATIONS

### A

$\alpha$  - Alpha

$\alpha$ -MEM - Alpha-Minimum Essential Medium

AB - Alamar blue

Abs - Absorbance

ABS - Acrylonitrile butadiene styrene

ACUC - Animal Care and Use Committee

AF - Annulus fibrosus

anti-TNF $\alpha$  - Anti tumor necrosis factor alpha

APPACDM - The Portuguese Association of Parents and Friends of Mentally Disabled Citizens

ATP - Adenosine triphosphate

ATR - Attenuated Total Reflectance

ATR - Attenuated total Reflection

ATR-FTIR - Attenuated total reflectance fourier transform infrared spectroscopy

Au - Gold

### B

$\beta$  - Beta

$\beta$ -sheet - Beta-sheet

$\beta$ -TCP - Beta-tricalcium phosphate

BC - Bacterial cellulose

BEP - Bony endplate

b-FGF - Basic fibroblast growth factor

### C

Cap. - Capitulo

Chap. - Chapter

Ca<sup>2+</sup> - Calcium ion  
CAD - Commercial computer aided design  
Calcein-AM - Calcein-Acetoxyethyl  
CaP - Calcium phosphate  
CEPs - Cartilaginous end-plates  
CH - Close from the head  
Cl<sup>-</sup> - Chloride ion  
cm - Centimeter  
cm<sup>-1</sup> - Reciprocal wavelength centimeter  
CMI - Collagen meniscus implant  
CO<sub>2</sub> - Carbon dioxide  
CPT - Current procedural terminology  
CS - Chondroitin sulfate  
CTGF - Connective tissue growth factor

## **D**

°C - Degree Celsius  
d - Day  
DAPS - Disc-like angle-ply structure  
DCB - Decellularized bone  
DEX - Dexamethasone  
DGAV - Direcção Geral de Alimentação e Veterinária  
DLP - Digital light processing  
DMA - Dynamic mechanical analysis  
DMAB – Dimethylaminobenzaldehyde  
DMB – Dimethylmethylene blue  
DMEM - Dulbecco's modified Eagle's medium.  
DMSO – Dimethylsulfoxide

DNA - Deoxyribonucleic acid

dsDNA - Double stranded DNA

## **E**

$E$  - Elastic modulus

*e.g.* – “for example”, form latin *exempli gratia*

$E'$  - Storage modulus

ECM - Extracellular matrix

*et al.* -And others

Ex/Em – Excitation/Emission

## **F**

FB - Fibrin

FBS - Fetal bovine serum

FCT - Foundation for Science and Technology

FDA - U.S. Food and Drug Administration

FDM - Fused deposition modeling

FGF-2 - Fibroblast growth factor 2

FH - Far from the head

Fig. - Figure

FITC - Fluorescein isothiocyanate

FLAD - Foundation Luso-American for Development

FLS - Fibroblast-like synoviocytes

FTIR - Fourier Transform Infrared

## **G**

G - Gauge

$G'$  - Storage modulus

$G''$  - Loss modulus

GAG - Glycosaminoglycan

GAGs - Glycosaminoglycans

GCSN - Glucosamine

GEL - Gelatin

GelMA - Gelatin methacrylated

GFs - Growth factors

GG - Gellan Gum

GH - Gelatin hydrogel

GlcNAc - N-acetyl-glucosamine

## **H**

<sup>1</sup>H-NMR - Hydrogen-1 nuclear magnetic resonance

h - Hour

H&E - Hematoxylin and Eosin

H<sub>2</sub>O - Water

H<sub>2</sub>O<sub>2</sub> - Hydrogen peroxide

HA - Hyaluronic acid

HANFS - Hyaluronic acid–nanofibrous scaffold

HAp - Hydroxyapatite

hASCs - Human adipose stem cells

HCL - Hydrochloric acid

HCO<sub>3</sub><sup>2-</sup> - Bicarbonate ion

HDC - High density gel

Hi - Hierarchical scaffolds

hMCs - Human meniscus cells

hMSCs - Human mesenchymal stem cells

hNDFs - Human neonatal dermal fibroblasts

hOBs - Human osteoblasts

HPO<sub>4</sub> - Hydrogen phosphate ion

HRP - Horseradish peroxidase

HUVECs - Human umbilical vein endothelial cells

Hz - Hertz

## I

IAF - Inner annulus fibrosus

*i.e.* - "in other words", form latin *id est*

IFIT3 - Interferon-induced protein with tetratricopeptide repeats 3

IGF-1 - Insulin-like growth factor

IGFBP3 - Insulin-like growth factor-binding protein-3

iGG-MA - Ionic-cross-linked methacrylated gellan gum

IL-1ra - Interleukin-1 receptor antagonist

IL-1 $\beta$  - Interleukin-1 beta

IL-6 - Interleukin 5

IMS - Injection molding system

ITOP - Integrated tissue-organ printer

ITS - Insulin-transferrin-selenium

IVD - Intervertebral disc

## K

K<sup>+</sup> - Potassium ion

kD - Kilodalton

Kg - Kilogram

kN - Kilonewton

kPa - Kilopascal

## L

L - Liter

L<sub>i</sub> SMA - Lysine integration signal of SF

L<sub>i</sub> SMA - Lysine integration signal of Silk-MA

L1-L2 IVD - Lumbar vertebra number 1 and lumbar vertebra number 2 of the intervertebral disc

LBP - Low back pain

LiBr - Lithium bromide

LMW HA - Low molecular weight hyaluronic acid

## **M**

µg - Microgram

µg.DNA - Microgram of Deoxyribonucleic acid

µm - Micrometer

m/v - Mass/volume

m - Meter

M - Molar

$m_{d,t}$  - Weight of the degraded sample at each time point

mg - Milligram

Mg<sup>2+</sup> - Magnesium ion

MHz - Megahertz

$m_i$  - Initial weight

Micro-CT - Micro-computed tomography

min - minute

mL - Milliliter

mm - Millimeter

mM - Millimolar

MMP-13 - Matrix metalloproteinase 13

MPa - Megapascal

MPCs - Mesenchymal precursor cells

MRI - Magnetic resonance imaging

MSCs - Mesenchymal stem cells

MT - Masson's trichrome

$m_{w,t}$  - Wet weight of the sample at each time point

mw/cm<sup>2</sup> - Millwatt/square centimeter

MWCO - Molecular weight cut off

## **N**

N - Newton

$n$  - Number of samples

Na<sup>+</sup> - Sodium ion

Na<sub>2</sub>CO<sub>3</sub> - Sodium carbonate

Na<sub>2</sub>CO<sub>3</sub> - Sodium carbonate

NaCl - Sodium chloride

NaOH - Sodium hydroxide

NFC - Nanofibrillated cellulose

nm - Nanometers

NP - Nucleus pulposus

## **O**

NR4A1 - Orphan nuclear receptor 4A1

OAF - Outer annulus fibrosus

## **P**

$p$  - Statistical level of significance

Pa - Pascal

PBS - Phosphate-buffered saline

PCL - Polycaprolactone

PCLA-PEG-PCLA - Poly( $\epsilon$ -caprolactone-co-lactide)-b-poly(ethylene glycol)-b-poly( $\epsilon$ -caprolactone-co-lactide)

PCL-T - Poly(caprolactone-triol)

PCU - Polycarbonate-urethane

Pd - Palladium

pDNA - Plasmid Deoxyribonucleic acid

PEGDE - Polyethylene glycol diglycidyl ether

PEGTA - Poly(ethylene glycol)-tetra-acrylate

PET - Polyethylene terephthalate

PGA - Poly(glycolic acid)

pH - Potential hydrogenionic

PHAs - Poly( $\alpha$ -hydroxy acids)

PI - Propidium iodide

PLA - Poly(lactic acid)

PLDLA - Poly(L-co-D,L-lactic acid)

PLGA - Poly [(lactic acid) -co- (glycolic acid)]

PLLA - Poly(L-lactic acid)

PMCs - Pig meniscus cells

PMs - Poly(ethylene glycol) diacrylate-derived microcryogels

PPD - Poly(p dioxanone)

PPF - Poly(propylene fumarate)

ppm - Part per million

PRP - Platelet-rich plasma

PTFE - Polytetrafluorethylene terephthalate

PTMC - Poly(trimethylene carbonate)

PU - Polyurethanes

PU-PLLA - Poly(urethane)-poly(L-lactide)

PVA - Poly(vinyl alcohol)

PVA-H - Poly(vinyl alcohol) hydrogel

## **R**

Ref. - Reference

RF - Rivoflavin

RFU – Relative fluorescence units



RGD - Arginine-glycine-aspartic acid

RPM - Rotations per minute

RT - Room temperature

## **S**

s - Seconds

SBF - Simulated Body Fluid

SD - Standard deviation

SEM - Scanning Electron Microscopy

SF - Silk fibroin

SI - Silk ink

SiI-MA - Silk methacrylated

SMMs - Shape memory materials

Sn - Strontium

SO<sub>4</sub><sup>2-</sup> - Sulfate ion

SP - Sodium pyruvate

## **T**

3D - Three-dimensional

TA - Tannic acid

Tan  $\delta$  - Loss factor

TE - Tissue Engineering

TGF- $\beta$ 1 - Transforming growth factor Beta 1

TGF- $\beta$ 3 - Transforming growth factor- $\beta$ 3

TLR4 - Toll-like receptor 4

TMJ - Temporomandibular joint

## **U**

U - Units

UV - Ultraviolet

## **V**

v/v - Volume/volume

VBs - Vertebral bodies

## **X**

XRD - X-Ray Diffraction

## **W**

$\lambda$  - Wavelength

w/v - Weight/volume

w/w - Weight/weight

wt% - Percentage of weight

## **Z**

Zn - Zinc

## LIST OF EQUATIONS

Equation IV-1 - Determination of the methacrylation degree. ....	97
Equation IV-2 - Determination of swelling ratio. ....	102
Equation IV-3 - Determination of weight loss ratio. ....	102
Equation IV-4 - Determination of the volume by the displacement method. ....	117
Equation V-1 - Determination of weight loss ratio. ....	133
Equation V-2 - Determination of swelling ratio. ....	133
Equation VII-1 - Determination of weight loss ratio. ....	182
Equation VIII-1 - Determination of weight loss ratio. ....	203
Equation VIII-2 - Determination of swelling ratio. ....	203
Equation IX-1 - Determination of methacrylation degree. ....	222
Equation IX-2 - Determination of swelling ratio. ....	223
Equation IX-3 - Determination of the volume by the displacement method. ....	228

## LIST OF FIGURES

Figure I-1 - Biomaterials in meniscus tissue engineering. (PET: Polyethylene terephthalate; PTFE: Polytetrafluorethylene terephthalate; PVA-H: Poly(vinyl alcohol) hydrogel; PCU: Polycarbonate-urethane; PHAs: Poly( $\alpha$ -hydroxy acids); PCL/HA: Polycaprolactone/Hyaluronic acid; PU: Polyurethanes). .....	5
Figure I-2 - Polycarbonate-urethane meniscal implant, with the stainless steel fixation bolt in the unfastened (I) and fastened state (II). Reprinted with permission from [25]. Copyright 2010, Springer.....	8
Figure I-3 - The total meniscus implant is augmented with circumferential PLA fibers. Reprinted with permission from [43]. Copyright 2006, Elsevier. ....	12
Figure I-4 - Actifit: appearance of the implant to the naked eye. Scale bar: 10 mm.....	14
Figure I-5 - Silk meniscus scaffold. Scale bar: 10 mm.....	17
Figure I-6 - CMI for the lateral meniscus (a) and CMI for the medial meniscus (b). ....	19
Figure II-1 - Gross anatomy of a disc. (a) Cross section of a disc in the coronal plane, (b) diagram of a transversely sliced IVD and (c) diagram showing the alternating fiber alignment in successive lamellae. AF: annulus fibrosus; CEP: cartilaginous endplate; BEP: bony endplate; NP: nucleus pulposus. ....	30
Figure II-2 - Pictures showing cell leakage in free cell injection group and leak-proof in poly(ethylene glycol) diacrylate-derived microcryogels (PMs) assisted cell delivery group <i>ex vivo</i> . (B) Scheme of a possible mechanism responsible for the leak-proof of the PMs injectable system. (C) Hematoxylin and eosin staining at 24 weeks showing a better IVD restoration when PMs+MSCs are used comparing with the control group (Sham) (Scale bar: 3mm). Reprinted with permission from [16]. .....	32
Figure II-3 - (A) Intraoperative images of the exposed disc space and implanted scaffold. (B) Pictures of the native IVD, the scaffold at day 0 and the implanted scaffold after 6 months of implantation. Reprinted with permission from [22]......	34
Figure II-4 - (A) Bovine caudal IVD samples were evaluated in three groups (Intact, Injured and Repaired). (B) Pictures of sagittal sections taken at Day 6. (Bi) Macroscopic image of the repaired IVD using the injected Fibrin-genipin system. (Bii) Microscopic images of sections stained with	

FAST from the intact IVD. (Biii and Biv) Microscopic images of sections stained with FAST from the repaired IVD. Reprinted with permission from [37].	37
Figure II-5 - (A) AF-like patient-specific implant before freeze-drying and (B) after freeze-drying (scale bars: 10 mm). (C) 3D reconstruction of AF substitute by Micro-CT (scale bar: 1mm). Reprinted with permission from [64].	41
Figure II-6 - (A) Enrolment of the electrospun fibers to produce the disc-like angle-ply structure (DAPS) (bottom) (scale bar: 1mm). (B) DAPS implantation into the rat caudal spine into the C8/C9 disc space. (C) Hematoxylin and eosin staining of sections at day 14 and day 28 after implantation for the discectomy group (Ci and Cii) and DAPS group (Ciii and Civ). (Cv and Cvi) Polarized pictures of the DAPS group after 14 and 28 days of implantation. Scale bar: 1mm. Reprinted with permission from [75].	43
Figure II-7 - (A) Multi-layered PU construct scaffold using a Teflon® tube. (B) Multi-layered PU scaffolds placed within a spinner flask bioreactor. (C) Immunofluorescence images of the outer (OAF) and inner (IAF) AF tissue formation using the indicated medium formulation. FBS: fetal bovine serum, ITS: insulin-transferrin-selenium, DEX: dexamethasone, SP: sodium pyruvate. * indicates PU scaffold. Scale bar: 100 µm. Reprinted with permission from [91].	46
Figure III-1 - Panel (A) depicts nanofibers containing a mix of nanoparticles. Scale bar represents 10 µm. The fluorescent micrograph in panel (B) illustrates two types of proteins electrospun and aligned perpendicular to each other. Scale bar represents 5 µm. Panel (C) shows a representative optical micrograph of a functional scaffold collected over 30 minutes. The scale bar denotes 50 µm. Adapted with permission from Suwan N. Jayasinghe [19].	61
Figure III-2 - Schematic diagram of bioprinted perfusable tubes displaying different outer diameters (A) and with the same outer but different inner diameters (B), and representative fluorescence micrographs. (C) Fluorescence photographs before (inset) and after injection with red fluorescent microbeads into the lumen of the single, continuous bioprinted tube. Adapted with permission from Jia <i>et al.</i> [29].	63
Figure III-3 - Design of the digitally tunable continuous multi-material extrusion bioprinter and multi-material bioprinting of 3D constructs. (A) Schematic representation showing the design of the seven-channel printhead connected to reservoirs that are individually actuated by programmable pneumatic valves. (B) Images of bioprinted (i) human organ-like constructs from multiple bioinks,	

including brain, lung, heart, liver, kidneys, pancreas, stomach, small/large intestines, bladder, and prostate (the organ-like constructs presented in this image were individually printed, photographed, and stitched together at relative locations as those in the human body); (ii) brain; (iii) lung vasculature; (iv) kidney; (v) left atrium of heart and (vi) bladder/prostate. Adapted with permission from Liu *et al.* [35]. ..... 65

Figure III-4 - Cell-free 3D printing approaches for fibrocartilage regeneration. (A) Anatomic reconstruction of human meniscus. Human meniscus scaffolds were 3D-printed by layer-by-layer deposition of PCL fibers (100  $\mu\text{m}$  diameter), forming 100 to 200  $\mu\text{m}$ -channels. (B) PLGA  $\mu\text{S}$  encapsulating CTGF and TGF- $\beta$ 3 were in physical contact with PCL microfibers. (C) Fluorescent dextrans simulating CTGF (green, 40 kD) and TGF- $\beta$ 3 (red, 10 kD) were delivered into the outer and inner zones, respectively, of human meniscus scaffolds to show scaffold loading. Distribution of dextrans was maintained from day 1 to day 8. (D) A scaffold was prepared for implantation with 2-0 Ethibond suture. The sheep medial meniscus was exposed by dislocating femoral condyle, followed by scaffold implantation. (E) Schematic process of the design of a porous meniscus implant composed by PTMC. (F) Porous meniscus scaffold after extraction and drying. Adapted with permission from (A-D) Lee *et al.* [42] and (E-F) Van Bochove *et al.* [43]. ..... 67

Figure III-5 - 3D printing cell-free approach using a fast setting enzymatic-cross-linked silk based bioinks. (A) Patient-specific silk fibroin human meniscus implant. (B) Representative image showing dead and live cells in 3D bioprinted silk fibroin constructs after 7 days of culture. (C) Patient-specific silk fibroin/Elastin human annulus fibrosus implant. (D) Representative image showing dead and live cells in 3D bioprinted silk fibroin/Elastin constructs after 21 days of culture. (E) i) Patient-specific memory-shape meniscus implant into Instron platform, ii) initial appearance before compression, iii) implant under a compressive strain of 80%, iv) returning to original shape. (F) Stress-strain plot of cyclic uniaxial compression test (five cycles). (G) Compressive stress of cyclic uniaxial compression test as function of strain (25%, 50%, and 80%). (E), (F) and (G) adapted with permission from Costa *et al.* [46]. ..... 68

Figure III-6 - Cell-laden 3D printing approaches for fibrocartilage regeneration. (A) Side and (B) top view of 3D printed sheep meniscus implant. (C) Representative images (at 4 $\times$  magnification) showing dead and live cells in 3D bioprinted constructs after 7 days of culturing. (D) Meniscus and (E) IVD printed grafts. IVD graft was printed with Bioink+Cartilage particles stained red (nucleus pulposus) and with Bioink+HA (annulus fibrosus). (F) Live dead staining from a central slice of a printed

young adult size nose graft. Adapted with permission from (A-C) <i>et al.</i> Markstedt <i>et al.</i> [50] and (D-F) Kesti <i>et al.</i> [52].	70
Figure IV-1 - Scheme representing the SF protein composition. (A) H-L complex formation. (B) H-chains organizing themselves together into $\beta$ -sheet structures. (C) $\beta$ -sheet structures linked by amorphous domains.	80
Figure IV-2 - Silk cocoons degumming process. (a) <i>Bombyx mori</i> silk cocoons. (b) Degumming process. (c) Purified SF after degumming procedure. Scale bar: 2 mm.	81
Figure IV-3 - ZnSr-doped $\beta$ -TCP particles. Scale bar: 2 mm.	83
Figure IV-4 - Acrylonitrile, butadiene and styrene chemical structure.	83
Figure IV-5 - Elastin chemical structure.	84
Figure IV-6 - Repeating units of chemical structure of a) native and b) deacetylated gellan gum.	85
Figure IV-7 - Representative scheme of the production of the indirect printed hierarchical patient-specific scaffolds.	88
Figure IV-8 - Envisiontec 3D Bioplotter. Scale bar: 10 cm.	89
Figure IV-9 - Scheme of the 3D bioprinting of cell-laden hybrid scaffolds: (A) printing of hybrid 3D constructs using a Silk-MA bioink and a cell-laden GG/FB bioink. (B) 3D bioprinting and post-printing processes for the production of 3D hybrid constructs and respective patterning. (UV: Ultraviolet light).	93
Figure IV-10 - Nova NanoSEM 200 (FEI). Scale bar: 10 cm.	94
Figure IV-11 - Micro-CT Skyscan 1072 scanner (Skyscan, Kontich). Scale bar: 10 cm.	95
Figure IV-12 - FTIR spectroscopy (Perkin-Elmer 1600 series equipment). Scale bar: 10 cm.	96
Figure IV-13 - Kinexus pro+ rheometer (Malvern Instruments). Scale bar: 10 cm.	98
Figure IV-14 - Instron 4505 Universal Machine (Instron Corporation). Scale bar: 10 cm.	99
Figure IV-15 - DMA TRI-TEC8000B model (Triton Technology manufacturer). Scale bar: 10 cm.	101
Figure IV-16 - Animal and sample distribution for <i>in vivo</i> animal assay.	114
Figure IV-17 - Animal and sample distribution for <i>in vivo</i> animal assay.	115

Figure IV-18 - Scheme describing how to determine the volume of the samples after subcutaneous implantation.....	116
Figure V-1 - Scheme of the production of indirect printed scaffolds. (a) Different steps were required to produce indirect printed cube-shape hierarchical scaffolds: (ai) design of the negative mold, (aii) printing of the negative mold, (aiii) mold casting of the SF, and (aiv) SF blending with $\beta$ -tricalcium phosphate. The same strategy was used to produce patient-specific indirect printed hierarchical scaffolds of human meniscus: (bi) model of the negative mold, (bii) patient-specific meniscus scaffold, and (biii) patient-specific meniscus scaffold tightly compressed and total original shape recovery. Scale bars: 1cm. ....	139
Figure V-2 - Macroscopic images of the indirect printed cube-shape scaffolds. (a-b) Macroscopic images of the negative molds, (c-d) Hi8, and (e-f) Hi16. Scale bars: 2 mm (a-c and e); and 1 mm (d and f). ....	140
Figure V-3 - SEM images and 3D reconstruction of the indirect printed hierarchical scaffolds. (a) SEM images of Hi8 and Hi16 scaffolds at different magnifications from the top layer (ai, aii and av, avi, respectively) and bottom layer (aiii, aiv and avii, aviii, respectively). (b) 3D reconstruction by micro-CT of the Hi8 and Hi16 (bi and biv, respectively), 2-D images from the top layer (bii and bv, respectively), and bottom layer (biii and bvi, respectively). Scale bars: 500 $\mu$ m (ai, iii, v and vii), 50 $\mu$ m (aii, vi, iv and viii), and 1 mm (bi-vi). ....	142
Figure V-4 - Chemical analysis, degradation and swelling behavior, and mechanical performance of the indirect printed hierarchical scaffolds. (a) ATR-FTIR spectra of the Hi8 and Hi16 top and bottom layers. (b-c) Degradation and swelling profiles of the Hi8 and Hi16, obtained in protease XIV and PBS solutions, respectively. (d-e) Storage modulus ( $E'$ ) and damping properties of the Hi8 and Hi16 obtained by DMA. (f) Stress-strain plot of the Hi8 and Hi16 and respective compressive modulus. ....	145
Figure V-5 - SEM micrographs of Hi8 top (a) and bottom (b) layers, and Hi16 top (d) and bottom (e) layers after 7 days of mineralization, and respective Ca and P wt.% obtained from EDS analysis after mineralization. Scale bars: 50 $\mu$ m (a, b, d and e); 5 $\mu$ m (c and f). ....	146
Figure V-6 - <i>In vitro</i> biological performance of the different layers of the indirect printed hierarchical scaffolds. (a) Live/dead staining of the SF8, SF16, SF8/TCP and SF16/TCP after 1, 3 and 7 days of culturing. (b) Metabolic activity by Alamar Blue assay normalized with DNA content. Results were obtained after 1, 3 and 7 days of culturing for the SF8 and SF16 (bi), and SF8/TCP and	



SF16/TCP (bii). Statistically significant differences were represented by * ( $p < 0.5$ ), ** ( $p < 0.01$ ), and *** ( $p < 0.001$ ). Scale bars: 200 $\mu\text{m}$ . .....	147
Figure V-7 - Subcutaneous implantation of the different layers of the indirect printed hierarchical scaffolds in CD-1 mice for 8 weeks. (a) Macroscopic images of the explants after 8 weeks of implantation. (b) H&E staining, and (c) MT staining of the explants. Scale bars: 4 mm (a) and 200 $\mu\text{m}$ (b and c). .....	148
Figure VI-1 - Schematic representation of the preparation of SF ink for 3D printing. ....	171
Figure VI-2 - 3D Printing of 3D structures a) 2-layer cube shape structure before freeze-drying and b) after freeze-drying. c) 6 layer cube shape (30x30mm) 3D structure. d) 6 layer cube shape (5x5 mm) structure after freeze-drying. e) human meniscus implant before freeze drying and f) after freeze-drying. Scale bars: 500 $\mu\text{m}$ (a and b); 1 mm (d, e and f); 10 mm (c). ....	171
Figure VI-3 - Steady-Shear rheological measurements (frequency 1 Hz) for enzymatically cross-linked silk inks at different concentration (8% (w/v) and 16% (w/v) of silk solution). ....	172
Figure VI-4 - Oscillatory rheological measurements (frequency 1 Hz) for enzymatically cross-linked silk inks at different concentration (8% (w/v) and 16% (w/v) of silk solution). ....	172
Figure VI-5 - Printed structures using S16 ink. (a) 1 layer, (b) 2 layers, (c) 4 layers, and (d) 5 layers cube shape printed structure. e), f) stereomicroscope images from 2 layers structures. g) 8 layers cube shape structure (30x30x4mm). .....	173
Figure VI-6 - 3D printed structures before (a and c) and after freeze-drying (b and d). .....	173
Figure VI-7 - ATR-FTIR spectra for the 3D structures after printing (day 0), after 7 days immersed in PBS (day 7), and after freeze drying (Freeze dry). .....	173
Figure VI-8 - Loss moduli ( $\tan \delta$ ) of the 3D structures obtained by DMA, tested at 37 °C in PBS. ....	174
Figure VI-9 - Storage modulus ( $E'$ ) of the 3D structures obtained by DMA, tested at 37 °C in PBS. ....	174
Figure VI-10 - SEM images of the 3D structures after freeze-drying. Scale bars: 500 $\mu\text{m}$ (a and b), and 100 $\mu\text{m}$ (c). .....	175
Figure VII-1 - Rheological behavior of silk fibroin (SF) bioinks and 3D Printing of 3D scaffolds. (a) Extrusion of silk by spider. (b) (i) Oscillatory rheological measurements as function of frequency (n=3), (ii) oscillatory rheological as function of shear stress (n=3), (iii) steady shear measurements at frequency of 1 Hz (n=3), and (iv) tack adhesion measurements (n=3). (c) Extrusion of SI25	

bioink. (d) (i) SF with amorphous scaffold (conformation before freeze-drying), (ii) SF with crystalline scaffold ( $\beta$ -sheet conformation) after freeze-drying, (iii) 6-layer cube shape 3D scaffold, (iv) 6 layer cube shape 3D scaffold after freeze-drying, (v) patient-specific memory-shape meniscus implant before freeze-drying, and (vi) after freeze-drying. Statistical significant differences were represented by \* ( $p < 0.5$ ), \*\* ( $p < 0.01$ ) and \*\*\* ( $p < 0.001$ ). Scale bars: 500  $\mu\text{m}$  (di and dii); 1 mm (div); 10 mm (diii, dv and dvi)..... 186

Figure VII-2 - Characterization of 3D silk scaffolds. (a) Chemical characterization of 3D scaffolds. FTIR spectra of the 3D scaffolds (day 0, day 7 and after freeze-drying) ( $n=3$ ). (b) *In vitro* degradation test. Degradation profile using 0.5 U.mL<sup>-1</sup> of protease XIV solution for the 3D scaffolds (day 0 and freeze-drying) ( $n=3$ ). (c) Storage modulus and (d) loss modulus of 3D scaffolds as function of frequency (0.1 to 10 Hz) ( $n=3$ ). (e) (i) Patient-specific memory-shape meniscus implant into Instron platform, (ii) initial appearance before compression, (iii) implant under a compressive strain of 80%, (iv) returning to original shape. (f) Stress-strain plot of cyclic uniaxial compression test (5 cycles) ( $n=3$ ). (g) Compressive stress of cyclic uniaxial compression test as function of strain (25%, 50% and 80%) ( $n=3$ ). ..... 189

Figure VII-3 - Morphology and *in vitro* biological evaluation of bioprinted SF scaffolds after freeze-drying. Evaluation was performed after 1, 3 and 7 days of culturing in scaffolds seeded hASCs. (a) SEM image of freeze-dried scaffolds. (b) SEM image of freeze-dried scaffolds at higher magnification. (c) 3D reconstruction by Micro-CT. (d) 3D reconstruction of patient-specific human meniscus implant. (e) Calcein AM and propidium iodide staining. (f) SEM image of the bioprinted scaffolds seeded with hASCs after culture for 7 days. (g) Metabolic activity by Alamar Blue assay normalized with DNA content. Statistical significant differences were represented by \* ( $p < 0.5$ ), \*\* ( $p < 0.01$ ) and \*\*\* ( $p < 0.001$ ). Scale bars: 500  $\mu\text{m}$  (a); 100  $\mu\text{m}$  (b); 1 mm (c); 2.5 mm (d); 200  $\mu\text{m}$  (e) and 50  $\mu\text{m}$  (f). ..... 191

Figure VIII-1 - Physico-chemical characterization of 3D SF/elastin scaffolds. (a) FTIR spectra. (b) Degradation profile in 0.5 U.ml<sup>-1</sup> of protease XIV solution. (c) Swelling profile in PBS solution. (d) Stress-strain plot and compressive modulus. (e) Storage modulus, and (f) loss modulus as function of frequency (0.1 to 10 Hz). ..... 208

Figure VIII-2 - Morphology of 3D SF/elastin scaffolds. (a) SEM image at different magnifications. (b) 3D reconstruction of the 3D scaffolds by Micro-CT. Scale bars: a) 500  $\mu\text{m}$  (i and ii) and 100  $\mu\text{m}$  (iii), and b) 1 mm..... 209

Figure VIII-3 - *In vitro* biological performance of the bioprinted SF/elastin scaffolds seeded with hASCs. Evaluation was performed after 1, 7, 14 and 21 days of culturing. (a) Calcein AM and propidium iodide staining. (b) Metabolic activity by Alamar Blue assay. (c) DNA content. Statistical significant differences were represented by \* ( $p < 0.5$ ), \*\* ( $p < 0.01$ ) and \*\*\* ( $p < 0.001$ ). Scale bar: a) 200  $\mu\text{m}$ . ..... 210

Figure VIII-4 - Production of a patient-specific AF substitute. (a) AF-like implant before freeze-drying and (b) after freeze-drying. (c) 3D reconstruction of AF substitute by Micro-CT. Scale bars: a-b) 10 mm, and c) 1 mm..... 211

Figure IX-1 - Scheme of the 3D bioprinting of cell-laden hybrid scaffolds: (A) printing of hybrid 3D constructs using a Sil-MA bioink and a cell-laden GG/FB bioink. (B) 3D bioprinting and post-printing processes for the production of 3D hybrid constructs and respective patterning. (UV: Ultraviolet light). ..... 219

Figure IX-2 - Physico-chemical and *in vitro* biological characterization of the GG/FB cell-laden bioinks. A GG group without FB was used as control. (A) Viscosity of GG/FB bioinks as function of shear rate. (B) Compressive elastic modulus of 3D GG/FB constructs (cylinders, 12 mm in diameter and 4 mm in thickness) at 3%, 6% and 12% of strain after enzymatic/ionic crosslink. (C) Fluorescence micrographs of encapsulate PMCs in GG and GG/FB4 3D bioprinted constructs showing viability on Day 1, Day 3, Day 7 and Day 14, where live cells were stained in green and dead cells in red. (D) Quantification of metabolic activity of PMCs encapsulated in GG and GG/FB4 3D bioprinted constructs on Day 1, Day 3, Day 7 and Day 14 using the Alamar Blue assay. (E) Quantification of collagen amount produced by the PMCs encapsulated in GG and GG/FB4 3D bioprinted constructs on Day 14 and Day 28. (F) Quantification of glycosaminoglycans amount produced by the PMCs encapsulated in GG and GG/FB4 3D bioprinted constructs on Day 14 and Day 28. (G) Non-polarized (i and iii) and polarized (ii and iv) histological images of GG and GG/FB4 3D cell-laden bioprinted constructs stained with a picosirius red staining after 28 days of culture. Statistical significant differences were represented by \* ( $p < 0.5$ ), \*\* ( $p < 0.01$ ), and \*\*\* ( $p < 0.001$ ). Scale bars: 50  $\mu\text{m}$  (G); 200  $\mu\text{m}$  (C). ..... 232

Figure IX-3 - Physico-chemical and *in vitro* biological characterization of the Sil-MA bioinks. (A) Viscosity of Sil-MA bioinks as function of shear rate. (B) Photographs of 3D Sil-MA constructs (cylinders, 12 mm in diameter and 4 mm in thickness) showing the change of conformation overtime. (C) Compressive elastic modulus of 3D Sil-MA constructs (cylinders, 12 mm in diameter and 4 mm in

thickness) at 12% of strain on Day 0, Day1, Day 7 and Day 14. (D) Scanning electron microscope images of 3D Sil-MA constructs produced using Sil-MA (H) bioink (i and ii), Sil-MA (M) bioink (iii and iv) and Sil-MA (L) bioink (v and vi) at different magnifications. (E) Fluorescence micrographs of seeded PMCs Sil-MA 3D constructs showing viability on Day 1, Day 3 and Day 7, where live cells were stained in green and dead cells in red. (F) Quantification of metabolic activity of PMCs seeded in Sil-MA 3D constructs on Day 1, Day 3 and Day 7 using the Alamar Blue assay. Statistical significant differences: (C) \* ( $p < 0.05$ ) compared with Sil-MA (L) at 0, 7, and 14 days; \*  $p < 0.05$  compared with Sil-MA (M) at 1 day and \*\* ( $p < 0.05$ ) compared with others. (F) N.S.: no significant. Scale bars: 5 mm (B); 200  $\mu\text{m}$  (E). ..... 236

Figure IX-4 - Physical characterization of 3D bioprinted constructs. (A) Stress–strain plot of compressive uniaxial compression test performed in 3D bioprinted constructs. (B) Compressive elastic modulus of 3D bioprinted constructs at 12% of strain on Day 0 and Day 14. (C) Macroscopic images of the 3D bioprinted constructs (Sil-MA (H) and Hybrid) before, under and after compression. (D) Stress-strain plot of the compressive uniaxial cyclic stress-relaxation test performed in the Sil-MA (H) 3D bioprinted constructs. (E) Stress-strain plot of the compressive uniaxial cyclic stress-relaxation test performed in the Hybrid 3D bioprinted constructs. Statistical significant differences: (B) \* ( $p < 0.05$ ) compared with GG/FB4, \*\*N.S.: no significant. .... 238

Figure IX-5 - *In vivo* biological characterization of 3D bioprinted constructs. (A) Scheme of the patterning used for the production of 3D bioprinted constructs and macroscopic images of the explants, 2 weeks, 5 weeks and 10 weeks after subcutaneous implantation. (B) Dimensional changes of the 3D bioprinted constructs after 2 weeks, 5 weeks and 10 weeks of subcutaneous implantation. (C) Compressive elastic modulus of 3D bioprinted constructs at 12% of strain after 2 weeks, 5 weeks and 10 weeks of subcutaneous implantation. Statistical significant differences: (B) and (C) \* ( $p < 0.05$ ), \*\*N.S.: no significant..... 239

Figure IX-6 - Histological analysis and quantification assays of the 3D bioprinted constructs after 2 weeks, 5 weeks and 10 weeks of subcutaneous implantation. (A) Histological images of GG/FB4 3D bioprinted cell-laden constructs stained with a Hematoxylin & Eosin, Safranin-O, Masson’s trichrome. (B) Histological images of hybrid 3D bioprinted cell-laden constructs stained with a Hematoxylin & Eosin, Safranin-O, Masson’s trichrome (C) Quantification of collagen deposition of the Sil-MA (H), GG/FB4, hybrid and GG/F4 without cells 3D bioprinted constructs. (D) Quantification of glycosaminoglycans deposition of the Sil-MA (H), GG/FB4, hybrid and GG/F4

without cells 3D bioprinted constructs. Statistical significant differences: \* ( $p < 0.05$ ) compared with GG/FB4 (-cells), \*\* ( $p < 0.05$ ) compared with Sil-MA (H), † ( $p < 0.05$ ) compared with others. Scale bars: 200  $\mu\text{m}$ . ..... 240

Figure IX-7 - Histological analysis and image analysis using MatLab, CT-FIRE, and CurveAlign of the 3D bioprinted constructs after 2 weeks, 5 weeks and 10 weeks of subcutaneous implantation. (A) Histological images of GG/FB4 3D bioprinted cell-laden constructs stained with Alcian Blue/Sirius red (not polarized and polarized images). (B) Histological images of hybrid 3D bioprinted cell-laden constructs stained with Alcian Blue/Sirius red (not polarized and polarized images). (C) Measured average percentage of each collagen fiber color in GG/FB4 3D bioprinted cell-laden constructs using a custom MATLAB code. (D) Measured average percentage of each collagen fiber color in hybrid bioprinted cell-laden constructs using a custom MATLAB code. (E) Representative polarized images of the GG/FB4 and hybrid 3D bioprinted cell-laden constructs (10 weeks after implantation) and Pig meniscus (native) at higher magnification that were used in the alignment analysis. (F) Alignment analysis of the fibers using a CruveAlign software (Laboratory for Optical and Computational Instrumentation, University of Wisconsin-Madison) where each fiber was overlaid and converted into a direction heat map to quantify the alignment coefficient; with zero being no alignment and one being complete alignment. Statistical significant differences: (F) \*  $p < 0.05$  compared with GG/FB4, N.S.: no significant. Scale bars: 100  $\mu\text{m}$  (A) and (B); 20  $\mu\text{m}$  (E). ..... 241

## LIST OF SUPPLEMENTARY FIGURES

Supplementary Figure V-1 - Storage modulus of the SF8, SF16, SF8/TCP and SF16/TCP obtained by DMA. ....	158
Supplementary Figure V-2 - Damping properties of the SF8, SF16, SF8/TCP and SF16/TCP obtained by DMA. ....	158
Supplementary Figure V-3 - Stress-strain plot of the SF8, SF16, SF8/TCP and SF16/TCP obtained in the Instron apparatus. ....	159
Supplementary Figure IX-1 - (A) Oscillatory rheological measurements of the GG/FB bioinks as function of frequency. (B) Steady shear measurements at frequency of 1 Hz of GG/FB bioinks. Cumulative release of FITC dextrans with different molecular weights of 4 kDa (C) and 70 kDa (D) from the GG/FB bioinks. (E) Swelling ratio of 3D GG/FB constructs (cylinders, 12 mm in diameter and 4 mm in thickness) in PBS after 24 hours of immersion. (F) Stress–strain plot of compressive uniaxial compression test performed in 3D GG/FB constructs (cylinders, 12 mm in diameter and 4 mm in thickness) after enzymatic/ionic crosslinking. ....	249
Supplementary Figure IX-2 - Histological images of GG and GG/FB4 3D cell-laden bioprinted constructs stained with a Hematoxylin & Eosin, Safranin-O and Alcian Blue/Sirius red after 14 days (2 weeks) and 28 days (4 weeks) of culture. Scale bars: 50 $\mu$ m. ....	250
Supplementary Figure IX-3 - $^1$ H-NMR spectra and methacrylation degree values of Sil-MA (H), Sil-MA (M) and Sil-MA (L) solutions. Silk solution was used as control.....	250
Supplementary Figure IX-4 - (A) Oscillatory rheological measurements of the Sil-MA bioinks as function of frequency. (B) steady shear measurements at frequency of 1 Hz of Sil-MA bioinks. (C) Stress–strain plot of compressive uniaxial compression test performed in 3D Sil-MA constructs (cylinders, 12 mm in diameter and 4 mm in thickness) after UV crosslinking. (D) Swelling ratio of 3D Sil-MA constructs (cylinders, 12 mm in diameter and 4 mm in thickness) in PBS after 14 days of immersion. ....	251
Supplementary Figure IX-5 - Histological images of GG/FB4 3D bioprinted constructs without cells stained with a Hematoxylin & Eosin, Safranin-O, Masson’s trichrome and Alcian Blue/Sirius red after 2 weeks, 5 weeks and 10 weeks of subcutaneous implantation. Scale bars: 200 $\mu$ m. ....	252

## LIST OF TABLES

Table I-1 - Summary of main studies concerning non-resorbable synthetic biomaterials.....	9
Table I-2 - Summary of main studies concerning resorbable synthetic biomaterials. ....	15
Table I-3 - Summary of main studies concerning resorbable natural biomaterials. ....	20
Table III-1 - Executive summary describing the state-of-art in recent advances on 3D printing of patient-specific implants for fibrocartilage tissue regeneration.....	71
Table IV-1 - Nomenclatures of the GG/FB bioinks. ....	91
Table IV-2 - Ions concentrations in the SBF solution (pH $\approx$ 7.4).....	103
Table V-1 - Microstructure of the indirect printed hierarchical scaffolds analyzed by micro-CT. ....	143
Table VI-1 - Micro-CT results of a 3D structures after freeze dry. Scale bar: 500 $\mu$ m.....	168
Table IX-1 - Nomenclatures of the GG/FB bioinks. ....	220

## LIST OF SUPPLEMENTARY TABLES

Supplementary Table V-1 - Compressive modulus of the SF8, SF16, SF8/TCP and SF16/TCP obtained in the Instron apparatus. ....	159
Supplementary Table VII-1 - Compressive modulus of the 3D Bioprinted scaffolds after freeze-drying over 5 cycles. ....	195
Supplementary Table VII-2 - Pore architecture evaluation of freeze-dried 3D scaffolds using Micro-CT. Values of mean porosity (%), mean pore size ( $\mu\text{m}$ ), and mean trabecular size ( $\mu\text{m}$ ) for micro and macro porosity in the freeze-dried 3D scaffolds. ....	196
Supplementary Table VIII-1 - Pore architecture evaluation of the 3D silk fibroin/elastin scaffolds using Micro-CT. Values of mean porosity (%), mean pore size ( $\mu\text{m}$ ), and mean trabecular size ( $\mu\text{m}$ ) in the 3D scaffolds. ....	214



## **SHORT *CURRICULUM VITAE***

João Pedro Bebiano e Costa was born on the 7<sup>th</sup> of March 1991, in Vila Real, Portugal. He is currently a PhD student at 3B's Research Group (Biomaterials, Biodegradables and Biomimetics), at University of Minho, Headquarters of the European Institute of Excellence on Tissue Engineering and Regenerative Medicine at Avepark, Caldas das Taipas, Guimarães, Portugal. This is a research unit that has been classified by the Foundation of Science and Technology (FCT) as excellent and is part of the Portuguese Associate Laboratory ICVs/3B's. He received his MSc degree in 2015 in Bioengineering, at Faculty of Engineering, University of Porto, Portugal with a final grade of 14 (0-20). In May 2015, he started pursuing his PhD with an awarded Foundation for Science and Technology (FCT) PhD scholarship (PD/BD/113803/2015) at 3B's Research Group, at University of Minho, Portugal, under the supervision of Dr. Joaquim Miguel Oliveira and Prof. Rui L. Reis. In 2018, he spent 9 months at Wake Forest Institute for Regenerative Medicine, Wake Forest University, Winston-Salem, North Carolina, USA, under the supervision of Dr. James Yoo and Dr. Sang Jin Lee. In addition, he was awarded a FLAD scholarship (Fundação Luso-Americana para o Desenvolvimento, Proj. 146/2018) supporting his investigation abroad.

As a result of his research work, he is author or co-author of 14 papers in international journals (10 published, 4 submitted), 1 journal cover, 1 book chapter and 3 filled international patents, 3 abstracts published in international conference proceedings, 5 oral presentations, and 11 poster presentations.

## LIST OF PUBLICATIONS

The work performed during the PhD period resulted in the publications listed below.

### *Papers in international scientific journals with referees (as first author)*

1. **Costa J. B.**, Park J.H., Silva-Correia J., Reis R. L., Oliveira J. M., Atala A., Yoo J. and Lee S. J., "3D Bioprinting of a Mechanically Reinforced Hybrid Tissue Construct for Advanced Fibrocartilaginous Regeneration", (Submitted), 2019.
2. **Costa J. B.**, Silva-Correia J., da Silva Morais A., Pina S., Vieira S., Pereira H., Espregueira-Mendes J., Reis R. L. and Oliveira J. M., "Indirect printing of hierarchical patient-specific scaffolds for meniscus tissue engineering", (Submitted), 2019.
3. **Costa J. B.**, Silva-Correia J., Ribeiro V. P., da Silva Morais A., Oliveira J. M., and Reis R. L., "Engineering patient-specific bioprinted constructs for treatment of degenerated intervertebral disc", *Materials Today Communications*, vol. 19, issue 2019, pp. 506-512, doi:10.1016/j.mtcomm.2018.01.011, 2019.
4. **Costa J. B.**, Silva-Correia J., Reis R. L., and Oliveira J. M., "Current Advances in Solid Free-Form Techniques for Osteochondral Tissue Engineering", *Bio-Design and Manufacturing*, vol. 1, issue 3, pp. 171-181, doi:10.1007/s42242-018-0017-y, 2018.
5. **Costa J. B.**, Silva-Correia J., Reis R. L., and Oliveira J. M., "Recent Advances on 3D Printing of Patient-Specific Implants for Fibrocartilage Tissue Regeneration", *Journal of 3D Printing in Medicine*, vol. 2, issue 3, pp. 129–140, doi:10.2217/3dp-2018-0006, 2018.
6. **Costa J. B.**, Pereira H., Espregueira-Mendes J., Khang G., Oliveira J. M., and Reis R. L., "Tissue Engineering in Orthopedic Sports Medicine", *Journal of ISAKOS (JISAKOS)*, doi:10.1136/jisakos-2016-000080, 2017.
7. **Costa J. B.**, Silva-Correia J., Oliveira J. M., and Reis R. L., "Fast Setting Silk Fibroin Bioink for Bioprinting of Patient-Specific Memory-Shape Implants", *Advanced Healthcare Materials*, vol. 6, issue 22, doi:10.1002/adhm.201701021, 2017.

### *Cover pictures in international scientific journals with referees*

1. **Costa J. B.**, Silva-Correia J., Oliveira J. M., and Reis R. L., " Memory-Shape Implants: Fast Setting Silk Fibroin Bioink for Bioprinting of Patient-Specific Memory-Shape Implants",

Advanced Healthcare Materials, vol. 6, issue 22, Cover picture, Published in 22 November 2017.

*Papers in international scientific journals with referees (as co-author)*

1. Carvalho C.R., **Costa J.B.**, Costa L., Silva-Correia J., Pina S., Moay Z.K., Ng K.W., Reis R.L. and Oliveira J.M., "Enhanced biological performance of chitosan/keratin novel materials for peripheral nerve applications", (Submitted), 2019.
2. Canadas R.F., Morais A., Gasperini L., **Costa J.B.**, Marques A.P., Reis R.L., Oliveira J.M., "Programmed density-based gradients with spatial control over small molecules distribution and mineralization for 3-D tissue interfaces", (Submitted), 2019.
3. Ribeiro V. P., Pina S., **Costa J. B.**, Cengiz I. F., García-Fernández L., Fernández-Gutierrez M., Paiva O. C., Oliveira A. L., San-Román J., Oliveira J. M., and Reis R. L., "Enzymatically Cross-Linked Silk Fibroin-Based Hierarchical Scaffolds for Osteochondral Regeneration", ACS Applied Materials & Interfaces, doi:10.1021/acsami.8b21259, 2019.
4. Carvalho C. R., **Costa J. B.**, Morais A., López-Cebral R., Silva-Correia J., Reis R. L., and Oliveira J. M., "Tunable Enzymatically Cross-linked Silk Fibroin Tubular Conduits for Guided Tissue Regeneration", Advanced Healthcare Materials, vol. 7, issue 17, pp. 1800186, doi:10.1002/adhm.201800186, 2018.
5. Murphy C. A., **Costa J. B.**, Silva-Correia J., Oliveira J. M., Reis R. L., and Collins M. N., "Biopolymers and Polymers in the Search of Alternative Treatments for Meniscal Regeneration: State of the Art and Future Trends", Applied Materials Today, vol. 12, issue 2018, pp. 51-71, doi:10.1016/j.apmt.2018.04.002, 2018.
6. Ribeiro V. P., da Silva Morais A., Maia F. R., Canadas R. F., **Costa J. B.**, Oliveira A. L., Oliveira J. M., and Reis R. L., "Combinatory approach for developing silk fibroin scaffolds for cartilage regeneration", Acta Biomaterialia, vol. 72, pp. 167-181, doi:10.1016/j.actbio.2018.03.047, 2018.
7. Maia F. R., David M., Naot D., da Silva L., Bastos A. R., **Costa J. B.**, Oliveira J. M., Correlo V. M., Reis R. L., and Cornish J., "Differentiation of osteoclast precursors on Gellan Gum-based spongy-like hydrogels for bone tissue engineering", Biomedical Materials, vol. 13, issue 3, doi:10.1088/1748-605X/aaaf29, 2018.

***Conference abstracts published in international scientific journals (as co-author)***

1. Maia F. R., Musson D. S., Naot D., da Silva L. P., Bastos A. R., **Costa J. B.**, Oliveira J. M., Correlo V. M., Reis R. L., and Cornish J., "Gellan Gum Spongy-like Hydrogels Reinforced with Hydroxyapatite for Bone Tissue Engineering Applications", 2017 TERMIS - Americas, vol. 23, issue S1, doi:0.1089/ten.tea.2017.29003.abstracts, 2017.
2. **Costa J. B.**, Silva-Correia J., Ribeiro V. P., da Silva Morais A., Oliveira J. M., and Reis R. L., "Engineering Personalized Constructs for Intervertebral Disc Regeneration", Tissue Engineering Part A, vol. 23, issue S1, pp. S-1-S-159, doi:https://3bs.uminho.pt/, 2017.
3. Oliveira J. M., Carvalho C. R., **Costa J. B.**, and Reis R. L., "Advanced Natural-based Biomaterials To Tackle The Current Challenges In Peripheral Nerve Regeneration", Tissue Engineering Part A, vol. 22, doi:10.1089/ten.tea.2016.5000.abstracts, 2016.

***Book Chapter***

1. **Costa J. B.**, Oliveira J. M., and Reis R. L., "Biomaterials in Meniscus Tissue Engineering", Regenerative Strategies for the Treatment of Knee Joint Disabilities, Studies in Mechanobiology, Tissue Engineering and Biomaterials, Eds. Oliveira J. M., and Reis R. L., vol. 21, doi:10.1007/978-3-319-44785-8\_13, 2017.

***Conference oral presentations (as first author and as speaker)***

1. Costa L., **Costa J. B.**, Oliveira J. M., Reis R. L., and Silva-Correia J., "Evaluating the Effect of Elastin in the Angiogenic Response of Silk Fibroin 3D Printed Scaffolds", Society for Biomaterials 2019, 2019.
2. Costa J. B., **Silva-Correia J.**, Ribeiro V. P., da Silva Morais A., Oliveira J. M., and Reis R. L., "Silk Fibroin/Elastin Bioinks for 3D Printing of Implants Respecting the Patient Intervertebral Disc Anatomy", 2018 Society For Biomaterials Annual Meeting & Exposition, 2018.

***Conference oral presentations (as co-author)***

1. Ribeiro V. P., Pina S., **Costa J. B.**, Cengiz I. F., García-Fernández L., Fernández-Gutierrez M., Oliveira A. L., San-Román J., Oliveira J. M., and Reis R. L., "Enzymatically cross-linked SF/SF- $\beta$  -TCP scaffolds incorporating Sr- and Zn-ions as hierarchical structures for osteochondral tissue engineering applications", Bioceramics 30, 2018.

2. Ribeiro V. P., Pina S., **Costa J. B.**, Cengiz I. F., García-Fernández L., Fernández-Gutierrez M., Oliveira A. L., San-Román J., Oliveira J. M., and Reis R. L., "Enzymatically cross-linked SF/SF- $\beta$ -TCP scaffolds incorporating Sr- and Zn-ions as hierarchical structures for osteochondral tissue engineering applications", *Bioceramics* 30, 2018.
3. Ribeiro V. P., Pina S., **Costa J. B.**, Cengiz I. F., García-Fernández L., Fernández-Gutierrez M., Oliveira A. L., San-Román J., Oliveira J. M., and Reis R. L., "Silk fibroin/ZnSr- $\beta$ -TCP bilayered scaffolds for osteochondral tissue engineering", *Chem2Nature Summer School*, 2018.

*Conference posters (as first author)*

1. **Costa J. B.**, Silva-Correia J., da Silva Morais A., Pina S., Vieira S., Pereira H., Espregueira-Mendes J., Reis R. L. and Oliveira J. M., "Indirect printed patient-specific scaffolds with a bioactive bottom layer for meniscus regeneration", *FORECAST*, 2019.
2. **Costa J. B.**, Silva-Correia J., Reis R. L., and Oliveira J. M., "Novel Enzymatically Cross-linked Silk Fibroin Bioink for Bioprinting of Patient-Specific Memory-Shape Implants for Meniscus Regeneration", *Society for Biomaterials 2019*, 2019.
3. **Costa J. B.**, Silva-Correia J., Ribeiro V. P., Morais A., Oliveira J. M., and Reis R. L., "3D printing of patient-specific silk fibroin/elastin implants for intervertebral disc regeneration", *TERSTEM / FORECAST 2017*, 2017.
4. **Costa J. B.**, Ribeiro V. P., Cengiz I. F., da Silva Morais A., Silva-Correia J., Oliveira J. M., and Reis R. L., "Advanced tissue engineering strategies for biofabrication of complex tissues", *Term Stem 2016*, 2016.

*Conference posters (as co-author)*

1. Pina S., Ribeiro V. P., Canadas R. F., **Costa J. B.**, Cengiz I. F., Reis R. L., and Oliveira J. M., "Bioresorbable Calcium Phosphates Nanocomposites for Tissue Engineering", *CHEM2NATURE Final Conference*, 2018.
2. Ribeiro V. P., Cengiz I. F., Canadas R. F., **Costa J. B.**, Vieira S., da Silva Morais A., Vilela C., García-Fernández L., Fernández-Gutierrez M., San-Román J., Oliveira J. M., and Reis R. L., "Hierarchical bilayered silk fibroin scaffolds containing ZnSr- $\beta$ -TCP particles for osteochondral tissue regeneration", *Chem2Nature*, 2018.

3. Pina S., Ribeiro V. P., Canadas R. F., **Costa J. B.**, Cengiz I. F., Reis R. L., and Oliveira J. M., "Innovative Bioceramics-based Nanocomposites towards Tissue Regeneration", TERMIS WC, 2018.
4. Costa L., **Costa J. B.**, Oliveira J. M., Silva-Correia J., and Reis R. L., "In ovo assessment of the angiogenic response of silk/elastin bioprinted scaffolds", TERM STEM/FORECAST 2017, 2017.
5. Ribeiro V. P., Pina S., **Costa J. B.**, Cengiz I. F., García-Fernández L., Fernández-Gutierrez M., Oliveira A. L., San-Román J., Oliveira J. M., and Reis R. L., "Novel bilayered silk fibroin-based scaffolds incorporating Sr- and Zn-ions for osteochondral tissue engineering", TERM STEM/FORECAST 2017, 2017.

### ***Patents***

1. Carvalho M.R., Caballero D., Carvalho C.R., **Costa J.B.**, Ribeiro V., Oliveira J.M., Kundu S.C., Reis R.L., "Implantable silk hydrogel microfluidic platform, methods of production and uses thereof", 2019.
2. Carvalho C. R., **Costa J. B.**, Ribeiro V. P., Silva-Correia J., Oliveira J. M., and Reis R. L., "Nerve guidance conduits derived from silk fibroin hydrogels: methods of production and uses thereof", WO/2018/025186, Priority date: 109562 01.08.2016 PT, 2018.
3. **Costa J. B.**, Silva-Correia J., Oliveira J. M., and Reis R. L., "INKS FOR 3D PRINTING, METHODS OF PRODUCTION AND USES THEREOF", WO/2018/225049, Priority date: 10136 09.06.2017 PT, 2017.

### ***Awarded grants***

1. Foundation for Science and Technology (FCT) PhD scholarship (PD/BD/113803/2015).
2. FLAD scholarship (Fundação Luso-Americana para o Desenvolvimento, Proj. 146/2018).

## INTRODUCTION TO THE THESIS FORMAT

The present thesis is divided into four main Sections (1 to 4) comprising ten Chapters (I to X). This structure was implemented to permit a suitable organization of the data presented in the various chapters. The **Section 1** addresses a general introduction to the biomaterials and state-of-art strategies used in cartilage regeneration (**Chapters I, II, and III**). The overview of the overall materials and methods used in the thesis is addressed in **Section 2 (Chapter IV)**. In **Section 3**, the experimental results are described and discussed, focusing on the production of patient-specific implants for fibrocartilage applications (**Chapters V to IX**). The main body of the thesis is based on a series of original works published in international journals or submitted for publication. Each individual chapter is presented in a manuscript form, *i.e.*, abstract, introduction, experimental section, results and discussion, conclusion, and acknowledgements. A list of relevant references is also provided as a subsection within each chapter.

Lastly, **Section 4 (Chapter X)** completes this thesis with concluding remarks.

### *Section I – General introduction*

Chapter I – Biomaterials in Meniscus Tissue Engineering: This chapter provides a general overview of last advances in meniscus tissue engineering focusing on the different biomaterials explored in this field.

Chapter II – Biomaterials in Intervertebral Disc Tissue Engineering: This chapter provides a general overview of last advances in intervertebral disc tissue engineering focusing on the different biomaterials explored in this field.

Chapter III – Recent Advances on 3D Printing of Patient-specific Implants for Fibrocartilage Tissue Regeneration: This chapter outlines the recent advances achieved in the 3D printing and biofabrication of patient-specific implants, focusing on the fibrocartilaginous tissue.

### *Section II – Detailed description of experimental materials and methodologies*

Chapter IV – Materials and Methods: A list of the materials, reagents, scaffold's production methods and characterization methods used to achieve the results described in this thesis is provided.

### *Section III – Development of patient-specific implants for fibrocartilage applications*

Chapter V – Indirect printing of hierarchical patient-specific scaffolds for meniscus tissue engineering: This chapter describes the production of indirect printed hierarchical patient-specific scaffolds combining SF and  $\beta$ -tricalcium phosphates. Two different SF concentrations (8% and 16% (w/v)) and several characterization techniques were used. The produced scaffolds showed suitable mechanical properties and good biological performance.

Chapter VI – Patent: INKS FOR 3D PRINTING, METHODS OF PRODUCTION AND USES THEREOF: This chapter refers to a patent that describes the development of a silk-based bioink using an innovative methodology.

Chapter VII – Fast Setting Silk Fibroin Bioink for Bioprinting of Patient-Specific Memory-Shape Implants: This chapter described the application of the new methodology (chapter VI) to produce patient-specific memory-shape implants. A 3D printing extrusion-based technology a novel fast setting SF bioink was developed by means of a horseradish peroxidase-mediated crosslinking system. The 3D bioprinted scaffolds and patient-specific implants exhibited unique characteristics such as good mechanical properties, memory-shape feature, suitable degradation, and tunable pore architecture and morphology.

Chapter VIII – Engineering patient-specific bioprinted constructs for treatment of degenerated intervertebral disc: In this chapter, the innovative methodology (chapter VI) was further explored combining the SF-based bioink with elastin. The SF/elastin bioink was used to bioprint patient-specific substitutes mimicking IVD ultrastructure, in particular the outer region of the IVD (*i.e.* annulus fibrosus, AF). The implantation of custom-made SF/elastin implants that best emulate a patient AF anatomy can potentially open up new personalized treatments for tackling IVD disorders by means of improving recovery time after surgery and helping to restore spine biofunctionality.

Chapter IX – 3D Bioprinting hybrid system to produce patient-specific fibrocartilaginous implants with reinforced mechanical performance and adequate biocompatibility: This chapter describes the application of a Gellan Gum/Fibrin (GG/FB) bioink and a Silk methacrylated (Sil-MA) bioink in an extrusion-based 3D printing hybrid system. This 3D bioprinting hybrid system is believed to offer a versatile and promising alternative, not only for the production of patient-specific fibrocartilaginous implants, but also to be applied in a variety of tissue engineering applications where customizable, mechanically reinforced and biocompatible implants are required.



#### *Section IV – Concluding remarks*

Chapter X – General Conclusions and Future Perspectives: The final section of the thesis presents the general conclusions and implications, current limitations and potential of the work described for application in patient-specific cartilage tissue regeneration. The main conclusions of each chapter as well as future perspectives of the advanced strategies developed in this thesis are provided.

*“Failure is an option here. If things are not failing, you are not innovating enough”*

***Elon Musk***

# **SECTION 1**

## **GENERAL INTRODUCTION**

# Chapter I

## Biomaterials in Meniscus Tissue Engineering

**Biomaterials in Meniscus Tissue Engineering\***

**ABSTRACT**

Meniscus is a complex tissue that plays important roles on the knee performance and homeostasis. The meniscus tissue is very susceptible to injury and despite the great advances in meniscus regeneration area, none of the current strategies for the treatment of meniscus lesions are completely effective. To overcome such great challenge, tissue engineering-based strategies have been attempted. One of the main targets in this research area is to find out a biomaterial or formulations that are able to mimic as much as possible the meniscus native extracellular matrix. In the last few years the characteristics and behaviors of different biomaterials were explored and several processing routes attempted to obtain an adequate architecture for proper cells adhesion, ingrowths, proliferation and differentiation. Herein, the panoply of biomaterials that have been used in meniscus tissue engineering strategies are overviewed.

---

\* This chapter is based on the following publication:

Costa J. B., Oliveira J. M., and Reis R. L., "Biomaterials in Meniscus Tissue Engineering", *Regenerative Strategies for the Treatment of Knee Joint Disabilities, Studies in Mechanobiology, Tissue Engineering and Biomaterials*, Eds. Oliveira J. M., and Reis R. L., vol. 21, doi:10.1007/978-3-319-44785-8\_13, 2017.

## I-1. INTRODUCTION

Meniscus plays an important role on the knee performance and it has been described as “functionless remnants of leg muscle origin” [1]. Due to forces that meniscus can be subjected and his location, he is very susceptible to injury. The mean incidence of meniscal injury in the United States is 66/100,000 [2, 3], which implies over 1 million surgical procedures each year in the United States [4]. Several strategies to repair and replace meniscus have been proposed, but only few of them have been shown to be effective [5]. Currently, the irreparable meniscal lesions are usually treated by partial or (sub) total meniscectomy. The clinical follow-up results showed knee osteoarthritis in all patients 14 years after partial meniscectomy [6], especially in young and middle aged patients [1], which is dramatic in all possible ways.

This is a major orthopedic operation with concomitant risks and costs. Since the current methods are not able to resolve this issue, it is very important to discover new strategies for this common problem in our daily life. Therefore, there has been an increase in scientific and clinical interest to find a meniscal substitute aimed to minimize the risk for developing knee osteoarthritis but also to offer a solution for patients suffering from enduring symptoms post meniscectomy [7]. The panoply of biomaterials that have been tested as a meniscus substitute/scaffold can be divided in two different categories, *i.e.* the non-resorbable polymers and resorbable polymers as depicted in **Figure I-1**. A non-resorbable polymer is used as a permanent implant with biomechanical properties similar of the native tissue. The resorbable polymers, that can be natural or synthetic, are used in strategies which is formed new meniscal tissue while occurs a slow degradation of the scaffold.

As non-resorbable polymers, can be identified biomaterials such as Polyethylene terephthalate (PET), Poly(vinyl alcohol) (PVA) and Polycarbonate-urethane (PCU). Elsner *et al.* [8], for example, developed a PCU synthetic meniscal implant that does not require surgical attachment but still provides the biomechanical function necessary for joint preservation. Regarding to the resorbable polymers, in particular the synthetic, the Polyurethanes (PU) have been widely used in the meniscus regeneration area. A scaffold composed of PU along with Polycaprolactone (PCL) that is another resorbable synthetic polymer, has been tested in clinical environment. A couple of studies have demonstrated that this synthetic scaffold commercially named as Actifit, showed good clinical results [9, 10]. In the last few years, the scientific community is concentrating their efforts on the discovery of biomaterials from natural sources. Natural polymers as collagen, silk, cellulose and gelatin, have shown interesting characteristics to be used as a meniscus substitute biomaterial. Rodkey *et al.* [11], using a collagen

based scaffold, showed that it is safe to implant the collagen meniscal implant leading to a protection of the articular cartilage from damage and a better knee function compared with partial meniscectomy. Herein, it will be made an overview about the different biomaterials and formulations that have been used in meniscus regeneration.

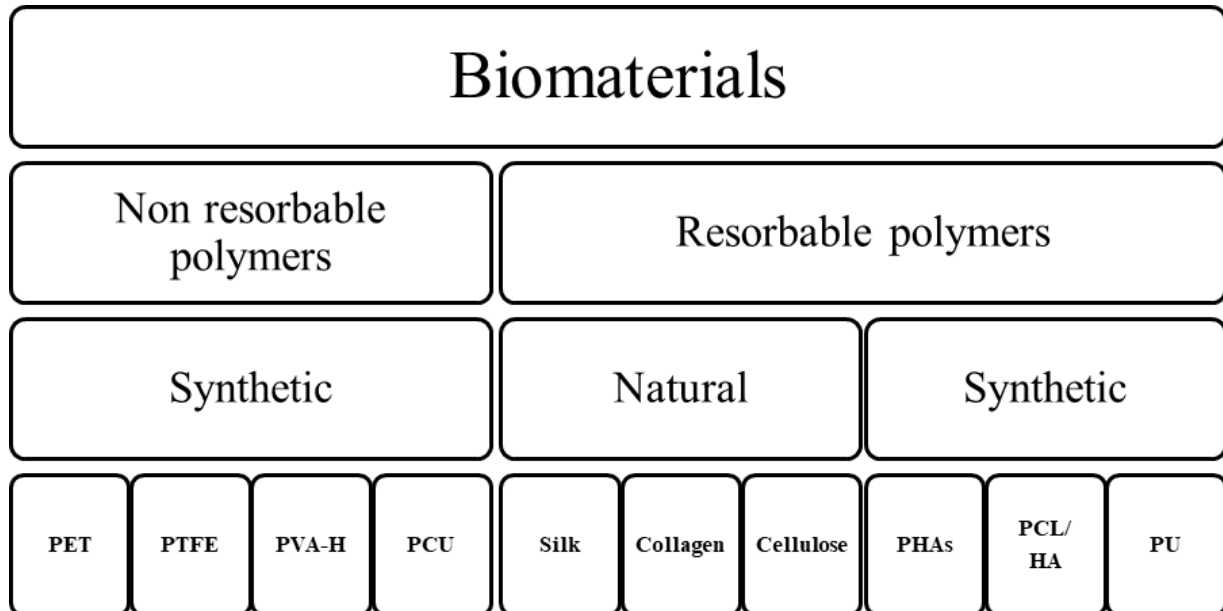


Figure I-1 - Biomaterials in meniscus tissue engineering. (PET: Polyethylene terephthalate; PTFE: Polytetrafluorethylene terephthalate; PVA-H: Poly(vinyl alcohol) hydrogel; PCU: Polycarbonate-urethane; PHAs: Poly( $\alpha$ -hydroxy acids); PCL/HA: Polycaprolactone/Hyaluronic acid; PU: Polyurethanes).

## I-2. NON-RESORBABLE POLYMERS

### I-2.1. Synthetic

#### I-2.1.1. Polyethylene terephthalate (PET)

A permanent prosthesis was evaluated by Sommerlath *et al.* [12]. This meniscus implant was composed by PET and coated with polyurethane. Dacron (PET) is non-resorbable polymer constituted by fibers with an outstanding crease and abrasion resistance [13]. Despite the potential characteristics of this PET implant, the studies reveal disappointing results. Sommerlath *et al.* showed that Dacron implant led to altered joint mechanics, osteophyte formation and synovitis caused by the non-normal biomechanics properties, the improper sizing and the impossibility to match the stress-relaxation of the native meniscus tissue [12].

### I-2.1.2. Polytetrafluorethylene terephthalate (PTFE)

PTFE, also known as Teflon, is a commercial polymer formed by the polymerization of tetrafluorethylene. It has a high molecular weight, is hydrophobic and has a very low coefficient of friction compared with any other solids [13].

Comparing PET and PTFE, it can be said that PTFE has similar compliance to the normal meniscus, showing compressive results more close to native meniscus [14]. However, some studies made by Messner *et al.* [15] in rabbit models proved that Teflon prosthesis has some issues. The PTFE implant lost its shape after implantation and it is prone to wear, resulting in debris formation and synovitis. A coated Teflon prosthesis was also tested. Polyurethane was the polymer chosen to coat the implant. The coated PTFE prosthesis gave the best overall results showing, on macroscopic examination, that the cartilage appeared similar to meniscus native tissue. Although the tendency to cartilage softening, osteophyte formation, and synovitis indicates that the procedure was not able to prevent all these problems [15, 16]. These disappointing results lead to a decrease of interest from the scientific community in this meniscus substitutes.

### I-2.1.3. Poly(vinyl alcohol) hydrogel (PVA-H)

PVA-H has been shown to have cartilage like viscoelasticity and excellent biocompatibility [17]. Hydrogels are biomaterials that consist of a water-swollen network of cross-linked polymer chains [18]. They can be made from chains of from synthetic polymers such as poly(vinyl alcohol) (PVA). Due to PVA-H hydrogels biocompatibility, ease of fabrication and viscoelastic properties several attempts at tissue engineering have previously been examined, including cartilage tissue engineering [19]. Kabayashi *et al.* [20] combined the PVA with the characteristics of a hydrogel and tested a poly(vinyl alcohol) hydrogel with a water content of 90%, a degree of polymerization of 17,500 and cross-linked as an implant in a rabbit model. In that study, with a timeframe of 2 year, it has proven that PVA-H implant was able to reduce the articular cartilage damaged compared to meniscectomy [20]. Kelly *et al.* [21] took the next step and assessed the PVA-H implant in a sheep. The results showed that, compared with meniscectomy, the PVA-H meniscal replacement resulted in a significantly decrease cartilage degeneration. Compared with meniscal allograft transplantation animals, after 4 months, the PVA-H implant had significantly increased cartilage degeneration in the peripheral zone of the tibial plateau [21].



The significantly cartilage degeneration and implant failure after 1 year as compared to allograft transplantation corroborate that, improvements in PVA-H properties, surface characteristics and a more accurate size matching must be done in the future in order to improve the clinical outcomes.

In order to overtake these challenges, a reinforced PVA-H implant was developed. A fibrous reinforcement of poly(vinyl alcohol) hydrogels is capable of increasing the hydrogel tensile modulus within the range of 0.23 and 260 MPa depending on fiber volume fraction [22]. However the interface of the reinforced PVA-H implant has been identified as a potential issue in meniscal replacements. Holloway *et al.* [23] developed a novel PVA grafting technique in order to create a covalent linkage and improve the interfacial properties. This approach led to an increase of the interfacial shear strength and more efficient stress transfer. These studies show that this biomaterial has some potential to be used as a meniscal implant, however further pre-clinical tests must be accessed.

#### I-2.1.4. Polycarbonate-urethane (PCU)

PCU is a tough polymer whose compliance can be customized by the mixture of hard and soft segments [24]. Due to his relatively low elastic modulus (10-100 MPa) it can potentially improve conformity and load distribution by permitting local material deformation [25]. Hereupon, polycarbonate-urethane possesses some features which make it a potential biomaterial to be used as a meniscal implant. PCU is durable, bio-stable and has excellent mechanical properties [26, 27].

Zur *et al.* [25] accessed the ability of a non-degradable, anatomically shaped artificial meniscal implant in a sheep model (**Figure I-2**). This experience occurred in a time frame of 6 months to test the hypothesis that PCU implant could provide a chondroprotective effect on cartilage. The PCU implants remained well secured throughout the experimental period and showed no signs of wear or changes in structural or material properties providing a chondroprotective protection to the cartilage. That study provided preliminary evidence for the ability of an artificial PCU meniscal implant to delay or prevent osteoarthritic changes in knee joint following complete medial meniscectomy [25].

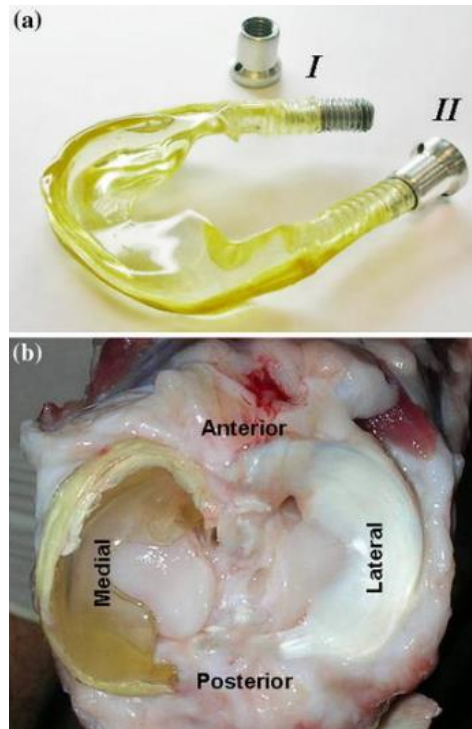


Figure I-2 - Polycarbonate-urethane meniscal implant, with the stainless steel fixation bolt in the unfastened (I) and fastened state (II). Reprinted with permission from [25]. Copyright 2010, Springer.

The viscoelastic properties of an improved PCU implant were accessed by measuring and characterization of the strain-rate response, after simulated use, by subjecting the implant to realistic joint loads [28]. This meniscus implant made of a compliant polycarbonate-urethane matrix reinforced with high modulus ultrahigh molecular weight polyethylene fibers can redistribute joint loads in a similar pattern to natural meniscus, without risking the integrity of the implant materials due to the optimal pressure distribution and similar shape of natural meniscus [8]. Regarding to the viscoelastic properties, the PCU implant was very flexible and able to deform relatively easily under low compressive loads ( $E=120\text{--}200$  kPa). Although, when the compressive load increase, the implant became stiffer ( $E=3.8\text{--}5.2$  MPa) to resist deformation. The meniscus implant behaved as a non-linear viscoelastic material. The meniscus implant appears well-matched to the viscoelastic properties of the natural meniscus, and importantly, these properties were found to remain stable and minimally affected by potentially degradative and loading conditions associated with long-term use [28].

The main synthetic non-resorbable polymers and outcome that have been explored as meniscus implants is summarized in **Table I-1**.

Table I-1 - Summary of main studies concerning non-resorbable synthetic biomaterials.

Biomaterial	Follow-up	Model	Results	References
<i>Pre-Clinical Trial</i>				
PET (Dacron)	3 months	Rabbit	Dacron implant led to altered joint mechanics, osteophyte formation and synovitis caused by the non-normal biomechanics properties, the improper sizing and the impossibility to match the stress-relaxation of the native meniscus tissue.	[12]
PTFE (Teflon)	3 months	Rabbit	The cartilage appeared similar to meniscus native tissue, however PTFE implant lost its shape after implantation and it is prone to wear, resulting in debris formation and synovitis PTFE implant lost its shape after implantation and it is prone to wear, resulting in debris formation and synovitis.	[16, 15]
PVA-H	12 months	Sheep	Compared with meniscectomy, the PVA-H meniscal replacement resulted in a significantly decrease cartilage degeneration. Compared with meniscal allograft transplantation animals, after 4 months, the implant had significantly increased cartilage degeneration in the peripheral zone of the tibial plateau.	[21]
PCU	6 months	Sheep	PCU implants remained well secured throughout the experimental period and showed no signs of wear or changes in structural or material properties providing a chondroprotective protection to the cartilage.	[25]

### I-3. RESORBABLE POLYMERS

#### I-3.1. Synthetic

##### I-3.1.1. Poly( $\alpha$ -hydroxy acids) (PHAs)

Poly(lactic acid) (PLA), poly(glycolic acid) (PGA), and their copolymer poly [(lactic acid) -co- (glycolic acid)] (PLGA), are part of a group of polymers called Poly( $\alpha$ -hydroxy acids), that due to their well-controlled architecture, inter pore connectivity, and mechanical properties, are widely used in tissue engineering applications [29].

Testa Pezzin *et al.* [30] developed bioreabsorbable polymer scaffold made of poly(L-lactic acid) (PLLA) and poly(*p*-dioxanone) (PPD) to be used as a temporary meniscal prosthesis to stimulate the formation of an in situ meniscal replication. That study was made in a rabbit model and revealed that PLLA has great potential to be used as a meniscal prosthesis, especially because, the new meniscus promoted a significant cartilage protection, allowed tissue ingrowth and induces the fibrocartilage [30].

Poly(lactic acid) has a long degradation time. Keeping this in mind, Esposito *et al.* [31] used the copolymer PLDLA [poly(L-co-D,L-lactic acid)] that has similar mechanical properties to poly(lactic acid) but with a short degradation time due to the greater degradation of poly(D,L lactic acid). Poly(caprolactone-triol) PCL-T was added, yielding a more hydrophilic polymer that results in an improvement of the interaction with cells and tissue. The results showed that the polymer biodegradability capability and the fact that allow formation fibrocartilaginous tissue, makes the PLDLA/PCL-T scaffolds very promising in the meniscus regeneration area [31].

Poly(glycolic acid) is a propitious synthetic material under investigation as a synthetic scaffold for meniscus tissue engineering. PGA is a biomaterial that is biocompatible and has the ability to load isolated fibrochondrocytes from menisci [32, 33]. A study by Kang *et al.* [34], using a meniscus-shaped PGA scaffold reinforced with PLGA (75:25) and seeded with fibrochondrocytes before implantation in rabbits, demonstrated that the regenerated neomenisci were similar to the native meniscus as well as zonal production of collagen I and II as seen in native menisci. However the tibial articular cartilage was not prevented and the novel meniscus tissue showed differences in collagen content and aggregate modulus in comparison with native meniscus [34].

Fox *et al.* [35] developed a fibroblast-like synoviocytes (FLS) strategy that consists in the seeding of these cells on PGA/PLLA scaffolds under the influence of growth factors. FLS were seeded onto synthetic scaffolds in a rotating bioreactor under the influence of three growth factor regimens: none, basic fibroblast growth factor (b-FGF) alone, and b-FGF plus transforming growth factor (TGF- $\beta$ 1) and insulin-like growth factor (IGF-1). The data suggests that this novel strategy may constitutively signal for production of type I collagen, and can be induced to signal for collagen II and aggrecan. This may prove favorable for *in vitro* fibrocartilage tissue engineering under appropriate conditions [35].

Another approach, developed by Freymann *et al.* [36], was the production of a three-dimensional (3D) bioresorbable polymer graft made of PGA and hyaluronic acid. The scaffold material was shown to be biocompatible and retained its initial shape stability over the cultivation period of 3 weeks. The focus of the *in vitro* study is limited to a first proof of biocompatibility of the meniscal cells with the scaffold material, along with a first insight into the differentiation of cells and potential meniscus matrix formation [36].

The poly [(lactic acid) -co- (glycolic acid)] scaffold comes up when PLA was added to PGA scaffolds in order to improve its mechanical properties. Gu *et al.* [37], used a PLGA scaffold loaded with autologous myoblasts and cultured in a chondrogenic medium for 14 days and tested it in a canine model. Comparing with cell-free PLGA scaffolds, the scaffolds loaded with myoblasts and pre-cultured in chondrogenic medium prior to the insertion into meniscal defects resulted in significantly better meniscal defect filling and meniscal regeneration. However, did not occur the full restoration of the surface area and the tissue quality of the normal meniscus [37].

Recently, Kwak *et al.* [38] test the hypothesis that platelet-rich plasma (PRP) pretreatment on a PLGA mesh scaffold enhances the healing capacity of the meniscus with human chondrocyte-seeded scaffolds *in vivo*, even when the seeded number of cells was reduced from 10 million to one million. The results showed PRP exerts a positive stimulatory effect on attachment of human chondrocytes onto the PLGA mesh scaffold. This is a clinically relevant finding because the number of donor cells can be reduced and donor site morbidity may be minimized. The objective of this study was not to restore the native tissue architecture but to encourage healing of the injured meniscal tissue. Once again PLGA scaffold helps because is easily degradable in *in vivo* conditions within several weeks and can work as a cell-delivery device [38].

### I-3.1.2. Polycaprolactone/Hyaluronic acid (PCL/HA)

Polycaprolactone (PCL), a semi-crystalline linear resorbable aliphatic polyester, is subjected to biodegradation because of the susceptibility of its aliphatic ester linkage to hydrolysis. PCL is regarded as a soft and hard-tissue compatible material including resorbable suture, drug delivery system, and recently bone graft substitutes [39].

Extensive *in vitro* and *in vivo* biocompatibility and efficacy studies have been performed, resulting in US Food and Drug Administration approval of a number of medical and drug delivery devices [40, 41].

Hyaluronic acid (HA) is a biodegradable and biocompatible polymer that is a suitable substrate to grow a variety of cell types [42].

Chiari *et al.* [43] developed a PCL/HA scaffold (**Figure I-3**) capable to be used as a partial or total meniscus substitute and was reinforced with circumferential PLA fibers and with a PET net respectively. The scaffold was introduced for meniscus replacement in a sheep model. The properties of the biomaterial in terms of tissue meniscus regeneration are promising: the implants remained in position, retained their shape, and showed adequate mechanical properties. However, compression of the implant led to extrusion, which mainly occurred in the posterior aspect. Complete ingrowth to the capsule and the formation of tissue between the implant and the original meniscus in the partial replacements, seen on gross inspection as well as histology, provided evidence of implant integration after 6 weeks [43].

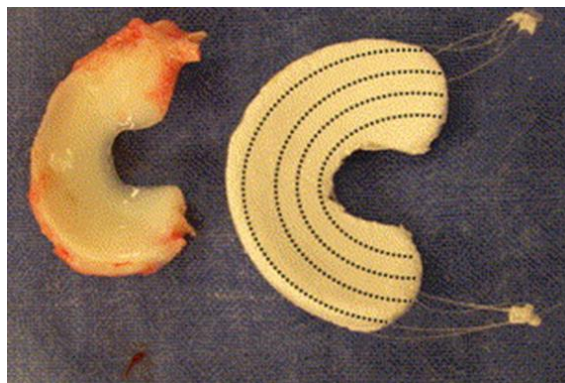


**Figure I-3** - The total meniscus implant is augmented with circumferential PLA fibers. Reprinted with permission from [43]. Copyright 2006, Elsevier.

In subsequent studies the implant show some issues. After 6 months, the PCL/HA scaffold reveals insufficient biomechanics properties and fixation related problems [44]. Kon *et al.* [44] also

demonstrated that, after 12 months, occurred an implant dislocation, a slight extrusion and wrinkling of the scaffold in the posterior region. Despite being obtained some promising results, damage to articular cartilage was not prevented and the biomechanical properties were not accessed in the subsequent studies.

### I-3.1.3. Polyurethanes (PU)

Polyurethane is a polymer that is formed by reacting a diisocyanate or a polymeric isocyanate (hard segment) with a polyol (soft segment) in the presence of suitable catalysts and additives. The wide range of possibilities in the components that can be used to produce PU, gives the possibility to produce a broad spectrum of materials to meet the needs of specific applications.

Polyurethane scaffolds shown its biodegradability, biocompatibility and elasticity in a couple of studies. The studies that used Poly(urethane)-poly(L-lactide) (PU-PLLA) and PU scaffolds (Estane 5701F) attempted to understand the potential of these implants in meniscus reconstruction. The authors used a canine model and realized that occurred a good tissue ingrowth due to the porosity of the PU scaffold. In conclusion, the repair of meniscal lesions in the avascular part of the meniscus is possible when a porous PU implant is used to guide repair tissue and blood vessels from the vascular peripheral part of the meniscus into the defect [45, 46].

Tienen *et al.* [47] accessed if an improved PU scaffold (Estane 5701F) was able to protect the cartilage from degeneration and develop into a neomeniscus. The implant was completely filled with fibrovascular tissue after 3 months and, after 6 months was observed cartilage-like tissue in the central areas of the implant. However, the PU scaffold was not able to mimic the mechanical properties of the native meniscus tissue and prevent the articular cartilage damage [47]. Afterwards, due to some carcinogenic problems with the Estane implant, Heijkants *et al.* [48] developed a polyurethane scaffold with polycaprolactone (PCL) as soft segment and 1,4-butanediisocyanate and 1,4-butanediol as uniform hard segments, resulting in better compressive characteristics [48]. Despite the lack of prevention on the articular cartilage damage, this new PU scaffold showed a faster tissue ingrowth 2 weeks after implantation [49].

A subsequent study, with a bigger timeframe (24 months) demonstrated the previous issues [50]. Meanwhile, the polyurethane implant, as it can be seen in **Figure I-4**, became commercialized and named Actifit (Orteq Ltd, London, United Kingdom). Therefore, Brophy *et al.* [51] tried a different

approach, and used the PU scaffold for partial meniscal replacement, instead of total meniscal replacement. First, a study was made in a cadaver model and reveals that polyurethane scaffold improved knee-contact mechanics. Further, an *in vivo* study demonstrated that there were no differences in the prevention of articular cartilage damage between scaffold and partial meniscectomy [52].

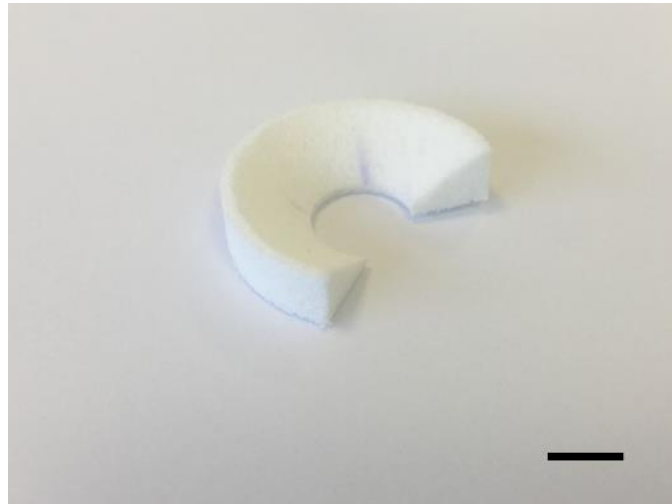


**Figure I-4 - Actifit: appearance of the implant to the naked eye. Scale bar: 10 mm.**

Actifit astoundingly managed to reach clinical trials. A set of clinical trials using Actifit was made over the past five years. The study of Verdonk *et al.* [53] revealed successful tissue ingrowth and biocompatibility and, for the first time, occurred a consistent regeneration of tissue when using an acellular polyurethane scaffold to treat irreparable partial meniscus tissue lesions. Further, a clinical case using 18 patients, proved again, that Actifit increases and promotes the meniscal regeneration by normal chondrocytes and fibrochondrocytes and reduces the risk of progression to knee osteoarthritis [10]. Bouyarmane *et al.* [54] carried out a study, involving 54 patients, and assessed the clinical outcomes at 24 months follow-up. Clinical results of this study demonstrate clinically and statistically significant improvements of pain and function scores and showed that Actifit scaffold is safe and effective in treating lateral meniscus defects [54]. A longer clinical trial with a timeframe of 48 months and involving 18 patients was made by Schuttler *et al.* [55]. Until this clinical case, no data concerning a longer follow-up than 2 years for Actifit scaffold are available, and, once again, the study revealed that polyurethane meniscal scaffold in patients with chronic segmental medial meniscus deficiency is not only a safe procedure but leads to good clinical results at a 4-year follow-up [9, 55]. Recently, Gelber *et al.* [56] tried to evaluate the influence of different degrees of articular chondral injuries on the imaging aspect of Actifit scaffold. As expected, patients without chondral injuries showed a better MRI aspect of



the polyurethane scaffold in terms of size and morphology and the implant provided also significant pain relief and functional improvement regardless the presence of advanced cartilage injuries after a 2 follow-up [56].

The main synthetic resorbable polymers and outcomes that have been explored as meniscus implants is summarized in **Table I-2**.

**Table I-2 - Summary of main studies concerning resorbable synthetic biomaterials.**

Biomaterial	Follow up	Model	Results	References
<i>Clinical trial</i>				
PU (Actifit)	24 months	Human	Significant improvements of pain and function scores; scaffold is safe and effective in treating lateral meniscus defects.	[54]
PU (Actifit)	24 months	Human	Safe implant procedure and leads to good clinical results.	[9]
PU (Actifit)	24 months	Human	Inducing and promoting meniscal regeneration by normal chondrocytes and fibrochondrocytes and decreases the risk of progression to knee osteoarthritis.	[10]
<i>Pre-clinical trial</i>				
PCL/HA	12 months	Sheep	Osteoarthritis was less in cell-seeded group than in meniscectomy group, however occurred an implant dislocation, a slight extrusion and wrinkling of the scaffold in the posterior region.	[44]
PGA	36 weeks	Rabbit	Reported proteoglycan types I and II collagen in neomenisci, however there was some differences in collagen content and aggregate modulus in comparison with native meniscus.	[26]
PLDLA/PCL-T	24 weeks	Rabbit	Without apparent rejection, infection, or chronic inflammatory response and good integration to native tissue.	[31]

PLGA	12 weeks	Canine	Fibrocartilage formation with hyaline-like regions with collagen I, II and aggrecan production.	[37]
<i>In vitro</i>				
PGA-PLLA	6 weeks		This novel strategy may prove favorable for <i>in vitro</i> fibrocartilage tissue engineering under appropriate conditions. No integration of cell-scaffold construct to meniscal tissue. No measurable collagen or GAGs.	[35]
PGA-Hyaluronan	3 weeks		Increase in matrix protein expression compared with control. Decrease in collagen X expression for all groups. Suggested redifferentiation of meniscus cells by scaffold.	[36]

### I-3.2. Natural

#### I-3.2.1. Silk

Silk is a natural resorbable material that has been applied in meniscal tissue engineering. Silks, as one group of fibrous proteins, are produced by a wide range of insects and spiders and can consist of helical,  $\beta$ -sheet (the chain axis is parallel to the fiber axis) or cross- $\beta$ -sheet (the chain axis is perpendicular to the fiber axis) secondary structures, depending on the organism [57]. Its versatility allied to its biocompatibility, good biomechanical properties and controlled durability make silk a suitable natural biomaterial for the production of scaffolds.

Mandal *et al.* [58] used silk fibroin from *Bombyx mori* silkworm cocoons to develop a multilayered, multiporous scaffold with the aim to mimic native meniscal architecture and morphology. In that study, human primary chondrocytes were seeded into the inside of the silk scaffold and human primary fibroblasts were seeded into the outside. The study showed that the constructs increased cellularity and provided the support to form an extra cellular matrix similar to native tissue. The compressive modulus and tensile modulus increased with time, however, they remained inferior to those of the native meniscus [58]. The same authors tried to use bone marrow stem cells as an alternative approach. The

silk scaffold had behavior similar to the previous study [59]. The poor mechanical properties of the silk scaffolds are the biggest obstacle and, with that in mind, Yan *et al.* [60] showed that it is possible to improve mechanical and structural properties (**Figure I-5**). The results revealed that mechanical properties of the silk fibroin scaffolds increased with increasing silk fibroin concentration. The scaffolds presented favorable stability as their structure integrity, morphology and mechanical properties were maintained after *in vitro* degradation for 30 days. However, with the increase in the silk fibroin concentration, the scaffold porosity and interconnectivity decreasing which can be a problem in cell encapsulation process [60].

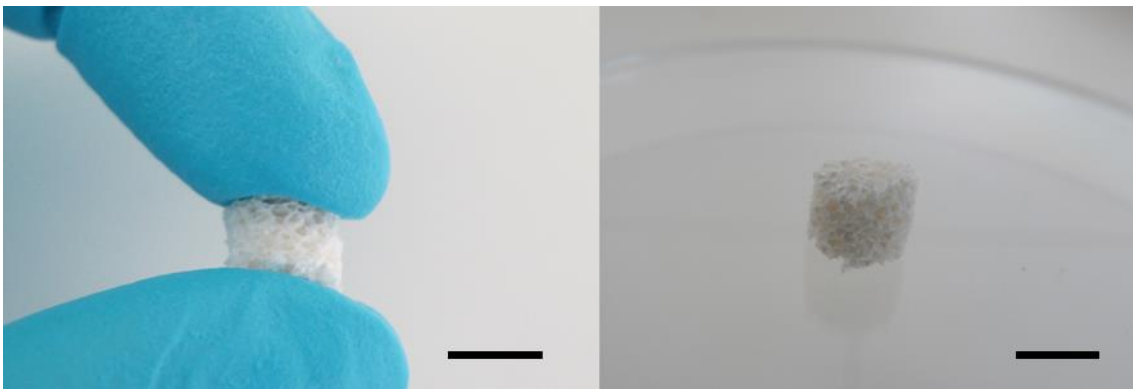


**Figure I-5 - Silk meniscus scaffold. Scale bar: 10 mm.**

Gruchenberg *et al.* [61] performed an *in vivo* trial using a sheep model. The silk scaffold caused no inflammatory reaction in the joint 6 months postoperatively, and there were no significant differences in cartilage degeneration between the scaffold and sham groups. The compressive properties of the scaffold approached those of meniscal tissue and there is preliminary evidence of chondroprotective properties. However, the scaffolds were not always stably fixed in the defect, leading to gapping between implant and host tissue or to total loss of the implant [61].

### I-3.2.2. Gelatin

Grogan *et al.* [62] present a three-dimensional methacrylated gelatin (GelMA) scaffolds patterned via projection stereolithography to emulate the circumferential alignment of cells in native meniscus tissue. That study showed that micropatterned GelMA scaffolds are non-toxic, provide organized cellular alignment, and promote meniscus-like tissue [62]. A couple of studies, added chitosan to gelatin to produce macroporous scaffolds. Han *et al.* [63] proved that gelatin/chitosan scaffolds are promising candidates for stem-cell-based tissue engineering. Sarem *et al.* [64], used the same biomaterials, to

produce a scaffold that were prepared using genipin as a biocompatible crosslinker. The results showed that all composite scaffolds showed favorable interaction with mixed population of meniscus derived cells, leading to a proliferation behavior that were directly correlating with the increase fraction of gelatin in the composite [64, 65].

An *in vivo* trial was made by Ishida *et al.* [66] in order to access if platelet-rich plasma (PRP) combined with gelatin hydrogel (GH) scaffolds could enhance meniscal regeneration. Histological scoring of the defect sites at 12 weeks revealed significantly better meniscal repair in animals that received PRP with GH, which confirms the hypothesis proposed by the authors. Narita *et al.* [67], also made an *in vivo* trial using a rabbit model. The aim of this study was to investigate the *in vivo* effects of GH incorporating fibroblast growth factor 2 (FGF-2) on meniscus repair. The results showed that GHs incorporating FGF-2 can significantly stimulate the cell proliferation and inhibited the death of meniscal cells until 4 weeks, thereby increasing meniscal cell density and enhancing meniscal repair [67].

### 1-3.2.3. Cellulose

Bacterial cellulose (BC) is an organic polysaccharide synthesized extracellularly as nanosized fibrils by the bacterium *Gluconacetobacter xylinus* bacterium. BC consists in a linear chain of several hundred to over ten thousand linked glucose units [68]. The *in vivo* biocompatibility of bacterial cellulose is good [69] and already showed that has potential as a scaffold for tissue engineering of cartilage [70]. Bodin *et al.* [71] accessed the potential of BC gel be used as a scaffold in meniscus tissue engineering. As advantages, BC scaffold is almost inexpensive, can be produced in a meniscus shape and promotes the cell migration. The results showed that compression modulus of the BC gel (1.8 kPa) was five times better than that of the collagen meniscal implant (0.23 kPa). However, it was inferior to the native pig meniscus (21 kPa). Further tests should be done to investigate the characteristics of the material [71].

A cellulose perforated by micro-channels has been developed by Martinez *et al.* [72] as a potential future scaffold material for meniscus implants. The BC scaffold was seeded with mouse fibroblasts and compared dynamic compression to that of a static culture. The results showed that the microchannel structure facilitated the alignment of cells and collagen fibers and provided guided tissue growth. This guiding process was important to obtain an ultrastructure mimicking that of the meniscus [72]. Recently, Markstedt *et al.* [73] used nanofibrillated cellulose (NFC) with alginate for 3D bioprinting of living soft tissue with cells. In this study, the authors were able to produce 3D printed structures with

meniscus shape and the results showed that NFC-based scaffold exhibited a good cell viability after 7 days of 3D culture [73]. As conclusion, the nanocellulose-based bioink is a suitable hydrogel for 3D bioprinting with living cells and can be subsequently used for meniscus tissue engineering.

#### I-3.2.4. Collagen

Resorbable collagen meniscus scaffolds are made from processed bovine Achilles tendon tissue from which type I collagen fibers are extracted and later cross-linked with glutaraldehyde to form a matrix-like scaffold material. The resulting product is a flexible disk that can be trimmed and shaped to fit a meniscus defect [74]. The Collagen Meniscus Implant (CMI, Ivy Sports Medicine GmbH, Gräfelfing, Germany, **Figure I-6**) is the first biologic scaffold used for the treatment of partial meniscal deficiencies [75].

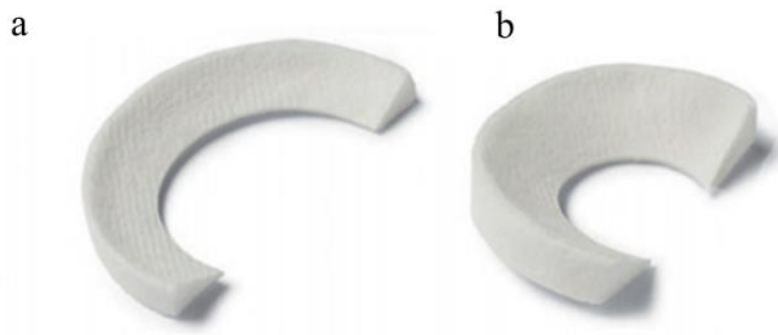


**Figure I-6 - CMI for the lateral meniscus (a) and CMI for the medial meniscus (b).**

Several clinical trials were made in the last few years. Like all scaffolds, CMI has different goals in meniscus tissue engineering. According to the literature [76], the resorption of the collagen scaffold results in a decrease of the final meniscus volume in terms of implant-new tissue complex. Steadman and Rodkey, showed that occurs a progressive invasion of the CMI with meniscus cells after 6 and 12 months [77]. Another study from Rodkey *et al.* [11], revealed similar results to the previous study occurring a continuous and uniform fibrocartilaginous matrix formation. This newly formed tissue can counterbalance the resorption of the meniscus implant ensuring restoration of the normal volume of meniscus tissue. In terms of prevention further degenerative changes associated with the loss of meniscus tissue, Zaffagnini *et al.* [78] results noted only a few patients with degenerative changes 120 months after collagen scaffold implantation. Monllau *et al.* [79] had the same results of the previous study, only a few patients had degenerative changes after CMI implantation. That study showed that

meniscus implantation provided significant pain relief and functional improvement after a minimum 10-year follow-up period. In comparison with partial meniscectomy, some studies showed that CMI provided an improvement in the clinical outcomes. Rodkey *et al.* [11] showed that only patients with chronic injuries were found to have regained a significantly greater proportion of their lost activity compared to patients that were submitted to a partial medial meniscectomy alone. In this study, the collagen scaffold revealed a biomechanical stability for more than 5 years [11]. On the other hand, Zaffagnini *et al.* [80] showed that collagen meniscus implantation resulted in improved pain, activity level, and radiologic outcomes after a minimum 10-year follow-up period when compared with partial medial meniscectomy alone. This study, unlike the previous one, had improvements in all patients with meniscus injuries (chronic and acute), not only in chronic injuries [80].

As summarized in **Table I-3**, from natural based polymers, collagen is the unique natural biomaterial that has reached clinical trials stage. Collagen meniscal implants offer good clinical and structural outcomes providing higher clinical outcomes compared with partial meniscectomy alone.

**Table I-3 - Summary of main studies concerning resorbable natural biomaterials.**

Biomaterial	Follow up	Model	Results	References
<i>Clinical trial</i>				
Collagen (CMI)	10 years	Human	Significant pain relief and functional improvement followed by no development or progression of degenerative knee joint disease in most of the cases.	[79]
Collagen (CMI)	10 years	Human	Pain, activity level, and radiological outcomes are significantly improved.	[80]
<i>Pre-clinical trial</i>				
Silk	6 months	Sheep	The compressive properties of the scaffold approached those of meniscal tissue. However, the scaffolds were not always stably fixed in the defect.	[61]
Gelatin	12 weeks	Rabbit	Gelatin hydrogel scaffold can significantly stimulate the cells proliferation and inhibited the death of meniscal cells until 4 weeks, thereby increasing meniscal cell density and	[67]

---

enhancing meniscal repair.

*In vitro*

Cellulose	28 days	Scaffold microchannels facilitated the alignment of cells and collagen fibers providing guided tissue growth.	[72]
-----------	---------	---	------

---

#### I-4. CONCLUSIONS AND FUTURE PERSPECTIVES

The research area of meniscus tissue engineering has achieved tremendous advancements, but there is still progress to be made to move with most developed biomaterials into clinical trial phase. Different biomaterials in meniscus tissue engineering were addressed as a potential meniscus substitute/scaffold with promising results in pre-clinical stages. Many authors developed scaffolds using different biomaterials that possess many attractive characteristics and behaviors. Regarding synthetic non-resorbable materials, the most important features is that the implant is biocompatible, intrinsically stable, safe, and mimic the biomechanical properties of the native meniscus. Concerning synthetic resorbable materials, the outcomes are more complex. In this type of materials it is important to access the tissue ingrowth and the degradation profile of the material. It is noteworthy that most of the literature has focused on biodegradable tissue engineered strategies, leaving a little aside the search for a permanent implant meniscus. As mentioned above, the only biomaterials that reached clinical trials as meniscal substitute/scaffold were 2 resorbable materials (Polyurethane and Collagen). However, any scaffold has not yet fully mimic the physical and chemical properties of native meniscus and scaffold fixation still presents a big challenge in meniscus tissue engineering area. Future research trends should focus on optimizing the processing routes to better tune the mechanical and chemical properties of meniscus substitute/scaffold and produce patient-specific implants, and in particular using natural-based biomaterials, in order to provide a better treatment for meniscus lesions.

#### I-5. REFERENCES

- [1] Scotti C, Hirschmann MT, Antinolfi P, Martin I, Peretti GM. Meniscus repair and regeneration: review on current methods and research potential. *European cells & materials* 2013;26:150-70.
- [2] Baker BE, Peckham AC, Puppato F, Sanborn JC. Review of meniscal injury and associated sports. *The American journal of sports medicine* 1985;13:1-4.

- [3] Hede A, Jensen DB, Blyme P, Sonne-Holm S. Epidemiology of meniscal lesions in the knee. 1,215 open operations in Copenhagen 1982-84. *Acta orthopaedica Scandinavica* 1990;61:435-7.
- [4] Khetia EA, McKeon BP. Meniscal allografts: biomechanics and techniques. *Sports medicine and arthroscopy review* 2007;15:114-20.
- [5] Longo UG, Loppini M, Forriol F, Romeo G, Maffulli N, Denaro V. Advances in Meniscal Tissue Engineering. *Stem Cells International* 2012;2012:11.
- [6] Guo W, Liu S, Zhu Y, Yu C, Lu S, Yuan M, *et al.* Advances and Prospects in Tissue-Engineered Meniscal Scaffolds for Meniscus Regeneration. *Stem Cells International* 2015;2015:13.
- [7] Rongen JJ, van Tienen TG, van Bochove B, Grijpma DW, Buma P. Biomaterials in search of a meniscus substitute. *Biomaterials* 2014;35:3527-40.
- [8] Elsner JJ, Portnoy S, Zur G, Guilak F, Shterling A, Linder-Ganz E. Design of a free-floating polycarbonate-urethane meniscal implant using finite element modeling and experimental validation. *Journal of biomechanical engineering* 2010;132:095001.
- [9] Schuttler KF, Pottgen S, Getgood A, Rominger MB, Fuchs-Winkelmann S, Roessler PP, *et al.* Improvement in outcomes after implantation of a novel polyurethane meniscal scaffold for the treatment of medial meniscus deficiency. *Knee surgery, sports traumatology, arthroscopy : official journal of the ESSKA* 2015;23:1929-35.
- [10] Baynat C, Andro C, Vincent JP, Schiele P, Buisson P, Dubrana F, *et al.* Actifit synthetic meniscal substitute: experience with 18 patients in Brest, France. *Orthopaedics & traumatology, surgery & research : OTSR* 2014;100:S385-9.
- [11] Rodkey WG, DeHaven KE, Montgomery WH, 3rd, Baker CL, Jr., Beck CL, Jr., Hormel SE, *et al.* Comparison of the collagen meniscus implant with partial meniscectomy. A prospective randomized trial. *The Journal of bone and joint surgery American volume* 2008;90:1413-26.
- [12] Sommerlath K, Gillquist J. The effect of a meniscal prosthesis on knee biomechanics and cartilage. An experimental study in rabbits. *The American journal of sports medicine* 1992;20:73-81.
- [13] Odian G. *Principles of Polymerization*. Wiley & Sons, Inc 2004.
- [14] Sommerlath K, Gallino M, Gillquist J. Biomechanical characteristics of different artificial substitutes for rabbit medial meniscus and effect of prosthesis size on knee cartilage. *Clinical biomechanics (Bristol, Avon)* 1992;7:97-103.
- [15] Messner K, Lohmander LS, Gillquist J. Cartilage mechanics and morphology, synovitis and proteoglycan fragments in rabbit joint fluid after prosthetic meniscal substitution. *Biomaterials* 1993;14:163-8.
- [16] Messner K, Gillquist J. Prosthetic replacement of the rabbit medial meniscus. *Journal of biomedical materials research* 1993;27:1165-73.



- [17] Noguchi T, Yamamuro T, Oka M, Kumar P, Kotoura Y, Hyon S, *et al.* Poly(vinyl alcohol) hydrogel as an artificial articular cartilage: evaluation of biocompatibility. *Journal of applied biomaterials : an official journal of the Society for Biomaterials* 1991;2:101-7.
- [18] Anseth KS, Bowman CN, Brannon-Peppas L. Mechanical properties of hydrogels and their experimental determination. *Biomaterials* 1996;17:1647-57.
- [19] Yamaoka H, Asato H, Ogasawara T, Nishizawa S, Takahashi T, Nakatsuka T, *et al.* Cartilage tissue engineering using human auricular chondrocytes embedded in different hydrogel materials. *Journal of biomedical materials research Part A* 2006;78:1-11.
- [20] Kobayashi M, Chang Y-S, Oka M. A two year *in vivo* study of polyvinyl alcohol-hydrogel (PVA-H) artificial meniscus. *Biomaterials* 2005;26:3243-8.
- [21] Kelly BT, Robertson W, Potter HG, Deng XH, Turner AS, Lyman S, *et al.* Hydrogel meniscal replacement in the sheep knee: preliminary evaluation of chondroprotective effects. *The American journal of sports medicine* 2007;35:43-52.
- [22] Holloway JL, Lowman AM, Palmese GR. Mechanical evaluation of poly(vinyl alcohol)-based fibrous composites as biomaterials for meniscal tissue replacement. *Acta biomaterialia* 2010;6:4716-24.
- [23] Holloway JL, Lowman AM, VanLandingham MR, Palmese GR. Interfacial optimization of fiber-reinforced hydrogel composites for soft fibrous tissue applications. *Acta biomaterialia* 2014;10:3581-9.
- [24] Scholes SC, Unsworth A, Jones E. Polyurethane unicondylar knee prostheses: simulator wear tests and lubrication studies. *Physics in medicine and biology* 2007;52:197-212.
- [25] Zur G, Linder-Ganz E, Elsner JJ, Shani J, Brenner O, Agar G, *et al.* Chondroprotective effects of a polycarbonate-urethane meniscal implant: histopathological results in a sheep model. *Knee surgery, sports traumatology, arthroscopy : official journal of the ESSKA* 2011;19:255-63.
- [26] Khan I, Smith N, Jones E, Finch DS, Cameron RE. Analysis and evaluation of a biomedical polycarbonate urethane tested in an *in vitro* study and an ovine arthroplasty model. Part II: *in vivo* investigation. *Biomaterials* 2005;26:633-43.
- [27] Bigsby RJ, Auger DD, Jin ZM, Dowson D, Hardaker CS, Fisher J. A comparative tribological study of the wear of composite cushion cups in a physiological hip joint simulator. *Journal of biomechanics* 1998;31:363-9.
- [28] Shemesh M, Asher R, Zylberberg E, Guilak F, Linder-Ganz E, Elsner JJ. Viscoelastic properties of a synthetic meniscus implant. *Journal of the Mechanical Behavior of Biomedical Materials* 2014;29:42-55.
- [29] Ma PX, Choi JW. Biodegradable polymer scaffolds with well-defined interconnected spherical pore network. *Tissue engineering* 2001;7:23-33.
- [30] Testa Pezzin AP, Cardoso TP, do Carmo Alberto Rincon M, de Carvalho Zavaglia CA, de Rezende Duek EA. Bioreabsorbable polymer scaffold as temporary meniscal prosthesis. *Artificial organs* 2003;27:428-31.

- [31] Esposito AR, Moda M, Cattani SM, de Santana GM, Barbieri JA, Munhoz MM, *et al.* PLDLA/PCL-T Scaffold for Meniscus Tissue Engineering. *BioResearch open access* 2013;2:138-47.
- [32] Ibarra C, Jannetta C, Vacanti CA, Cao Y, Kim TH, Upton J, *et al.* Tissue engineered meniscus: a potential new alternative to allogeneic meniscus transplantation. *Transplantation proceedings* 1997;29:986-8.
- [33] Aufderheide AC, Athanasiou KA. Comparison of scaffolds and culture conditions for tissue engineering of the knee meniscus. *Tissue engineering* 2005;11:1095-104.
- [34] Kang SW, Son SM, Lee JS, Lee ES, Lee KY, Park SG, *et al.* Regeneration of whole meniscus using meniscal cells and polymer scaffolds in a rabbit total meniscectomy model. *Journal of biomedical materials research Part A* 2006;78:659-71.
- [35] Fox DB, Warnock JJ, Stoker AM, Luther JK, Cockrell M. Effects of growth factors on equine synovial fibroblasts seeded on synthetic scaffolds for avascular meniscal tissue engineering. *Research in veterinary science* 2010;88:326-32.
- [36] Freymann U, Endres M, Neumann K, Scholman HJ, Morawietz L, Kaps C. Expanded human meniscus-derived cells in 3-D polymer-hyaluronan scaffolds for meniscus repair. *Acta biomaterialia* 2012;8:677-85.
- [37] Gu Y, Zhu W, Hao Y, Lu L, Chen Y, Wang Y. Repair of meniscal defect using an induced myoblast-loaded polyglycolic acid mesh in a canine model. *Experimental and therapeutic medicine* 2012;3:293-8.
- [38] Kwak HS, Nam J, Lee JH, Kim HJ, Yoo JJ. Meniscal repair *in vivo* using human chondrocyte-seeded PLGA mesh scaffold pretreated with platelet-rich plasma. *Journal of tissue engineering and regenerative medicine* 2017;11:471-80.
- [39] Kweon H, Yoo MK, Park IK, Kim TH, Lee HC, Lee H-S, *et al.* A novel degradable polycaprolactone networks for tissue engineering. *Biomaterials* 2003;24:801-8.
- [40] Bezwada RS, Jamiolkowski DD, Lee IY, Agarwal V, Persivale J, Trenka-Benthin S, *et al.* Monocryl suture, a new ultra-pliable absorbable monofilament suture. *Biomaterials* 1995;16:1141-8.
- [41] Darney PD, Monroe SE, Klaisle CM, Alvarado A. Clinical evaluation of the Capronor contraceptive implant: preliminary report. *American journal of obstetrics and gynecology* 1989;160:1292-5.
- [42] Milella E, Brescia E, Massaro C, Ramires PA, Miglietta MR, Fiori V, *et al.* Physico-chemical properties and degradability of non-woven hyaluronan benzylic esters as tissue engineering scaffolds. *Biomaterials* 2002;23:1053-63.
- [43] Chiari C, Koller U, Dorotka R, Eder C, Plasenzotti R, Lang S, *et al.* A tissue engineering approach to meniscus regeneration in a sheep model. *Osteoarthritis Cartilage* 2006;14:1056-65.
- [44] Kon E, Filardo G, Tschon M, Fini M, Giavaresi G, Marchesini Reggiani L, *et al.* Tissue engineering for total meniscal substitution: animal study in sheep model—results at 12 months. *Tissue engineering Part A* 2012;18:1573-82.

- [45] Elema H, de Groot JH, Nijenhuis AJ, Pennings AJ, Veth RPH, Klompmaker J, *et al.* Use of porous biodegradable polymer implants in meniscus reconstruction. 2) Biological evaluation of porous biodegradable polymer implants in menisci. *Colloid and Polymer Science* 1990;268:1082-8.
- [46] Klompmaker J, Jansen HW, Veth RP, de Groot JH, Nijenhuis AJ, Pennings AJ. Porous polymer implant for repair of meniscal lesions: a preliminary study in dogs. *Biomaterials* 1991;12:810-6.
- [47] Tienen TG, Heijkants RG, de Groot JH, Pennings AJ, Schouten AJ, Veth RP, *et al.* Replacement of the knee meniscus by a porous polymer implant: a study in dogs. *The American journal of sports medicine* 2006;34:64-71.
- [48] Heijkants RG, van Calck RV, De Groot JH, Pennings AJ, Schouten AJ, van Tienen TG, *et al.* Design, synthesis and properties of a degradable polyurethane scaffold for meniscus regeneration. *Journal of materials science Materials in medicine* 2004;15:423-7.
- [49] Tienen TG, Heijkants RG, de Groot JH, Schouten AJ, Pennings AJ, Veth RP, *et al.* Meniscal replacement in dogs. Tissue regeneration in two different materials with similar properties. *Journal of biomedical materials research Part B, Applied biomaterials* 2006;76:389-96.
- [50] Hannink G, van Tienen TG, Schouten AJ, Buma P. Changes in articular cartilage after meniscectomy and meniscus replacement using a biodegradable porous polymer implant. *Knee surgery, sports traumatology, arthroscopy : official journal of the ESSKA* 2011;19:441-51.
- [51] Brophy RH, Cottrell J, Rodeo SA, Wright TM, Warren RF, Maher SA. Implantation of a synthetic meniscal scaffold improves joint contact mechanics in a partial meniscectomy cadaver model. *Journal of biomedical materials research Part A* 2010;92:1154-61.
- [52] Maher SA, Rodeo SA, Doty SB, Brophy R, Potter H, Foo LF, *et al.* Evaluation of a porous polyurethane scaffold in a partial meniscal defect ovine model. *Arthroscopy : the journal of arthroscopic & related surgery : official publication of the Arthroscopy Association of North America and the International Arthroscopy Association* 2010;26:1510-9.
- [53] Verdonk R, Verdonk P, Huysse W, Forsyth R, Heinrichs EL. Tissue ingrowth after implantation of a novel, biodegradable polyurethane scaffold for treatment of partial meniscal lesions. *The American journal of sports medicine* 2011;39:774-82.
- [54] Bouyarmane H, Beaufils P, Pujol N, Bellemans J, Roberts S, Spalding T, *et al.* Polyurethane scaffold in lateral meniscus segmental defects: clinical outcomes at 24 months follow-up. *Orthopaedics & traumatology, surgery & research : OTSR* 2014;100:153-7.
- [55] Schuttler KF, Haberhauer F, Gesslein M, Heyse TJ, Figiel J, Lorbach O, *et al.* Midterm follow-up after implantation of a polyurethane meniscal scaffold for segmental medial meniscus loss: maintenance of good clinical and MRI outcome. *Knee surgery, sports traumatology, arthroscopy : official journal of the ESSKA* 2016;24:1478-84.
- [56] Gelber PE, Petrica AM, Isart A, Mari-Molina R, Monllau JC. The magnetic resonance aspect of a polyurethane meniscal scaffold is worse in advanced cartilage defects without deterioration of clinical outcomes after a minimum two-year follow-up. *Knee* 2015;22:389-94.

- [57] Valluzzi R, Winkler S, Wilson D, Kaplan DL. Silk: molecular organization and control of assembly. *Philosophical transactions of the Royal Society of London Series B, Biological sciences* 2002;357:165-7.
- [58] Mandal BB, Park SH, Gil ES, Kaplan DL. Multilayered silk scaffolds for meniscus tissue engineering. *Biomaterials* 2011;32:639-51.
- [59] Mandal BB, Park SH, Gil ES, Kaplan DL. Stem cell-based meniscus tissue engineering. *Tissue engineering Part A* 2011;17:2749-61.
- [60] Yan LP, Oliveira JM, Oliveira AL, Caridade SG, Mano JF, Reis RL. Macro/microporous silk fibroin scaffolds with potential for articular cartilage and meniscus tissue engineering applications. *Acta biomaterialia* 2012;8:289-301.
- [61] Gruchenberg K, Ignatius A, Friemert B, von Lubken F, Skaer N, Gellynck K, *et al.* *In vivo* performance of a novel silk fibroin scaffold for partial meniscal replacement in a sheep model. *Knee surgery, sports traumatology, arthroscopy : official journal of the ESSKA* 2015;23:2218-29.
- [62] Grogan SP, Chung PH, Soman P, Chen P, Lotz MK, Chen S, *et al.* Digital micromirror device projection printing system for meniscus tissue engineering. *Acta biomaterialia* 2013;9:7218-26.
- [63] Thein-Han WW, Saikhun J, Pholpramoo C, Misra RD, Kitiyanant Y. Chitosan-gelatin scaffolds for tissue engineering: physico-chemical properties and biological response of buffalo embryonic stem cells and transfectant of GFP-buffalo embryonic stem cells. *Acta biomaterialia* 2009;5:3453-66.
- [64] Sarem M, Moztarzadeh F, Mozafari M. How can genipin assist gelatin/carbohydrate chitosan scaffolds to act as replacements of load-bearing soft tissues? *Carbohydr Polym* 2013;93:635-43.
- [65] Sarem M, Moztarzadeh F, Mozafari M, Shastri VP. Optimization strategies on the structural modeling of gelatin/chitosan scaffolds to mimic human meniscus tissue. *Materials science & engineering C, Materials for biological applications* 2013;33:4777-85.
- [66] Ishida K, Kuroda R, Miwa M, Tabata Y, Hokugo A, Kawamoto T, *et al.* The regenerative effects of platelet-rich plasma on meniscal cells *in vitro* and its *in vivo* application with biodegradable gelatin hydrogel. *Tissue engineering* 2007;13:1103-12.
- [67] Narita A, Takahara M, Sato D, Ogino T, Fukushima S, Kimura Y, *et al.* Biodegradable gelatin hydrogels incorporating fibroblast growth factor 2 promote healing of horizontal tears in rabbit meniscus. *Arthroscopy : the journal of arthroscopic & related surgery : official publication of the Arthroscopy Association of North America and the International Arthroscopy Association* 2012;28:255-63.
- [68] Brown RM, Jr., Willison JH, Richardson CL. Cellulose biosynthesis in *Acetobacter xylinum*: visualization of the site of synthesis and direct measurement of the *in vivo* process. *Proc Natl Acad Sci U S A* 1976;73:4565-9.
- [69] Helenius G, Backdahl H, Bodin A, Nannmark U, Gatenholm P, Risberg B. *In vivo* biocompatibility of bacterial cellulose. *Journal of biomedical materials research Part A* 2006;76:431-8.

- [70] Svensson A, Nicklasson E, Harrah T, Panilaitis B, Kaplan DL, Brittberg M, *et al.* Bacterial cellulose as a potential scaffold for tissue engineering of cartilage. *Biomaterials* 2005;26:419-31.
- [71] Bodin A, Concaro S, Brittberg M, Gatenholm P. Bacterial cellulose as a potential meniscus implant. *Journal of tissue engineering and regenerative medicine* 2007;1:406-8.
- [72] Martinez H, Brackmann C, Enejder A, Gatenholm P. Mechanical stimulation of fibroblasts in microchanneled bacterial cellulose scaffolds enhances production of oriented collagen fibers. *Journal of biomedical materials research Part A* 2012;100:948-57.
- [73] Markstedt K, Mantas A, Tournier I, Martínez Ávila H, Hägg D, Gatenholm P. 3D Bioprinting Human Chondrocytes with Nanocellulose–Alginate Bioink for Cartilage Tissue Engineering Applications. *Biomacromolecules* 2015;16:1489-96.
- [74] Warth RJ, Rodkey WG. Resorbable Collagen Scaffolds for the Treatment of Meniscus Defects: A Systematic Review. *Arthroscopy: The Journal of Arthroscopic & Related Surgery* 2015;31:927-41.
- [75] Stone KR, Rodkey WG, Webber R, McKinney L, Steadman JR. Meniscal regeneration with copolymeric collagen scaffolds. *In vitro* and *in vivo* studies evaluated clinically, histologically, and biochemically. *The American journal of sports medicine* 1992;20:104-11.
- [76] Hansen R, Bryk E, Vigorita V. Collagen scaffold meniscus implant integration in a canine model: a histological analysis. *Journal of orthopaedic research : official publication of the Orthopaedic Research Society* 2013;31:1914-9.
- [77] Steadman JR, Rodkey WG. Tissue-engineered collagen meniscus implants: 5- to 6-year feasibility study results. *Arthroscopy : the journal of arthroscopic & related surgery : official publication of the Arthroscopy Association of North America and the International Arthroscopy Association* 2005;21:515-25.
- [78] Zaffagnini S, Marcheggiani Muccioli GM, Bulgheroni P, Bulgheroni E, Grassi A, Bonanzinga T, *et al.* Arthroscopic collagen meniscus implantation for partial lateral meniscal defects: a 2-year minimum follow-up study. *The American journal of sports medicine* 2012;40:2281-8.
- [79] Monllau JC, Gelber PE, Abat F, Pelfort X, Abad R, Hinarejos P, *et al.* Outcome after partial medial meniscus substitution with the collagen meniscal implant at a minimum of 10 years' follow-up. *Arthroscopy : the journal of arthroscopic & related surgery : official publication of the Arthroscopy Association of North America and the International Arthroscopy Association* 2011;27:933-43.
- [80] Zaffagnini S, Marcheggiani Muccioli GM, Lopomo N, Bruni D, Giordano G, Ravazzolo G, *et al.* Prospective long-term outcomes of the medial collagen meniscus implant versus partial medial meniscectomy: a minimum 10-year follow-up study. *The American journal of sports medicine* 2011;39:977-85.

## Chapter II

# Biomaterials in Intervertebral Disc Tissue Engineering

## Chapter II

### Biomaterials in Intervertebral Disc Tissue Engineering

#### ABSTRACT

Intervertebral disc (IVD) is a fibrocartilaginous tissue that has a critical role in the motion and flexibility of the entire spine. The IVD is comprised by 3 focal elements: nucleus pulposus (NP), annulus fibrosus (AF) and cartilaginous end-plates. Furthermore, the degeneration of this complex tissue is considered the main reason for low back pain (LBP). LBP is a common painful condition that has a huge socioeconomic impact and is highly associated to a massive number of medical visits and hospitalization. In addition, the current available treatments are mainly focused on pain relief and/or invasive surgeries that have produced, so far, poor and/or inconclusive clinical outcomes. The recent past of this field is characterized by the development of novel approaches, especially tissue engineering-based strategies, capable to replace and proper regenerate the IVD tissue. Different biomaterial-based strategies have been attempted aiming to develop newly biomaterial formulations capable to address the current clinical needs in this field. Despite some promising results obtained in pre-clinical studies, the clinical translation of biomaterials capable to stimulate a suitable IVD regeneration is considered a distant future. In this chapter, an overview of diverse biomaterials that have been used in IVD tissue engineering is provided.

## II-1. INTRODUCTION

The intervertebral disc (IVD) is a fibrocartilaginous tissue that lies between two adjacent vertebrae. This tissue has three main constituents (**Figure II-1**): a soft, deformable, nucleus pulposus (NP), which is surrounded by the fibrous concentric layers of the annulus fibrosus (AF), and bonded above and below to adjacent vertebral bodies (VBs) by the thin layers of the cartilaginous end plates (CEPs) [1]. This entire structure contribute to weight bearing, motion and flexibility while protecting the neural anatomy of the entire spine. In addition, this tissue is subjected to multiple cycles of torsion and compression loadings that generate IVD pressures of 0.1 to 3 MPa [2].

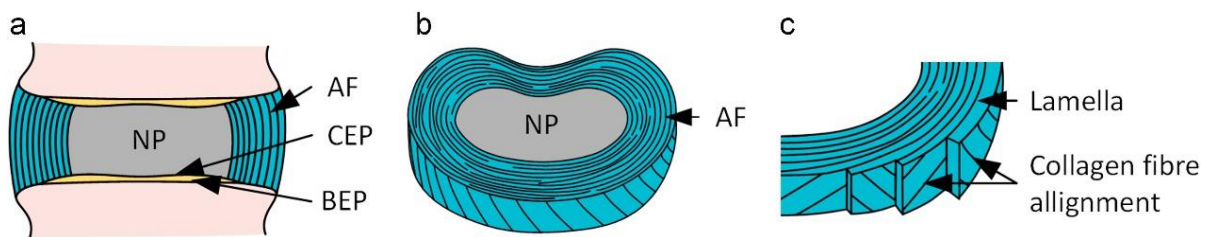


**Figure II-1 - Gross anatomy of a disc. (a) Cross section of a disc in the coronal plane, (b) diagram of a transversely sliced IVD and (c) diagram showing the alternating fiber alignment in successive lamellae. AF: annulus fibrosus; CEP: cartilaginous endplate; BEP: bony endplate; NP: nucleus pulposus.**

The degeneration of IVD is mainly due to ageing, nutrition, genetics, abnormal loading conditions and systemic diseases that lead to earlier degeneration processes [3]. These degeneration disorders are highly associated with low back pain (LBP) producing disability, neurological deficits and pain. LBP was responsible for the visit of more than 52 million of individuals to medical facilities with an estimated medical costs of \$253 billion during the year of 2012 [4]. Furthermore, the recognized treatment approaches for patients are mainly conservative and aim for alleviation of the pain contributing to LBP being ranked #1 in disability-adjusted life years [5]. However, depending on the level of the injury and pain, surgical spinal fusion, and discectomies are suggested. Those surgeries do not address the main cause of degeneration and are highly invasive being the only goal the pain source removal and the kinematical restoration function. In this sense, surgical procedures can lead to instability and spondylosis, finishing, in some cases, in reoperation procedures. In addition, the replacement of the degenerated discs using artificial implants has been shown inclusive clinical outcomes leading to a huge dilemma in the IVD replacement field [6]. Therefore, novel strategies focused on regeneration of the IVD have been developed using the tissue engineering (TE) triad. Growth factors, cells and biomaterials have been used, either alone or combined, and have shown promising results in different



aspects of IVD regeneration processes. Cells and growth factors are responsible for the extracellular matrix (ECM) homeostasis as well as anabolic effects on the cell population [7, 8]. Differently, biomaterials can be used as biological delivery systems and as structural scaffolds. In the first case, the developed biomaterials should facilitate the release of therapeutic agents, while mimicking the microenvironment of the native tissue. In opposite, as structural scaffold, the improvement of the disc height and mechanical stability of the vertebral segments are the two main features that need to be addressed. Herein, in this chapter it will be made an overview of the natural-based and synthetic-based biomaterials used in IVD TE applications.

## II-2. NATURAL-BASED BIOMATERIALS

### II-2.1. Alginate

Alginate is a natural-based anionic polymer typically obtained from brown seaweed, and has been extensively investigated and used for many biomedical applications, due to its biocompatibility, low toxicity, relatively low cost, and mild gelation by addition of divalent cations such as  $\text{Ca}^{2+}$  [9]. Alginate-based gels can also be cross-linked using covalent and thermal processes through chemical modification and addition of thermoresponsive hydrogels, respectively [9].

Bron *et al.* [10] tested different concentrations of alginate to assess the hydrogel stiffness that better mimic the viscoelastic properties of the NP. In this work, 2% (w/v) alginate hydrogels have revealed similar stiffness compared with the native tissue. However, despite the suitable mechanical properties, poor long-term stability and cell adhesion was observed. Using a different crosslinking method, photo cross-linked alginate hydrogels were developed and tested *in vitro* and *in vivo*. The mechanical properties were improved as well as an enhanced ECM deposition was observed in the *in vivo* tests [11, 12]. However, the alginate biological properties were not attractive and some strategies have been attempted to improve its biological performance. Foss *et al.* [13] supplemented the alginate hydrogels with glucosamine (GCSN) and chondroitin sulfate (CS). This chondroprotective supplementation resulted in an enhancement of NP cells differentiation and ECM deposition. In a similar approach, collagen was added to the alginate hydrogels and *in vitro* and *ex vivo* tests were performed. The addition of collagen resulted in an increasing of cell adhesion and proliferation as well as ECM production [14]. Re'em *et al.* [15] used arginine-glycine-aspartic acid (RGD) peptides to

promote a better differentiation of human bone marrow-derived mesenchymal stem cells in alginate hydrogels. As expected, the cell morphology, viability and proliferation was affected and the presence of the RGD peptides leading to an efficient chondrogenic stem-cell differentiation. Similar to the biological properties enhancement, the mechanical behavior of alginate hydrogels have been improved by combination with synthetic polymers. Zen *et al.* [16], developed an injectable microcryogels reinforced alginate system capable to prevent the leakage after interdiscal injection. The reinforcement provided by the poly(ethylene glycol) diacrylate-derived microcryogels led to an improvement in terms of cell retention and survival as well as a reduced IVD degeneration in a canine model (**Figure II-2**).

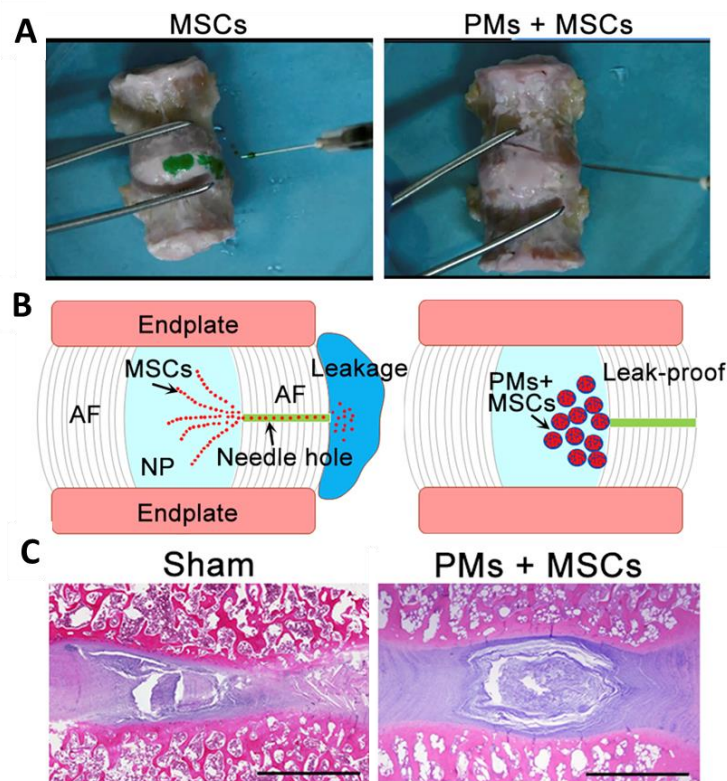


**Figure II-2** - Pictures showing cell leakage in free cell injection group and leak-proof in poly(ethylene glycol) diacrylate-derived microcryogels (PMs) assisted cell delivery group *ex vivo*. (B) Scheme of a possible mechanism responsible for the leak-proof of the PMs injectable system. (C) Hematoxylin and eosin staining at 24 weeks showing a better IVD restoration when PMs+MSCs are used comparing with the control group (Sham) (Scale bar: 3mm). Reprinted with permission from [16].

In sum, alginate can be considered a very versatile material with promising features for IVD tissue engineering, especially NP regeneration.

## II-2.2. Collagen

Collagen is the most abundant protein present in the ECM and its fibrillar structure has been exploited in several tissue engineering applications [17]. In addition, collagen offers good biocompatibility and biodegradability and has capability to regulate the morphology, adhesion and differentiation of cells [18]. Despite the promising features, the collagen constructs present lack of mechanical strength and structural stability upon hydration making it a big limitation for its application in certain tissues. However, the mechanical properties could be improved by a physical or chemical intermolecular crosslinking or through the blend of collagen with other materials.

Bron *et al.* [19] developed dense collagen scaffolds with mechanical properties that resemble the native NP. Later on, using the same scaffolds the migration of IVD cells was assessed [20]. The results revealed a successful migration of the cells into 3% (w/v) collagen scaffolds making it suitable for IVD regeneration. In a similar approach, Grunert *et al.* [21] used a high-density collagen gel (HDC) as an injectable system for AF regeneration. The goal of this work was to evaluate the ability of HDC to repair a needle-puncture AF defect in the rat-tail spine and to assess the influence of riboflavin (RF) crosslinking mediated process into the AF regeneration. The results revealed that the crosslinking step is crucial in the AF regeneration process. The stiffness of cross-linked HDC seems to positively affect the AF repair mechanism. In a total IVD replacement, Bowles *et al.* [22] also used a collagen-based scaffold as outer part of the IVD. The authors developed a tissue-engineered IVD composed of a gelatinous nucleus pulposus surrounded by an aligned collagenous annulus fibrosus. The produced scaffold was implanted into the rat caudal spine and was capable to maintain the disc space height and generate ECM (**Figure II-3**). Furthermore, a good spine integration yielding an intact motion segment with dynamic mechanical properties similar to native IVD was observed [22].

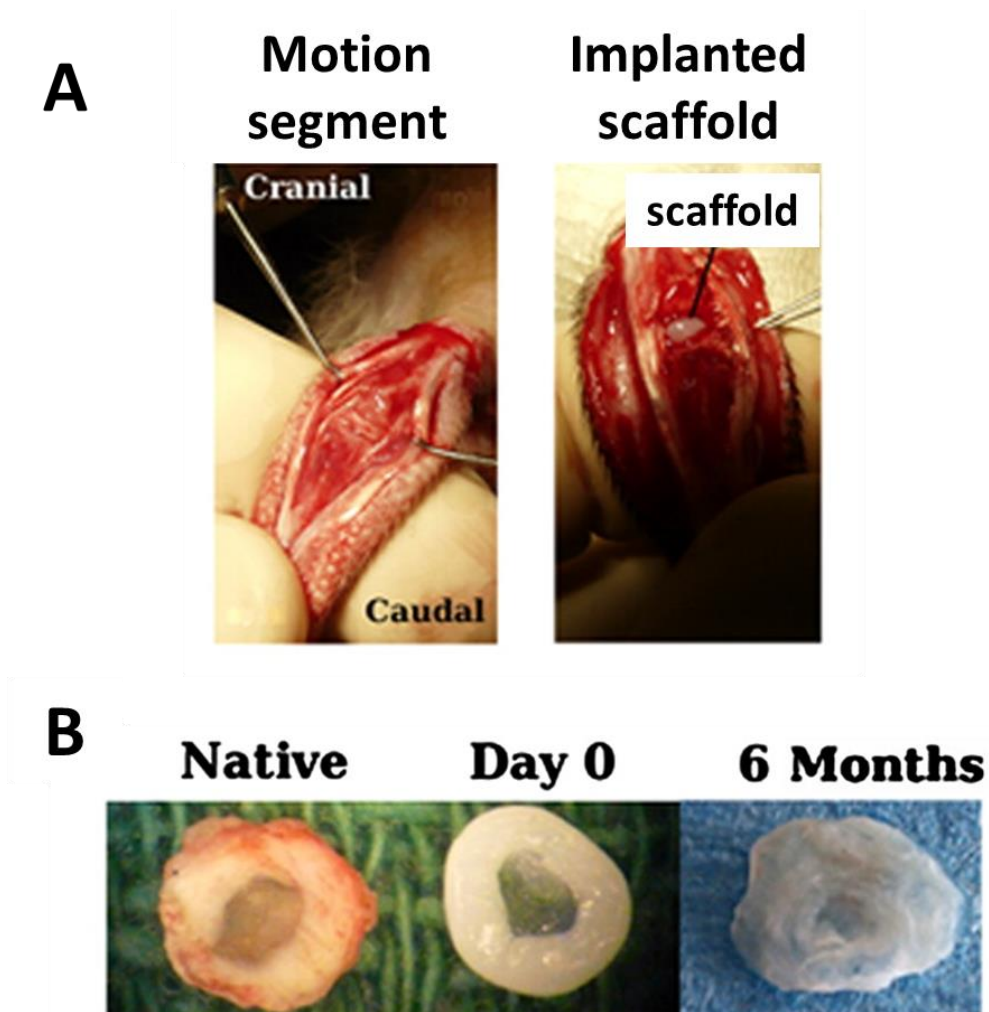


Figure II-3 - (A) Intraoperative images of the exposed disc space and implanted scaffold. (B) Pictures of the native IVD, the scaffold at day 0 and the implanted scaffold after 6 months of implantation. Reprinted with permission from [22].

In a different approach, collagen, hyaluronan and chondroitin-6-sulfate were combined to develop a tri-copolymer construct [23]. After the promising *in vitro* tests, the constructs seeded with NP cells were implanted directly into the disc space after nucleotomy in a rabbit model [24]. Results documented survival of the allografted NP cells and extracellular matrix deposition, which resulted in maintenance of disc height.

Different biomaterials have been used as a delivery system of mesenchymal stem cells (MSCs) for the treatment of IVD degeneration [25]. Furthermore, collagen has been used to develop a microencapsulation platform, which entraps MSCs in a solid microsphere [26]. This porous collagen nanofiber meshwork was capable to support MSCs attachment, survival, proliferation, migration, differentiation, and matrix remodeling. The delivery platform was posteriorly tested in a rabbit model, where autologous MSCs were interdiscally injected either packaged within collagen microspheres or

directly suspended in saline solution [27]. The collagen-based delivery system revealed a better maintenance of the dynamical mechanical behavior and reduced the risk of osteophyte formation. Similar results were obtained using a genipin mediated crosslinking system for AF regeneration [28]. In a similar strategy, a type II collagen/chondroitin sulfate (CS) composite hydrogel-like delivery system was developed [29]. The results showed that the delivery system cross-linked with 0.02% genipin was biocompatible and promoted the expressions of NP-specific genes. After the injection in rat coccygeal vertebrae degeneration model, a partly restoration of the disc height and structure of the degenerated NP was observed. The injection systems have been widely used in IVD regeneration, especially in NP applications. Combining two biomaterials, including collagen, Tsaryk *et al.* [30] produced a collagen-low molecular weight hyaluronic acid (LMW HA) semi-interpenetrating network which was loaded with gelatin microspheres. In this work, the gelatin microspheres were used as growth factor delivery system allowing the chondrogenic differentiation of MSCs loaded in the hydrogel. Once again, collagen revealed suitable properties to work as a cell carrier system for NP regeneration.

Despite the promising results, collagen hydrogels can prove to be difficult to work with due to their low mechanical properties and easily denaturation. The blend with other biomaterials can be a suitable solution for the use of this integral part of native ECM.

### **II-2.3. Fibrin**

Fibrin is an insoluble degradable protein capable to form a gel by mimicking the last step of the blood coagulation cascade. Thus, fibrin gels are produced by a thrombin-mediated polymerization of fibrinogen [31]. This polymerization reaction is responsible by the removal of peptides present in fibrin, leading to a structural conformation change of the protein [32]. In this sense, fibrin has been reported as a promising material for applications in biomedical engineering owing not only to its biocompatibility and biodegradability but also due to its capability to provide cell binding sites for cell attachment, migration, and proliferation [33].

Regarding IVD regeneration, fibrin has been used in several strategies for AF regeneration. In the majority of the studies, fibrin is used as sealant/glue to prevent NP leakages. In 2008, Heuer *et al.* [34] investigated different conventional surgical methods for AF closure: suture alone, and fibrin glue and cyanoacrylate glue, alone and with suture. The results showed that closing the AF incision using the fibrin glue might not be suitable. In contrast, the cyanoacrylate glue with suture provided a longest

duration of closure but failed in reaching the maximum number of fatigue cycles. Nonetheless, this work highlights the request for an appropriate AF sealant system with good long-term reliability. Later on, different studies showed the development of genipin-cross-linked fibrin hydrogels. This genipin-mediated system aimed to improve the fibrin hydrogels mechanical properties. Schek *et al.* [35] developed a genipin cross-linked fibrin hydrogel with mechanical properties in the range of native AF tissue. Although fibrin hydrogel showed good biocompatibility and excellent adhesive properties, a low cell proliferation and rounded morphology were also observed, making them not suitable for AF regeneration. In a similar approach, a genipin crosslinkable fibrin gel was combined with cell-adhesion molecules (fibronectin and collagen) [36]. In this study, series of *in vitro* tests were performed and a fibrin gel without adhesion molecules was used as control. The hydrogels revealed mechanical properties that resemble the compressive properties of the IVD. However, the addition of fibronectin did not significantly affect cell adhesion and elongation. Nevertheless, the authors conclude that their developed fibrin gel has promising features to be used as sealant in small AF defects and can be combined with other biomaterials to act as an adhesive system in larger defects. Furthermore, the *in vivo* degradability of a genipin cross-linked fibrin hydrogel was assessed through a subcutaneous model in rats [37]. As expected, compared with fibrin alone, the genipin-mediated system has higher *in vivo* longevity. In addition, the hydrogels supported AF cells adhesion and migration, and maintained the disc height in a bovine *ex vivo* defect model (**Figure II-4**). Later on, the same author, used the same hydrogel in an anti-Tumor necrosis factor alpha (anti-TNF $\alpha$ ) drug delivery system [38]. The fibrin hydrogel was functionalized with collagen type I spheres loaded with anti-TNF $\alpha$ . Anti-TNF $\alpha$  is responsible to regulate the production of pro-inflammatory cytokines and pain mediators. The results showed that this system has potential to be used as a sealant in AF defects and partially restore IVD biomechanics. However, further *in vivo* assays are required to assess the effectiveness of the drug releasing to prevent IVD degeneration.

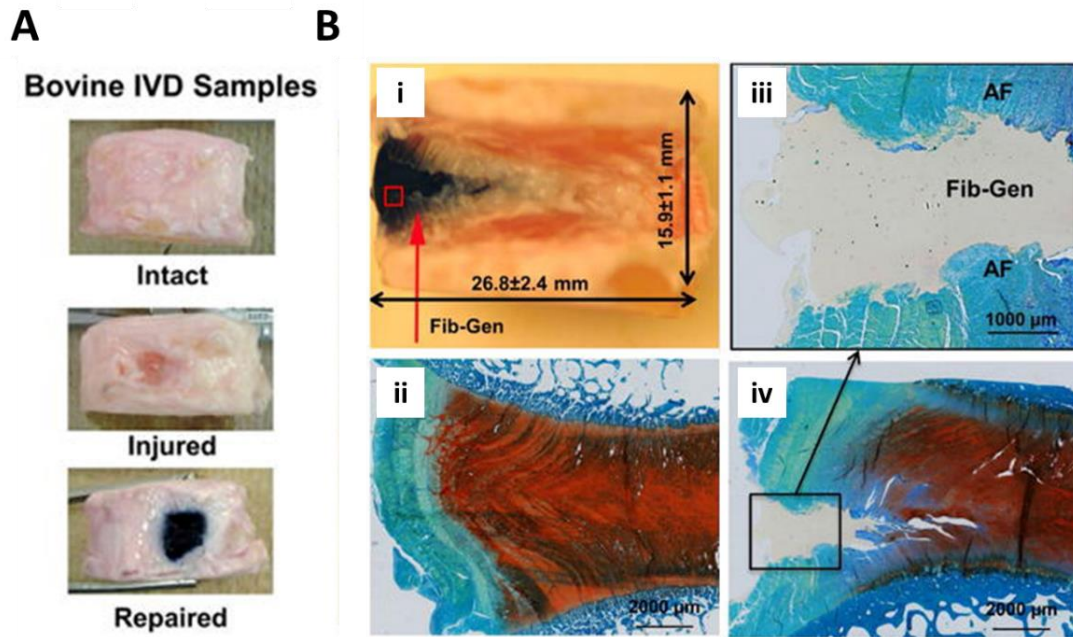


Figure II-4 - (A) Bovine caudal IVD samples were evaluated in three groups (Intact, Injured and Repaired). (B) Pictures of sagittal sections taken at Day 6. (Bi) Macroscopic image of the repaired IVD using the injected Fibrin-genipin system. (Bii) Microscopic images of sections stained with FAST from the intact IVD. (Biii and Biv) Microscopic images of sections stained with FAST from the repaired IVD. Reprinted with permission from [37].

Recently, Cruz *et al.* [39] performed a screening test to assess the “perfect” balance in terms of fibrinogen and genipin concentration. The results revealed that the F70G1 (70 mg.mL<sup>-1</sup> fibrinogen; 1 mg.mL<sup>-1</sup> genipin) formulation revealed a good balance between the biological and biomechanical performance. This study was useful to show the versatility of the genipin-mediated system and proved its tunable capability by playing with the fibrinogen and genipin concentrations.

As mentioned before, fibrin can be considered a promising biomaterial to be combined with other materials. The combination of fibrin with hyaluronic acid (HA) is one example of a multi-material hydrogel for IVD regeneration. The presence of HA contributed to a better restoration of disc height as well as to achieve a stiffness similar to native NP levels [40]. In this study, the results proved that the addition of HA is able to enhance the hydrogel mechanical performance and integration with the native NP tissue. In addition, silk fibroin was added to this promising combination leading to an improvement of the mechanical strength and to the shrinkage prevention *in vivo* [41].

In sum, Fibrin presents great biological features that can be explored and considered in the development of hydrogels/scaffolds for IVD regeneration.

## II-2.4. Hyaluronic acid

Hyaluronic acid is a linear polysaccharide and is one of the most important components of ECM. Some studies revealed that HA can play an important role in regulating cell differentiation, migration, angiogenesis and inflammation responses [42]. HA structure is rich in carboxyl and hydroxyl groups, which makes possible to form a hydrogel using different crosslink methods [43]. Its biodegradation occurs by action of hyaluronidases and can be tuned by using different molecular weights or types of crosslinking [44].

HA-based hydrogels were mainly tested in NP regeneration strategies. Preliminary studies revealed the prominence of HA hydrogels to inhibit the degenerative cascade of the disc degeneration [45]. From bench to pre-clinical research, several studies showed that HA is a promising material for IVD regeneration. An oxidized HA-gelatin implant was used in a ovine model and showed good outcomes in terms of restoration of the motion segment stability [46]. In a similar approach and using an *in vivo* porcine model, a Thiol-Modified HA and Elastin-Like Polypeptide construct revealed good outcomes and was capable to restore the initial mechanical behavior in early-stage disc degeneration [47]. Two HA-derived polymeric substitute materials, HYAFF® 120 and HYADD® 3, were also tested in an *in vivo* porcine model [48]. As control, a nucleotomy was performed and, as expected, a loss of normal IVD structure with narrowing, fibrous tissue replacement and disruption of the bony end-plates were observed. In opposite, the HA-based materials prevented these changes showing close similarity to the normal biconvex structure. Despite the good results, long-term follow-ups are needed to better understand the regeneration processes. In a different study, a polymerized HA and collagen implant material developed for NP replacement showed achieved good results in an *in vivo* study. However, the developed implant induced harmful effects in the AF structure [49]. In this sense, this study showed that IVD regeneration strategies should also focus on the prevention of annular damage. Recently, researchers have been focusing on producing a composite IVD scaffold capable to mimic the AF. Jeong *et al.* [50] developed HA-poly(ethylene glycol) composite hydrogels targeting both NP and AF regeneration. Results showed that hydrogel mechanical properties can range from 70-489 kPa depending on HA molecular weight. In a different approach, a cell-seeded HA gel core was surrounded by an electrospun, nanofibrous scaffold to represent integrated NP and AF, respectively [51]. The cartilaginous HA–nanofibrous scaffold (HANFS) construct architecturally resembled a native IVD, with an outer annulus fibrosus–like region and inner nucleus pulposus–like region [51]. Furthermore, the cells seeded on top of the scaffold helped in the maintenance of the native IVD microarchitecture.



Recently, a novel system that consisted in HA hydrogels chemically cross-linked by polyethylene glycol diglycidyl ether (PEGDE) and treated with tannic acid (TA) was developed [52]. TA treatment was performed as an attempt to enhance the mechanical properties of HA hydrogels. As expected, the mechanical properties were improved and the hydrogels supported cell proliferation and attachment without cytotoxicity. In addition, TA also has properties as a hyaluronidase inhibitor and antioxidant, improving the stability of the hydrogel.

HA can also acts in the down-regulation of inflammatory markers. It was found that interferon-induced protein with tetratricopeptide repeats 3 (IFIT3) and proapoptotic insulin-like growth factor-binding protein-3 (IGFBP3) is downregulated while collagen I and aggrecan are upregulated after HA treatment [53]. Furthermore, injection of HA hydrogels has recently been demonstrated to effectively alleviate the inflammatory pain induced by IVD injury in rats [54].

HA has been widely used as a cell carrier for NP regeneration and has demonstrated desirable biological, degradation, or bioinductive effects. Indeed, HA stands apart for its broader acceptance in clinical trials as cell carrier (Clinical trial NCT01290367 and NCT02338271).

Overall, HA can be considered an interesting biomaterial for IVD regeneration. However, different outcomes were observed when different molecular weights were used. In one hand, higher molecular weight HA resembles the IVD mechanical performance but inhibits cell proliferation and ECM deposition. One other hand, the biological performance is enhanced when lower molecular weight formulations are used. However, these formulations do not present mechanical properties suitable for IVD regeneration.

## **II-2.5. Silk fibroin**

Silk fibroin (SF) have been extensively studied as one of the most promising candidates in different application fields, such as technical textiles, structural applications, biosensors, biomedical applications, tissue engineering and drug delivery [55]. SF is composed by two animal-based proteins, fibroin and sericin, in which the fibroin protein is embedded in the glue-like sericin protein. SF can be effectively used for the fabrication of biomedical composite materials in several forms, including fibers, films, sponges and hydrogels [55]. This biomaterial possesses high biocompatibility, controllable biodegradability, low immunogenicity excellent mechanical properties and structural integrity making it a desirable polymer in TE [56].

In 2007, Chang *et al.* [57] developed a SF-based foam functionalized with arginine-glycine-aspartic acid (RGD) peptide. The foam supported AF cells attachment, proliferation and ECM deposition. The coupling the SF scaffold with RGD-peptides affected cell morphology. However, no differences were found in terms of cell attachment and tissue formation. Furthermore, the cells had higher levels of type II collagen and aggrecan gene expression when compared to cells grown on non-modified scaffolds. Later, the same author tried to improve cell infiltration and matrix accumulation using a dynamic culturing system [58]. The results revealed that dynamic culture improved AF tissue formation by enhancing ECM deposition.

In a more advanced approach, Park *et al.* [59] developed a SF lamellar scaffold in order to mimic the lamellar morphology of the AF tissue. In this work, a porous SF scaffold was used as control. The inter-lamellar spacing was 150–250  $\mu\text{m}$  and the average pore sizes were 100–250  $\mu\text{m}$ . The biological results revealed a favorable ECM expression and tissue function when lamellar scaffolds were used. Later on, a total IVD replacement strategy was developed by the same author. A biphasic biomaterial structure was generated by using SF for the AF and fibrin/hyaluronic acid gels for the NP [60]. Histology, biochemical assays, and gene expression indicated that the lamellar scaffolds supported AF-like tissue over 2 weeks. In addition, porcine chondrocytes formed NP-like phenotype within the hydrogel after 4 weeks of culture. Then, the hydrogel was combined with the lamellar scaffold to produce a total IVD implant [60].

SF has been widely used to develop AF lamellar scaffolds [61-63]. Bhattacharjee *et al.* [61] designed a novel silk-based scaffold using a custom-made winding machine, with fiber alignment resembling the anatomical criss-cross lamellar fibrous orientation of AF. Chondroitin sulfate (CS) was added in crosslinking step to help in the enhancement of the mechanical and biological properties. The scaffolds, with or without CS, induced an alignment of expanded human chondrocytes and ECM deposition while supporting their chondrogenic redifferentiation. Furthermore, the scaffolds were tested under dynamic conditions. As expected, the dynamic culture conditions improved the cellular metabolic rate and ECM production and a tissue gradient within the constructs was observed. The inner region presented higher deposition of collagen II, glycosaminoglycan (GAG), and stiffer in compression, whereas an outer region was richer in collagen I and stiffer in tension. In a similar approach, Bhunia *et al.* [63] produced a SF-based bioartificial disc adopting a directional freezing technique. The fabricated SF scaffolds supported primary AF or human mesenchymal stem cell proliferation, differentiation and no significant immune response was observed when the construct was implanted subcutaneously.

In an advanced 3D printing approach, Costa *et al.* [64] engineered a 3D bioprinted patient-specific scaffold for IVD regeneration (**Figure II-5**). In this work, a bioink composed by a SF hydrogel combined with elastin was used. Following a reverse engineering approach, the proposed strategy makes use of a 3D model of AF obtained by semi-automatic morphological segmentation from magnetic resonance imaging dataset of human IVD. The bioprinted SF/elastin scaffolds were shown to possess structural and mechanical properties similar to the native AF and supported cell attachment and growth up to 21 days of culturing.

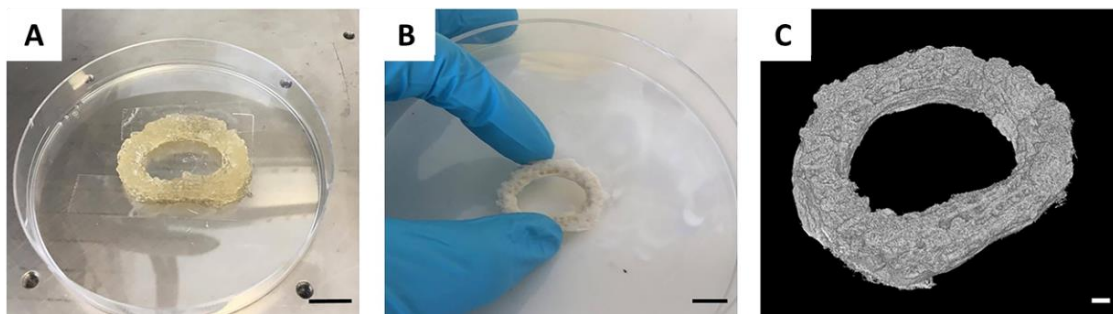


**Figure II-5 - (A) AF-like patient-specific implant before freeze-drying and (B) after freeze-drying (scale bars: 10 mm). (C) 3D reconstruction of AF substitute by Micro-CT (scale bar: 1mm). Reprinted with permission from [64].**

Owing to its greater mechanical properties, SF has been extensively explored in AF regeneration strategies. However, some studies also revealed their propensity to be used in NP regeneration approaches. Porous SF scaffolds fabricated by paraffin-sphere-leaching methods showed suitable architecture and mechanical properties when compared with NP native tissue [65]. In addition, the scaffolds showed capability to provide an appropriate microstructure and environment to support adhesion, proliferation and infiltration of NP cells. Similar results were obtained by Du *et al.* [66], where a similar paraffin sphere-leaching method was used. The authors were capable to control the pore size and mechanical properties of the scaffold to better mimic the IVD native tissue.

SF injectable hydrogels can also offer a good alternative for treatment of degenerated IVD due to their ability to withstand adequate loads. In an injectable approach, a SF/polyurethane (SF/PU) composite hydrogel revealed adequate mechanical properties to be used in NP regeneration [67]. In a combinatorial approach, Neo *et al.* [68] tested the combination of poly(vinyl) alcohol cryogels with SF. The presence of SF enhanced the swelling ability of the cryogels as well as and the surface hydrophobicity that subsequently improved the cell-hosting abilities.

Murab *et al.* [69] developed an injectable hydrogel composed by N-acetyl-glucosamine (GlcNAc) loaded silk hollow spheres embedded in silk hydrogel. This composite system not only provided

adequate structural support to the *ex vivo* degenerated disc model but also enhanced proteoglycan production from adipose stem cells. The spatiotemporal and controlled release of GlcNAc was the main responsible for the increasing of proteoglycan production.

SF has been tested in different biomedical applications, mostly in musculoskeletal tissue repair strategies. SF presents high biocompatibility, a relatively slow rate of degradation and high mechanical performance making it a promising biomaterial for AF repair.

## II-3. SYNTHETIC-BASED BIOMATERIALS

### II-3.1. Polycaprolactone

Polycaprolactone (PCL) is a linear aliphatic polyester characterized by its hydrophobicity, semi-crystallinity (50%), biocompatibility and has a relatively slow degradation [70]. This polymer has been widely used in the biomedical field due its good stability, ease of processing and has already been approved for clinical use by the U.S. Food and Drug Administration [71].

As mentioned in previous sections, AF comprises a lamellar morphology. Koepsell *et al.* [72] tried to mimic this architecture by the fabrication of electrospun nanofibrous PCL scaffolds. In this work, random, aligned, and round-end configurations were used. The round-end PCL scaffolds substantially outperformed the other conformations in terms of cell adhesion. However, the scaffold with aligned nanofibers strongly affected the orientation of cells mimicking the native microenvironment. In a similar approach, electrospun nanofibrous PCL scaffolds seeded with mesenchymal stem cells (MSCs) were produced in order to replicate the angle-ply multi-lamellar AF morphology [73]. These scaffolds induced the deposition of an organized collagen-rich ECM, mimicking the angle-ply and multi-lamellar architecture after 10 weeks of *in vitro* culture. In addition, a mechanical parity with native tissue was also observed. The same research group, developed a total disc replacement implant. A disc-like angle-ply structure composed by agarose hydrogel to form the central NP and oriented electrospun nanofibrous PCL scaffold to form the AF was developed [74]. The implants revealed mechanical behaviors qualitatively similar to native tissue. Furthermore, cells seeded into both regions acquired distinct morphologies that mirror those seen in native tissue. This implant was subsequently translated to a small animal model where the disc height was maintained when combined with spinal fixation [75] (**Figure II-6**). Later on, a long-term study using the same methodology was performed and similar

results were observed [76]. Despite the promising results, the developed implant did not totally integrate with the native tissue and a displacement of around 50% from the disc space was observed when the implant was not fixed.

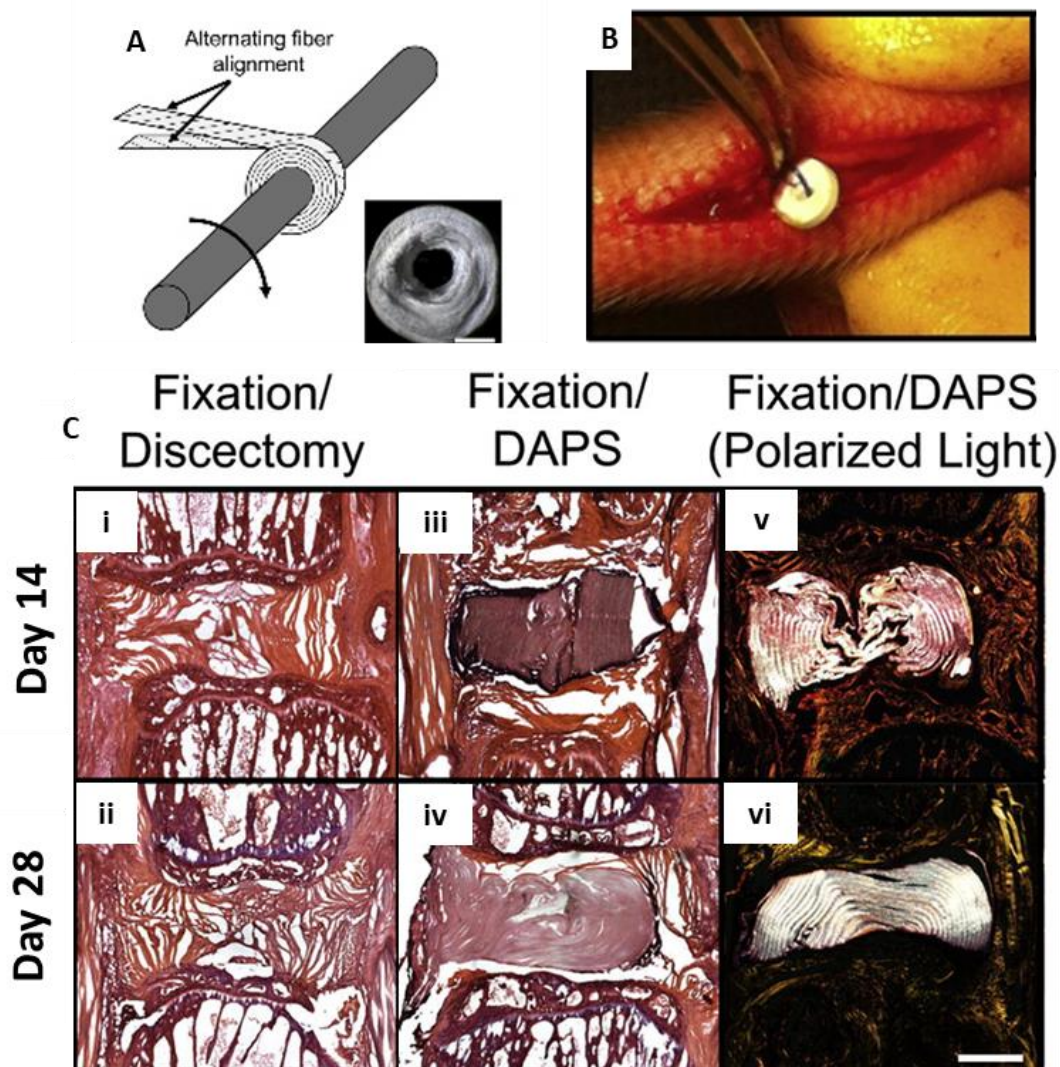


Figure II-6 - (A) Enrolment of the electrospun fibers to produce the disc-like angle-ply structure (DAPS) (bottom) (scale bar: 1mm). (B) DAPS implantation into the rat caudal spine into the C8/C9 disc space. (C) Hematoxylin and eosin staining of sections at day 14 and day 28 after implantation for the discectomy group (Ci and Cii) and DAPS group (Ciii and Civ). (Cv and Cvi) Polarized pictures of the DAPS group after 14 and 28 days of implantation. Scale bar: 1mm. Reprinted with permission from [75].

Recently, a intradiscal application system comprising a poly( $\epsilon$ -caprolactone-co-lactide)-b-poly(ethylene glycol)-b-poly( $\epsilon$ -caprolactone-co-lactide) PCLA-PEG-PCLA hydrogel that releases celecoxib (COX-2 inhibitor) was developed [77]. In this study, ten client-owned dogs with chronic low back pain received an interdiscal injection of the celecoxib-loaded hydrogel. Clinical improvements were achieved by reduction of back pain in 9 of 10 dogs. Nevertheless, in 3 of 10 dogs, back pain recurred after 3

months. Despite the short-term clinical improvement, the safety and effectiveness of interdiscal PCLA-PEG-PCLA hydrogel injections using an *in vivo* canine model was revealed.

PCL is capable to resemble the AF mechanical properties and the combination with other materials allows the production of injectable hydrogels for AF regeneration. However, its hydrophobicity is a major drawback in TE applications.

### II-3.2. Polyethylene glycol

Polyethylene glycol (PEG) is a synthetic polyether and has been an important hydrophilic polymer in biomedical applications, including surface modification, bioconjugation, drug delivery and tissue engineering [78]. PEG hydrogels present good biocompatibility, non-immunogenicity, and resistance to protein adsorption and most importantly they induce water absorption making them good candidates for NP regeneration.

Although PEG-based hydrogels present good biocompatibility and mechanical behavior they are considered non-cell adhesive structures. In this sense, these hydrogels are usually functionalized or combined with other polymers. An advanced delivery system composed by PEG and HA has been developed for IVD regeneration [79, 80]. This hydrogel incorporating mesenchymal precursor cells (MPCs) and pentosan polysulfate endorsed higher cell viability and accelerated ECM deposition of type II collagen and GAG without an exacerbated immune response *in vivo*. Using the same combination of polymers, a promising PEG-based gel covalently linked to serum albumin and mixed with high molecular weight HA was developed [81]. This gel revealed anti-angiogenic properties *in vitro* and *in vivo* as well as an increased expression of collagen II and aggrecan in IVD cells. Furthermore, this PEG-based gel was tested *in vivo* using a sheep model [82]. Although no adverse effects were observed after gel administration inconclusive outcomes were obtained. Regardless the absence of strong signals for disc regeneration *in vivo*, a randomized clinical trial was initiated for patients with disc herniation using this approach (Clinical trial NCT01640457).

In another approach, PEG was combined with laminin. It has been reported that NP contains different forms of laminin and NP cells prefer the attachment to laminin receptors [83]. Moreover, an injectable *in situ* forming hydrogel incorporating full-length laminins was developed [84, 85]. This composed biomaterial resulted in the promotion of NP cells attachment and appropriate cell signaling.

In addition, gene expression for NP-specific molecules was observed as well as higher sulfated GAG production.

PEG hydrogels can be promising candidates for IVD TE, especially NP regeneration, due to their ease of processing and tuning capability.

### II-3.3. Polyurethane

Polyurethanes (PU) are polymers usually used in the production of hard plastics. However, urethane-based biomaterials have been the most promising polymers due their capability of cellular adhesion and cell proliferation and controlled degradation kinetics. In addition, they possess high tenacity, hardness, chemical resistance, flexibility, biocompatibility and excellent processing capability [86].

In terms of mechanical performance, PU-based hydrogels revealed similar behavior comparing with the native tissues withstanding adequate loading compression forces [87]. When combined with SF, an injectable system composed by PU and SF showed suitable degradation rate and mechanical properties [67].

Regarding AF regeneration, electrospun scaffolds were developed in different studies. The scaffolds were combined with cell attachment proteins, such as fibronectin, to promote cell adhesion and proliferation in the PU-based constructs [88, 89]. In these studies, the scaffolds supported AF cells attachment and proliferation as well as ECM deposition. In a different approach, a PU-based mass was used for AF regeneration [90]. In this work, the PU-based mass allowed to maintain the compressive stiffness, disc height and cell viability. Furthermore, the adenosine triphosphate (ATP), lactate and the proteoglycan contents in the device group were significantly higher indicating that the implantation of the PU mass transfer device can promote the nutrient transport.

Recently, Lu *et al.* [91] developed a bioengineered AF implant recapitulating the inner and the outer regions of the AF tissue. The authors used PU scaffolds coated with fibronectin to generate a multi-lamellar AF tissue with ECM compositions that resemble the inner and outer AF regions (**Figure II-7A and B**). The results showed that, playing with different media supplementations, was possible to mimic the two distinct regions of the AF (**Figure II-7C and D**).



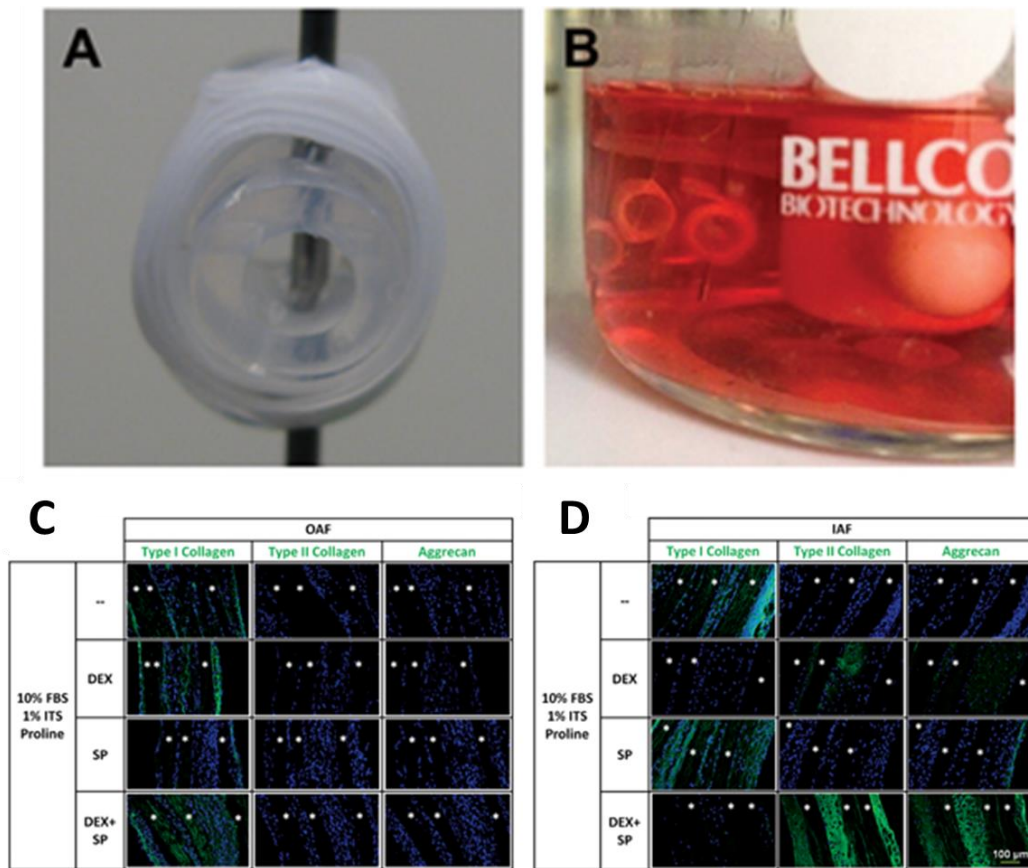


Figure II-7 - (A) Multi-layered PU construct scaffold using a Teflon® tube. (B) Multi-layered PU scaffolds placed within a spinner flask bioreactor. (C) Immunofluorescence images of the outer (OAF) and inner (IAF) AF tissue formation using the indicated medium formulation. FBS: fetal bovine serum, ITS: insulin-transferrin-selenium, DEX: dexamethasone, SP: sodium pyruvate. \* indicates PU scaffold. Scale bar: 100 μm. Reprinted with permission from [91].

PU-based scaffolds present promising features to be used in IVD regeneration strategies mainly due to their ease of use. However, long-term follow-up are needed mainly in NP applications.

#### II-3.4. Polylactide and polyglycolide

Polylactide (PLA) and Polyglycolide (PGA) are two biodegradable synthetic polymers commonly used in tissue engineering [92]. Regarding PLA, different racemic mixtures have been used, such as poly(L-lactide) (PLLA) and poly(D, L-lactide) (PDLLA). Helen *et al.* [93] developed PDLLA/Bioglass composite foams capable to support a suitable cell microenvironment that led to an enhancement in terms of cell proliferation and GAG and type I and II collagen production. In a different approach, a PLLA-based electrospun aligned scaffold used for AF regeneration revealed axial compression and



tensile properties resembling AF tissue as well as suitable cell infiltration and cell–scaffold interaction [94].

Composites of PLA and PGA termed poly(lactide-co-glycolide) (PLGA) appear to have better properties for IVD TE. PLGA has attracted a considerable awareness for biomedical applications owing to its: (i) biocompatibility; (ii) tailored biodegradation rate; (iii) approval for clinical use in humans by the U.S. Food and Drug Administration (FDA); (iv) potential to modify surface properties to provide better interaction with biological materials; and (v) suitability for export to countries and cultures where implantation of animal-derived products is unpopular [95]. One of the applications where PLGA has FDA approval to be used in the human body is related with drug release approaches [96]. A recent study aimed to control the pathogenic fibrosis of NP by encapsulating interleukin-1 receptor antagonist (IL-1ra) in PLGA microspheres [97]. IL-1ra is responsible for the attenuation of IL-1 $\beta$  mediated matrix degradative enzymes (ADMTS-4 and MMP-13), nitric oxide production (iNOS) and inflammatory markers (IL-1 $\beta$ , IL-6 and TLR-4) in NP cells. This *in vitro* study showed promising results in terms of attenuation of the degradative effects of IL-1 $\beta$  on the NP, making it a promising therapeutic strategy for treating early-stage IVD degeneration. Furthermore, a study reported that polyplexes of hyperbranched polymers with high plasmid DNA (pDNA) binding affinity encapsulated in injectable PLGA microspheres, allowed temporal release and higher transfection of the plasmid DNA [98]. The plasmid DNA encoding orphan nuclear receptor 4A1 (NR4A1) was capable to prevent fibrosis and increased disc height and GAG deposition.

PLGA scaffolds were also used for NP regeneration and showed an extensive ECM deposition when seeded with NP cells and implanted subcutaneously in mice [99]. Furthermore, using a canine model, PLGA constructs seeded with NP cells were implanted and evaluated in terms of disc height, segment stability, and biomechanics and immunohistochemical analysis. The results showed that NP cell-PLGA scaffold composite can prevent or delay the degeneration process, presenting better outcomes than nucleotomy alone or PLGA constructs alone [100]. Nevertheless, a cell-free approach using a PGA-based scaffold in a rabbit model also revealed adequate cell migration and ECM deposition making it a promising alternative for IVD regeneration [101].

In a combinatory approach, nanostructured 3D PLGA microspheres loaded with dexamethasone and basic fibroblast growth factor (b-FGF) embedded in heparin/poly(L-lysine) nanoparticles were able to support rat mesenchymal stem cells proliferation and differentiation into NP like cells [102]. Later on, the PLGA microspheres were evaluated using a rat model. The microspheres alone and loaded with

adipose-derived stem cells revealed that are capable of partially restoring the IVD and a reestablishing proteoglycan accumulation, after 24 weeks of implantation [103].

#### II-4. FINAL CONSIDERATIONS

Nowadays LBP is considered a universal concern in modern society. TE approaches hold great promise in the development of IVD replacement implants to improve the current clinical outcomes for IVD degeneration treatments.

Although great achievements has been accomplished in this field in the past years substantial challenges still need to be addressed. Besides that, a big issue that needs to be reconsidered is that IVD degeneration processes are not only focused on NP. The degenerative processes that occur in the AF and EP should also be considered. Major improvements in imaging diagnostic systems in order to design custom-made biomaterial-based constructs should be performed. In addition, future experiments might be focused in the IVD regeneration and pain relief relationship. It is important to guarantee a suitable IVD regeneration process but also to create a treatment that allows a fast pain removal from the patient. It is important to guarantee that the developed scaffold is capable to withstand significant mechanical loads as well as a suitable integration/anchorage and nutrient diffusion. In this sense, tissue engineers have been used different biomaterials in order to overcome the current challenges and subsequently move forward in this particular field.

This chapter reviews the use of natural-based and synthetic-based materials for IVD regeneration. Natural-based materials present several advantages including an established degradation pathway, biocompatibility and safety. Overall, they provide suitable environments and biological cues for cell proliferation and regeneration. In opposite, their processing is very difficult to control and very expensive manufacturing processes are needed in some cases. Regarding synthetic-materials, their ease and reproducible manufacturing and their simple chemical properties tunability make them very popular among the research community. However, their degradation can lead to the production of harmful by-products and their interaction with cells is often inadequate. For these reasons, most of the current IVD regeneration approaches use the combination of two or more materials, most of the times a natural-based and a synthetic-based material.

Different biomaterials and different mixtures of biomaterials have been attempted and only a

reduced number of them reached the clinical trials. This lack of a significant advancement in the application of biomaterials in the IVD regeneration field should be consciously addressed and answers should be provided. For this reason, in our opinion, a high throughput screening of the biomaterials characteristics using standardize characterization processes should be performed. Reference biomaterials for IVD regeneration strategies should be found and used as starting point for the development of more advanced approaches.

Regarding the type of approaches that have been used, in the NP regeneration processes the injection of hydrogels appeared to be the most promising strategy. However, as mentioned before, a fully restoration of IVD might also address AF regeneration. In this sense, future research guidelines addressing the total IVD substitution/regeneration should be considered. Furthermore, these approaches should also comprise the production of patient-specific implants by means of using reverse engineering, *i.e.* combining imaging techniques (*e.g.* MRI and micro-CT) and 3D bioprinting technology. It is the author's conviction, that the implantation of a custom-made implant in terms of size, shape, mechanical performance and biodegradability, can improve patient's recovery and fully reestablish the spine biofunctionality.

## II-5. REFERENCES

- [1] Newell N, Little JP, Christou A, Adams MA, Adam CJ, Masouros SD. Biomechanics of the human intervertebral disc: A review of testing techniques and results. *Journal of the Mechanical Behavior of Biomedical Materials* 2017;69:420-34.
- [2] Neidlinger-Wilke C, Galbusera F, Pratsinis H, Mavrogonatou E, Mietsch A, Kleitsas D, *et al.* Mechanical loading of the intervertebral disc: From the macroscopic to the cellular level. *European Spine Journal* 2014;23:S333-S43.
- [3] Adams MA, Roughley PJ. What is intervertebral disc degeneration, and what causes it? *Spine* 2006;31:2151-61.
- [4] Bowles RD, Setton LA. Biomaterials for intervertebral disc regeneration and repair. *Biomaterials* 2017;129:54-67.
- [5] Murray CJL, Lopez AD. Measuring the Global Burden of Disease. *New England Journal of Medicine* 2013;369:448-57.
- [6] Janssen M, Garcia R, Miller L, Reed W, Zigler J, Ferko N, *et al.* Challenges and Solutions for Lumbar Total Disc Replacement Implantation. *Spine* 2017;42 Suppl 24:S108-s11.

- [7] Chan SC, Gantenbein-Ritter B. Intervertebral disc regeneration or repair with biomaterials and stem cell therapy—feasible or fiction? *Swiss medical weekly* 2012;142:w13598.
- [8] Yim RL, Lee JT, Bow CH, Meij B, Leung V, Cheung KM, *et al.* A systematic review of the safety and efficacy of mesenchymal stem cells for disc degeneration: insights and future directions for regenerative therapeutics. *Stem cells and development* 2014;23:2553-67.
- [9] Lee KY, Mooney DJ. Alginate: properties and biomedical applications. *Progress in polymer science* 2012;37:106-26.
- [10] Bron JL, Vonk LA, Smit TH, Koenderink GH. Engineering alginate for intervertebral disc repair. *Journal of the Mechanical Behavior of Biomedical Materials* 2011;4:1196-205.
- [11] Chou AI, Nicoll SB. Characterization of photocross-linked alginate hydrogels for nucleus pulposus cell encapsulation. *Journal of biomedical materials research Part A* 2009;91:187-94.
- [12] Chou AI, Akintoye SO, Nicoll SB. Photo-cross-linked alginate hydrogels support enhanced matrix accumulation by nucleus pulposus cells *in vivo*. *Osteoarthritis Cartilage* 2009;17:1377-84.
- [13] Foss BL, Maxwell TW, Deng Y. Chondroprotective supplementation promotes the mechanical properties of injectable scaffold for human nucleus pulposus tissue engineering. *Journal of the Mechanical Behavior of Biomedical Materials* 2014;29:56-67.
- [14] Guillaume O, Naqvi SM, Lennon K, Buckley CT. Enhancing cell migration in shape-memory alginate-collagen composite scaffolds: *In vitro* and *ex vivo* assessment for intervertebral disc repair. *Journal of biomaterials applications* 2015;29:1230-46.
- [15] Re'em T, Tsur-Gang O, Cohen S. The effect of immobilized RGD peptide in macroporous alginate scaffolds on TGFbeta1-induced chondrogenesis of human mesenchymal stem cells. *Biomaterials* 2010;31:6746-55.
- [16] Zeng Y, Chen C, Liu W, Fu Q, Han Z, Li Y, *et al.* Injectable microcryogels reinforced alginate encapsulation of mesenchymal stromal cells for leak-proof delivery and alleviation of canine disc degeneration. *Biomaterials* 2015;59:53-65.
- [17] Gelse K, Poschl E, Aigner T. Collagens—structure, function, and biosynthesis. *Advanced drug delivery reviews* 2003;55:1531-46.
- [18] Chevallay B, Herbage D. Collagen-based biomaterials as 3D scaffold for cell cultures: applications for tissue engineering and gene therapy. *Medical and Biological Engineering and Computing* 2000;38:211-8.
- [19] Bron JL, Koenderink GH, Everts V, Smit TH. Rheological characterization of the nucleus pulposus and dense collagen scaffolds intended for functional replacement. *Journal of orthopaedic research : official publication of the Orthopaedic Research Society* 2009;27:620-6.
- [20] Bron JL, Mulder HW, Vonk LA, Doulabi BZ, Oudhoff MJ, Smit TH. Migration of intervertebral disc cells into dense collagen scaffolds intended for functional replacement. *Journal of materials science Materials in medicine* 2012;23:813-21.

- [21] Grunert P, Borde BH, Hudson KD, Macielak MR, Bonassar LJ, Hartl R. Annular repair using high-density collagen gel: a rat-tail *in vivo* model. *Spine* 2014;39:198-206.
- [22] Bowles RD, Gebhard HH, Härtl R, Bonassar LJ. Tissue-engineered intervertebral discs produce new matrix, maintain disc height, and restore biomechanical function to the rodent spine. *Proceedings of the National Academy of Sciences* 2011;108:13106-11.
- [23] Zhuang Y, Huang B, Li CQ, Liu LT, Pan Y, Zheng WJ, *et al.* Construction of tissue-engineered composite intervertebral disc and preliminary morphological and biochemical evaluation. *Biochemical and biophysical research communications* 2011;407:327-32.
- [24] Huang B, Zhuang Y, Li CQ, Liu LT, Zhou Y. Regeneration of the intervertebral disc with nucleus pulposus cell-seeded collagen II/hyaluronan/chondroitin-6-sulfate tri-copolymer constructs in a rabbit disc degeneration model. *Spine* 2011;36:2252-9.
- [25] Longo UG, Papapietro N, Petrillo S, Franceschetti E, Maffulli N, Denaro V. Mesenchymal stem cell for prevention and management of intervertebral disc degeneration. *Stem Cells Int* 2012;2012:921053.
- [26] Chan BP, Hui TY, Yeung CW, Li J, Mo I, Chan GC. Self-assembled collagen-human mesenchymal stem cell microspheres for regenerative medicine. *Biomaterials* 2007;28:4652-66.
- [27] Li YY, Diao HJ, Chik TK, Chow CT, An XM, Leung V, *et al.* Delivering mesenchymal stem cells in collagen microsphere carriers to rabbit degenerative disc: reduced risk of osteophyte formation. *Tissue engineering Part A* 2014;20:1379-91.
- [28] Chik TK, Ma XY, Choy TH, Li YY, Diao HJ, Teng WK, *et al.* Photochemically cross-linked collagen annulus plug: A potential solution solving the leakage problem of cell-based therapies for disc degeneration. *Acta biomaterialia* 2013;9:8128-39.
- [29] Zhou X, Wang J, Fang W, Tao Y, Zhao T, Xia K, *et al.* Genipin cross-linked type II collagen/chondroitin sulfate composite hydrogel-like cell delivery system induces differentiation of adipose-derived stem cells and regenerates degenerated nucleus pulposus. *Acta biomaterialia* 2018;71:496-509.
- [30] Tsaryk R, Gloria A, Russo T, Anspach L, De Santis R, Ghanaati S, *et al.* Collagen-low molecular weight hyaluronic acid semi-interpenetrating network loaded with gelatin microspheres for cell and growth factor delivery for nucleus pulposus regeneration. *Acta biomaterialia* 2015;20:10-21.
- [31] Wolberg AS. Thrombin generation and fibrin clot structure. *Blood Reviews* 2007;21:131-42.
- [32] Li Y, Meng H, Liu Y, Lee BP. Fibrin Gel as an Injectable Biodegradable Scaffold and Cell Carrier for Tissue Engineering. *The Scientific World Journal* 2015;2015:10.
- [33] Joo JY, Amin ML, Rajangam T, An SSA. Fibrinogen as a promising material for various biomedical applications. *Molecular & Cellular Toxicology* 2015;11:1-9.
- [34] Heuer F, Ulrich S, Claes L, Wilke HJ. Biomechanical evaluation of conventional anulus fibrosus closure methods required for nucleus replacement. Laboratory investigation. *Journal of neurosurgery Spine* 2008;9:307-13.

- [35] Schek RM, Michalek AJ, Iatridis JC. Genipin-cross-linked fibrin hydrogels as a potential adhesive to augment intervertebral disc annulus repair. *European cells & materials* 2011;21:373-83.
- [36] Guterl CC, Torre OM, Purmessur D, Dave K, Likhitpanichkul M, Hecht AC, *et al.* Characterization of Mechanics and Cytocompatibility of Fibrin-Genipin Annulus Fibrosus Sealant with the Addition of Cell Adhesion Molecules. *Tissue Engineering Part A* 2014;20:2536-45.
- [37] Likhitpanichkul M, Dreischarf M, Illien-Junger S, Walter BA, Nukaga T, Long RG, *et al.* Fibrin-genipin adhesive hydrogel for annulus fibrosus repair: performance evaluation with large animal organ culture, in situ biomechanics, and *in vivo* degradation tests. *European cells & materials* 2014;28:25-37; discussion -8.
- [38] Likhitpanichkul M, Kim Y, Torre OM, See E, Kazezian Z, Pandit A, *et al.* Fibrin-genipin annulus fibrosus sealant as a delivery system for anti-TNF $\alpha$  drug. *The spine journal : official journal of the North American Spine Society* 2015;15:2045-54.
- [39] Cruz MA, Hom WW, DiStefano TJ, Merrill R, Torre OM, Lin HA, *et al.* Cell-Seeded Adhesive Biomaterial for Repair of Annulus Fibrosus Defects in Intervertebral Discs. *Tissue engineering Part A* 2018;24:187-98.
- [40] Li Z, Kaplan KM, Wertz A, Peroglio M, Amit B, Alini M, *et al.* Biomimetic fibrin-hyaluronan hydrogels for nucleus pulposus regeneration. *Regenerative medicine* 2014;9:309-26.
- [41] Park S-H, Cho H, Gil ES, Mandal BB, Min B-H, Kaplan DL. Silk-fibrin/hyaluronic acid composite gels for nucleus pulposus tissue regeneration. *Tissue engineering Part A* 2011;17:2999-3009.
- [42] Allison DD, Grande-Allen KJ. Review. Hyaluronan: a powerful tissue engineering tool. *Tissue engineering* 2006;12:2131-40.
- [43] Collins MN, Birkinshaw C. Hyaluronic acid based scaffolds for tissue engineering—A review. *Carbohydrate Polymers* 2013;92:1262-79.
- [44] Kim IL, Mauck RL, Burdick JA. Hydrogel design for cartilage tissue engineering: a case study with hyaluronic acid. *Biomaterials* 2011;32:8771-82.
- [45] Nakashima S, Matsuyama Y, Takahashi K, Satoh T, Koie H, Kanayama K, *et al.* Regeneration of intervertebral disc by the intradiscal application of cross-linked hyaluronate hydrogel and cross-linked chondroitin sulfate hydrogel in a rabbit model of intervertebral disc injury. *Bio-medical materials and engineering* 2009;19:421-9.
- [46] Malhotra NR, Han WM, Beckstein J, Cloyd J, Chen W, Elliott DM. An Injectable Nucleus Pulposus Implant Restores Compressive Range of Motion in the Ovine Disc. *Spine* 2012;37.
- [47] Leckie AE, Akens MK, Woodhouse KA, Yee AJM, Whyne CM. Evaluation of Thiol-Modified Hyaluronan and Elastin-Like Polypeptide Composite Augmentation in Early-Stage Disc Degeneration: Comparing 2 Minimally Invasive Techniques. *Spine* 2012;37.
- [48] Revell PA, Damien E, Di Silvio L, Gurav N, Longinotti C, Ambrosio L. Tissue engineered intervertebral disc repair in the pig using injectable polymers. *Journal of Materials Science: Materials in Medicine* 2007;18:303-8.

- [49] Omlor GW, Nerlich AG, Lorenz H, Bruckner T, Richter W, Pfeiffer M, *et al.* Injection of a polymerized hyaluronic acid/collagen hydrogel matrix in an *in vivo* porcine disc degeneration model. *European spine journal : official publication of the European Spine Society, the European Spinal Deformity Society, and the European Section of the Cervical Spine Research Society* 2012;21:1700-8.
- [50] Jeong CG, Francisco AT, Niu Z, Mancino RL, Craig SL, Setton LA. Screening of hyaluronic acid-poly(ethylene glycol) composite hydrogels to support intervertebral disc cell biosynthesis using artificial neural network analysis. *Acta biomaterialia* 2014;10:3421-30.
- [51] Nesti LJ, Li W-J, Shanti RM, Jiang YJ, Jackson W, Freedman BA, *et al.* Intervertebral Disc Tissue Engineering Using a Novel Hyaluronic Acid–Nanofibrous Scaffold (HANFS) Amalgam. *Tissue Engineering Part A* 2008;14:1527-37.
- [52] Lee HY, Hwang CH, Kim HE, Jeong SH. Enhancement of bio-stability and mechanical properties of hyaluronic acid hydrogels by tannic acid treatment. *Carbohydr Polym* 2018;186:290-8.
- [53] Kazezian Z, Li Z, Alini M, Grad S, Pandit A. Injectable hyaluronic acid down-regulates interferon signaling molecules, IGFBP3 and IFIT3 in the bovine intervertebral disc. *Acta biomaterialia* 2017;52:118-29.
- [54] Mohd Isa IL, Abbah SA, Kilcoyne M, Sakai D, Dockery P, Finn DP, *et al.* Implantation of hyaluronic acid hydrogel prevents the pain phenotype in a rat model of intervertebral disc injury. *Science Advances* 2018;4:eaq0597.
- [55] Li Z-H, Ji S-C, Wang Y-Z, Shen X-C, Liang H. Silk fibroin-based scaffolds for tissue engineering. *Frontiers of Materials Science* 2013;7:237-47.
- [56] Ma D, Wang Y, Dai W. Silk fibroin-based biomaterials for musculoskeletal tissue engineering. *Materials Science and Engineering: C* 2018;89:456-69.
- [57] Chang G, Kim HJ, Kaplan D, Vunjak-Novakovic G, Kandel RA. Porous silk scaffolds can be used for tissue engineering annulus fibrosus. *European Spine Journal* 2007;16:1848-57.
- [58] Chang G, Kim HJ, Vunjak-Novakovic G, Kaplan DL, Kandel R. Enhancing annulus fibrosus tissue formation in porous silk scaffolds. *Journal of Biomedical Materials Research Part A* 2010;92A:43-51.
- [59] Park S-H, Gil ES, Mandal BB, Cho H, Kluge JA, Min B-H, *et al.* Annulus fibrosus tissue engineering using lamellar silk scaffolds. *Journal of tissue engineering and regenerative medicine* 2012;6:s24-s33.
- [60] Park S-H, Gil ES, Cho H, Mandal BB, Tien LW, Min B-H, *et al.* Intervertebral Disk Tissue Engineering Using Biphasic Silk Composite Scaffolds. *Tissue Engineering Part A* 2011;18:447-58.
- [61] Bhattacharjee M, Miot S, Gorecka A, Singha K, Loparic M, Dickinson S, *et al.* Oriented lamellar silk fibrous scaffolds to drive cartilage matrix orientation: Towards annulus fibrosus tissue engineering. *Acta biomaterialia* 2012;8:3313-25.
- [62] Bhattacharjee M, Chameettachal S, Pahwa S, Ray AR, Ghosh S. Strategies for Replicating Anatomical Cartilaginous Tissue Gradient in Engineered Intervertebral Disc. *ACS Applied Materials & Interfaces* 2014;6:183-93.

- [63] Bhunia BK, Kaplan DL, Mandal BB. Silk-based multilayered angle-ply annulus fibrosus construct to recapitulate form and function of the intervertebral disc. *Proceedings of the National Academy of Sciences* 2018;115:477.
- [64] Costa JB, Silva-Correia J, Ribeiro VP, da Silva Morais A, Oliveira JM, Reis RL. Engineering patient-specific bioprinted constructs for treatment of degenerated intervertebral disc. *Materials Today Communications* 2018.
- [65] Zeng C, Yang Q, Zhu M, Du L, Zhang J, Ma X, *et al.* Silk fibroin porous scaffolds for nucleus pulposus tissue engineering. *Materials science & engineering C, Materials for biological applications* 2014;37:232-40.
- [66] Du L, Zhu M, Yang Q, Zhang J, Ma X, Kong D, *et al.* A novel integrated biphasic silk fibroin scaffold for intervertebral disc tissue engineering. *Materials Letters* 2014;117:237-40.
- [67] Hu J, Chen B, Guo F, Du J, Gu P, Lin X, *et al.* Injectable silk fibroin/polyurethane composite hydrogel for nucleus pulposus replacement. *Journal of Materials Science: Materials in Medicine* 2012;23:711-22.
- [68] Neo PY, Shi P, Goh JC-H, Toh SL. Characterization and mechanical performance study of silk/PVA cryogels: towards nucleus pulposus tissue engineering. *Biomedical Materials* 2014;9:065002.
- [69] Murab S, Samal J, Shrivastava A, Ray AR, Pandit A, Ghosh S. Glucosamine loaded injectable silk-in-silk integrated system modulate mechanical properties in bovine ex-vivo degenerated intervertebral disc model. *Biomaterials* 2015;55:64-83.
- [70] Nair LS, Laurencin CT. Biodegradable polymers as biomaterials. *Progress in Polymer Science* 2007;32:762-98.
- [71] Griffith M, Venkatraman SS. Polycaprolactone-based biomaterials for tissue engineering and drug delivery: Current scenario and challenges AU - Mondal, Debasish. *International Journal of Polymeric Materials and Polymeric Biomaterials* 2016;65:255-65.
- [72] Koepsell L, Zhang L, Neufeld D, Fong H, Deng Y. Electrospun Nanofibrous Polycaprolactone Scaffolds for Tissue Engineering of Annulus Fibrosus. *Macromolecular Bioscience* 2011;11:391-9.
- [73] Nerurkar NL, Baker BM, Sen S, Wible EE, Elliott DM, Mauck RL. Nanofibrous biologic laminates replicate the form and function of the annulus fibrosus. *Nature Materials* 2009;8:986.
- [74] Nerurkar NL, Sen S, Huang AH, Elliott DM, Mauck RL. Engineered Disc-Like Angle-Ply Structures for Intervertebral Disc Replacement. *Spine* 2010;35:867-73.
- [75] Martin JT, Milby AH, Chiaro JA, Kim DH, Hebela NM, Smith LJ, *et al.* Translation of an engineered nanofibrous disc-like angle-ply structure for intervertebral disc replacement in a small animal model. *Acta biomaterialia* 2014;10:2473-81.
- [76] Martin JT, Kim DH, Milby AH, Pfeifer CG, Smith LJ, Elliott DM, *et al.* *In vivo* performance of an acellular disc-like angle ply structure (DAPS) for total disc replacement in a small animal model. *Journal of Orthopaedic Research* 2017;35:23-31.



- [77] Tellegen AR, Willems N, Beukers M, Grinwis GCM, Plomp SGM, Bos C, *et al.* Intradiscal application of a PCLA–PEG–PCLA hydrogel loaded with celecoxib for the treatment of back pain in canines: What's in it for humans? *Journal of tissue engineering and regenerative medicine* 2018;12:642-52.
- [78] Zhu J. Bioactive modification of poly(ethylene glycol) hydrogels for tissue engineering. *Biomaterials* 2010;31:4639-56.
- [79] Frith JE, Cameron AR, Menzies DJ, Ghosh P, Whitehead DL, Gronthos S, *et al.* An injectable hydrogel incorporating mesenchymal precursor cells and pentosan polysulphate for intervertebral disc regeneration. *Biomaterials* 2013;34:9430-40.
- [80] Frith JE, Menzies DJ, Cameron AR, Ghosh P, Whitehead DL, Gronthos S, *et al.* Effects of bound versus soluble pentosan polysulphate in PEG/HA-based hydrogels tailored for intervertebral disc regeneration. *Biomaterials* 2014;35:1150-62.
- [81] Benz K, Stippich C, Osswald C, Gaissmaier C, Lembert N, Badke A, *et al.* Rheological and biological properties of a hydrogel support for cells intended for intervertebral disc repair. *BMC musculoskeletal disorders* 2012;13:54.
- [82] Benz K, Stippich C, Fischer L, Möhl K, Weber K, Lang J, *et al.* Intervertebral disc cell- and hydrogel-supported and spontaneous intervertebral disc repair in nucleotomized sheep. *European spine journal : official publication of the European Spine Society, the European Spinal Deformity Society, and the European Section of the Cervical Spine Research Society* 2012;21:1758-68.
- [83] Jing L, Gilchrist CL, Richardson WJ, Fitch RD, Setton LA. Expression of Laminin Isoforms, Receptors, and Binding Proteins Unique to Nucleus Pulposus Cells of Immature Intervertebral Disc AU - Chen, Jun. *Connective Tissue Research* 2009;50:294-306.
- [84] Francisco AT, Mancino RJ, Bowles RD, Brunger JM, Tainter DM, Chen YT, *et al.* Injectable laminin-functionalized hydrogel for nucleus pulposus regeneration. *Biomaterials* 2013;34:7381-8.
- [85] Francisco AT, Hwang PY, Jeong CG, Jing L, Chen J, Setton LA. Photocrosslinkable laminin-functionalized polyethylene glycol hydrogel for intervertebral disc regeneration. *Acta biomaterialia* 2014;10:1102-11.
- [86] Agnol LD, Gonzalez Dias FT, Nicoletti NF, Falavigna A, Bianchi O. Polyurethane as a strategy for annulus fibrosus repair and regeneration: a systematic review. *Regenerative medicine* 2018;13:611-26.
- [87] Dahl MC, Ahrens M, Sherman JE, Martz EO. The restoration of lumbar intervertebral disc load distribution: a comparison of three nucleus replacement technologies. *Spine* 2010;35:1445-53.
- [88] Attia M, Santerre JP, Kandel RA. The response of annulus fibrosus cell to fibronectin-coated nanofibrous polyurethane-anionic dihydroxyoligomer scaffolds. *Biomaterials* 2011;32:450-60.
- [89] Yeganegi M, Kandel RA, Santerre JP. Characterization of a biodegradable electrospun polyurethane nanofiber scaffold: Mechanical properties and cytotoxicity. *Acta biomaterialia* 2010;6:3847-55.
- [90] Wang Y-F, Levene HB, Gu W, Huang CYC. Enhancement of Energy Production of the Intervertebral Disc by the Implantation of Polyurethane Mass Transfer Devices. *Annals of Biomedical Engineering* 2017;45:2098-108.

- [91] lu J, Santerre JP, Kandel RA. Towards engineering distinct multi-lamellated outer and inner annulus fibrosus tissues. *Journal of Orthopaedic Research* 2018;36:1346-55.
- [92] Pan Z, Ding J. Poly(lactide-co-glycolide) porous scaffolds for tissue engineering and regenerative medicine. *Interface focus* 2012;2:366-77.
- [93] Helen W, Merry CL, Blaker JJ, Gough JE. Three-dimensional culture of annulus fibrosus cells within PDLLA/Bioglass composite foam scaffolds: assessment of cell attachment, proliferation and extracellular matrix production. *Biomaterials* 2007;28:2010-20.
- [94] Ma J, He Y, Liu X, Chen W, Wang A, Lin C-Y, *et al.* A novel electrospun-aligned nanoyarn/three-dimensional porous nanofibrous hybrid scaffold for annulus fibrosus tissue engineering. *International journal of nanomedicine* 2018;13:1553-67.
- [95] Gentile P, Chiono V, Carmagnola I, Hatton PV. An overview of poly(lactic-co-glycolic) acid (PLGA)-based biomaterials for bone tissue engineering. *International journal of molecular sciences* 2014;15:3640-59.
- [96] Lai P, Daear W, Lobenberg R, Prenner EJ. Overview of the preparation of organic polymeric nanoparticles for drug delivery based on gelatine, chitosan, poly(d,l-lactide-co-glycolic acid) and polyalkylcyanoacrylate. *Colloids and surfaces B, Biointerfaces* 2014;118:154-63.
- [97] Gorth DJ, Mauck RL, Chiaro JA, Mohanraj B, Hebela NM, Dodge GR, *et al.* IL-1ra delivered from poly(lactic-co-glycolic acid) microspheres attenuates IL-1 $\beta$ -mediated degradation of nucleus pulposus *in vitro*. *Arthritis research & therapy* 2012;14:R179-R.
- [98] Feng G, Zhang Z, Dang M, Zhang X, Doleyres Y, Song Y, *et al.* Injectable nanofibrous spongy microspheres for NR4A1 plasmid DNA transfection to reverse fibrotic degeneration and support disc regeneration. *Biomaterials* 2017;131:86-97.
- [99] Kim HY, Kim HN, Lee SJ, Song JE, Kwon SY, Chung JW, *et al.* Effect of pore sizes of PLGA scaffolds on mechanical properties and cell behaviour for nucleus pulposus regeneration *in vivo*. *Journal of tissue engineering and regenerative medicine* 2017;11:44-57.
- [100] Ruan D-K, Xin H, Zhang C, Wang C, Xu C, Li C, *et al.* Experimental Intervertebral Disc Regeneration with Tissue-Engineered Composite in a Canine Model. *Tissue Engineering Part A* 2010;16:2381-9.
- [101] Endres M, Abbushi A, Thomale UW, Cabraja M, Kroppenstedt SN, Morawietz L, *et al.* Intervertebral disc regeneration after implantation of a cell-free bioresorbable implant in a rabbit disc degeneration model. *Biomaterials* 2010;31:5836-41.
- [102] Liang CZ, Li H, Tao YQ, Zhou XP, Yang ZR, Xiao YX, *et al.* Dual delivery for stem cell differentiation using dexamethasone and bFGF in/on polymeric microspheres as a cell carrier for nucleus pulposus regeneration. *Journal of materials science Materials in medicine* 2012;23:1097-107.
- [103] Liang CZ, Li H, Tao YQ, Peng LH, Gao JQ, Wu JJ, *et al.* Dual release of dexamethasone and TGF-beta3 from polymeric microspheres for stem cell matrix accumulation in a rat disc degeneration model. *Acta biomaterialia* 2013;9:9423-33.

## Chapter III

# Recent Advances on 3D Printing of Patient-Specific Implants for Fibrocartilage Tissue Regeneration

## Recent Advances on 3D Printing of Patient-Specific Implants for Fibrocartilage Tissue Regeneration<sup>2</sup>

### ABSTRACT

Fibrocartilage is a very peculiar type of tissue that can be found in intervertebral disc and meniscus. It is characterized by its avascular nature and for the shear and compressive forces that can be subjected. The number of individuals affected by the degeneration of fibrocartilaginous tissues has been growing and the poor outcomes of the current treatments have led to an increased interest in new alternative approaches. Therefore, the combination of reverse engineering with 3D printing has been extensively explored in order to produce patient-specific implants capable of improving the current clinical outcomes. This review outlines the recent advances achieved in tissue engineering field, especially focusing on fibrocartilaginous tissue.

---

<sup>2</sup> This chapter is based on the following publication:

Costa J. B., Silva-Correia J., Reis R. L., and Oliveira J. M., "Recent Advances on 3D Printing of Patient-Specific Implants for Fibrocartilage Tissue Regeneration", *Journal of 3D Printing in Medicine*, vol. 2, issue 3, pp. 129–140, doi:10.2217/3dp-2018-0006, 2018.

### III-1. INTRODUCTION

Fibrocartilage is an avascular and aneural tissue that can be histologically identified by the presence of rounded or oval cells embedded in a readily visible extracellular matrix (ECM) [1]. Comparing with the other types of cartilage, fibrocartilage is a specialized type of cartilage that can be found in areas requiring tough support or great tensile strength [2]. This type of cartilage, characterized by the predominance of collagen type I over collagen type II, can be found in different tissues, such as intervertebral disc (IVD) and meniscus. In comparison, hyaline cartilage, that is the most abundant type of cartilage, is characterized by predominance of collagen type II and can be found in the nasal septum, trachea, ends of the growing bones, and in between the ribs and the sternum [2]. Unlike fibrocartilage that acts as a shock absorber, the purpose of hyaline cartilage is to cover the surfaces of joints, allowing bones to slide over one another, thus reducing friction and preventing damage in lubricated movements of the bones at joints [3]. Lastly, elastic cartilage that is known as yellow cartilage has the role to support structures subjected to frequent deformation, including the larynx, epiglottis, and external ear. Elastic cartilage is similar to hyaline cartilage but contains elastic bundles (elastin) scattered throughout the matrix providing a tissue that is stiff yet elastic [2]. The poor regenerative properties of this tissue due to the restricted number of cells and lack of vascular supply as well as the number of individuals affected by the degeneration of these tissues has seized the scientific community awareness [4]; 5 million people are estimated to be affected by lower back pain attributed to IVD degeneration, whereas 600,000 knee surgeries are performed per year in the United States due to meniscus lesions [5]. The current available treatments and diagnostic methods, adequate treatment choice and respective outcomes have generated large discussions within the medical community [6, 7]. Furthermore, none of the currently available treatments could be consensually designated as the “gold” standard treatment. This dilemma in the medical community combined with the progression of scientific knowledge and technology, instigated the interest for new alternatives in this field. Tissue engineering and regenerative medicine approaches have been using the combination of cells, scaffolds and biological factors, in order to achieve better a regeneration process capable of overcoming the current issues [8-11]. Despite the promising results, some challenges are delaying the translation of these approaches to the clinics. Biocompatibility, mechanical performance, biodegradability and implant anchorage are some of the most common features that require scaffolds’ optimization, however one of which we believe that stands out the most is the capability to fabricate patient-specific implants. Patient-specificity can bring some advantages in terms of implant alignment leading to a faster and better regeneration process

[12]. Furthermore, the concept of patient-specificity is not only related with the customized shape of the implant but also the histocompatibility features of the implant. The cell spatial distribution over the implant as well as the vasculature and architecture are also some challenges that need to be addressed to develop patient-specific implants in order to mimic as much as possible the native tissue. In this sense, the combination of high-resolution imaging techniques (*e.g.* Magnetic resonance imaging (MRI) and micro computed tomography (micro-CT)) with 3D printing can be a powerful approach for the development of personalized treatments and achieving the much-desired patient-specificity. Herein, the recent achievements, applications and future trends of 3D printing in the meniscus and IVD TE field are overviewed.

### III-2. 3D PRINTING IN TISSUE ENGINEERING APPROACHES

Additive manufacturing (AM), commonly known as 3D printing is a well-established technology in the field of materials processing and has been widely used for the last few decades [13]. The intense exploitation of this promising technology has led to the appearance of several processes that can be classified into seven categories: 1) binder jetting; 2) directed energy deposition; 3) material extrusion; 4) material jetting; 5) powder bed fusion; 6) sheet lamination; and 7) vat photopolymerization [14]. In fact, the first technique used for the directly handling living cells was the Ink-jet printing where multidimensional cellular structures have been fabricated by means of this approach, revealing great promise for the fabrication of biologically viable tissues, and one day possibly organs [15]. However, this is very limited in terms of the concentration of cells that can be processed and printing resolution. Therefore, new techniques based on the same principles have been developed. The cell electrospinning and the bioelectrosprays are an example of that, where high-intensity electric fields have been used to jet living cells without causing any effect on cell behavior [16-19] (**Figure III-1**). Although these approaches already showed their potential by generating droplets a few tens of microns in size there is still a lack of studies related with tissue regeneration.

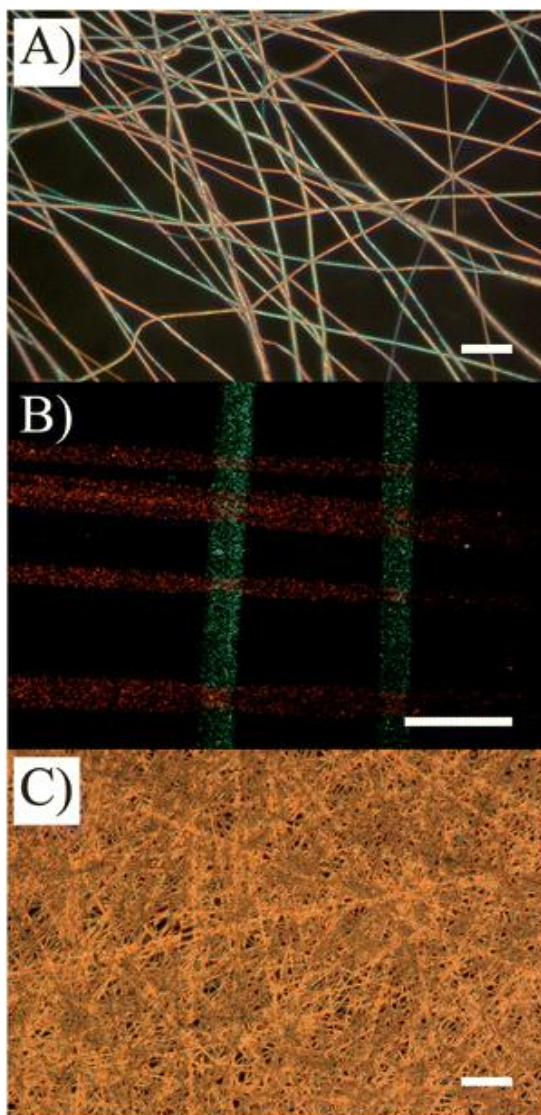


Figure III-1 - Panel (A) depicts nanofibers containing a mix of nanoparticles. Scale bar represents 10  $\mu\text{m}$ . The fluorescent micrograph in panel (B) illustrates two types of proteins electrospun and aligned perpendicular to each other. Scale bar represents 5  $\mu\text{m}$ . Panel (C) shows a representative optical micrograph of a functional scaffold collected over 30 minutes. The scale bar denotes 50  $\mu\text{m}$ . Adapted with permission from Suwan N. Jayasinghe [19].

The versatility provided by these different processes allowed the use of 3D printing in several applications [14]. One of them is Tissue Engineering (TE), where 3D printing has been used for the biofabrication of different tissues. In TE-based approaches, scaffold's architecture should allow cell infiltration and proliferation, to give space for ECM generation and physical connections for injured tissue [20]. The possibility to control the scaffold macro- and micro-structures given by the 3D printing technology, offers the necessary freedom to produce customized scaffolds that meet all the requirements for tissue regeneration. In other words, parameters like shape, porosity, pore size, mechanical performance, cells spatial distribution, and the introduction of biological signals can be

totally tuned during the 3D printing process. In these type of TE approaches, the material selection is critical since some materials present better features for specific applications. Soft tissue engineering (*e.g.* cartilage) has been using synthetic biodegradable polymers, natural polymers, and various combinations, whereas hard tissue engineering (*e.g.* bone) has been mainly exploring the combination of synthetic polymers with ceramic materials, such as hydroxyapatite (HAp), that are known to be favorable for bone ingrowth [21]. These biomaterials, in addition to being printable, must have a set of special characteristics. For instance, the biocompatibility and biodegradability are very important properties since a minimal inflammatory response and accumulation of nontoxic degradation products must be assured. The printable biomaterial also needs to support cellular attachment, proliferation and differentiation. Biomaterials derived from natural polymers like alginate, collagen, chitosan and hyaluronic acid are some examples of materials that can easily mimic cells ECM, enhancing the biological performance of the 3D printed scaffold. Although natural biomaterials are favorable for biological processes, the use of synthetic polymers like poly( $\epsilon$ -caprolactone) (PCL) and poly(D, L-lactic-co-glycolic acid) (PLGA) in 3D printing, can led to the production of implants with better mechanical properties and controllable degradation rates. However, these synthetic polymers have relatively low biological activity, considering their potential for tissue regeneration, as compared to natural polymers [22, 23]. In cell-free printing approaches, the synthetic polymers are usually the first choice. Recently, Buyuksungur *et al.* [24] developed PCL scaffolds for the treatment of bone defects. The scaffolds were printed by fused deposition modelling and were further modified with nano-HAp and poly(propylene fumarate) (PPF) to create a mechanically strong implant with well-defined pore size and porosity, controllable surface hydrophilicity (promoted by PPF) and osteoconductivity (induced by HAp). In another study, Hung *et al.* [25] blended decellularized bone (DCB) matrix particles with PCL. This is a good example of a synthetic material with well-defined material properties and printing parameters that was modified with a natural compound to better mimic the native tissue.

Regarding soft tissues, where the mechanical performance would not be so demanding, some progresses have been made using natural-based polymers. Kuo *et al.* [26] combined 3D printing with endoscopic imaging to produce customized scaffolds for tympanic membrane regeneration. The 3D printed gelatin methacrylate (GelMA) constructs showed good cell invasion and proliferation in *in vitro* assays. The customized scaffolds were also implanted in a chinchilla model for the period of 28 days. The results presented a complete healing of the tympanic membrane with a total maintenance of scaffolds integrity until complete degradation and subsequent replacement by the native tissue. In another recent work, Bakarich *et al.* [27] developed a new extrusion-based gradient printing system with



the capability to control the rates at which two inks are dispensed through a mixing nozzle. In this study, gradient scaffolds were printed by altering the ratio of a soft alginate/polyacrylamide-based hydrogel and a hard UV-curable ink (Emax 904 Gel-SC). Furthermore, this novel system allowed the direct fabrication of composite implants with a smooth and continuous gradient of stiffness between the soft hydrogel and the harder acrylated urethane material. The tuning ability provided by this approach was suggested to be very useful in the production of bioinspired structures for tendon or osteochondral TE.

The printing principles of cell-laden approaches are slightly different from those applied in cell-free strategies. While the conventional 3D printing technologies are actually being applied for biological or biomedical applications, 3D bioprinting involving direct printing of cells and other biological substances for TE applications is taking its first steps [28]. One of the main challenges in TE field, which can be overcome with the emerging field of 3D bioprinting, is the capability to produce well-organized 3D vascular networks. Jia *et al.* [29] developed a versatile 3D bioprinting approach that allows the fabrication perfusable vascular structures with highly ordered arrangements in a single-step process. In other words, a cell-responsive bioink composed by gelatin methacryloyl, sodium alginate, and 4-arm poly(ethylene glycol)-tetra-acrylate (PEGTA) was used to produce 3D perfusable hollow tubes (**Figure III-2A-B**). This blend bioink also displayed favorable biological characteristics that supported the spreading and proliferation of encapsulated endothelial and stem cells in the bioprinted constructs, leading to the formation of biologically relevant, highly organized, perfusable vessels (**Figure III-2C**).

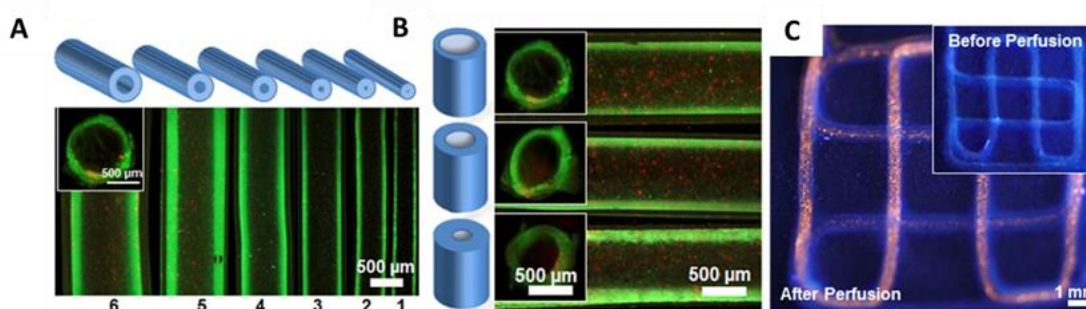


**Figure III-2** - Schematic diagram of bioprinted perfusable tubes displaying different outer diameters (A) and with the same outer but different inner diameters (B), and representative fluorescence micrographs. (C) Fluorescence photographs before (inset) and after injection with red fluorescent microbeads into the lumen of the single, continuous bioprinted tube. Adapted with permission from Jia *et al.* [29].

In a similar approach, Kolesky *et al.* [30] integrated parenchyma, stroma, and endothelium into a single thick tissue by co-printing multiple inks composed of human mesenchymal stem cells (hMSCs) and human neonatal dermal fibroblasts (hNDFs) within a customized ECM alongside embedded vasculature, which is subsequently lined with human umbilical vein endothelial cells (HUVECs). In short,

vascularized human tissues with tunable cellular heterogeneity have been fabricated by multi-material 3D bioprinting. That 3D tissue manufacturing platform enables to recapitulate 3D tissue environments, providing the opportunity to fabricate and investigate human tissues for both *ex vivo* and *in vivo* applications.

Following the same principles and based on a cell-laden approach, recent studies using 3D printing have shown promising results in terms of cardiac repair [31] and liver TE [32, 33]. However, two recent works where a multi-material bioprinting strategy was developed are highlighted in this review. Kang *et al.* [34] developed an integrated tissue-organ printer (ITOP) capable of biofabricating mechanically stable constructs by printing cell-laden hydrogels combined with biodegradable polymers. The authors were able to produce human-scale bioprinted mandibles, calvarial bone, cartilage and skeletal muscle due to several important features present in this ITOP system: 1) multi-dispensing modules for delivering various cell types and polymers in a single construct; 2) an optimized carrier material for delivering cells to discrete locations in the 3D structure in a liquid form; 3) a sophisticated nozzle system with a resolution down to 2  $\mu\text{m}$  for biomaterials and down to 50  $\mu\text{m}$  for cells; 4) crosslinking of cell-laden hydrogels after passage through the nozzle system; 5) capability to simultaneously print an outer sacrificial acellular hydrogel mold that is dissolved after the tissue construct acquires enough rigidity to retain its shape; and 6) the creation of a lattice structure of microchannels permissive to nutrient and oxygen diffusion into the printed tissue constructs. Furthermore, the *in vitro* and *in vivo* evaluation of the bioprinted structures showed good biological performance, presenting tissue maturation and organization. In another work, Liu *et al.* [35] reported a multi-material extrusion bioprinting platform slightly different from the conventional multi-nozzle bioprinters. The authors developed a system capable of extruding seven types of bioinks, both independently and simultaneously, through the integration of a digitally tunable pneumatic single-print-head system (**Figure III-3A**). This system was able to achieve biofabrication of multi-component complex and gradient structures which can be applied in TE applications (**Figure III-3Bi-vi**). Furthermore, compared with the existing nozzle-based approaches, the authors were capable to print at a speed up to 15 times faster. This strategy can open new horizons in the biofabrication of scaffolds with multiple cell types and architectures, thus overcoming all the current issues in terms of cells spatial distribution.

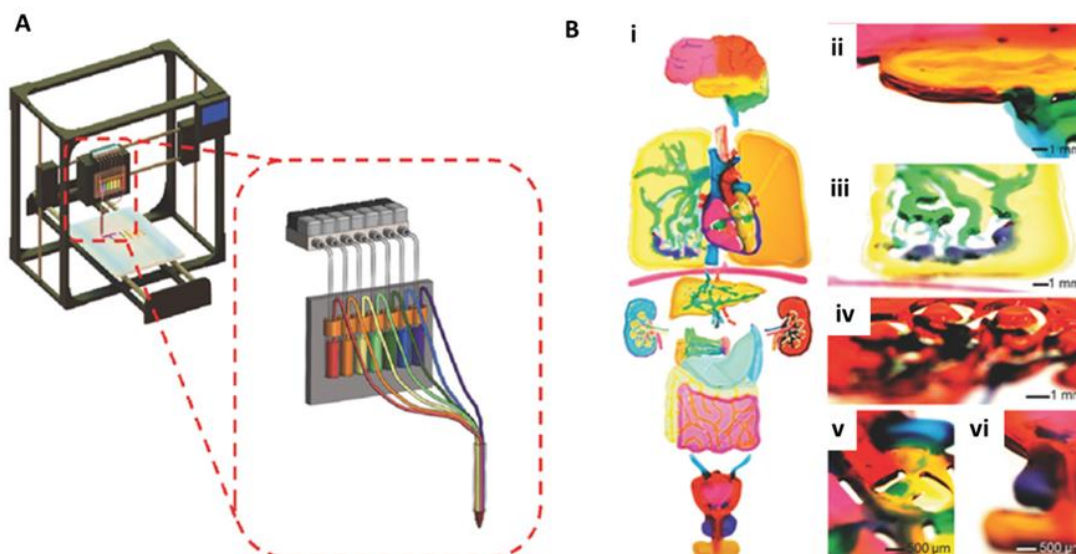


Figure III-3 - Design of the digitally tunable continuous multi-material extrusion bioprinter and multi-material bioprinting of 3D constructs. (A) Schematic representation showing the design of the seven-channel printhead connected to reservoirs that are individually actuated by programmable pneumatic valves. (B) Images of bioprinted (i) human organ-like constructs from multiple bioinks, including brain, lung, heart, liver, kidneys, pancreas, stomach, small/large intestines, bladder, and prostate (the organ-like constructs presented in this image were individually printed, photographed, and stitched together at relative locations as those in the human body); (ii) brain; (iii) lung vasculature; (iv) kidney; (v) left atrium of heart and (vi) bladder/prostate. Adapted with permission from Liu *et al.* [35].

### III-3. 3D PRINTING FOR FIBROCARILAGE TISSUE REGENERATION

The 3D printing of fibrocartilaginous tissue, such as meniscus or IVD, has been exploited in many works that already showed promising results. First, the possibility to build 3D models of meniscus tissue and IVD from a MRI dataset has already been showed in two different works. Cengiz *et al.* [36] and Oner *et al.* [37], used high-quality MRI volumetric images to developed 3D models for meniscus and outer region of the IVD (annulus fibrosus), respectively. In both works, an advanced segmentation software, *i.e.* RheumaSCORE, for semi-automatic MRI image segmentation of the tissues was used. In the end, the authors were able to perform a full 3D segmentation that resulted in a reliable 3D model for 3D printing of patient-specific implants.

Fibrocartilaginous tissues are subjected to different types of loads. To develop a 3D printed implant, it is important to biofabricate a structure capable of maintaining the integrity after implantation and that provides a mechanical performance similar to the tissue to regenerate. Therefore, synthetic

polymers have been the common choice regarding cell-free approaches. Szojka *et al.* [38] developed 3D printed PCL scaffolds capable of recapitulating the shape and structural components of meniscus ECM. The scaffolds were produced by layer-by-layer with a biomimetic fiber architecture inspired in the circumferentially- and radially- oriented collagen fiber bundles found in the native tissue. Different fiber architectures with varied fiber spacings, offsets between layers and circumferential orientation were tested. The results showed that the scaffolds presented a good mechanical behavior, being promising structures for meniscus tissue engineering. In another work, van Uden *et al.* [39] performed an analogous study, producing PCL scaffolds with different geometries, but in this case directed to IVD regeneration. All the geometries presented higher compressive stiffness as compared to the human IVD, and no cytotoxicity were observed when annulus fibrosus cells were in contact with the scaffold's leachables. In a similar approach, Warren *et al.* [40] produced 3D scaffolds made of PCL with 100, 200, or 400  $\mu\text{m}$  of interstrand spacing that were posteriorly implanted in a subcutaneous rat model for 4, 8, or 12 weeks. In terms of infiltration, cells had already penetrated deep into the 3D printed scaffolds after 4 weeks. Collagen aligned fibers were also observed. The 100  $\mu\text{m}$ -scaffolds presented the most highly oriented fibers, whereas the 400  $\mu\text{m}$ -scaffolds had less oriented fibers. The 200  $\mu\text{m}$ -scaffolds presented an intermediate behavior. The presence of more polymeric strands in the 100  $\mu\text{m}$ -scaffolds can serve as instructional cues for cells, leading to a high deposition of aligned collagen fibers. In a further approach, Zhang *et al.* [41] tried to increase the biological performance of PCL 3D printed scaffolds by seeding MSCs before implantation. In this *in vivo* study, seventy-two New Zealand White rabbits were divided into four groups: cell-seeded scaffold, cell-free scaffold, sham operation and total meniscectomy alone. The performance of the cell-seeded and cell-free PCL scaffolds were assessed in terms of mechanical properties, by performing a tensile and compressive test and assessing tissue regeneration by histological and scanning electron microscope analysis. The results revealed that the cell-seeded scaffold showed notably better gross appearance, lower cartilage degeneration and better mechanical performance. In short, this study proved that augmentation of the PCL scaffolds with bone marrow-derived MSCs increases tissue regeneration and mechanical strength, which can be a good alternative to current treatments. In another study, Lee *et al.* [42] also attempted to improve the biological performance of 3D printed PCL scaffolds. In this work, the authors produced PLGA microspheres ( $\mu\text{S}$ ) loaded with human connective tissue growth factor (CTGF) and transforming growth factor- $\beta$ 3 (TGF- $\beta$ 3), that were physically attached to the PCL meniscus scaffolds afterwards (**Figure III-4A,B**). The introduction of the  $\mu\text{S}$  in the 3D printed scaffolds allowed a spatiotemporal release of both growth factors, which enhanced the regeneration process (**Figure III-4C**). The 3D printed scaffolds were

posteriorly implanted in a meniscus sheep model for *in vivo* biocompatibility assessment. The results of the *in vivo* assay showed that the presence of the growth factors yielded the production of native-like fibrocartilage and revealed the presence of zone-specific cell phenotypes similar to the native tissue. In addition, the spatiotemporally delivered CTGF and TGF- $\beta$ 3 also restored inhomogeneous mechanical properties of the regenerated sheep meniscus leading to a complete regeneration of the sheep meniscus. Besides PCL, other synthetic polymers such as poly(trimethylene carbonate) (PTMC) (**Figure III-4E,F**) [43], acrylonitrile butadiene styrene (ABS) and poly(lactic acid) (PLA) [44], and a composite of resin reinforced with multiwall carbon nanotubes [45] have been investigated for 3D printing of fibrocartilaginous tissues.

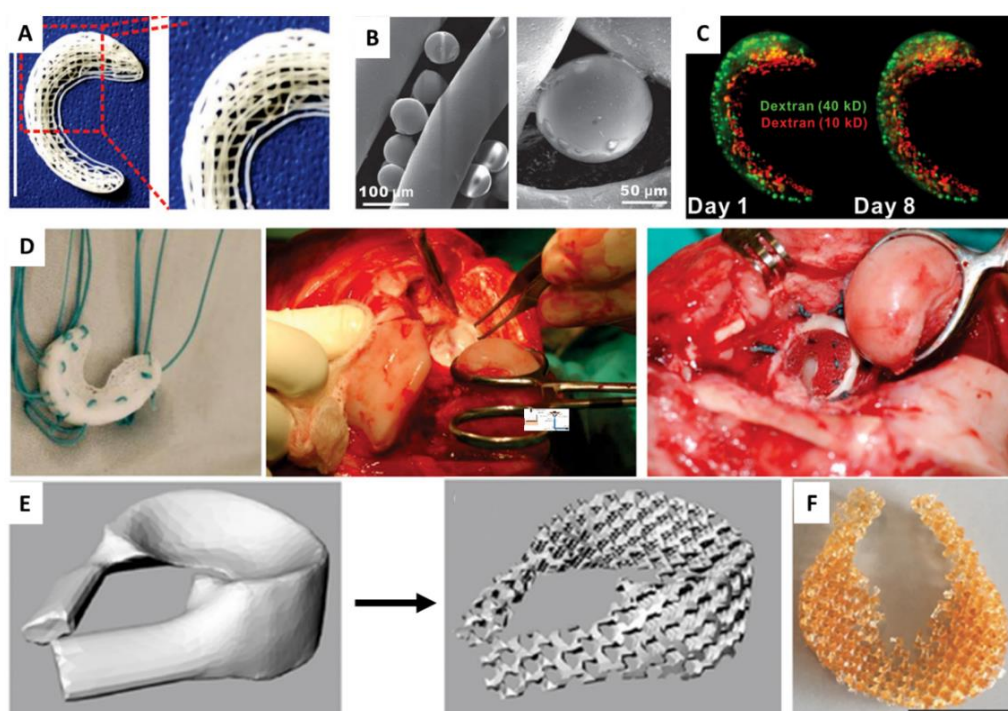


**Figure III-4** - Cell-free 3D printing approaches for fibrocartilage regeneration. (A) Anatomic reconstruction of human meniscus. Human meniscus scaffolds were 3D-printed by layer-by-layer deposition of PCL fibers (100  $\mu\text{m}$  diameter), forming 100 to 200  $\mu\text{m}$ -channels. (B) PLGA  $\mu\text{S}$  encapsulating CTGF and TGF- $\beta$ 3 were in physical contact with PCL microfibers. (C) Fluorescent dextrans simulating CTGF (green, 40 kD) and TGF- $\beta$ 3 (red, 10 kD) were delivered into the outer and inner zones, respectively, of human meniscus scaffolds to show scaffold loading. Distribution of dextrans was maintained from day 1 to day 8. (D) A scaffold was prepared for implantation with 2-0 Ethibond suture. The sheep medial meniscus was exposed by dislocating femoral condyle, followed by scaffold implantation. (E) Schematic process of the design of a porous meniscus implant composed by PTMC. (F) Porous meniscus scaffold after extraction and drying. Adapted with permission from (A-D) Lee *et al.* [42] and (E-F) Van Bochove *et al.* [43].

Costa *et al.* [46, 47] recently developed a novel silk and silk/elastin bioink for 3D printing of patient-specific and memory-shape implants for meniscus (**Figure III-5A**) and IVD (**Figure III-5C**)



regeneration, respectively. Unlike the previous works, in this approach the authors used a natural-based polymer. The authors were capable of producing a human meniscus implant and human annulus fibrosus implant using a fast setting enzymatic-cross-linked silk fibroin-based bioink. The bioink presented good reliability, and the produced structures showed promising features in terms of biocompatibility (**Figure III-5B and D**) and memory-shape properties (**Figure III-5E-G**). This promising bioink can open new horizons in terms of patient-specific implants for fibrocartilaginous tissues, since it joins the best of both worlds, *i.e.* natural and synthetic: 1) a good mechanical performance suitable for this type of tissues and comparable to the synthetic-based implants and 2) the use of a natural-based polymer (*i.e.* silk fibroin) that provides, in terms of biological performance, better characteristics as compared to the synthetic-based implants and better mechanical performance as compared to the common natural-based polymers usually used in this type of approaches.

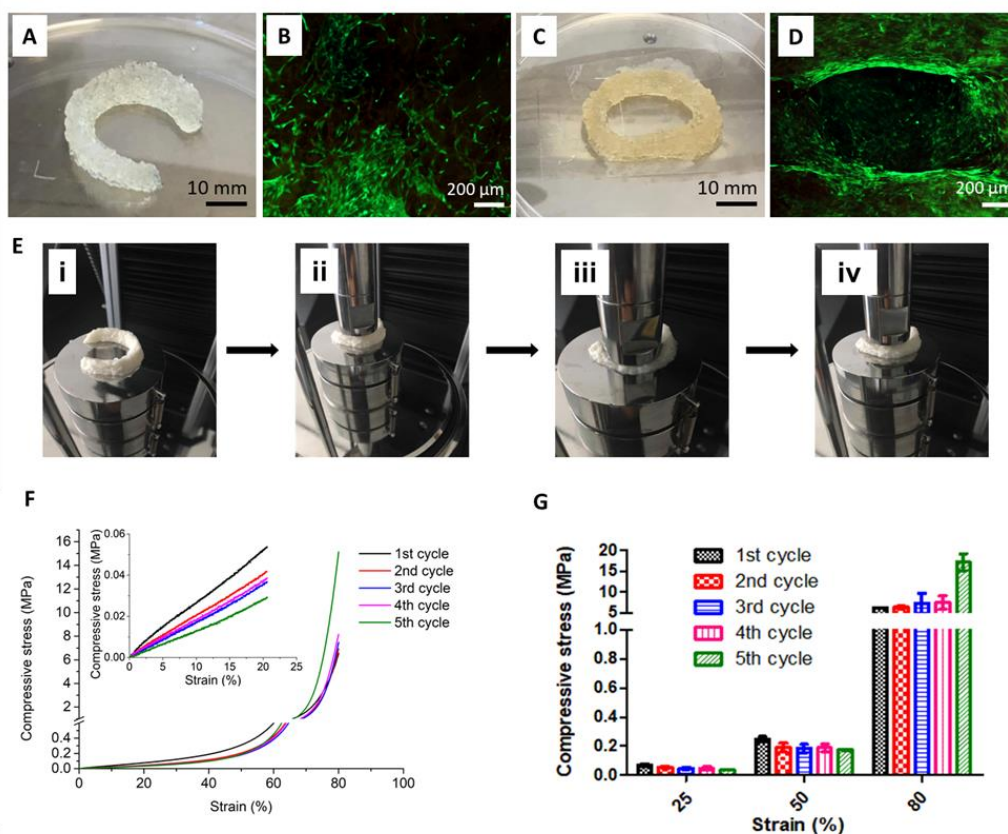


**Figure III-5 - 3D printing cell-free approach using a fast setting enzymatic-cross-linked silk based bioinks. (A)** Patient-specific silk fibroin human meniscus implant. **(B)** Representative image showing dead and live cells in 3D bioprinted silk fibroin constructs after 7 days of culture. **(C)** Patient-specific silk fibroin/Elastin human annulus fibrosus implant. **(D)** Representative image showing dead and live cells in 3D bioprinted silk fibroin/Elastin constructs after 21 days of culture. **(E)** i) Patient-specific memory-shape meniscus implant into Instron platform, ii) initial appearance before compression, iii) implant under a compressive strain of 80%, iv) returning to original shape. **(F)** Stress–strain plot of cyclic uniaxial compression test (five cycles). **(G)** Compressive stress of cyclic

uniaxial compression test as function of strain (25%, 50%, and 80%). (E), (F) and (G) adapted with permission from Costa *et al.* [46].

However, the printing of cell-laden biomaterials is the only way to take advantage of the full potential of 3D printing. The capability to control cells' spatial distribution is very important in fibrocartilage TE approaches, since, for example, three different types of cells have been identified in meniscus structure: fibroblasts, chondrocytes and fibrochondrocytes [48]. On the other hand, this type of approach can also be used to encapsulate different biological factors in the bioink that can help to control the vascularization of the fibrocartilaginous tissues. The fibrocartilage is an avascular tissue, and the blood supply of the enthesis is derived largely from vessels in the peritenon and adjacent bone marrow [49].

The development of alginate-based bioinks combined with different polymers have been proposed. Markstedt *et al.* [50] developed a bioink that combines the outstanding shear thinning properties of nanofibrillated cellulose (NFC) with the fast crosslinking ability of alginate. Different cartilaginous structures, including sheep meniscus (**Figure III-6A and B**), were printed based on MRI and CT images. The alginate-based bioink showed good print fidelity and biocompatibility. Bioprinted human chondrocytes exhibited a cell viability of 86% after 7 days of 3D culturing (**Figure III-6C**). Using a similar approach, Narayanan *et al.* [51] blended the alginate with PLA fibers to bioprint cell-laden structures. Human adipose-derived stem cells were encapsulated in the bioink, which was further used to print a human knee meniscus model. Biological *in vitro* tests showed high cell proliferation and density, as well as the presence of collagen and proteoglycans after 8 weeks of culturing. In another study, Kesti *et al.* [52] also described the use of an alginate-based bioink. Furthermore, the authors used two unmodified FDA-compliant polysaccharides, gellan and alginate combined with the clinical product BioCartilage (cartilage ECM particles). In this case, cell-friendly physical gelation was used, where the bioink crosslinking occurred by the co-extrusion of a cation-loaded transient support polymer. Using this method, the authors were able to develop a bioink with cartilage particles (Bioink+Cartilage) and a bioink with hydroxyapatite particles (Bioink+HA) that presented an optimal shear thinning and shear recovery properties for high-fidelity bioprinting. 3D meniscal grafts (**Figure III-6D**) and IVD grafts (**Figure III-6E**) were bioprinted based on CT data. The bioink biocompatibility was assessed by a cellular bioprinting process of a young adult sized nose graft using the Bioink+HA. The graft revealed decreased viability in the center of the scaffold (60% viable cells) at day 7, as compared to 96% viability in the periphery (**Figure III-6F**), suggesting the need for incorporating internal porosity or channels to enhance nutrition transport. However, the histological evaluation performed after 8 weeks of *in vitro* culturing

suggested that the grafts are able to support chondrocytes proliferation and, in the presence of TGF- $\beta$ 3, enhance a strong deposition of cartilage matrix proteins. The incorporation of growth factors can be a good approach to improve the biological performance of these patient-specific implants and also, in case of a strategy that uses undifferentiated cells, can assist in promoting an adequate differentiation. Romanazzo *et al.* [53] incorporated ECM-derived proteins in their alginate-based bioink. The bioink was loaded with infrapatellar fat pad-derived stem cells, and in the absence of exogenously supplied growth factors, inner meniscus ECM promoted chondrogenesis of fat pad-derived stem cells, whereas outer meniscus ECM promoted a more elongated cell morphology and the development of a more fibroblastic phenotype.

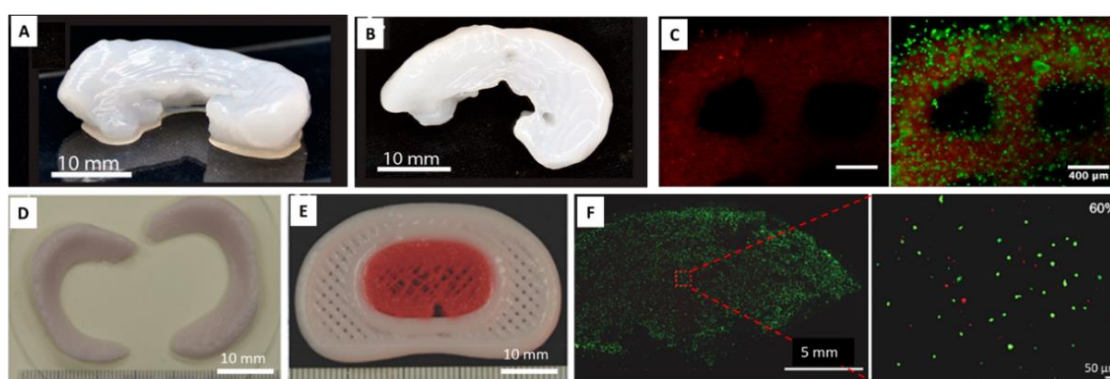


**Figure III-6 - Cell-laden 3D printing approaches for fibrocartilage regeneration. (A)** Side and **(B)** top view of 3D printed sheep meniscus implant. **(C)** Representative images (at 4 $\times$  magnification) showing dead and live cells in 3D bioprinted constructs after 7 days of culturing. **(D)** Meniscus and **(E)** IVD printed grafts. IVD graft was printed with Bioink+Cartilage particles stained red (nucleus pulposus) and with Bioink+HA (annulus fibrosus). **(F)** Live dead staining from a central slice of a printed young adult size nose graft. Adapted with permission from **(A-C)** *et al.* Markstedt *et al.* [50] and **(D-F)** Kesti *et al.* [52].

These promising results have endorsed that the presence of biological factors can enhance the biological performance of the patient-specific implants and, more importantly, can help to better mimic the native tissue structure. Other biomaterials such as collagen [54] and hyaluronic acid [55] have been explored in 3D printing cell-laden approaches for the production of fibrocartilaginous patient-specific implants. In a recent study, Daly *et al.* [56] compared the performance of four different hydrogel bioinks (*i.e.* agarose, alginate, GelMA and BioINK™) in terms of their printing properties and capacity to support the *in vitro* development of either hyaline cartilage or fibrocartilage. Each hydrogel was seeded with MSCs, cultured for 28 days in the presence of TGF- $\beta$ 3 and then analyzed for markers indicative of differentiation towards either a fibrocartilaginous or hyaline cartilage-like phenotype. This study demonstrated that the bioinks have a powerful effect on phenotype induction of encapsulated cells. The results showed that the alginate and agarose bioinks supported the development of hyaline-like cartilage



tissues, while the bioinks GelMA and BioINK™ (composed by poly(ethylene glycol) methacrylate) induced the development of a fibrocartilaginous tissue. Therefore, the importance of the choice of the bioink when bioprinting different cartilaginous tissues for musculoskeletal applications not only relies on the printing fidelity of each bioink but also should consider the tissue that is aimed to regenerate.

**Table III-1 - Executive summary describing the state-of-art in recent advances on 3D printing of patient-specific implants for fibrocartilage tissue regeneration.**

---

#### **Executive summary**

##### **3D Printing in Tissue Engineering Approaches**

- Recent advances in 3D printing field regarding tissue engineering applications.
- Different biomaterials have been used if the aim is to mimic hard or soft tissues or if is a 3D printing cell-laden approach or not.

##### **3D Printing for Fibrocartilage Tissue Regeneration**

- Development of 3D models of meniscus and intervertebral disc by reverse engineering.
- Synthetic and natural polymers used in 3D printing of fibrocartilaginous tissues.
- Recent works related with the development of cell-free and cell-laden 3D printing approaches for the regeneration of fibrocartilage.
- Development of a novel fast-setting silk fibroin bioinks with memory-shape properties.

##### **Final Remarks and Future Perspectives**

- 3D printing of patient-specific implants for tissue engineering applications, especially for meniscus and intervertebral disc regeneration, has evolved in last few years showing some promising results. However, some challenges such as the development of bioinks that better mimic the native tissue, the associated costs or the implantation of regulatory certifications in this field need to be urgently addressed in order to occur the translation from the laboratory to the clinics.

#### III-4. CONCLUSIONS AND FUTURE PERSPECTIVES

Recently, the scientific and medical community has been making huge efforts to achieve better treatment alternatives for fibrocartilage regeneration in order to overcome some of the existing issues present in the current available procedures. Current available procedures comprise implant replacement, meniscectomy (in case of meniscus) or a non-operative approach. All these procedures have been shown poor clinical outcomes (early arthritic changes and poor implant anchorage) leading to what appear to be a gap in science and medicine. The efforts are moving towards precision medicine, where each patient is indicated to a particular treatment according to his injury and medical past, *i.e.* one of the most desired goals, which has been hardly attempted to achieve, is patient-specificity. In this sense, the combination of reverse engineering with 3D Printing has been a trending subject in many recent works in the fibrocartilage TE field, and we strongly believe that this can be the solution to solve the existing issues present the current available treatments specially, in terms of implant anchorage and regeneration process. There are already some promising results that can be considered a boost in terms of hope for seeing these technologies in the clinics, and immense advances have been made regarding printing fidelity, speed and development of bioinks. However, there are some challenges that are still in great need to be addressed. A wider panoply of bioinks has been exploited and the pursuit for bioinks that better mimic the native tissue has evolved. Nevertheless, the common problems related to mechanical performance, biocompatibility, degradation behavior, and implants' anchorage still remains. The standardization of the characterization of the printing structures, printing parameters or bioinks biocompatibility must be implanted in a near future to better understand these novel systems. Furthermore, challenges related with the high-costs associated to such technologies and regulatory certifications of 3D printing methodologies, 3D printers and bioinks should be addressed in future, in order to increase the possibility of making the transition from the bench side to the clinics.

There is still a long path to go in respect to development of bioinks for 3D printing in personalized approaches, but it is vital to state that the field of 3D printing has had major advances in the last few years. This promising field can lead to the development of patient-specific and memory-shape implants, where therapeutic cells and bioinks are printed in combination, especially to address fibrocartilage defects and injuries.

### III-5. REFERENCES

- [1] Benjamin M, Ralphs JR. Biology of fibrocartilage cells. *International review of cytology* 2004;233:1-45.
- [2] Parvizi J, Kim GK. Chapter 39 - Cartilage. *High Yield Orthopaedics*. Philadelphia: W.B. Saunders; 2010. p. 80-1.
- [3] Watkins J, Mathieson I. CHAPTER 4 - Connective tissues. *The Pocket Podiatry Guide: Functional Anatomy*. Edinburgh: Churchill Livingstone; 2009. p. 107-56.
- [4] Embree MC, Chen M, Pylawka S, Kong D, Iwaoka GM, Kalajzic I, *et al*. Exploiting endogenous fibrocartilage stem cells to regenerate cartilage and repair joint injury. *Nature Communications* 2016;7:13073.
- [5] Lowe J, Almarza AJ. A review of in-vitro fibrocartilage tissue engineered therapies with a focus on the temporomandibular joint. *Archives of oral biology* 2017;83:193-201.
- [6] Modic MT, Ross JS. Lumbar Degenerative Disk Disease. *Radiology* 2007;245:43-61.
- [7] Beaufils P, Becker R, Kopf S, Englund M, Verdonk R, Ollivier M, *et al*. Surgical management of degenerative meniscus lesions: the 2016 ESSKA meniscus consensus. *Knee surgery, sports traumatology, arthroscopy : official journal of the ESSKA* 2017;25:335-46.
- [8] Niu W, Guo W, Han S, Zhu Y, Liu S, Guo Q. Cell-Based Strategies for Meniscus Tissue Engineering. *Stem Cells International* 2016;2016:4717184.
- [9] Buma P, Ramrattan NN, van Tienen TG, Veth RP. Tissue engineering of the meniscus. *Biomaterials* 2004;25:1523-32.
- [10] O'Connell GD, Leach JK, Klineberg EO. Tissue Engineering a Biological Repair Strategy for Lumbar Disc Herniation. *BioResearch Open Access* 2015;4:431-45.
- [11] Kandel R, Roberts S, Urban JPG. Tissue engineering and the intervertebral disc: the challenges. *European Spine Journal* 2008;17:480-91.
- [12] Maniar RN, Singhi T. Patient specific implants: scope for the future. *Current Reviews in Musculoskeletal Medicine* 2014;7:125-30.
- [13] Ngo TD, Kashani A, Imbalzano G, Nguyen KTQ, Hui D. Additive manufacturing (3D printing): A review of materials, methods, applications and challenges. *Composites Part B: Engineering*.
- [14] Lee J-Y, An J, Chua CK. Fundamentals and applications of 3D printing for novel materials. *Applied Materials Today* 2017;7:120-33.
- [15] Jayasinghe SN. Direct cell engineering reaches the jet age. *Materials Today* 2007;10:60.
- [16] Jayasinghe SN, Warnes G, Scotton CJ. Bio-electrosprayed living composite matrix implanted into mouse models. *Macromolecular bioscience* 2011;11:1364-9.

- [17] Ng KE, Joly P, Jayasinghe SN, Vernay B, Knight R, Barry SP, *et al.* Bio-electrospraying primary cardiac cells: *in vitro* tissue creation and functional study. *Biotechnology journal* 2011;6:86-95.
- [18] Jayasinghe SN, Auguste J, Scotton CJ. Platform Technologies for Directly Reconstructing 3D Living Biomaterials. *Advanced materials (Deerfield Beach, Fla)* 2015;27:7794-9.
- [19] Jayasinghe SN. Cell electrospinning: a novel tool for functionalising fibres, scaffolds and membranes with living cells and other advanced materials for regenerative biology and medicine. *The Analyst* 2013;138:2215-23.
- [20] Chia HN, Wu BM. Recent advances in 3D printing of biomaterials. *Journal of Biological Engineering* 2015;9:4.
- [21] Richards DJ, Tan Y, Jia J, Yao H, Mei Y. 3D Printing for Tissue Engineering. *Israel journal of chemistry* 2013;53:805-14.
- [22] Asti A, Gioglio L. Natural and synthetic biodegradable polymers: different scaffolds for cell expansion and tissue formation. *The International Journal of Artificial Organs* 2016;37:187-205.
- [23] Do A-V, Khorsand B, Geary SM, Salem AK. 3D Printing of Scaffolds for Tissue Regeneration Applications. *Advanced healthcare materials* 2015;4:1742-62.
- [24] Buyuksungur S, Endogan Tanir T, Buyuksungur A, Bektas EI, Torun Kose G, Yucel D, *et al.* 3D printed poly(epsilon-caprolactone) scaffolds modified with hydroxyapatite and poly(propylene fumarate) and their effects on the healing of rabbit femur defects. *Biomaterials science* 2017;5:2144-58.
- [25] Hung BP, Naved BA, Nyberg EL, Dias M, Holmes CA, Elisseff JH, *et al.* Three-Dimensional Printing of Bone Extracellular Matrix for Craniofacial Regeneration. *ACS Biomaterials Science & Engineering* 2016;2:1806-16.
- [26] Kuo CY, Wilson E, Fuson A, Gandhi N, Monfaredi R, Jenkins A, *et al.* Repair of Tympanic Membrane Perforations with Customized Bioprinted Ear Grafts Using Chinchilla Models. *Tissue engineering Part A* 2017.
- [27] Bakarich SE, Gorkin Iii R, Gately R, Naficy S, in het Panhuis M, Spinks GM. 3D printing of tough hydrogel composites with spatially varying materials properties. *Additive Manufacturing* 2017;14:24-30.
- [28] Gao G, Huang Y, Schilling AF, Hubbell K, Cui X. Organ Bioprinting: Are We There Yet? *Adv Healthc Mater* 2018;7.
- [29] Jia W, Gungor-Ozkerim PS, Zhang YS, Yue K, Zhu K, Liu W, *et al.* Direct 3D bioprinting of perfusable vascular constructs using a blend bioink. *Biomaterials* 2016;106:58-68.
- [30] Kolesky DB, Homan KA, Skylar-Scott MA, Lewis JA. Three-dimensional bioprinting of thick vascularized tissues. *Proceedings of the National Academy of Sciences* 2016;113:3179-84.
- [31] Jang J, Park HJ, Kim SW, Kim H, Park JY, Na SJ, *et al.* 3D printed complex tissue construct using stem cell-laden decellularized extracellular matrix bioinks for cardiac repair. *Biomaterials* 2017;112:264-74.

- [32] Nguyen DG, Funk J, Robbins JB, Crogan-Grundy C, Presnell SC, Singer T, *et al.* Bioprinted 3D Primary Liver Tissues Allow Assessment of Organ-Level Response to Clinical Drug Induced Toxicity *In Vitro*. *PloS one* 2016;11:e0158674.
- [33] Lee H, Cho DW. One-step fabrication of an organ-on-a-chip with spatial heterogeneity using a 3D bioprinting technology. *Lab on a chip* 2016;16:2618-25.
- [34] Kang H-W, Lee SJ, Ko IK, Kengla C, Yoo JJ, Atala A. A 3D bioprinting system to produce human-scale tissue constructs with structural integrity. *Nature Biotechnology* 2016;34:312.
- [35] Liu W, Zhang YS, Heinrich MA, De Ferrari F, Jang HL, Bakht SM, *et al.* Rapid Continuous Multimaterial Extrusion Bioprinting. *Advanced Materials* 2017;29:1604630-n/a.
- [36] Cengiz IF, Pitikakis M, Cesario L, Parascandolo P, Vosilla L, Viano G, *et al.* Building the basis for patient-specific meniscal scaffolds: From human knee MRI to fabrication of 3D printed scaffolds. *Bioprinting* 2016;1-2:1-10.
- [37] Oner T, Cengiz I, Pitikakis M, Cesario L, Parascandolo P, Vosilla L, *et al.* 3D segmentation of intervertebral discs: from concept to the fabrication of patient-specific scaffolds. *Journal of 3D Printing in Medicine* 2017;1:91-101.
- [38] Szojka A, Lalh K, Andrews SHJ, Jomha NM, Osswald M, Adesida AB. Biomimetic 3D printed scaffolds for meniscus tissue engineering. *Bioprinting* 2017;8:1-7.
- [39] van Uden S, Silva-Correia J, Corrello VM, Oliveira JM, Reis RL. Custom-tailored tissue engineered polycaprolactone scaffolds for total disc replacement. *Biofabrication* 2015;7:015008.
- [40] Warren PB, Huebner P, Spang JT, Shirwaiker RA, Fisher MB. Engineering 3D-Bioploted scaffolds to induce aligned extracellular matrix deposition for musculoskeletal soft tissue replacement. *Connective tissue research* 2017;58:342-54.
- [41] Zhang ZZ, Wang SJ, Zhang JY, Jiang WB, Huang AB, Qi YS, *et al.* 3D-Printed Poly(epsilon-caprolactone) Scaffold Augmented With Mesenchymal Stem Cells for Total Meniscal Substitution: A 12- and 24-Week Animal Study in a Rabbit Model. *The American journal of sports medicine* 2017;45:1497-511.
- [42] Lee CH, Rodeo SA, Fortier LA, Lu C, Eriskin C, Mao JJ. Protein-releasing polymeric scaffolds induce fibrochondrocytic differentiation of endogenous cells for knee meniscus regeneration in sheep. *Science translational medicine* 2014;6:266ra171-266ra171.
- [43] van Bochove B, Hannink G, Buma P, Grijpma DW. Preparation of Designed Poly(trimethylene carbonate) Meniscus Implants by Stereolithography: Challenges in Stereolithography. *Macromolecular bioscience* 2016;16:1853-63.
- [44] Rosenzweig DH, Carelli E, Steffen T, Jarzem P, Haglund L. 3D-Printed ABS and PLA Scaffolds for Cartilage and Nucleus Pulposus Tissue Regeneration. *International Journal of Molecular Sciences* 2015;16:15118-35.

- [45] Yang Y, Chen Z, Song X, Zhang Z, Zhang J, Shung KK, *et al.* Biomimetic Anisotropic Reinforcement Architectures by Electrically Assisted Nanocomposite 3D Printing. *Advanced materials* (Deerfield Beach, Fla) 2017;29.
- [46] Costa JB, Silva-Correia J, Oliveira JM, Reis RL. Fast Setting Silk Fibroin Bioink for Bioprinting of Patient-Specific Memory-Shape Implants. *Advanced Healthcare Materials* 2017;6.
- [47] Costa JB, Silva-Correia J, Ribeiro VP, da Silva Morais A, Oliveira JM, Reis RL. Engineering patient-specific bioprinted constructs for treatment of degenerated intervertebral disc. *Materials Today Communications* 2018.
- [48] Verdonk PC, Forsyth RG, Wang J, Almqvist KF, Verdonk R, Veys EM, *et al.* Characterisation of human knee meniscus cell phenotype. *Osteoarthritis and cartilage* 2005;13:548-60.
- [49] McGonagle D, Benjamin M. 123 - Enthesopathies A2 - Hochberg, Marc C. In: Silman AJ, Smolen JS, Weinblatt ME, Weisman MH, editors. *Rheumatology* (Sixth Edition). Philadelphia: Content Repository Only!; 2015. p. 1014-20.
- [50] Markstedt K, Mantas A, Tournier I, Martínez Ávila H, Hägg D, Gatenholm P. 3D Bioprinting Human Chondrocytes with Nanocellulose–Alginate Bioink for Cartilage Tissue Engineering Applications. *Biomacromolecules* 2015;16:1489-96.
- [51] Narayanan LK, Huebner P, Fisher MB, Spang JT, Starly B, Shirwaiker RA. 3D-Bioprinting of Polylactic Acid (PLA) Nanofiber–Alginate Hydrogel Bioink Containing Human Adipose-Derived Stem Cells. *ACS Biomaterials Science & Engineering* 2016;2:1732-42.
- [52] Kesti M, Eberhardt C, Pagliccia G, Kenkel D, Grande D, Boss A, *et al.* Bioprinting Complex Cartilaginous Structures with Clinically Compliant Biomaterials. *Advanced Functional Materials* 2015;25:7406-17.
- [53] Romanazzo S, Vedicherla S, Moran C, Kelly DJ. Meniscus ECM-functionalised hydrogels containing infrapatellar fat pad-derived stem cells for bioprinting of regionally defined meniscal tissue. 2017.
- [54] Rhee S, Puetzer JL, Mason BN, Reinhart-King CA, Bonassar LJ. 3D Bioprinting of Spatially Heterogeneous Collagen Constructs for Cartilage Tissue Engineering. *ACS Biomaterials Science & Engineering* 2016;2:1800-5.
- [55] Mouser VH, Abbadessa A, Levato R, Hennink WE, Vermonden T, Gawlitta D, *et al.* Development of a thermosensitive HAMA-containing bio-ink for the fabrication of composite cartilage repair constructs. *Biofabrication* 2017;9:015026.
- [56] Daly AC, Critchley SE, Rencsok EM, Kelly DJ. A comparison of different bioinks for 3D bioprinting of fibrocartilage and hyaline cartilage. *Biofabrication* 2016;8:045002.

## **SECTION 2**

# **EXPERIMENTAL DESIGN**

# Chapter IV

## Materials & Methods



## Materials and Methods

### OVERVIEW

In this chapter, the different materials, reagents and methodologies used to produce the patient-specific implants are described. The patient-specific implants developed and characterized in this thesis were obtained using different natural-based biomaterials as main components including silk fibroin, elastin, gellan-gum and fibrinogen. In addition,  $\beta$ -tricalcium phosphate powders were also used to produce hierarchical scaffolds. Regarding the production techniques, two different 3D printing technologies were used to print the patient-specific implants (*e.g.*, indirect printing and extrusion-based printing).

Different characterization methodologies were applied in order to evaluate the physico-chemical and biological performance of the produced scaffolds. Moreover, a brief introduction of the materials and procedures was described to better understand the proposed methodologies.

## IV-1. MATERIALS

### IV-1.1. Silk Fibroin (SF)

Silk fibroin (SF) is a protein that can be synthesized in the glands of different arthropod insects [1]. This protein is spun into fibers by silkworms and spiders through a process that involves the production of an insoluble filament from an aqueous protein solution [2].

Due to ease of domestication, *Bombyx mori* silkworm is the most used and most well-known source to obtain SF [3]. The SF protein obtained from the cocoons produced by the *Bombyx mori* silkworm has shown to possess unique properties in several biomedical applications, including biodegradability, biocompatibility and impressive mechanical performance [4-6]. Herein, *Bombyx mori* silkworm cocoons were used on this thesis as source of SF.

The SF fibers comprise two components, a light (L) chain ( $\approx 26$  kDa) and heavy (H) chain ( $\approx 390$  kDa), which are present in a 1:1 ratio and linked by a single disulfide bond at a C-terminus of the H-chain (**Figure IV-1a**) [7]. These chains can be distinguished by the hydrophobic domains of the H-chains interspaced by hydrophilic regions at the L-chains. The H-chains domains contain a primary structure formed by repetitive sequences of Glycine-Y (Y being Alanine, Serine, Tyrosine, and Valine). The secondary structure is mainly formed by anti-parallel assembly of  $\beta$ -sheets that results in a crystalline structure (**Figure IV-1b**). This crystalline structure is responsible for the enhanced stability and mechanical properties of the spun fibers. Furthermore, these crystalline domains are separated by hydrophilic regions that constitute the amorphous phase of the protein (**Figure IV-1c**).

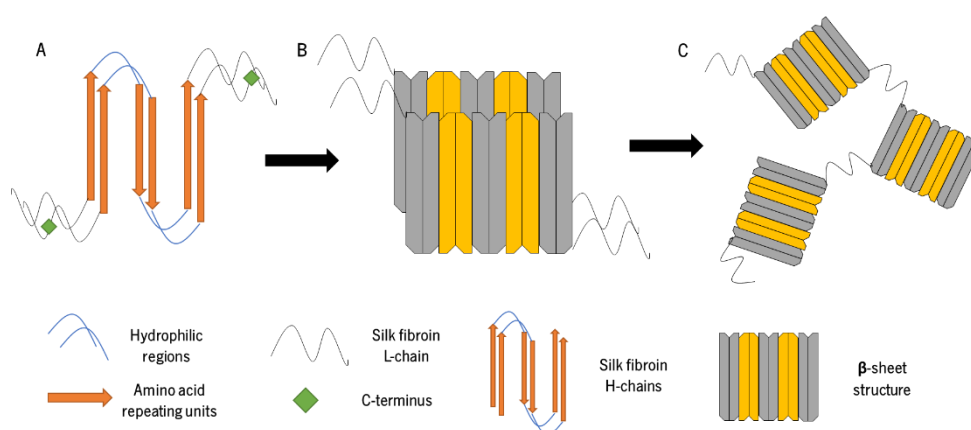


Figure IV-1 - Scheme representing the SF protein composition. (A) H-L complex formation. (B) H-chains organizing themselves together into  $\beta$ -sheet structures. (C)  $\beta$ -sheet structures linked by amorphous domains.

These components are coated with a hydrophilic protein named sericin (20-310 kDa) [8]. Sericin can be removed from SF through a purification boiling process in an alkaline solution (degumming process) (Figure IV-2). The removal of sericin is an obligatory processing step since it was proved that its presence induces immunological reactions [9]. However, when isolated is possible to apply sericin in the production of scaffolds for tissue engineering applications [10].

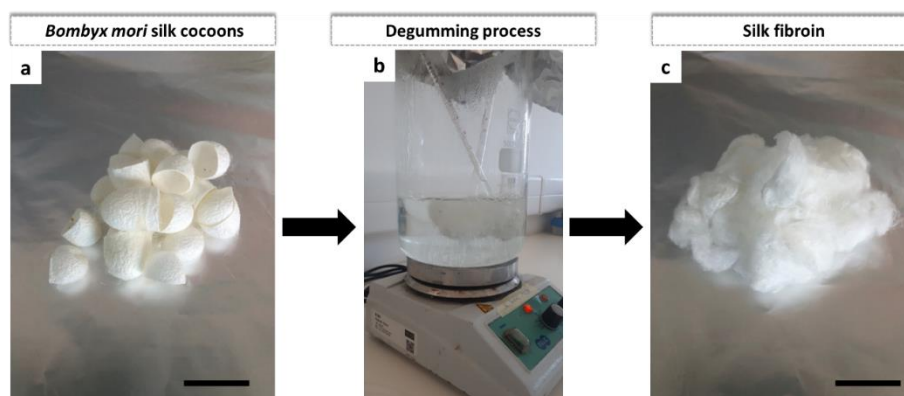


Figure IV-2 - Silk cocoons degumming process. (a) *Bombyx mori* silk cocoons. (b) Degumming process. (c) Purified SF after degumming procedure. Scale bar: 2 mm.

The degummed SF has been effectively used for decades as surgical suture material [11] and more recently has been explored in tissue engineering applications including scaffolds, hydrogels, membranes and drug delivery systems [12, 13]. In order to explore degummed SF, SF solutions have been obtained by the dissolution of the raw material using different organic solvents [14-16]. In addition, the constructs obtained using regenerated SF solutions suffer an spontaneous transition to  $\beta$ -sheet conformation [17]. Moreover, this transition can be controlled using chemical and physical methods such as addition of sodium chloride [18], immersion in alcohol solutions [19], ultrasonication [20] and vortex induction [21]. Herein, during the development of 3D scaffolds is possible to use SF-based structures in an amorphous state or in a  $\beta$ -sheet crystalline conformation. Scientific evidences showed that the presence of  $\beta$ -sheet enhances the mechanical properties and decreases the biodegradability of structures [19]. In contrast, SF hydrogels which have predominance of amorphous conformation revealed suitable properties for soft tissues applications [22]. For other applications, SF has been combined with several materials using chemical modifications such as coupling reactions, amino-acid modifications and grafting reactions [23]. For instance, the addition of methacrylate groups to the amine-containing side groups of SF has been used to make it light polymerizable. Herein, SF is a highly versatile biomaterial being possible to tailor its physico-chemical and biological properties, including mechanical strength, cell-adhesion properties, and biodegradability [24].

In this thesis, *Bombyx mori* silk cocoons were purified and posteriorly dissolved in a lithium bromide solution to obtain silk-based scaffolds and bioinks. The cocoons were supplied by the Portuguese Association of Parents and Friends of Mentally Disabled Citizens (APPACDM, Castelo Branco, Portugal). SF was used in the **Chapters V, VI, VII, VIII and IX** of the thesis.

#### IV-1.2. $\beta$ -Tricalcium phosphate ( $\beta$ -TCP)

Calcium phosphate ceramics (CaPs) are bioactive materials that have been extensively used in different biomedical applications [25]. These chemical compounds present a unique resemblance with the inorganic compounds present in calcified human tissues [26]. Furthermore, CaPs have proved to have good biological performance. They are comprised by hydroxyapatite (HAp),  $\beta$ -tricalcium phosphate ( $\beta$ -TCP),  $\alpha$ -tricalcium phosphate ( $\alpha$ -TCP) or biphasic calcium phosphate (BCP) [27].

TCP ( $\text{Ca}_3(\text{PO}_4)_2$ ) presents a Ca/P ratio of 1.5 and take place in two phases ( $\alpha$  and  $\beta$ ). Comparing both phases, they reveal identical chemistries, different crystal structures and both are less stable than HAp and more soluble in aqueous environments [28]. However,  $\beta$ -TCP present a faster and complete biological reabsorption when compared with HAp [29, 30].  $\beta$ -TCP can be obtained by thermal decomposition of CaPs at temperatures above 800 °C and is considered both osteoconductive and osteoinductive. Moreover, due to its low interfacial energy with respect to apatite, it can provoke the precipitation of an apatite layer upon incubation in aqueous ionic solutions being extensively used in bone TE [31-33].

The  $\beta$ -TCP's structural, physico-chemical, and biological properties can be tailored by the addition of foreign ions (*e.g.*, strontium (Sr) and zinc (Zn)). In previous studies, ionic-doped  $\beta$ -TCP was used in the production of TE scaffolds and revealed enhanced bone bonding capability and osteogenesis [34, 35].

In this thesis, ZnSr-doped  $\beta$ -TCP particles (**Figure IV-3**) were produced aiming to improve the anchorage capability of the patient-specific 3D indirect printed constructs. The details of the synthesis and processing of ZnSr-doped  $\beta$ -TCP particles will be described in the sub-section IV-3.1. of this chapter and have been used in the **Chapter V** of this thesis.



Figure IV-3 - ZnSr-doped  $\beta$ -TCP particles. Scale bar: 2 mm.

#### IV-1.3. Acrylonitrile-butadiene-styrene (ABS)

Acrylonitrile-butadiene-styrene (ABS) is one of the most used polymers in 3D printing. ABS is a group of thermoplastic called “terpolymers” that typically contains 15% to 35% acrylonitrile, 5% to 30% butadiene and 40% to 60% styrene (Figure IV-4) [36]. These components are able to provide chemical resistance and impact resistance, toughness and rigidity, and easy post-processing [37]. Therefore, ABS has become a common material in 3D printing due to its several advantages, which also includes recycling capacity and low cost.

In this thesis, this thermoplastic was used in the production of the indirect printed 3D scaffolds in the Chapter V.

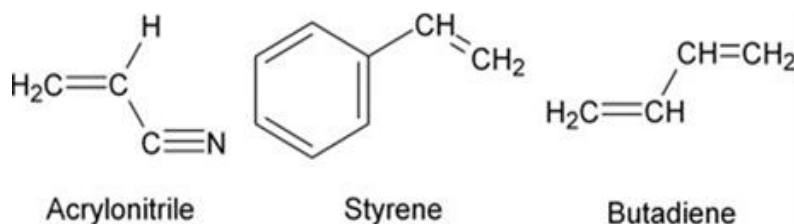


Figure IV-4 - Acrylonitrile, butadiene and styrene chemical structure.

#### IV-1.4. Elastin

Elastin is an extracellular matrix protein and is abundant in tissues where elasticity is of major importance, such as blood vessels, skin, lung, ligaments and cartilage/fibrocartilage tissues (Figure IV-

5). In these tissues, the stretch-relaxation process occurs more than a billion times during lifetime [38]. Biomaterials based upon elastin and elastin-derived molecules have been widely investigated in different tissue engineering applications [39]. This increase of the scientific community awareness for the use of elastin in different applications is due to the remarkable properties of this structural protein, such as elasticity, self-assembly, long-term stability, and biological activity [40]. Elastin can be applied in different forms, including insoluble elastin fibers, hydrolyzed soluble elastin, recombinant tropoelastin (fragments), repeats of synthetic peptide sequences and as block copolymers of elastin, possibly in combination with other biopolymers [40].

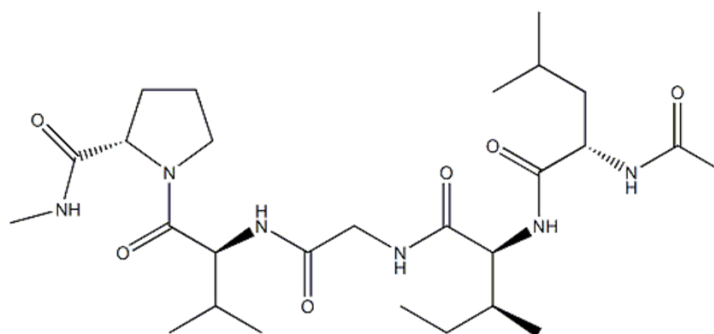


Figure IV-5 - Elastin chemical structure.

Ultrastructural studies of intervertebral disc have described mature elastic fibers in the annulus fibrosus [41, 42]. In terms of content, a study used a commercial dye-binding assay to show that a non-degenerated intervertebral disc contains approximately 2% (w/v) elastin (in dry weight terms) and no significant differences in content between the inner annulus, outer annulus and nucleus were found [43].

In **Chapter VIII** of this thesis, soluble elastin was used to develop a silk fibroin/elastin bioink to produce patient-specific annulus fibrosus implants mimicking the native ultrastructure.

#### IV-1.5. Gellan Gum (GG)

Gellan gum (GG) is an anionic extracellular polysaccharide that can be produced by aerobic submerged fermentation of *Sphingomonas elodea* [44]. GG is a linear anionic polysaccharide composed by tetrasaccharide (1,3- $\beta$ -D-glucose, 1,4- $\beta$ -D-glucuronic acid, 1,4- $\beta$ -D-glucose, 1,4- $\alpha$ -L-rhamnose) repeating units, containing one carboxyl side group [45]. This biomaterial has been used in food industry and biomedical fields, mostly due to its capability to produce resistant transparent gels. In addition, GG can be found in two forms, acetylated (high acyl form) (**Figure IV-6a**) and deacetylated

(low acyl form) (**Figure IV-6b**), with the low acyl form being most common and commercially available one [46]. Both forms of GG present a thermally reversible behavior with excellent stability and high gel strength. However, the high acyl form of GG produces transparent, elastic and flexible gels, while the low acyl form creates brittle gels [47]. Herein, the possibility to use two types of crosslinking (physical and ionic) and their promising characteristics has led to the application of this biomaterial in different TE applications [48].

Regarding 3D printing, a GG-based bioink has shown cartilage-like tissue formation when encapsulated with chondrocytes [49]. In **Chapter IX** of this thesis, GG was used to develop a cell-laden bioink to produce patient-specific implants.

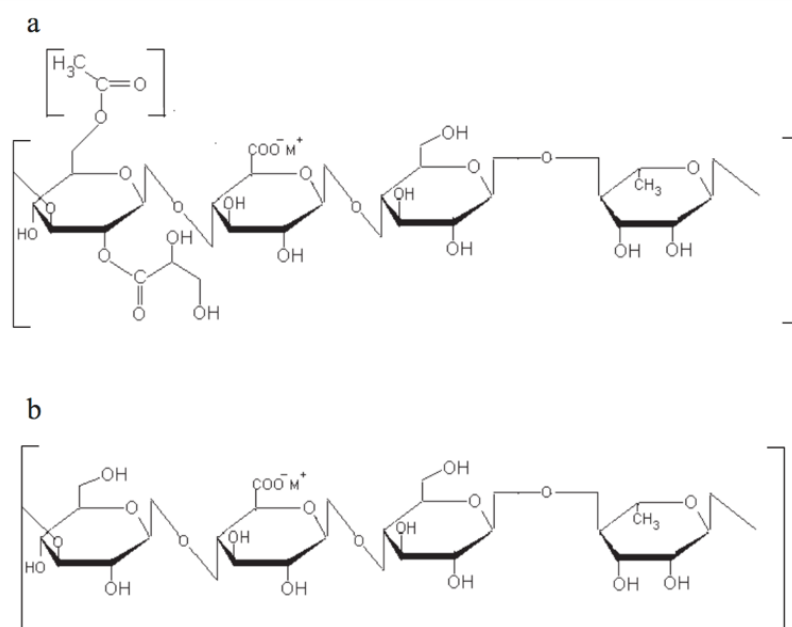


**Figure IV-6 - Repeating units of chemical structure of a) native and b) deacetylated gellan gum.**

#### IV-1.6. Fibrinogen (FB)

Fibrin and Fibrinogen (FB) plays important roles in important processes such as blood clotting, fibrinolysis, cellular and matrix interactions, inflammatory response, wound healing and neoplasia [50]. Fibrin is a biopolymer of the monomer fibrinogen that is formed after thrombin-mediated cleavage of fibrinopeptide A from the A $\alpha$  chains and fibrinopeptide B from the B $\alpha$  chains. This process leads to a subsequent conformational change and exposure of the polymerization sites [50]. This enzymatic crosslink reaction produces a fibrin monomer that has propensity to self-associate and form insoluble fibrin. This protein has been used as hemostatic agent where allogeneic fibrin sealants such as

Tisseel<sup>®</sup>, Evicel<sup>™</sup>, and Crosseal<sup>™</sup> have been approved by the Food and Drug Administration (FDA) for clinical use [51]. Regarding tissue regeneration, FB has been used in several applications including delivery systems [52], scaffolding [53], 3D printing [54] and clinical applications as sealant or glue [55]. In terms of cartilage tissue engineering, FB has been applied in several preclinical studies by means of chondrocyte-fibrin constructs or injectable fibrin gel containing cells to promote cartilage formation [56].

In **Chapter IX** of this thesis, FB has been combined with GG to develop a cell-laden bioink for the production of patient-specific fibrocartilage implants.

## IV-2. REAGENTS

Unless stated otherwise, all the reagents used in this thesis were purchased from Sigma-Aldrich (St. Louis, MO, USA).

## IV-3. PRODUCTION OF PATIENT-SPECIFIC IMPLANTS

### IV-3.1. Indirect Printing of hierarchical patient-specific scaffolds

One of the main drawbacks observed in scaffold fabrication methodologies is that each technique is applicable only in specific circumstances (*e.g.*, rheology, pressure, temperature, voltage) limiting the choice of material [57]. Natural-based materials (*e.g.*, collagen, gelatin, hyaluronic acid, gellan gum, silk fibroin) present intrinsic biocompatibility and biodegradability as well as biological cues for cell differentiation [58]. However, these biomaterials do not present ease processing which has been leading to the use of indirect fabrication techniques as an alternative (*e.g.*, casting a biomaterial into a sacrificial mold formed by additive manufacturing processes). Indirect printing methodologies to produce personalized scaffolds have emerged in several approaches with encouraging outcomes [59].

In **Chapter V** of this thesis, this printing technology was used to fabricate ABS molds that were further used to produce hierarchical patient-specific scaffolds (**Figure IV-7**). The ABS molds were designed using a commercial computer aided design (CAD) software (Autodesk Inventor Professional 2017, Autodesk) and manufactured using a Creatr Dual Extruder 3D Printer (Leapfrog, Netherlands). The design selected for the mold was a cube shape with 36 mm<sup>2</sup> of base area and 5 mm of height. Properly centered, 4 cylindrical pillars with 5 mm of height and 1 mm of diameter were designed. The molds were used to produce all the scaffolds for further characterization. In addition, by using a human



meniscus model previously developed in our group through a reverse engineering approach, an ABS human meniscus mold was printed in order to produce an indirect printed hierarchical patient-specific meniscus implant [60].

Purified SF solution was prepared by removing the glue-like protein sericin from the cocoons in a 0.02 M boiling sodium carbonate solution for 1 hour, followed by rinsing with distilled water. Then, the purified SF was dissolved in a 9.3 M lithium bromide solution for 1 hour at 70 °C and dialyzed in distilled water for 48 hours using a benzoylated dialysis tubing (MWCO: 2 kDa). The obtained SF aqueous solution was concentrated using 20% (w/v) poly(ethylene glycol) for at least 6 hours. The final concentration of SF was determined by assessing the dry weight of the solution placed overnight at 70 °C. The SF was diluted to 16% (w/v) and 8% (w/v) in distilled water, and stored at 4 °C until further use.

$\beta$ -tricalcium phosphate (TCP) powders doped with 10 mol% of Sr and Zn (were prepared as described elsewhere [61]. Briefly, the powders were synthesized by aqueous precipitation using adequate starting chemical precursors for calcium, phosphorous, Sr, and Zn, with molar ratio of  $(Ca+X)/P = 1.48$ , (where X corresponds to Sr + Zn) and pH of  $\approx 7$ . The precipitated suspensions were kept for 4 hours under constant stirring and matured for further 20 hours under rest conditions, at 50 °C. The resulting precipitates were filtered, dried at 100 °C, and heat treated for 2 hours at 1100 °C, followed by milling and sieving by a mesh size of 63  $\mu\text{m}$ , yielding a final average particle size of  $\approx 1\text{-}10$   $\mu\text{m}$ .

Hierarchical indirect printed scaffolds were fabricated comprising two layers, *i.e.* SF layer in the upper zone and SF mixed with ionic-doped TCP in a bottom layer. For that, enzymatic-cross-linked SF hydrogels were firstly prepared by mixing SF solutions (with 8% or 16% (w/v)) with 10% (v/v) horseradish peroxidase solution (HRP type VI, 0.84  $\text{mg}\cdot\text{mL}^{-1}$ ) and 6.5% (v/v) hydrogen peroxide solution ( $\text{H}_2\text{O}_2$ , 0.36% (v/v); Panreac, Barcelona, Spain), and a total volume of 200  $\mu\text{L}$  was used to fill the cube shape mold. The incubation was performed at 37 °C for 15 minutes for SF (16% (w/v)) and 25 minutes for SF (8% (w/v)). For the bottom layer, using the abovementioned enzymatic crosslinking process, 150  $\mu\text{L}$  of SF solutions (8% or 16% (w/v)) were mixed with ionic-doped TCP powder using blend ratios of 80/20 (w/w) of SF/ionic-doped TCP, and added on the top of the SF layer, followed by incubation at 37 °C for 30 minutes. After the gelation process, the final indirect printed scaffolds were frozen at -80 °C and lyophilized during 3 days (CRYODOS-80; Telstar, Barcelona, Spain). The scaffolds were posteriorly immersed in a 70% (v/v) ethanol solution and easily removed from the molds. The produced indirect

printed hierarchical scaffolds were abbreviated to Hi8 and Hi16 when SF solutions at 8% (w/v) and 16% (w/v) were used, respectively. For further characterization, pure SF monolayer scaffolds (SF8 and SF16) and SF/TCPs monolayer scaffolds (SF8/TCP and SF16/TCP) were also prepared.

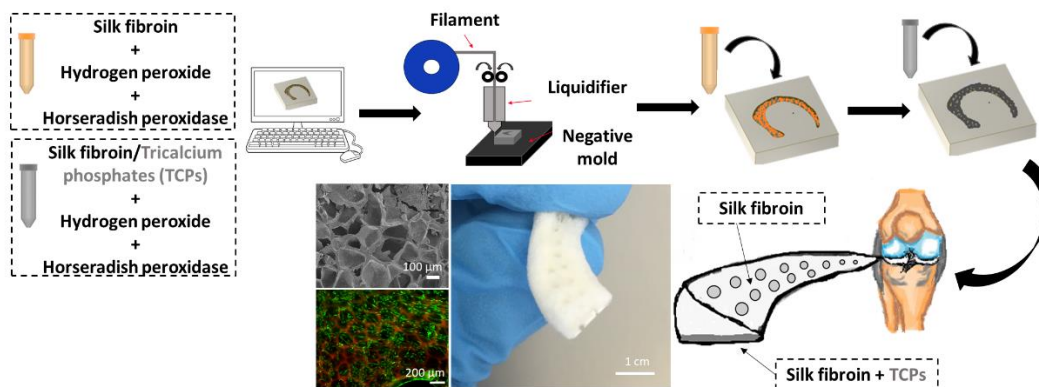


Figure IV-7 - Representative scheme of the production of the indirect printed hierarchical patient-specific scaffolds.

### IV-3.2. Development of a SF-based bioink and production of patient-specific memory-shape implants

3D extrusion-based bioprinting (also known as bioplotting) is a technique that uses cell-laden hydrogels as carrier biomaterial or hydrogels/biomaterials that are directly extruded by the application of pressure [62]. This technique allows the deposition of different cell types and different biomaterials in the same construct [57].

In **Chapter VII** of this thesis, a novel fast-setting SF bioink was developed for further use in 3D extrusion-based bioprinting to produce patient-specific memory-shape implants.

Purified SF solution was prepared using the same methodology described in the sub-section IV-3.1. of this chapter. Furthermore, SF solution was diluted to 16% (w/v) in distilled water and combined with HRP (type VI, 0.84 mg.mL<sup>-1</sup>) and hydrogen peroxide solution (H<sub>2</sub>O<sub>2</sub>, 0.36% (v/v); Panreac, Barcelona, Spain). A mixture of SF ink, 5% (v/v) HRP solution and H<sub>2</sub>O<sub>2</sub> solution at three different concentrations, 1.5% (SI15), 2.5% (SI25), and 3.5% (SI35) (v/v) was prepared and incubated at 37 °C for 30 minutes. After rheological characterization and extrusion tests the SI25 was selected to be printed.

The SI25 was prepared directly in the cartridge and incubated at 37 °C for 30 minutes using a 4th generation Envisiontec 3D Bioplotter (**Figure IV-8**). The bioink was extruded pneumatically. The nozzle size had 400 μm of diameter and the 3D scaffolds were constructed using pressures ranging from 250 to 350 kPa at a speed of 5 to 8 mm.s<sup>-1</sup>. The SF patient-specific memory-shape implants of human

meniscus were printed through a reverse engineering approach. For that, a semi-automatic methodology approach of segmenting meniscus tissue from volumetric MRI datasets and reconstruction of 3D models with an advanced segmentation software was used [60]. The scaffolds and implants were further frozen at -80 °C for 2 days and freeze-dried for 3 days (Telstar-Cryodos -80, Spain). In order to access the changing of conformation to  $\beta$ -sheet over time, SF scaffolds and implants were both immersed directly in PBS after printing. Before any characterization test, the freeze-dried scaffolds were immersed in ethanol 70% for 3 hours and then in PBS overnight.

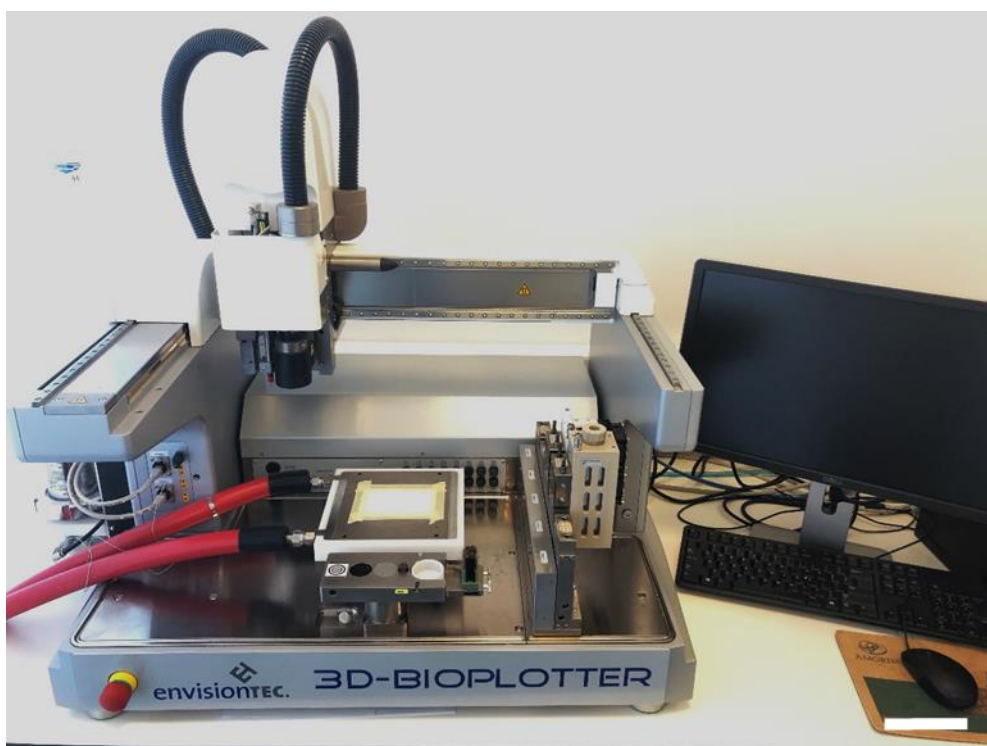


Figure IV-8 - Envisiontec 3D Bioplotter. Scale bar: 10 cm.

### IV-3.3. Development of a SF/Elastin bioink and production of patient-specific annulus fibrosus implants

In **Chapter VIII** of this thesis, a SF/Elastin bioink was developed for further use in 3D extrusion-based bioprinting to produce patient-specific annulus fibrosus implants.

Purified SF solution was prepared using the same methodology described in the sub-section IV-3.1. of this chapter. The SF was diluted to 16% (w/v) in distilled water and an elastin solution was prepared at 16% (w/v) also in distilled water. A SF/elastin solution was obtained through the mixture of both solutions at a ratio of 90:10 respectively. SF/elastin ink was produced by adding horseradish peroxidase solution (HRP type VI, 0.84 mg.mL<sup>-1</sup>) and hydrogen peroxide solution (H<sub>2</sub>O<sub>2</sub>, 0.36% (v/v);

Panreac, Barcelona, Spain). A mixture of SF/elastin solution, 5% (v/v) HRP solution and 2.5% (v/v) H<sub>2</sub>O<sub>2</sub> was prepared inside the cartridge and incubated at 37 °C for 30 minutes.

Using the same printing parameters and post-printing process described in the sub-section IV-3.2. of this chapter, SF/Elastin scaffolds were produced. In addition, a patient-specific SF/elastin AF substitute was printed using a model previously developed in our group [63]. In brief, a 47-year-old male patient underwent an MRI scan in head-first supine position using a 3.0-T scanner (Siemens MAGNETOM Spectra, Munich, Germany). Thereafter, a three-stage reconstruction (image segmentation, manual corrections and 3D reconstruction) was performed to obtain a 3D model of the L1-L2 IVD of the patient. The patient-specific implant mimicking the patient AF anatomy was produced using the same printing parameters as described for printing the SF/elastin scaffolds.

#### **IV-3.4. Development of GG/FB and Silk methacrylated bioink and production of patient-specific hybrid implants**

3D extrusion-based bioprinting technology has proved to be useful in the production of patient-specific scaffolds [64]. Advanced bioinks have been designed and numerous natural and synthetic materials have been exploited in the biofabrication of 3D constructs and, in some cases, used together to produce hybrid constructs. The use of hybrid structures in 3D Bioprinting aims to produce biologically and mechanically suitable implants by means of using two bioinks: (i) one to give the biological functionality by carrying cells and biological factors, and (ii) other to impart the proper mechanical strength to the implant.

In **Chapter IX** of this thesis, GG/FB and Silk methacrylated bioinks were developed to produce patient-specific hybrid implants.

Different concentrations of fibrinogen were tested in the preparation of the GG/FB bioink. Briefly, different concentrations (25, 50, 75, 100, 125, and 150 mg.mL<sup>-1</sup>) of a FB solution were prepared by mixing in PBS at 37 °C for 2 hours. The fibrinogen was previously sterilized by UV radiation for 30 minutes. A solution of GG at 12 mg.mL<sup>-1</sup> was mixed with sucrose in distilled water at room temperature (RT) under constant stirring. The final concentration of sucrose was 0.25 M. The solution was progressively heated to 84 °C in an oil bath and kept at this temperature for 20 minutes under constant stirring. In addition, the solution was filtered using a 0.45 µm syringe filter and kept at 37 °C until further use. The GG solution was mixed with each of the FB solutions in a final ratio of 1:25. In the

end, it was obtained GG/FB bioinks with different concentrations of FB (1, 2, 3, 4, 5, and 6 mg.mL<sup>-1</sup>). In the following table are represented the nomenclatures of the bioinks formulations.

**Table IV-1 - Nomenclatures of the GG/FB bioinks.**

Starting solutions	Mixing ratio	Bioink formulations	Nomenclatures
GG 12 mg.mL <sup>-1</sup>	1:25	GG	GG
GG 12 mg.mL <sup>-1</sup> + FB 25 mg.mL <sup>-1</sup>	1:25	GG + FB 1 mg.mL <sup>-1</sup>	GG/FB1
GG 12 mg.mL <sup>-1</sup> + FB 50 mg.mL <sup>-1</sup>	1:25	GG + FB 2 mg.mL <sup>-1</sup>	GG/FB2
GG 12 mg.mL <sup>-1</sup> + FB 75 mg.mL <sup>-1</sup>	1:25	GG + FB 3 mg.mL <sup>-1</sup>	GG/FB3
GG 12 mg.mL <sup>-1</sup> + FB 100 mg.mL <sup>-1</sup>	1:25	GG + FB 4 mg.mL <sup>-1</sup>	GG/FB4
GG 12 mg.mL <sup>-1</sup> + FB 125 mg.mL <sup>-1</sup>	1:25	GG + FB 5 mg.mL <sup>-1</sup>	GG/FB5
GG 12 mg.mL <sup>-1</sup> + FB 150 mg.mL <sup>-1</sup>	1:25	GG + FB 6 mg.mL <sup>-1</sup>	GG/FB6

Regarding the Sil-MA bioink preparation, purified silk fibroin (SF) was prepared by removing the glue-like protein sericin from the cocoons in a 0.02 M boiling sodium carbonate solution for 1 hour, followed by rinsing with distilled water in order to fully remove the degumming solution. A 9.3 M lithium bromide solution was used to dissolve the purified SF for 1 hour at 70 °C. After dissolution, 1, 2, and 3 mL of glycidyl methacrylate solution was added to 50 mL of silk solution. The reaction occurred under stirring at 55 °C for 3 hours. From this process, a high (Sil-MA (H)), a medium (Sil-MA (M)) and a low (Sil-MA (L)) methacrylate silk solutions were obtained. Then, the solutions were dialyzed in distilled water for 7 days using the benzoylated dialysis tubing (MWCO: 2 kDa). Sil-MA solutions were concentrated against poly (ethylene glycol) for at least 6 hours. The final concentration of the solutions was determined by measuring the dry weight in the oven at 70 °C overnight. In order to print the Sil-MA solutions gelatin and glycerol were used as printing support materials. The Sil-MA solutions at a final concentration of 16% (w/v) were mixed with glycerol and gelatin at a final concentration of 8% (w/v) and 4.5% (w/v), respectively. The solutions were incubated for 45 minutes at 65 °C. Then, the addition of Irgacure 2959 at a final concentration of 0.2 % (w/v) was the final step in the Sil-MA bioinks production. The support materials were washed out after printing.

The printing process was conducted in the house-made 3D ITOP system. The system includes an XYZ stage/controller, multiple dispensing modules, a pneumatic pressure controller, and a closed chamber with a temperature controller. Printed constructs were designed with 3D computer-aided design (CAD) modeling using our customized software. The created models were converted to a motion program containing the path information and printing speed and air pressure were controlled. The environmental temperature was kept at 20 °C. Regarding the GG/FB bioinks, a microscale nozzle (240  $\mu\text{m}$  of diameter, TECDIA, Inc., Tokyo, Japan) was used to print 3D constructs at a speed of 250  $\text{mm}\cdot\text{min}^{-1}$  and air pressures ranging 45 to 65 kPa. After printing, the constructs were cross-linked using a PBS/Thrombin solution (20  $\text{U}\cdot\text{mL}^{-1}$ ) for 30 minutes at RT.

Regarding the SiI-MA bioinks, a microscale nozzle (300  $\mu\text{m}$  of diameter, TECDIA, Inc., Tokyo, Japan) was used to print 3D constructs at a speed of 250  $\text{mm}\cdot\text{min}^{-1}$  and air pressures ranging 450 to 550 kPa. After printing, the constructs were UV cross-linked by a BlueWave® MX<sup>1</sup>50 LED Spot-Curing System (Dymax, USA) for 120 seconds at an intensity of 400  $\text{mw}\cdot\text{cm}^{-2}$ .

To produce the hybrid constructs, the same printing parameters and post-printing processes for each bioink were used (**Figure IV-9**).

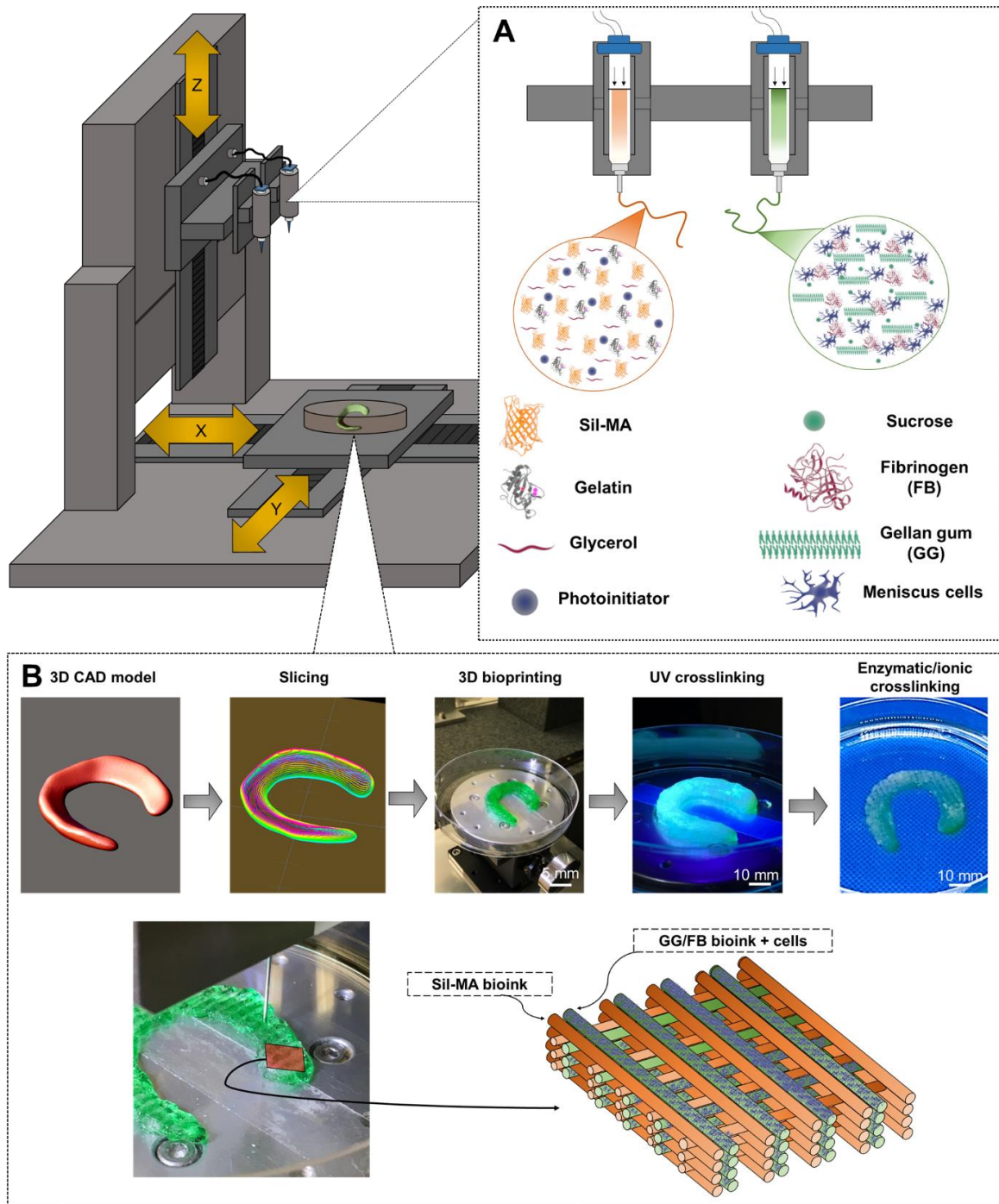


Figure IV-9 - Scheme of the 3D bioprinting of cell-laden hybrid scaffolds: (A) printing of hybrid 3D constructs using a Silk-MA bioink and a cell-laden GG/FB bioink. (B) 3D bioprinting and post-printing processes for the production of 3D hybrid constructs and respective patterning. (UV: Ultraviolet light).

#### IV-4. PHYSICO-CHEMICAL CHARACTERIZATION

##### IV-4.1.1. Morphology and microstructure evaluation

###### IV-4.1.1.1 *Scanning Electron Microscopy and Energy*

Scanning Electron Microscopy (SEM) is an imaging technique that provides high-resolution 2D images of a sample. The sample's surface is scanned with a focused beam of electrons that interact with the atoms of the sample at various depths. When in contact with the atoms at the sample's surface, the electrons produce several signals containing the collected information [65]. The scattered electrons produce diverse type of signals which are detectable by the SEM equipment, and transformed into a 2D image. SEM provides qualitative information regarding sample's surface morphology, including microstructure, pore geometry, topography and elemental information.

In **Chapters V, VI, VII** and **VIII** the morphology and pore architecture of the produced scaffolds was observed using SEM (Nova NanoSEM 200; FEI, Hillsboro, OR, USA) (**Figure IV-10**). Before the observation, the scaffolds were coated with one layer of Gold/Palladium (Au/Pd) (SC502–314B) in a coater (E6700; Quorum Technologies, East Grinstead, UK). In **Chapter V**, the elemental characterization of the hierarchical scaffolds after *in vitro* mineralization was performed with an Energy Dispersive Spectrometer (EDS; Pegasus X4M) coupled to the SEM.



Figure IV-10 - Nova NanoSEM 200 (FEI). Scale bar: 10 cm.

In **Chapter IX**, the morphology of the constructs was observed under a SEM (FlexSEM 1000 VP-SEM (Hitachi, Japan). Before observation, the constructs were dried by critical point drying (Leica EM



CPD300 (Leica, USA) and coated with one layer of 4 nm of Au/Pd in a leica EM ACE600 coater (Leica, USA).

#### IV-4.1.1.2 *Micro-Computed Tomography (Micro-CT)*

Micro-CT analysis is a powerful and invasive tool used to analyze the microstructure of scaffolds in a 3D perspective. Micro-CT uses X-ray to scan and obtain the 3D reconstruction of samples and reach cross-section information of the object. The obtained data set, when processed by the software allow to quantify the microstructure data of scaffolds, including pore size, porosity, interconnectivity, pore-wall size, and phase distribution [66].

In **Chapters V, VI, VII and VIII**, the micro architecture of the scaffolds was investigated using a high-resolution Micro-CT Skyscan 1072 scanner (Skyscan, Kontich, Belgium) (**Figure IV-11**) with a pixel size of 10  $\mu\text{m}$ . Standardized cone-beam reconstruction software (NRecon v1.4.3, SkyScan) was used for data sets reconstructions. Representative data set of the samples was segmented into binary images with a dynamic threshold of 22-40 (grey values). Then, the binary images obtained were used for morphometric analysis (CT Analyser, v1.5.1.5, SkyScan) and construction of three-dimensional models (ANT 3D creator, v2.4, SkyScan).



Figure IV-11 - Micro-CT Skyscan 1072 scanner (Skyscan, Kontich). Scale bar: 10 cm.

#### IV-4.1.2. Chemical analysis

##### IV-4.1.2.1 *Fourier Transform Infrared Spectroscopy (FTIR)*

Fourier Transform Infrared Spectroscopy (FTIR) is a cost-effective methodology that identifies the

chemical groups in materials. Similar chemical groups absorb in the IR at similar frequencies, which enables to screen the ratio of the components in the tested material. Fourier transformation algorithm allied to IR spectroscopy gives a spectrum of IR absorption per frequency/wavelength [67].

In **Chapters V, VI, VII and VIII** the SF-based scaffolds conformation and composition information were evaluated by FTIR spectroscopy (Perkin-Elmer 1600 series equipment, CA, USA) (**Figure IV-12**) under an attenuated total reflectance (ATR) model (IRPrestige-21, Shimadzu, Japan). All spectra were obtained between 4600 to 800  $\text{cm}^{-1}$  at a 4  $\text{cm}^{-1}$  resolution with 50 scans.



Figure IV-12 - FTIR spectroscopy (Perkin-Elmer 1600 series equipment). Scale bar: 10 cm.

#### IV-4.1.2.2 *Proton-Nuclear Magnetic Resonance analysis ( $^1\text{H-NMR}$ )*

Proton-Nuclear Magnetic Resonance ( $^1\text{H-NMR}$ ) is an extensively used technique to identify polymers and analyze their chemical modifications [68]. The magnetic resonance of protons that is obtained by the small magnetic fields produced by the movement of electrons is measured and the distribution of electrons in molecules is distinct in different chemical groups. However, they have proximal resonances in identical chemical groups, enabling its identification. The addition or modification of a proton in a chemical group, results in the modification of its magnetic resonance and hence a chemical shift or a new peak is created in the  $^1\text{H-NMR}$  spectrum. In this sense, functionalization degree can be assessed by the ratio of the integrated modified and non-modified chemical groups.

The different degrees of methacrylation were measure through  $^1\text{H-NMR}$  at a frequency of 400 MHz using a Bruker NMR Spectrometer (Bruker, Billerica, MA). Silk MA solutions were frozen in  $-80\text{ }^\circ\text{C}$  for 12 hours and freeze-dried for 48 hours. A 9.3M lithium bromide solution was prepared in deuterium oxide ( $\text{D}_2\text{O}$ , Sigma-Aldrich). Lyophilized Silk MA powders were re-dissolved at a final concentration of 50  $\text{mg}\cdot\text{mL}^{-1}$ . SF solution was used as control. The degree of methacrylation was defined according to the

percentage of  $\epsilon$ -amino groups of lysine in SF that are modified in Silk-MA. Therefore, the lysine methylene signals (2.4–2.6 ppm) of samples were integrated to obtain the areas. The degree of methacrylation was obtained by the equation

**Equation IV-1 - Determination of the methacrylation degree.**

$$\text{Methacrylation degree (\%)} = 1 - \left[ \frac{L_iSMA}{L_iSF} \right] \times 100\%$$

where,  $L_iSMA$  is the lysine integration signal of Sil-MA and  $L_iSF$  is the lysine integration signal of SF.

### IV-4.1.3. Mechanical properties

#### IV-4.1.3.1 Rheological analysis

Rheology provides the analysis in terms of deformation and flow of matter solids [69]. The results obtained by this technique is given in terms of the elasticity, viscosity and plastic behavior of materials under changes of strain, frequency, time, or temperature.

In **Chapters VI** and **VII**, The rheological analyses of the developed silk fibroin bioinks were performed using a Kinexus pro+ rheometer (Malvern Instruments, UK) (**Figure IV-13**) and using the acquisition software rSpace (Malvern Instruments, UK). For the oscillatory experiments the measuring system was equipped with stainless steel (316 grade) parallel plates using an upper measurement geometry plate of 20 mm diameter. Frequency-sweep and strain sweep experiments were performed using SF inks prepared as described above. For the rotational experiments, the measuring system was equipped with an upper measurement geometry cone (40 mm diameter and 4° angle). In addition, a tack adhesion test was performed with a Peltier plate cartridge using a 20 mm upper plate and 65 mm lower plate (stainless steel). Following a contact period of 2 seconds, the gap was increased linearly at 0.01 mm.s<sup>-1</sup> and the normal force recorded as a function of time. These experiments were performed at room temperature and all plots represent the average of at least three samples.

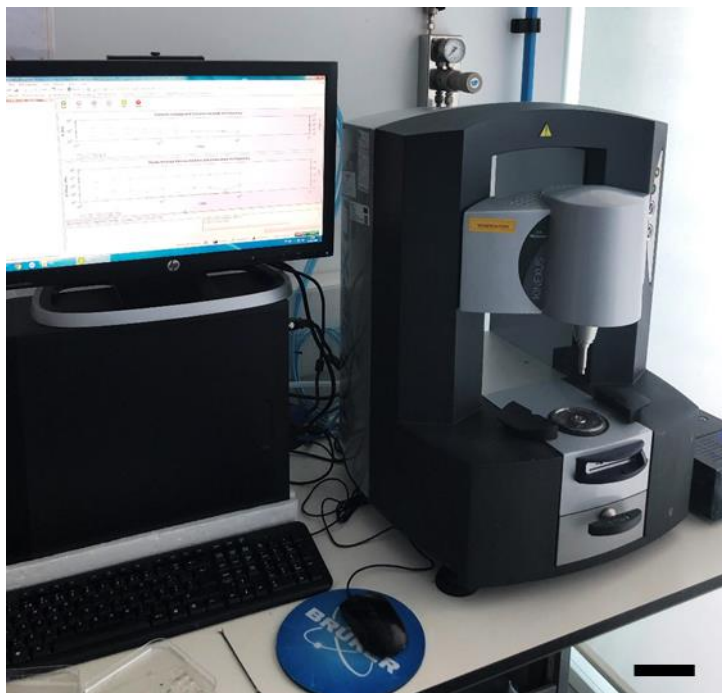


Figure IV-13 - Kinexus pro+ rheometer (Malvern Instruments). Scale bar: 10 cm.

In **Chapter IX**, the rheological analyses of the developed bioinks were performed using a Discovery HR-2 (TA instruments, US) and using the acquisition software TRIOS (TA instruments, US). For the oscillatory experiments the measuring system was equipped with stainless steel parallel plates using an upper measurement geometry plate of 12 mm diameter. Frequency-sweep and strain sweep experiments were performed. For the rotational experiments, the measuring system was equipped with an upper measurement cone geometry (40 mm diameter and  $1^\circ$  angle). These experiments were performed at  $20^\circ\text{C}$  and all plots represent the average of at least three samples.

#### IV-4.1.3.2 *Compression tests*

Uniaxial compression tests assess the deformation of a materials under compressive forces. From the compressive tests, it is possible to obtain a stress vs strain plot and the compressive elastic modulus of the samples. The scaffolds are subjected a compressive forces *in vivo*, thus is important to comprehend the mechanical behavior of the produced constructs to better select the most suitable for the desire application.

In **Chapters V, VII and VIII**, the compressive tests were using the Instron 4505 Universal Machine (Instron Corporation, MA, USA) in compression mode (**Figure IV-14**). Instron electromechanical universal testing machines are capable to perform tensile, compression, bend, peel, tear, and other

mechanical tests on materials. The tests were performed using a 1 kN load cell and at room temperature (RT). Before testing, the scaffolds were immersed in PBS overnight at 37 °C. In **Chapters V** and **VIII**, the cross-head speed was set at 2 mm.min<sup>-1</sup> and tests were run until achieving a 60% reduction in specimen height. The elastic modulus was defined by the slope of the initial linear section of the stress–strain curve. A minimum number of 5 samples were tested per condition, with the compressive modulus values being the average of all the measurements.



**Figure IV-14 - Instron 4505 Universal Machine (Instron Corporation). Scale bar: 10 cm.**

In **Chapter VII**, the cross-head speed was 2 mm.min<sup>-1</sup> and tests were run until achieving 80% reduction in specimen height. The test was repeated over five cycles. The compressive modulus was defined by the slope of the initial linear section of the stress–strain curve. A minimum number of three samples were tested.

In **Chapter IX**, compressive tests were performed using a Universal Testing Machine (Instron 5544) with a 100 N cell load at RT. The cross-head speed was set at 2 mm.min<sup>-1</sup> and tests were run until achieving 60% reduction in specimen height. From the stress-strain curve, the secant modulus was calculated at 3%, 6% and 12% of strain. A minimum number of three samples was tested, with the compressive modulus values being the average of all the measurements. . Under the same operating conditions, a cyclic stress-relaxation compression test was performed. The samples were subjected to 5

cycles of compression with a strain of 60%.

#### IV-4.1.3.3 *Dynamic Mechanical Analysis (DMA)*

As mentioned before, the produced scaffolds will be subjected to physical loads after *in vivo* implantation. In addition, these mechanical loads are dynamic and with different frequencies. Dynamic mechanical analysis (DMA) is a helpful technique that allows assessing the scaffold's viscoelastic behavior under dynamic conditions. Using this technique, is possible to characterize the mechanical properties of the scaffolds as a function of temperature, time, stress, atmosphere, frequency, or by the combination of these parameters. DMA equipment applies cyclic sinusoidal deformation to the sample under a controlled stress or strain. DMA measures stiffness and damping, these are reported as modulus ( $E'$ ) and tan delta ( $\tan \delta$ ). This modulus can be expressed as storage modulus, which measures the elastic response of samples, and loss modulus, that measures the viscous response of the samples. From the ratio between the loss and storage modulus is possible to obtain the tan delta that is often called damping factor, measuring the damping of materials. Damping is the dissipation of energy in a material under cyclic load giving the measure of how well a material can get rid of energy.

In **Chapters V, VI, VII and VIII**, the DMA analysis was performed using a TRI-TEC8000B model from Triton Technology manufacturer (Lincolnshire, UK) (**Figure IV-15**) in the compressive mode. The measurements were performed at 37 °C in the hydrated state, by immersing the samples in PBS solution in a Teflon® reservoir and clamped in the DMA apparatus. After equilibration at 37 °C, the DMA spectra were obtained in a frequency scan between 0.1 and 10 Hz. The experiments were performed under a constant strain amplitude of 50  $\mu\text{m}$ .

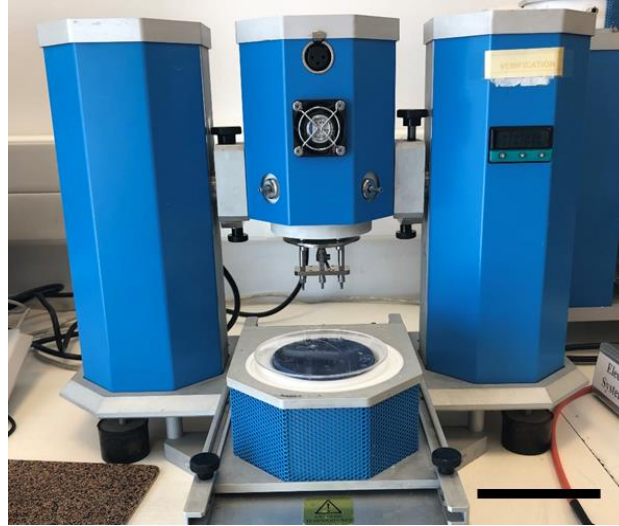


Figure IV-15 - DMA TRI-TEC8000B model (Triton Technology manufacturer). Scale bar: 10 cm.

#### IV-4.1.4. Swelling ratio

The swelling ratio or water-uptake behavior of the scaffolds can give a better understanding in terms of the performance of a biomaterial in contact with hydrated medium. This can predict the scaffold's interactions with the surrounding tissues, especially in terms of adjustability to the defect sites and medium absorption.

In **Chapters V** and **VIII** the swelling ration of the scaffolds was evaluated after immersion in PBS for time periods ranging from 3 hours to 28 days. All experiments were conducted at 37 °C in static conditions. At each time point, the samples were removed from PBS, the excess of surface water was absorbed using a filter paper, and the weight immediately determined.

In **Chapter IX**, The swelling ratio of the constructs was evaluated after immersion in PBS for time periods ranging from 1 hour to 14 days. All experiments were conducted at 37 °C in static conditions. At each time point, the samples were removed from PBS, the excess of surface water was absorbed using a filter paper, and the weight immediately determined. In the end, the samples were dried at 60 °C and weight.

The swelling ratio was obtained using the following equation:

Equation IV-2 - Determination of swelling ratio.

$$\text{swelling ratio (\%)} = \left[ \frac{(m_{w,t} - m_i)}{m_i} \right] \times 100\%$$

where,  $m_i$  is the initial weight of the sample, and  $m_{w,t}$  is the wet weight of the sample at each time point. A minimum number of three samples were tested.

#### IV-4.1.5. Degradation profile

TE applications consist in the use of biodegradable materials where the scaffolds maintain their function during the regeneration process, while the remodeling process occurs at the same rate of scaffold degradation. After implantation, it is expected degradation of the biomaterial through dissolution or erosion, hydrolysis, enzymatic degradation, and phagocytosis. Among these processes in human body, the proteolysis is mainly conducted by enzymes which degrade proteins with high efficiency. In this sense, it is important to assess the *in vitro* degradation of the produced scaffolds in order to predict their behavior *in vivo*.

In **Chapters V, VII** and **VIII** the scaffolds was assessed by an enzymatic degradation assay using Protease XIV. The solution was prepared by dissolving the enzyme in distilled water at a concentration of 1.0 U.mL<sup>-1</sup> in **Chapter V** and 0.5 U.mL<sup>-1</sup> in **Chapters VII** and **VIII**. The initial weight of the scaffolds was measured, and then the scaffolds were hydrated in PBS at 37 °C overnight, followed by immersion in 5 mL of protease solution. The enzyme solution was changed every 48 hours. The samples were weight after 0.16, 0.33, 1, 7, 14, 21 and 28 days of immersion in the degradation solution at 37 °C in static conditions. The weight loss ratio was obtained using the following equation:

Equation IV-3 - Determination of weight loss ratio.

$$\text{weight loss ratio} = \left[ \frac{(m_i - m_{d,t})}{m_i} \right] \times 100\%$$

where,  $m_i$  is the initial weight of the sample, and  $m_{d,t}$  is the weight of the degraded sample at each time point (n=3 per group).



#### IV-4.1.6. *In vitro* bioactivity tests

The bone-bonding capability of a scaffold can be assessed by examining the apatite creation on the surface of scaffolds immersed in simulated body fluid (SBF). SBF contains ions concentrations nearly equal to those of human blood plasma. This *in vitro* assay can predict the *in vivo* bone bioactivity of the produced scaffolds. In this thesis, the *in vitro* bioactivity evaluation was performed by immersing the scaffolds in SBF solution following the method proposed by Tas *et al.* [70] and adapted by Pina *et al.* [71].

In **Chapter V**, to evaluate the *in vitro* bioactivity of the scaffolds before cell culture, the scaffolds were placed into polystyrene flasks containing (1.5x) SBF with ionic concentrations (**Table IV-2**) nearly equivalent to the human blood plasma for 7 days. The scaffolds were continuously shaken at a rate of 60 rpm, at 37 °C, and the liquid was refreshed every 2 days. Then, the scaffolds were allowed to dry at 37 °C for 1 day and analyzed by means of SEM/EDS analyses. All experiments were carried out in triplicate for each separated layer.

Table IV-2 - Ions concentrations in the SBF solution (pH ≈ 7.4).

Ions	Ion concentration (mM.L <sup>-1</sup> )
Na <sup>+</sup>	213.0
K <sup>+</sup>	7.5
Ca <sup>2+</sup>	3.75
Mg <sup>2+</sup>	2.25
Cl <sup>-</sup>	223.2
HPO <sub>4</sub> <sup>-</sup>	1.5
HCO <sub>3</sub> <sup>2-</sup>	6.3
SO <sub>4</sub> <sup>2-</sup>	0.75

#### IV-4.1.7. Diffusion tests

The fluidic exchanges and the nutrient diffusion of cell-laden hydrogels are two key features in the fabrication of 3D constructs [58, 72]. The fast nutrient diffusion during the post-printing processes is a key factor to guarantee cell viability in cell-laden hydrogels. Biofabrication of 3D printed constructs using cell-laden bioinks can take several minutes and the development of highly permeable hydrogels is a critical step.

In **Chapter IX**, diffusion tests were performed in the GG/FB bioinks using fluorescein isothiocyanate dextrans (FITC dextrans, Sigma-Aldrich, St. Louis, USA) with two different molecular weights (4 and 70 kDa). FITC dextrans were dissolved in 1 mL of a 12 mg.mL<sup>-1</sup> GG solution and kept at 37 °C. The GG/FITC dextran solutions were posteriorly mixed with the FB solutions obtaining a final concentration of FITC of 0.2 mg.mL<sup>-1</sup>. Then, 100 µL of the mixture was added to a 2 mL Eppendorf tube. The samples were incubated at 37 °C and 1 mL of PBS buffer, pH 7.4, was added to each tube. After 1, 3, 6, and 24 hours of incubation, the amount of dye present in the release medium (PBS) was determined by measuring fluorescence intensity ( $\lambda_{ex}$  490 nm,  $\lambda_{em}$  525 nm) using a plate reader (SpectraMax M5, Molecular Devices, USA). A minimum number of three samples were tested.

#### **IV-5. *IN VITRO* BIOLOGICAL CHARACTERIZATION**

##### **IV-5.1. Cell sources**

###### **IV-5.1.1. Isolation of human meniscus cell (hMCs)**

Human meniscus cells (HMCs) were isolated from meniscus tissue samples obtained from surgery procedures performed after patient's informed consent and using a protocol previously established with the Orthopedic department of Póvoa de Varzim Hospital (Póvoa de Varzim, Portugal). HMCs were isolated following an enzymatic digestion-based method (collagenase type II) from human meniscus tissue obtained from patients submitted to surgery. The extracted tissue was placed in PBS solution (pH 7.4) and washed several times with PBS containing 1% (v/v) antibiotic/antimycotic mixture until total removal of blood or other bodily contaminants. Meniscus tissue was then separated from fat and vascularized tissue and washed several times. Then, the meniscus was cut into small pieces. Tissue digestion was performed by incubation at 37 °C in a water bath for 24 hours in 10-20 mL of a mixture of cell medium  $\alpha$ -MEM supplemented with 10% (v/v) fetal bovine serum (FBS; Biochrom AG, Germany), 1% (v/v) antibiotic/antimycotic solution (final concentration of penicillin 100 U.mL<sup>-1</sup> and streptomycin 100 mg.mL<sup>-1</sup>, Gibco, GB) mixture and collagenase type II (1:1). The isolated HMCs were then expanded in basal medium consisting  $\alpha$ -MEM w/o nucleosides (MEM alpha medium; Life Technologies, Scotland) supplemented with 10% (v/v) FBS and 1% (v/v) antibiotic/antimycotic solution. Cells were cultured until confluence at 37 °C in an atmosphere of 5% CO<sub>2</sub> incubator, changing the culture medium every 2 days.

#### **IV-5.1.2. Human osteoblast (hOBs)**

Primary human osteoblasts (hOBs) were purchased from sigma (Ref. 406-05A, Sigma-Aldrich, St. Louis, MO, USA) and cultured in non-coated T150 cell culture flasks using Human Osteoblasts Growth Medium (Sigma-Aldrich, St. Louis, MO, USA). Cells were cultured until confluence at 37 °C in an atmosphere of 5% CO<sub>2</sub> incubator, changing the culture medium every 2 days.

#### **IV-5.1.3. Human adipose-derived stem cell (hASCs)**

The human adipose-derived stem cells (hASCs) were isolated from the adipose fat tissue, which was obtained from liposuction procedures. The use of the hASCs was approved by the Ethics Committee of University of Minho.

hASCs were isolated from abdominal subcutaneous adipose tissue samples obtained from liposuction procedures on healthy male and female donors with ages between 18 and 57 years, after informed consent, under established cooperative agreements between Hospital da Senhora da Oliveira (Guimarães, Portugal) and 3B's Research Group. After the liposuction procedure, the samples were processed within 24 hours and hASCs were enzymatically isolated. The expansion procedure occurred in basal medium consisting of Minimum Essential Medium Eagle - Alpha Modification ( $\alpha$ -MEM; Life Technologies, Scotland) supplemented with 10% (v/v) FBS (Biochrom AG, Germany) and 1% (v/v) antibiotic/antimycotic solution (final concentration of penicillin 100 U.mL<sup>-1</sup> and streptomycin 100 mg.mL<sup>-1</sup>; Gibco, GB). Cells were cultured until confluence, at 37 °C in an atmosphere of 5% CO<sub>2</sub> incubator, by changing the culture medium every 2 days.

The phenotype of hASCs has been extensively characterized using tissue samples obtained from the same anatomic region (abdominal subcutaneous adipose tissue), collected using similar techniques and isolated following the same procedure [73, 74].

#### **IV-5.1.4. Isolation of pig meniscus cell (PMCs)**

Pig meniscus cells (PMCs) were isolated from meniscus tissue samples obtained from euthanized pigs. PMCs were isolated following an enzymatic digestion-based method (collagenase type II and pronase). The extracted tissue underwent 3 washing steps: (1) povidone iodine, (2) PBS containing 10% (v/v) antibiotic/antimycotic mixture and (3) PBS containing 2% (v/v) antibiotic/antimycotic mixture. The

washing steps were performed until the total removal of blood or other bodily contaminants. Meniscus tissue was then separated from the fat and vascularized tissue and was cut into small pieces. Tissue digestion was performed by incubation at 37°C in an orbital stirring for 24 h in 10-20 mL of a mixture of cell medium Alpha-MEM ( $\alpha$ -MEM, Life Technologies, Carlsbad, CA) supplemented with 10% (v/v) FBS, 1% (v/v) antibiotic/antimycotic solution, 0.3% (w/v) collagenase type II and 0.5 mg/mL of pronase. The isolated PMCs were then expanded in basal medium consisting Alpha-MEM w/o nucleosides (MEM alpha medium; Life Technologies, Scotland) supplemented with 10% (v/v) FBS and 1% (v/v) antibiotic/antimycotic solution. Cells were cultured until confluence at 37 °C in an atmosphere of 5% CO<sub>2</sub> incubator, changing the culture medium every 2 days.

## IV-5.2. Cryopreservation

The cryopreservation of the cells used in this thesis was performed using a Statebourne Biosystem 24 cryogenic tank (Statebourne Cryogenics Ltd., UK) in **Chapters V, VII and VIII** and a liquid nitrogen tank in **Chapter IX**. Briefly, cell suspensions of  $1 \times 10^6$  cells.mL<sup>-1</sup> were prepared in a cryopreservation solution, consisting of 10% (v/v) dimethylsulfoxide (DMSO) in medium, and transferred into 1.5 mL cryovials. Then, cell suspensions were gently cooled down, first at -20 °C for at least 2 hours and then moved to -80 °C freezer for a minimum period of 12 hours. The cryovials were subsequently stored in the cryogenic tank.

## IV-5.3. Cell seeding procedures

### IV-5.3.1. Seeding of hMCs and hOBs on the indirect printed hierarchical scaffolds

In **Chapter V**, hMCs and hOBs were seeded in the indirect printed hierarchical scaffolds. Before cell seeding, all scaffolds were sterilized overnight in ethanol and washed 3x in PBS. Then, the samples were incubated in  $\alpha$ -MEM overnight. In the following day, the scaffolds were transferred to 24-well suspension cell culture plates (Cellstar, Greiner Bio-One, Austria). Confluent HMCs (at passage 4-5) were detached with TrypLE Express (1X) (Life Technologies, Carlsbad, CA, USA) and seeded in the SF8 and SF16 scaffolds at a density of  $1.5 \times 10^5$  cells/scaffold. The HObs after confluence were also detached with TrypLE Express (1X) (Life Technologies, Carlsbad, CA, USA) and seeded SF8/TCP and SF16/TCP scaffolds at a density of  $1.5 \times 10^5$  cells/scaffold. Each scaffold was kept in the CO<sub>2</sub> incubator at 37 °C for 2 hours, and then 3 mL of the respective culture medium were added to each well.

Samples were retrieved at different culture times (1, 3 and 7 days) and the culture medium was changed every 2 days.

#### IV-5.3.2. Seeding of hASCs on the SF and SF/Elastin bioprinted scaffolds

In **Chapters VII** and **VIII**, hASCs were cultured in the SF and SF/Elastin bioprinted scaffolds.

In **Chapter VI**, 3D bioprinted scaffolds in the form of a cylinder with 4 mm of diameter and 2 mm of height were used. The samples were immersed in ethanol 70% (6 hours) for sterilization. Before cell seeding, all samples were washed 3x in PBS and then left in  $\alpha$ -MEM overnight. The scaffolds were transferred to 48-well suspension cell culture plates (Cellstar, Greiner Bio-One, Austria). Confluent hASCs (at passage 3) were detached with TrypLE Express (1X) (Life Technologies, Carlsbad, CA, USA) and seeded at a density of  $8 \times 10^4$  cells/scaffold. The 48-well suspension cell culture plates were kept in the CO<sub>2</sub> incubator at 37 °C for 2 hours, and then 1 mL of  $\alpha$ -MEM culture medium were added to each well. Culture medium was changed every 2 days and samples were removed at different culture times (1, 3, and 7 days).

In **Chapter VIII**, 3D SF/elastin scaffolds in the form of a cube were used. Before cell seeding, all samples were removed from ethanol and washed 3x in PBS. Then, the samples were incubated in DMEM:F12 overnight. In the following day, the scaffolds were transferred to 24-well suspension cell culture plates (Cellstar, Greiner Bio-One, Austria). Confluent hASCs (at passage 2) were detached with TrypLE Express (1X) (Life Technologies, Carlsbad, CA, USA) and seeded at a density of  $2 \times 10^6$  cells/scaffold to develop the SF/elastin constructs. Each scaffold was kept in the CO<sub>2</sub> incubator at 37 °C for 2 hours, and then 2 mL of DMEM:F12 culture medium were added to each well. SF/elastin constructs were retrieved at different culture times (0, 1, 7, 14 and 21 days) and the culture medium was changed every 2 days.

#### IV-5.3.3. Encapsulation of PMCs on the GG and GG/FB4 bioprinted constructs

In **Chapter IX**, PMCs were used to evaluate the *in vitro* biological performance of the developed bioinks. In this section, only the GG and GG/FB4 bioinks were used.

3D printed cell-laden constructs were produced. Using the previous developed bioink formulations (GG and GG/FB4), cube shape constructs were printed using the 3D ITOP system. Confluent PMCs (Passage 4-5) were detached with trypsin and encapsulated in the bioinks at a density of  $1.5 \times 10^7$

cells/mL. The constructs were posteriorly cross-linked with a PBS/thrombin solution for 30 minutes at RT. Then, fresh  $\alpha$ -MEM was added. The medium was changed every 2-3 days. The samples were removed at different time points. The timepoints 1, 3, 7, and 14 days were used for live/dead and viability tests and the time points 14 and 28 days were used for total collagen quantification, glycosaminoglycans (GAGs) quantification, and histology analysis.

#### **IV-5.3.4. Surface seeding of PMCs on the Sil-MA 3D constructs**

As mentioned before, PMCs were used in **Chapter IX** to evaluate the biological performance of the developed bioinks. In a 48 well plate, 200  $\mu$ L of each formulation was added to each well and posteriorly UV cross-linked for 120 sec at an intensity of 400 mw/cm<sup>2</sup>. Confluent PMCs (Passage 4 -5) were detached with trypsin and seeded at a density of  $2.5 \times 10^4$  cells per well. Culture medium was changed every 2-3 days and samples were removed at different culture times (1, 3, and 7 days) to perform live/dead and viability tests.

#### **IV-5.4. Metabolic activity and cell viability examination**

##### **IV-5.4.1. Alamar blue assay**

Alamar blue assay evaluates the metabolic activity of cells. Alamar blue is a cell viability reagent which contains a cell permeable, non-toxic and weakly fluorescent blue indicator dye called resazurin. When cells are metabolically active they maintain a reducing environment capable to reduce resazurin to resorufin. Resorufin is a compound that is red in color and highly fluorescent. Viable cells are continuously reducing resazurin in resorufin, increasing the overall fluorescence and color of the media surrounding the cells [75].

In **Chapters V, VII** and **VIII** an Alamar blue working solution containing 10% (v/v) AlamarBlue® (BioRad, Hercules, CA, USA) solution and 90% culture medium was prepared and protected from light. The working solution was added to the different culture wells and incubated for 4 hours at 37 °C in an atmosphere of 5% CO<sub>2</sub>. Then, 100  $\mu$ L of solution from each well were transferred to white opaque 96-well plates, in triplicates. Fluorescence was monitored at Ex/Em  $\approx$  530/590 nm, using a microplate reader (Synergy HT, BioTek Instruments, USA). PBS was used to wash the AB reagent and fresh medium was added. The metabolic activity values were calculated by normalization with the mean

fluorescence value obtained for the controls (scaffolds without cells).

In **Chapter IX**, following the manufacturer's instructions, after each time point, a solution of 10% (v/v) AlamarBlue® (DAL1100; Life Technologies, Carlsbad, CA, USA) prepared in  $\alpha$ -MEM medium, was transferred to the culture plates in 500  $\mu$ L/scaffold. In the encapsulation assay, the 3D printed cell-laden constructs were transferred to a new culture plate before the addition of the reagent. After 3 hours of reaction with cells at 37 °C in the CO<sub>2</sub> incubator, 100  $\mu$ L of Alamar blue solution was taken from each well and placed in a 96-well white opaque plate in triplicate. The absorbance was measured in a microplate reader (SpectraMax M5, Molecular Devices, USA) at 2 different wavelengths (570 nm and at 600 nm). PBS was used to wash the AB reagent and fresh medium was added. The calculations were made according with the manufacturer's instructions.

#### IV-5.4.2. Live/Dead staining assay

Calcein-AM/Propidium iodide (PI) staining is a qualitative method that allows the visualization of live and dead cells. This method firstly consists in the incubation of cells with calcein acetoxymethyl (Calcein AM). This reagent is a non-fluorescent and cell-permeant derivative of calcein that is transported through the cellular membrane. In live cells the nonfluorescent calcein AM is converted to a green-fluorescent calcein after acetoxymethyl ester hydrolysis by intracellular esterases. When the intracellular esterases of living cells remove the acetomethoxy group, this probe became green fluorescent. Regarding the dead cells, intracellular esterases are inactive and the acetoxymethyl ester stays intact. To observe the dead cells, PI is usually used. PI is a popular red-fluorescent nuclear and chromosome counterstain and is not permeant to live cells. PI binds to DNA after disruption of the dead cells membrane.

In **Chapters V, VII** and **VIII** the cell viability was assessed by staining the cells with calcein-AM (1  $\mu$ g.mL<sup>-1</sup>) and propidium iodide (PI; 2  $\mu$ g.mL<sup>-1</sup>). Briefly, cell seeded scaffolds were immersed in a calcein AM/propidium iodide (PI) solution at 1:3 ratio in culture medium for 10-40 minutes. The scaffolds were transferred for an incubator at 37 °C in an atmosphere of 5% CO<sub>2</sub>, protected from light. Viable cells metabolize calcein AM (Invitrogen, USA 1 mg.mL<sup>-1</sup>) into green fluorescent calcein (Ex/Em  $\approx$  495/515 nm), while dead cells find their DNA stained red by PI (Invitrogen, USA 1 mg.mL<sup>-1</sup>; Ex/Em  $\approx$  493/636 nm). After a washing step with PBS, samples were imaged using a Transmitted and Reflected Light Microscope (Zeiss Axio Imager.Z1m, Zeiss, Germany).

In **Chapter IX**, cell viability of the PMCs was confirmed by performing a calcein-AM (Life Technologies, Carlsbad, CA, USA) and propidium 269 iodide (PI; Life Technologies, Carlsbad, CA, USA) staining. At the end of each time-point, two samples of each formulation were incubated in  $1 \mu\text{g}\cdot\text{mL}^{-1}$  calcein-AM and  $5 \mu\text{g}\cdot\text{mL}^{-1}$  PI prepared in PBS, for 30 minutes at  $37^\circ\text{C}$  in the  $\text{CO}_2$  incubator. After washing in PBS, samples were immediately examined under fluorescence microscopy (Calcein-AM in green: Ex/Em  $\approx 495/515$  nm; PI in red: Ex/Em  $\approx 495/635$  nm) in a reflected light Leica TCS LSI macro confocal (Leica Microsystems Inc., Germany).

## IV-5.5. Biochemical characterization

### IV-5.5.1. DNA quantification

In **Chapters V, VII and VIII** proliferation of seeded cells was analyzed by the total double stranded DNA (dsDNA) content using a fluorimetric dsDNA quantification kit (PicoGreen, Molecular Probes, Invitrogen Corporation, USA). The PicoGreen® fluorescent marker specifically binds to the double-stranded DNA of the cells emitting fluorescence. The fluorescence is read at 480 nm (excitation) and 520 nm (emission). DNA content was further determined through a DNA standard curve, prepared using standard dsDNA solutions with concentrations ranging from 0 to  $2 \mu\text{g}\cdot\text{mL}^{-1}$ .

The seeded constructs were removed from the culture medium at the end of each time-point, washed with PBS solution, and transferred into 1.5 mL centrifuge tubes containing 1 mL of ultrapure water. The samples were placed for 1 hour at  $37^\circ\text{C}$  in the  $\text{CO}_2$  incubator, and stored at  $-80^\circ\text{C}$  until further analysis.

The quantity of double stranded DNA (dsDNA), directly proportional to cell number, was determined using a fluorimetric dsDNA quantification kit (PicoGreen, Molecular Probes, Invitrogen Corporation, USA), according to the manufacturer's instructions. After each time point, the constructs were washed twice with PBS solution and kept in 1 mL of ultrapure water at  $-80^\circ\text{C}$ , until further analysis. Constructs were thawed at RT, sonicated for 1 hour to induce complete membrane lysis, and centrifuged at 300g for 5 minutes to spin down all non-genomic materials. After centrifugation, the scaffold was discarded and the supernatant collected to new 1.5 mL sterile Eppendorf tubes. Supernatant fluorescence was measured at an excitation wavelength ( $\lambda$ ) of 485/20 nm and at an emission  $\lambda$  of 528/20 nm, in a microplate reader (Synergy HT, BioTek Instruments). The quantification of dsDNA was calculated according to a standard curve prepared with concentrations ranging between 0 and  $2 \mu\text{g}\cdot\text{mL}^{-1}$ , relating



quantity of DNA and fluorescence intensity. Scaffolds without cells were used as controls.

#### IV-5.5.2. Glycosaminoglycans (GAGs) and total collagen quantification

The glycosaminoglycans (GAGs) matrix production and collagen production was evaluated in **Chapter IX**.

A dimethyl methylene blue (DMB) based-kit (Blyscan, Biocolor Ltd, UK) was used for sulfated glycosaminoglycans (GAGs) quantification, according to the manufacturer's instructions. After each time point, the constructs were washed with PBS solution and frozen at -80 °C until further analysis. Samples were digested overnight at 65 °C in 1 mL papain digestion solution, prepared by adding to each 50 mL of digestion buffer, 25 mg of papain and 48 mg of n-acetyl cysteine. Digestion buffer was composed of 200 mM of phosphate buffer (sodium phosphate monobasic) containing 1 mM ethylenediaminetetraacetic acid (EDTA) (pH 6.8). Then, samples were centrifuged at 10,000 rpm for 10 minutes and the supernatants collected. Furthermore, the GAGs content was determined according to the manufacturer's instructions by adding the DMB dye. The absorbance was measured in a microplate reader with a wavelength of 656 nm. A chondroitin sulphate stock solution was used to make a standard curve with concentrations ranging from 0 to 5  $\mu\text{g}\cdot\text{mL}^{-1}$ . All the results were normalized against the day 1 obtained values.

The amount of collagen was determined using a total collagen assay kit (Biovision, USA). The assay is based on the acid hydrolysis of samples to form hydrolysates and hydroxyproline. The oxidation of the hydroxyproline leads to the production of an intermediate that forms a chromophore (Abs 560 nm). After each time point, the constructs were washed with PBS solution and frozen at -80 °C until further analysis. Following the manufacturer's instructions, the samples were hydrolyzed at 75 °C overnight using an HCl solution ( $\approx 12$  M). Then, the samples were vortexed and centrifuged at 10,000 rpm for 3 minutes and 25  $\mu\text{L}$  of each hydrolyzed sample were transferred in triplicate to 96-well plate. The plate was posteriorly placed in an oven in order to evaporate. A standard curve was obtained by using the same procedure with a Collagen type I Standard. After drying, 100  $\mu\text{L}$  of the Chloramine T reagent was added to each well and incubate at RT for 5 minutes. Then, 100  $\mu\text{L}$  of the DMAB reagent was added to each well and incubate for 90 minutes at 60 °C. The absorbance was measured in a microplate reader with a wavelength of 560 nm. All the results were normalized against day 1 obtained values.

## IV-5.6. Histological procedures

In **Chapter IX**, histological analysis was performed on *in vitro* samples. All samples were first fixed in 10% (v/v) formalin, dehydrated in a graded series of ethanol baths and xylene, and embedding in paraffin. Sections of 7.5  $\mu\text{m}$  thick were prepared using the microtome. After sectioning, the specimens were transferred to glass slides and stored until further analysis. Paraffin-embedded sections were deparaffinized in xylene, rehydrated and stained following the protocols described below. As last step, sections were washed in distilled water, dehydrated and mounted. Slides were observed under transmitted microscopy, using the transmitted and reflected light microscope.

### IV-5.6.1. Hematoxylin & eosin staining

Hematoxylin and eosin (H&E) is one of the most used staining used in histology. This staining allows visualizing different cell components. Hematoxylin is a base that preferentially stains the acidic components of cells in blue, including some proteins, nuclei, DNA and RNA, or the endoplasmic reticulum. Eosin, as an acid, dyes the basic components of cells with a pink color, such as, the cytoplasm or collagen fibrils. In **Chapter IX**, representative sections of the cell-laden GG and GG/FB4 were automatically processed for H&E staining following the standard protocol.

### IV-5.6.2. Safranin O staining

Safranin O is used to visualize the glycosaminoglycans (GAGs) and cartilage components present on tissue engineered constructs. This is a cationic dye that in dehydrated cartilage sections gets its orthochromatic form resulting in a link of the dye to GAGs present in the tissues. The cartilage will be stained orange to red, and the nuclei will be stained black. The background is stained bluish green. In **Chapter IX**, Safranin-O (0.1% (v/v); Honeywell Fluka, Morris Plains, NJ, USA) was used to stain representative sections of the cell-laden GG and GG/FB4 constructs. Sections were counterstained with Gill-2 hematoxylin (Thermo Scientific, Waltham, MA, USA; dilution 1:2 in distilled water) and Fast green (0.02% (v/v); Honeywell Fluka, Morris Plains, NJ, USA), to simultaneously distinguish the nuclei of cells and the non-collagenous proteins of the ECM.

### IV-5.6.3. Alcian blue/Sirius red staining

Alcian Blue is a polyvalent basic dye, used to stain acidic polysaccharides such as GAGs in cartilage tissue or cartilage matrix producing samples. A Sirius red dye was also used to stain the collagen content.

In **Chapter IX**, representative sections of cell-laden GG and GG/FB4 constructs were stained with Alcian Blue 8GX (1% (v/v) in 0.5 mol.L<sup>-1</sup> acetic acid glacial; VWR BDH Prolabo, Briare, France) and picosirius red staining solution (0.1 g sirius red (also called direct red) in 100 mL saturated picric acid), following standard protocol.

### IV-5.6.4. Picosirius red staining

A picosirius red staining was also performed to visualize the collagen I and III fibers.

In **Chapter IX**, a Picro-Sirius Red Stain Kit was used to stain representative sections of cell-laden GG and GG/FB4 constructs using the standard protocol. This staining may be viewed using standard light microscopy. However, picosirius red staining has also been used with polarized light to better differentiate the collagen fibers from the background.

## IV-6. *IN VIVO* STUDIES

In **Chapter V**, Animal manipulation for *in vivo* studies was performed only by qualified personnel and following the Principle of the 3Rs. The host institution is authorized by the DGVA (Direção Geral de Alimentação e Veterinária) to perform animal experimentation. All animal protocols were conducted in accordance with the Portuguese legislation (Portaria no1005/92) and international standards on animal welfare as defined by the EC Directive 2010/63/EU. In **Chapter IX**, animal manipulation was also performed. This animal study was performed at the Wake Forest Institute for Regenerative Medicine and conducted in accordance with Wake Forest University Animal Care and Use Committee (ACUC) regulations.

### IV-6.1. Subcutaneous implantation

In **Chapter V**, scaffolds were tested for the *in vivo* biological performance by subcutaneous implantation in Hsd:ICR (CD-1) mice. Six mice Hsd:ICR (CD-1) of 5-weeks old and average weight of 25-30g (Charles River Laboratories, Massachusetts, USA) were used in this study. Each mouse was anesthetized by intraperitoneal injection of: ketamine (25 mg.Kg<sup>-1</sup>) and medetomidine (0.15 mg.Kg<sup>-1</sup>) for anesthesia; cephalexin (15 mg.Kg<sup>-1</sup>) as antibiotic; and bupivacaine, pethidine (5-10 mg.Kg<sup>-1</sup>) as analgesic. The mice hair was shaved at the implantation area, followed by disinfection with 70% ethanol and iodine. In each mouse, four skin incisions (1 cm length) were made in the dorsal midline, one close from the head (CH) and the other far from the head (FH). In the following, one specimen of each formulation (SF8, SF16, SF8/TCP and SF16/TCP) was implanted subcutaneously into the respective pocket and then the skin was sutured. Four specimens of both formulations were implanted. The scheme of animals and sample distribution can be seen in **Figure IV-16**. Eight weeks post-surgery, the mice were euthanized by injection of overdose pentobarbital sodium followed by harvesting of the implanted materials.

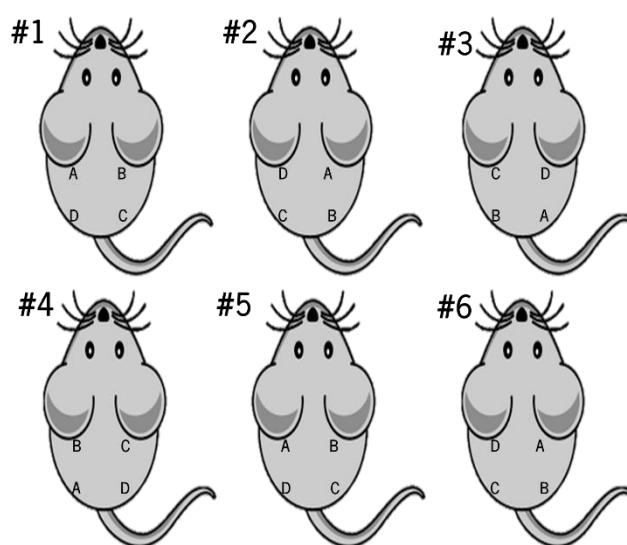


**Figure IV-16** - Animal and sample distribution for *in vivo* animal assay.

In **Chapter IX**, the produced constructs were implanted in dorsal subcutaneous pockets in athymic nude mice. All animal studies were conducted in accordance with Wake Forest University Animal Care and Use Committee (ACUC) regulations. General anesthesia was induced using an anesthesia machine that mixed isoflurane with oxygen. Isoflurane was used with a dose between 0-5% (up to 5% induction, 1-3% maintenance). Before the surgery, Ketoprofen (for analgesic purposes, 3-5 mg.kg<sup>-1</sup>) were

administered subcutaneously. After shaving the surgical site on the left limb, local anesthesia (Bupivacaine, diluted to 0.25%, 2.5 mg.kg<sup>-1</sup>) was also administered. The shaved area was then cleaned by scrubbing three pairs of alternating applications of chlorhexidine followed by 70% isopropyl alcohol in circular motions. Under general anesthesia, the dorsal surface was cleaned and sterilized with betadine and wiped with 70% alcohol. All surgical procedures were performed aseptically. A dorsal or paramedian longitudinal incision of approximately 2 cm long was made and two subcutaneous pockets (left and right sides) were created. Two bioprinted constructs were placed in the subcutaneous space and the wound was closed in a routine fashion way using a single layer interrupted non-absorbable sutures or staples. Sutures were removed within 14 days of placement. In this study, four groups (Sil-MA (H), GG/FB4 with and without cells and hybrid constructs) were tested and a total of 10 constructs from each group were used for implantation (**Figure IV-17**). The implanted constructs were harvested after 2 weeks, 5 weeks and 10 weeks.

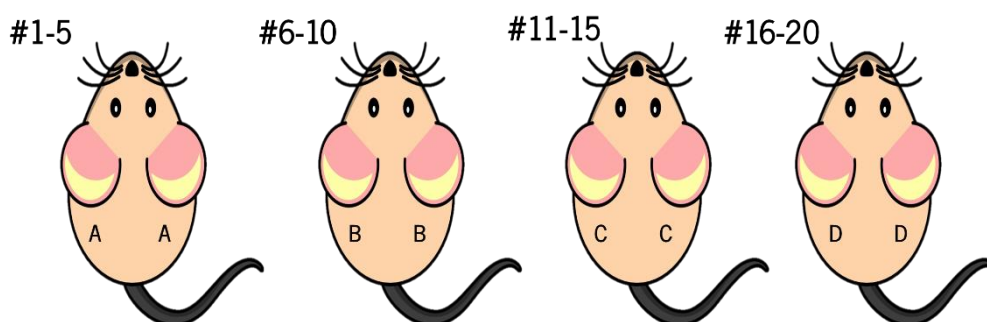


Figure IV-17 - Animal and sample distribution for *in vivo* animal assay.

## IV-6.2. Explants characterization

### IV-6.2.1. Histological examination

In **Chapters V** and **IX**, histological analysis was performed to the explants after subcutaneous implantation. Explants were collected and processed for histological analysis following the standard procedures. The collected explants were sectioned with 20  $\mu\text{m}$  (**Chapter V**) and 7.5  $\mu\text{m}$  (**Chapter IX**) thick in a microtome.

In **Chapter V**, representative samples were stained with H&E (sub-section IV-5.6.1. of this chapter) and Masson's trichrome. Masson's trichrome staining was performed using a Bio-Optica staining kit (Milan, Italy) following the manufacturer's instructions. The kit comprises four different dyes, including weigert's iron hematoxylin for nuclei, picric acid for erythrocytes, a mixture of acid dyes for cytoplasm and aniline blue for connective tissue. This staining usually results in the coloring of the cell's nuclei with, cytoplasm with red, collagen with blue and erythrocytes with yellow.

In **Chapter IX**, representative samples were stained with H&E, Safranin O, Masson's trichrome, Alcian Blue/Sirius red and Picrosirius red. The staining was performed following the protocols above mentioned and described in the sub-section IV-5.6. of this chapter.

#### IV-6.2.2. Dimensional changes

In **Chapter IX**, the dimensional changes of the constructs were assessed after subcutaneous implantation. The volume of the constructs was measure using a displacement method (**Figure IV-18**).

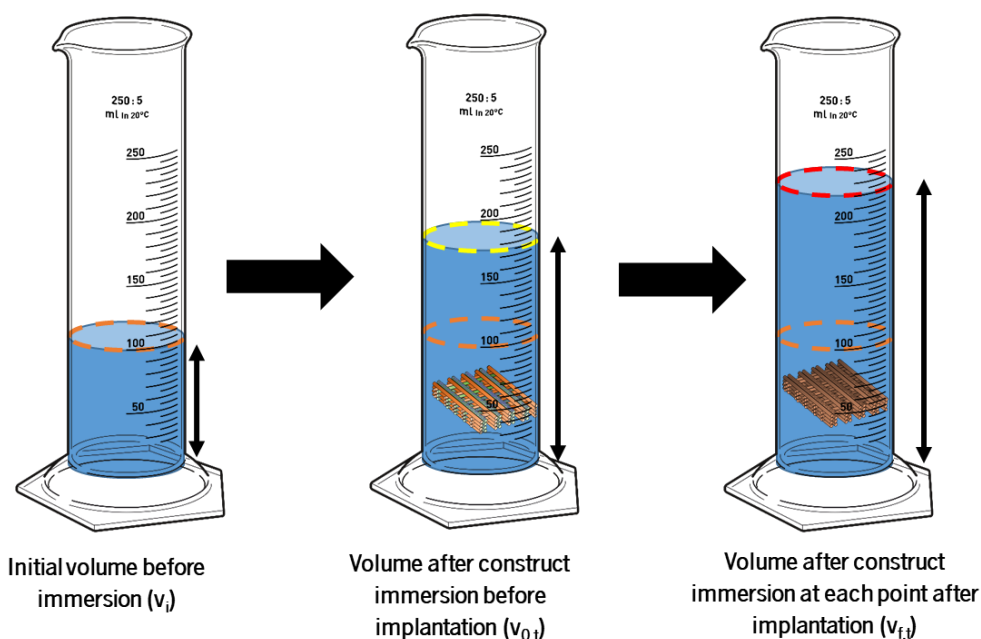


Figure IV-18 - Scheme describing how to determine the volume of the samples after subcutaneous implantation.

The calculation of the percentage by volume was obtained using the following equation:

Equation IV-4 - Determination of the volume by the displacement method.

$$\text{Volume percentage} = \frac{v_{f,t} - v_i}{v_{0,t} - v_i} \times 100$$

where,  $v_{0,t}$  is the initial volume of the sample before implantation,  $v_{f,t}$  is the volume of the sample at each time point and  $v_i$  is the initial volume before immersion of the construct. A minimum number of three samples were tested.

#### IV-6.2.3. Mechanical properties

In Chapter IX, the mechanical performance of the constructs was assessed after subcutaneous implantation. The assay was performed according with the protocol described in the sub-section IV-4.1.3.2.

#### IV-6.2.4. Alcian Blue/Sirius Red polarized image analysis with MatLab, CT-FIRE, and CurveAlign

In Chapter IX, the captured Alcian Blue/Sirius red polarized images were analyzed with CurveAlign program (Laboratory for Optical and Computational Instrumentation, University of Wisconsin-Madison) and the output data were analyzed and graphed using MATLAB. Each collagen fiber was overlaid and converted into a direction heat map to quantify the alignment coefficient; with zero being no alignment and one being complete alignment. About 300 fibers per image were analyzed (3 images per sample; 3 samples per group). The alignment coefficient and collagen fiber color were both quantified using a custom MatLab code. The color threshold for the image was used to isolate the four main colors (red, yellow, orange, and green) seen in picosirius red stained samples under polarized light. The relative percentage of each color was quantified by dividing the pixel count of each color by the total pixel count in each image.

### IV-7. STATISTICAL ANALYSIS

Statistical analysis was performed using a GraphPad Prism 5.0 software (GraphPad Software, La Jolla, CA, USA) where statistical significance was set to \* ( $p < 0.05$ ), \*\* ( $p < 0.01$ ), \*\*\* ( $p < 0.001$ ).

In **Chapters V, VII, VIII** and **IX**, the numerical results are presented as mean  $\pm$  standard deviation. First, a Shapiro-Wilk normality test was performed to assess data normality. Data that followed a normal distribution was analyzed using a one-way analysis of variance followed by Turkey multiple comparison test when more than two groups were compared. Data that did not follow a normal distribution was analyzed using the Kruskal-Wallis test followed by Dunn's multiple comparison test when more than two groups were compared.

#### IV-8. REFERENCES

- [1] Sutherland TD, Young JH, Weisman S, Hayashi CY, Merritt DJ. Insect silk: one name, many materials. *Annual review of entomology* 2010;55:171-88.
- [2] Jin HJ, Kaplan DL. Mechanism of silk processing in insects and spiders. *Nature* 2003;424:1057-61.
- [3] Numata K, Kaplan DL. Silk-based delivery systems of bioactive molecules. *Adv Drug Deliv Rev* 2010;62:1497-508.
- [4] Omenetto FG, Kaplan DL. New opportunities for an ancient material. *Science (New York, NY)* 2010;329:528-31.
- [5] Vepari C, Kaplan DL. Silk as a Biomaterial. *Progress in polymer science* 2007;32:991-1007.
- [6] Altman GH, Diaz F, Jakuba C, Calabro T, Horan RL, Chen J, *et al.* Silk-based biomaterials. *Biomaterials* 2003;24:401-16.
- [7] Zhou CZ, Confalonieri F, Medina N, Zivanovic Y, Esnault C, Yang T, *et al.* Fine organization of *Bombyx mori* fibroin heavy chain gene. *Nucleic acids research* 2000;28:2413-9.
- [8] Inoue S, Tanaka K, Arisaka F, Kimura S, Ohtomo K, Mizuno S. Silk fibroin of *Bombyx mori* is secreted, assembling a high molecular mass elementary unit consisting of H-chain, L-chain, and P25, with a 6:6:1 molar ratio. *The Journal of biological chemistry* 2000;275:40517-28.
- [9] Wray LS, Hu X, Gallego J, Georgakoudi I, Omenetto FG, Schmidt D, *et al.* Effect of processing on silk-based biomaterials: reproducibility and biocompatibility. *Journal of biomedical materials research Part B, Applied biomaterials* 2011;99:89-101.
- [10] Lamboni L, Gauthier M, Yang G, Wang Q. Silk sericin: A versatile material for tissue engineering and drug delivery. *Biotechnology Advances* 2015;33:1855-67.
- [11] Thilagavathi G, Viju S. 11 - Silk as a suture material. In: Basu A, editor. *Advances in Silk Science and Technology*; Woodhead Publishing; 2015. p. 219-32.
- [12] Kasoju N, Bora U. Silk fibroin in tissue engineering. *Advanced healthcare materials* 2012;1:393-412.



- [13] Yucel T, Lovett ML, Kaplan DL. Silk-based biomaterials for sustained drug delivery. *Journal of controlled release : official journal of the Controlled Release Society* 2014;190:381-97.
- [14] Nazarov R, Jin H-J, Kaplan DL. Porous 3-D scaffolds from regenerated silk fibroin. *Biomacromolecules* 2004;5:718-26.
- [15] Silva SS, Popa EG, Gomes ME, Oliveira MB, Nayak S, Subia B, *et al.* Silk hydrogels from non-mulberry and mulberry silkworm cocoons processed with ionic liquids. *Acta Biomater* 2013;9:8972-82.
- [16] Li M, Tao W, Lu S, Kuga S. Compliant film of regenerated *Antheraea pernyi* silk fibroin by chemical crosslinking. *International Journal of Biological Macromolecules* 2003;32:159-63.
- [17] Chen X, Shao Z, Knight DP, Vollrath F. Conformation transition kinetics of *Bombyx mori* silk protein. *Proteins: Structure, Function, and Bioinformatics* 2007;68:223-31.
- [18] Yan L-P, Oliveira JM, Oliveira AL, Caridade SG, Mano JF, Reis RL. Macro/microporous silk fibroin scaffolds with potential for articular cartilage and meniscus tissue engineering applications. *Acta biomaterialia* 2012;8:289-301.
- [19] Yan LP, Oliveira JM, Oliveira AL, Reis RL. Core - shell silk hydrogels with spatially tuned conformations as drug - delivery system. *Journal of tissue engineering and regenerative medicine* 2016.
- [20] Wang X, Kluge JA, Leisk GG, Kaplan DL. Sonication-induced gelation of silk fibroin for cell encapsulation. *Biomaterials* 2008;29:1054-64.
- [21] Yucel T, Cebe P, Kaplan DL. Vortex-induced injectable silk fibroin hydrogels. *Biophysical journal* 2009;97:2044-50.
- [22] Harkin DG, George KA, Madden PW, Schwab IR, Hutmacher DW, Chirila TV. Silk fibroin in ocular tissue reconstruction. *Biomaterials* 2011;32:2445-58.
- [23] Kim SH, Yeon YK, Lee JM, Chao JR, Lee YJ, Seo YB, *et al.* Precisely printable and biocompatible silk fibroin bioink for digital light processing 3D printing. *Nature Communications* 2018;9:1620.
- [24] Omenetto FG, Kaplan DL. New opportunities for an ancient material. *Science* 2010;329:528-31.
- [25] Dorozhkin SV, Epple M. Biological and medical significance of calcium phosphates. *Angewandte Chemie (International ed in English)* 2002;41:3130-46.
- [26] Dorozhkin SV. Calcium orthophosphates in nature, biology and medicine. *Materials* 2009;2:399-498.
- [27] Farokhi M, Mottaghitalab F, Samani S, Shokrgozar MA, Kundu SC, Reis RL, *et al.* Silk fibroin/hydroxyapatite composites for bone tissue engineering. *Biotechnology advances* 2017.
- [28] Samavedi S, Whittington AR, Goldstein AS. Calcium phosphate ceramics in bone tissue engineering: A review of properties and their influence on cell behavior. *Acta Biomaterialia* 2013;9:8037-45.

- [29] Takahashi Y, Yamamoto M, Tabata Y. Osteogenic differentiation of mesenchymal stem cells in biodegradable sponges composed of gelatin and  $\beta$ -tricalcium phosphate. *Biomaterials* 2005;26:3587-96.
- [30] Ginebra M-P, Traykova T, Planell J. Calcium phosphate cements as bone drug delivery systems: a review. *Journal of Controlled Release* 2006;113:102-10.
- [31] Bohner M, Lemaître J. Can bioactivity be tested *in vitro* with SBF solution? *Biomaterials* 2009;30:2175-9.
- [32] Gao P, Zhang H, Liu Y, Fan B, Li X, Xiao X, *et al.* Beta-tricalcium phosphate granules improve osteogenesis *in vitro* and establish innovative osteo-regenerators for bone tissue engineering *in vivo*. *Scientific Reports* 2016;6:23367.
- [33] Hu J, Hou Y, Park H, Lee M. Beta-tricalcium phosphate particles as a controlled release carrier of osteogenic proteins for bone tissue engineering. *Journal of biomedical materials research Part A* 2012;100:1680-6.
- [34] Pina S, Vieira S, Goetz - Neunhoffer F, Neubauer J, Da Cruz e Silva O, Da Cruz e Silva E, *et al.* *In vitro* performance assessment of new brushite - forming Zn - and ZnSr - substituted  $\beta$  - TCP bone cements. *Journal of Biomedical Materials Research Part B: Applied Biomaterials* 2010;94:414-20.
- [35] Pina S, Ferreira JM. Brushite-forming Mg-, Zn-and Sr-substituted bone cements for clinical applications. *Materials* 2010;3:519-35.
- [36] Padzi MM, Bazin MM, Muhamad WMW. Fatigue Characteristics of 3D Printed Acrylonitrile Butadiene Styrene (ABS). *IOP Conference Series: Materials Science and Engineering* 2017;269:012060.
- [37] Zhang H, Cai L, Golub M, Zhang Y, Yang X, Schlarman K, *et al.* Tensile, Creep, and Fatigue Behaviors of 3D-Printed Acrylonitrile Butadiene Styrene. *Journal of Materials Engineering and Performance* 2018;27:57-62.
- [38] Faury G. Function-structure relationship of elastic arteries in evolution: from microfibrils to elastin and elastic fibres. *Pathologie-biologie* 2001;49:310-25.
- [39] Yeo GC, Mithieux SM, Weiss AS. The elastin matrix in tissue engineering and regeneration. *Current Opinion in Biomedical Engineering* 2018;6:27-32.
- [40] Daamen WF, Veerkamp JH, van Hest JCM, van Kuppevelt TH. Elastin as a biomaterial for tissue engineering. *Biomaterials* 2007;28:4378-98.
- [41] Buckwalter JA, Cooper RR, Maynard JA. Elastic fibers in human intervertebral discs. *The Journal of bone and joint surgery American volume* 1976;58:73-6.
- [42] Mikawa Y, Hamagami H, Shikata J, Yamamuro T. Elastin in the human intervertebral disk. A histological and biochemical study comparing it with elastin in the human yellow ligament. *Archives of orthopaedic and traumatic surgery Archiv fur orthopadische und Unfall-Chirurgie* 1986;105:343-9.

- [43] Cloyd JM, Elliott DM. Elastin content correlates with human disc degeneration in the annulus fibrosus and nucleus pulposus. *Spine* 2007;32:1826-31.
- [44] Sworn G. 9 - Gellan gum. In: Phillips GO, Williams PA, editors. *Handbook of Hydrocolloids (Second Edition)*: Woodhead Publishing; 2009. p. 204-27.
- [45] Jansson P-E, Lindberg B, Sandford PA. Structural studies of gellan gum, an extracellular polysaccharide elaborated by *Pseudomonas elodea*. *Carbohydrate Research* 1983;124:135-9.
- [46] Oliveira JT, Martins L, Picciochi R, Malafaya PB, Sousa RA, Neves NM, *et al.* Gellan gum: A new biomaterial for cartilage tissue engineering applications. *Journal of Biomedical Materials Research Part A* 2010;93A:852-63.
- [47] Miyoshi E, Takaya T, Nishinari K. Rheological and thermal studies of gel-sol transition in gellan gum aqueous solutions. *Carbohydrate Polymers* 1996;30:109-19.
- [48] Stevens LR, Gilmore KJ, Wallace GG, in het Panhuis M. Tissue engineering with gellan gum. *Biomaterials science* 2016;4:1276-90.
- [49] Mouser VH, Melchels FP, Visser J, Dhert WJ, Gawlitta D, Malda J. Yield stress determines bioprintability of hydrogels based on gelatin-methacryloyl and gellan gum for cartilage bioprinting. *Biofabrication* 2016;8:035003.
- [50] Mosesson MW, Siebenlist KR, Meh DA. The structure and biological features of fibrinogen and fibrin. *Annals of the New York Academy of Sciences* 2001;936:11-30.
- [51] Ahmed TAE, Dare EV, Hincke M. Fibrin: A Versatile Scaffold for Tissue Engineering Applications. *Tissue Engineering Part B: Reviews* 2008;14:199-215.
- [52] Tajdaran K, Shoichet MS, Gordon T, Borschel GH. A novel polymeric drug delivery system for localized and sustained release of tacrolimus (FK506). *Biotechnology and bioengineering* 2015;112:1948-53.
- [53] Park CH, Oh JH, Jung HM, Choi Y, Rahman SU, Kim S, *et al.* Effects of the incorporation of epsilon-aminocaproic acid/chitosan particles to fibrin on cementoblast differentiation and cementum regeneration. *Acta Biomater* 2017;61:134-43.
- [54] Kang H-W, Lee SJ, Ko IK, Kengla C, Yoo JJ, Atala A. A 3D bioprinting system to produce human-scale tissue constructs with structural integrity. *Nature Biotechnology* 2016;34:312.
- [55] Santoro E, Agresta F, Buscaglia F, Mulieri G, Mazzarolo G, Bedin N, *et al.* Preliminary experience using fibrin glue for mesh fixation in 250 patients undergoing minilaparoscopic transabdominal preperitoneal hernia repair. *Journal of laparoendoscopic & advanced surgical techniques Part A* 2007;17:12-5.
- [56] Park CH, Woo KM. Fibrin-Based Biomaterial Applications in Tissue Engineering and Regenerative Medicine. In: Noh I, editor. *Biomimetic Medical Materials: From Nanotechnology to 3D Bioprinting*. Singapore: Springer Singapore; 2018. p. 253-61.

- [57] Moroni L, Boland T, Burdick JA, De Maria C, Derby B, Forgacs G, *et al.* Biofabrication: A Guide to Technology and Terminology. Trends in biotechnology 2018;36:384-402.
- [58] Zhu J, Marchant RE. Design properties of hydrogel tissue-engineering scaffolds. Expert review of medical devices 2011;8:607-26.
- [59] De Maria C, De Acutis A, Vozzi G. Chapter 8 - Indirect Rapid Prototyping for Tissue Engineering. In: Atala A, Yoo JJ, editors. Essentials of 3D Biofabrication and Translation. Boston: Academic Press; 2015. p. 153-64.
- [60] Cengiz IF, Pitikakis M, Cesario L, Parascandolo P, Vosilla L, Viano G, *et al.* Building the basis for patient-specific meniscal scaffolds: From human knee MRI to fabrication of 3D printed scaffolds. Bioprinting 2016;1-2:1-10.
- [61] Pina S, Canadas RF, Jimenez G, Peran M, Marchal JA, Reis RL, *et al.* Biofunctional Ionic-Doped Calcium Phosphates: Silk Fibroin Composites for Bone Tissue Engineering Scaffolding. Cells, tissues, organs 2017;204:150-63.
- [62] Landers R, Hübner U, Schmelzeisen R, Mülhaupt R. Rapid prototyping of scaffolds derived from thermoreversible hydrogels and tailored for applications in tissue engineering. Biomaterials 2002;23:4437-47.
- [63] Oner T, Cengiz IF, Pitikakis M, Cesario L, Parascandolo P, Vosilla L, *et al.* 3D segmentation of intervertebral discs: from concept to the fabrication of patient-specific scaffolds. Journal of 3D Printing in Medicine 2017;1:91-101.
- [64] Moroni L, Burdick JA, Highley C, Lee SJ, Morimoto Y, Takeuchi S, *et al.* Biofabrication strategies for 3D *in vitro* models and regenerative medicine. Nature Reviews Materials 2018;3:21-37.
- [65] Reichelt R. Scanning electron microscopy. Science of microscopy: Springer; 2007. p. 133-272.
- [66] Oliveira A, Malafaya P, Costa S, Sousa R, Reis R. Micro-computed tomography ( $\mu$ -CT) as a potential tool to assess the effect of dynamic coating routes on the formation of biomimetic apatite layers on 3D-plotted biodegradable polymeric scaffolds. Journal of Materials Science: Materials in Medicine 2007;18:211-23.
- [67] Theophanides T. Introduction to infrared spectroscopy. Infrared Spectroscopy-Materials Science, Engineering and Technology: InTech; 2012.
- [68] Sørensen OW. James Keeler. Understanding NMR Spectroscopy. Magnetic Resonance in Chemistry 2006;44:820-.
- [69] Barnes HA, Hutton JF, Walters K. An introduction to rheology: Elsevier; 1989.
- [70] Tas AC. Synthesis of biomimetic Ca-hydroxyapatite powders at 37 C in synthetic body fluids. Biomaterials 2000;21:1429-38.
- [71] Pina S, Canadas R, Jiménez G, Perán M, Marchal J, Reis R, *et al.* Biofunctional Ionic-Doped Calcium Phosphates: Silk Fibroin Composites for Bone Tissue Engineering Scaffolding. Cells Tissues Organs 2017;204.

- [72] Figueiredo L, Pace R, D'Arros C, Réthoré G, Guicheux J, Le Visage C, *et al.* Assessing glucose and oxygen diffusion in hydrogels for the rational design of 3D stem cell scaffolds in regenerative medicine. *Journal of tissue engineering and regenerative medicine* 2018;12:1238-46.
- [73] Carvalho PP, Wu X, Yu G, Dias IR, Gomes ME, Reis RL, *et al.* The effect of storage time on adipose-derived stem cell recovery from human lipoaspirates. *Cells Tissues Organs* 2011;194:494-500.
- [74] Cerqueira M, Pirraco RP, Santos T, Rodrigues D, Frias A, Martins A, *et al.* Human adipose stem cells cell sheet constructs impact epidermal morphogenesis in full-thickness excisional wounds. *Biomacromolecules* 2013;14:3997-4008.
- [75] O'brien J, Wilson I, Orton T, Pognan F. Investigation of the Alamar Blue (resazurin) fluorescent dye for the assessment of mammalian cell cytotoxicity. *The FEBS Journal* 2000;267:5421-6.

## **SECTION 3**

### **EXPERIMENTAL STUDIES**

## **CHAPTER V**

# **Indirect Printing of Hierarchical Patient-Specific Scaffolds for Meniscus Tissue Engineering**

Indirect Printing of Hierarchical Patient-Specific Scaffolds for Meniscus Tissue Engineering<sup>‡</sup>

## ABSTRACT

The complex meniscus tissue plays a critical role in the knee. The high susceptibility to injury has led to an intense pursuit for better tissue engineering (TE) regenerative strategies, where scaffolds play a major role. In this study, indirect printed hierarchical multilayered scaffolds composed by a silk fibroin (SF) upper layer and an 80/20 (w/w) ratio of SF/ionic-doped  $\beta$ -tricalcium phosphate (TCP) bottom layer were developed. Furthermore, a comparative analysis between two types of scaffolds produced using different SF concentrations, *i.e.* 8% (w/v) (Hi8) and 16% (w/v) (Hi16) was performed. In terms of architecture and morphology, the produced scaffolds presented homogeneous porosity in both layers and no differences were observed when comparing both scaffolds. A decrease in terms of mechanical performance of the scaffolds was observed when SF concentration decreased from 16% to 8% (w/v). Hi16 revealed a static compressive modulus of  $0.66 \pm 0.05$  MPa and dynamical mechanical properties ranging from  $2.17 \pm 0.25$  MPa to  $3.19 \pm 0.38$  MPa. By its turn, Hi8 presented a compressive modulus of  $0.27 \pm 0.08$  MPa and dynamical mechanical properties ranging from  $1.03 \pm 0.08$  MPa to  $1.56 \pm 0.13$  MPa. *In vitro* bioactivity studies showed formation of apatite crystals onto the surface of Hi8 and Hi16 bottom layers. Human meniscus cells (hMCs) and human primary osteoblasts (hOBs) were cultured separately onto the top layer (SF8 and SF16) and bottom layer (SF8/TCP and SF16/TCP) of the hierarchical scaffolds Hi8 and Hi16, respectively. Both cell types showed good adhesion and proliferation as denoted by the live/dead staining, Alamar Blue assay and DNA quantification analysis. Subcutaneous implantation in mice revealed weak inflammation and scaffold's integrity. The hierarchical indirect printed SF scaffolds can be promising candidate for meniscus TE scaffolding applications due their suitable mechanical properties, good biological performance and possibility of being applied in a patient-specific approach.

<sup>‡</sup> This chapter is based on the following publication:

Costa J. B., Silva-Correia J., da Silva Morais A., Pina S., Vieira S., Pereira H., Espregueira-Mendes J., Reis R. L. and Oliveira J. M., "Indirect printing of hierarchical patient-specific scaffolds for meniscus tissue engineering", *Bio-Design and Manufacturing* (Submitted), 2019.



## V-1. INTRODUCTION

The important role of meniscus in the knee and its high susceptibility to injury led to an intensification of the interest and awareness in this field from the scientific and medical community [1]. Current treatment options for meniscal injuries rely into three strategies: (1) non-operative, (2) meniscectomy, and (3) meniscal repair. The decision for the most suitable strategy in each case depends on several factors such as patient age, location of tear, and type and size of tear. For older patients, there are already some evidences proving that it is better to proceed with a non-operative approach rather than meniscectomy, since partial meniscectomy only showed reasonable outcomes when the peripheral meniscal rim is intact [2]. Furthermore, there has been an increasing number of meniscus repairs being performed by arthroscopically-assisted inside-out techniques (CPT codes 29882 and 29883) over the past 7 years, suggesting that this strategy has been preferentially performed over meniscectomies in case of younger patients [3]. In sum, new and more effective approaches for meniscus repair are needed as there is still space for improvements of the current used techniques. Several strategies have already been proposed, but only few of them have been shown to be effective [4]. Tissue engineering (TE) approaches have been applied in the orthopedic field, namely for meniscus regeneration showing very promising pre-clinical results and high potential for clinical applications in a near future [5]. Associated to advances in engineering of scaffolds, patient-specificity is becoming an important requisite in many TE approaches and orthopedic applications, including the treatment of meniscus lesions [6]. These can allow reducing the overall procedure costs, minimizing the surgical time, and more importantly address the need for enhancing implant anchorage for ultimately achieving a better biomechanical stability and biofunctionality [7]. By means of combining reverse engineering with a rapid prototyping technique, it is possible to print custom-made scaffolds with appropriate size and shape. In terms of biocompatibility and ability to provide an advantageous microenvironment for cells, the natural polymers are preferable as compared to synthetic polymers due to their biocompatibility. However, the natural polymers present low printability resolution, which can be a huge drawback for patient-specific approaches. Therefore, indirect printing can be a great alternative to fabricate 3D scaffolds using natural polymers. This strategy is based on the production of a negative mold followed by the casting of the desired polymer, typically using a drying method. The application of indirect printing approaches has proven to be a useful tool to tackle some direct printing limitations, offering both the opportunity to produce 3D scaffolds from biomaterials with mismatched processing properties and thermally unstable materials such as ceramics and composites [8]. Lee *et al.* [9] already

demonstrated the potential of this approach for developing complex constructs in terms of micro- and macro-scale. In that study, we fabricated porous Poly((lactic acid) -co- (glycolic acid)) (PLGA) scaffolds using a water-based negative mold. The indirect printed scaffolds showed good biological performance, by supporting cell growth in culture. In other study, Lee *et al.* [10] were able to reproduce a Polycaprolactone/chitosan (PCL/chitosan) human mandibular condyle implant using a gelatin negative mold. The negative mold was produced by 3D printing, followed by the mold casting of the PCL/chitosan blend. Furthermore, the scaffolds were coated with bioactive apatite, which conferred osteoinductive properties. The *in vitro* biological tests performed with bone marrow stromal cells showed good cell viability, with the apatite-coating further enhancing cellular spreading and proliferation. Recently, Park *et al.* [11] created an advanced indirect 3D printing technique using an alkali-soluble photopolymer sacrificial mold produced by projection-based microstereolithography. In that study, PCL scaffolds were fabricated by either solvent-based or thermal molding using the injection molding system (IMS). The scaffolds produced by IMS showed substantial reduction in scaffold fabrication time and higher mechanical properties.

Different natural polymers have been used in indirect printing strategies revealing good outcomes [12-14]. Liu *et al.* [15] combined indirect printing with freeze-drying technique to produce silk fibroin (SF) scaffolds with macro- and micro-structures. The produced scaffolds presented suitable mechanical properties for cartilage tissue engineering and appropriated cell migration, attachment and proliferation. In another study, Chen *et al.* [16] have developed SF 3D scaffolds also presenting micropores and interconnected channels using thermoplastic negative molds. The *in vitro* and *in vivo* studies (12 weeks) were performed using porcine articular chondrocytes and the results revealed extracellular matrix production and maintenance of the chondrogenic phenotype. In sum, SF has been showing to present suitable features for indirect printing approaches. Thus, we hypothesized that the above mentioned challenges of the current available treatments could probably be overcome by means of developing patient-specific hierarchical scaffolds comprising a ceramic-based bottom layer that can improve the implant anchorage.

In this work, an indirect printing approach is proposed to produce hierarchical and multilayered patient-specific meniscus implants using SF. The desired patient-specificity was achieved using a well-established reverse engineering strategy as described elsewhere [6]. The gelation methods based on the enzymatic-crosslinking reactions have also been investigated by our group which are advantageous due to the fast-setting processing, high versatility, biocompatibility and remarkable mechanical

properties [17, 18]. Therefore, an enzymatic-crosslinking step was introduced during the scaffold fabrication. To the best of our knowledge, it is the first time that indirect printing approaches combining *in situ* enzymatic-driven gelation method are applied to the development of hierarchical SF scaffolds. The introduction of this middle step, mediated by horseradish peroxidase (HRP) and hydrogen peroxide, aims not only to produce scaffolds with better mechanical properties and adequate shape for meniscus TE, but also to enable the production of hierarchical structures. In other words, taking advantage of the tuning capability provided by the enzymatic middle-step, a bottom layer composed by SF blended with calcium phosphates, namely  $\beta$ -tricalcium phosphate (TCP), incorporated with zinc (Zn) and strontium (Sr), was introduced. With the addition of this bottom layer it is envisioned to enhance the interaction of the bone-scaffold to improve its anchorage properties, which problems have been evidenced by the conventional methods [19]. Furthermore, ionic-doped  $\beta$ -TCP materials have shown osteogenesis and neovascularization ability, making them suitable for the strategy herein described [20, 21]. Gruchenberg *et al.* [22] have already showed the difficulty in implant fixation using a silk scaffold. They reported an *in vivo* trial using a sheep model and, after 6 months, the constructs were not firmly fixed in the defect, which led to the appearance of a gap between the native tissue and the construct and or its total loss. In order to produce the molds, fused deposition modeling (FDM) was used since it is the most common 3D printing method, mainly due to easy handling and cost-efficiency. The choice of the mold polymer fell in the acrylonitrile-butadiene-styrene (ABS). ABS is a cost-effective engineering polymer, easy to process and fabricate and it has good impact resistance, excellent machinability, as well as appropriate strength and stiffness [23].

Furthermore, freeze-drying was used as drying method whereas it was found to be the most suitable for indirect printing strategies. This method causes less shrinkage, resulting in a precise reproduction of the envisioned architecture [8]. The produced indirect printed hierarchical SF scaffolds was characterized in terms of physico-chemical properties and *in vitro* and *in vivo* biological performance. The scaffolds morphology and architecture were evaluated by scanning electron microscopy (SEM) and micro-computed tomography (Micro-CT), respectively, whereas the chemical structure was studied by Fourier transform infrared spectroscopy (FTIR). *In vitro* assays were also performed in order to assess the degradation, swelling, mechanical behavior and bioactivity. Biological performance of human meniscus cells (hMCs) and human primary osteoblasts (hOBs) seeded onto the SF scaffolds were also assessed up to 7 days of culture. In addition, *in vivo* assays were performed through subcutaneous implantation in mice in order to evaluate possible inflammatory response.

## V-2. MATERIALS AND METHODS

### V-2.1. Materials

Silkworm *Bombyx mori* cocoons were provided by the Portuguese Association of Parents and Friends of Mentally Disabled Citizens (APPACDM, Castelo Branco, Portugal). Acrylonitrile butadiene styrene (ABS) was purchased from Leapfrog (Netherlands). Human Primary Osteoblasts (hOBs) were purchased from Sigma-Aldrich (St. Louis, MO, USA). All reagents were purchased from Sigma-Aldrich (St. Louis, MO, USA) unless otherwise stated.

### V-2.2. Production of indirect printed hierarchical scaffolds

#### V-2.2.1. Production of ABS molds through a rapid prototyping approach

The ABS molds were designed using a commercial computer aided design (CAD) software (Autodesk Inventor Professional 2017, Autodesk) and manufactured using a Creatr Dual Extruder 3D Printer (Leapfrog, Netherlands) (**Figure V-1ai, aii**). The design selected for the mold was a cube shape with 36 mm<sup>2</sup> of base area and 5 mm of height. Properly centered, it was also designed 4 cylindrical pillars with 5 mm of height and 1 mm of diameter. The molds were used to produce all the scaffolds for further characterization. In addition, by using a human meniscus model previously developed in our group through a reverse engineering approach [6], an ABS human meniscus mold was printed in order to produce an indirect printed hierarchical patient-specific meniscus implant.

#### V-2.2.2. Preparation of SF solution

Purified SF solution was prepared by removing the glue-like protein sericin from the cocoons in a 0.02 M boiling sodium carbonate solution for 1 hour, followed by rinsing with distilled water. Then, the purified SF was dissolved in a 9.3 M lithium bromide solution for 1 hour at 70 °C and dialyzed in distilled water for 48 hours using a benzoylated dialysis tubing (MWCO: 2 kDa). The obtained SF aqueous solution was concentrated using 20% (w/v) poly(ethylene glycol) for at least 6 hours. The final concentration of SF was determined by assessing the dry weight of the solution placed overnight at 70 °C. The SF was diluted to 16% and 8% (w/v) in distilled water, and stored at 4 °C until further use.

### V-2.2.3. Preparation of ionic-doped $\beta$ -tricalcium phosphate powders

$\beta$ -tricalcium phosphate (TCP) powders doped with 10 mol% of Sr and Zn (were prepared as described elsewhere [21]). Briefly, the powders were synthesized by aqueous precipitation using adequate starting chemical precursors for calcium, phosphorous, Sr, and Zn, with molar ratio of  $(Ca+X)/P = 1.48$ , (where X corresponds to Sr + Zn) and pH of  $\approx 7$ . The precipitated suspensions were kept for 4 h under constant stirring and matured for further 20 h under rest conditions, at 50 °C. The resulting precipitates were filtered, dried at 100 °C, and heat treated for 2 h at 1100 °C, followed by milling and sieving by a mesh size of 63  $\mu\text{m}$ , yielding a final average particle size of  $\approx 1\text{-}10 \mu\text{m}$ .

### V-2.2.4. Mold casting

Hierarchical indirect printed scaffolds were fabricated comprising two layers, *i.e.* SF layer in the upper zone and SF mixed with ionic-doped TCP in a bottom layer. For that, enzymatic-cross-linked SF hydrogels were firstly prepared by mixing SF solutions (with 8% or 16% (w/v)) with 10% (v/v) horseradish peroxidase solution (HRP type VI, 0.84  $\text{mg}\cdot\text{mL}^{-1}$ ) and 6.5% (v/v) hydrogen peroxide solution ( $\text{H}_2\text{O}_2$ , 0.36% (v/v); Panreac, Barcelona, Spain), and a total volume of 200  $\mu\text{L}$  was used to fill the cube shape mold (**Figure V-1a**iii). The incubation was performed at 37 °C for 15 minutes for SF (16% (w/v)) and 25 minutes for SF (8% (w/v)). For the bottom layer, using the abovementioned enzymatic crosslinking process, 150  $\mu\text{L}$  of SF solutions (8% or 16% (w/v)) were mixed with ionic-doped TCP powder using blend ratios of 80/20 (w/w) of SF/ionic-doped TCP, and added on the top of the SF layer, followed by incubation at 37 °C for 30 minutes (**Figure V-1**iv). After the gelation process, the final indirect printed scaffolds were frozen at -80 °C and lyophilized during 3 days (CRYODOS-80; Telstar, Barcelona, Spain). The scaffolds were posteriorly immersed in a 70% (v/v) ethanol solution and easily removed from the molds. The indirect printed hierarchical scaffolds produced were abbreviated to Hi8 and Hi16 when SF solutions at 8% and 16% (w/v) were used, respectively. For further characterization, pure SF monolayer scaffolds (SF8 and SF16) and SF/TCPs monolayer scaffolds (SF8/TCP and SF16/TCP) were also prepared.

### V-2.3. Physico-chemical characterization of the indirect printed hierarchical SF scaffolds

#### V-2.3.1. Scanning Electron Microscopy (SEM)

The morphology of the Hi8 and Hi16 scaffolds was observed under an SEM (Nova NanoSEM 200; FEI, Hillsboro, OR, USA) with a coupled Energy-dispersive X-ray detector (EDS). Prior to analysis under SEM, the scaffolds were coated with Gold/Palladium (Au/Pd) (SC502–314B) in a coater (E6700; Quorum Technologies, East Grinstead, UK). The elemental composition was performed by energy dispersive spectroscopy (EDS; Pegasus X4M) coupled to the SEM. For EDS analysis independent regions were selected in the SF8, SF16, SF8/TCP and SF16/TCP scaffolds.

#### V-2.3.2. Micro-computed tomography (Micro-CT)

The micro architecture of the scaffolds was investigated using a high-resolution Micro-CT Skyscan 1072 scanner (Skyscan, Kontich, Belgium) with a pixel size of 10  $\mu\text{m}$ . Standardized cone-beam reconstruction software (NRecon v1.4.3, SkyScan) was used for data sets reconstructions. Representative data set of the samples was segmented into binary images with a dynamic threshold of 22-40 (grey values). Then, the binary images obtained were used for morphometric analysis (CT Analyser, v1.5.1.5, SkyScan) and construction of three-dimensional models (ANT 3D creator, v2.4, SkyScan).

#### V-2.3.3. Fourier transform infrared spectroscopy (FTIR)

The structural conformation and chemical composition of the top layer and bottom layer of Hi8 and Hi16 were evaluated by FTIR spectroscopy (Perkin-Elmer 1600 series equipment, CA, USA) under an attenuated total reflectance (ATR) model (IRPrestige-21, Shimadzu, Japan). All spectra were obtained between 4600 to 800  $\text{cm}^{-1}$  at a 4  $\text{cm}^{-1}$  resolution with 50 scans.

#### V-2.3.4. *In vitro* degradation

The stability of the hierarchical scaffolds was assessed by enzymatic degradation assay. Protease XIV solution (1.0  $\text{U}\cdot\text{mL}^{-1}$ ) was prepared by dissolving the enzyme in distilled water. The initial weight of

the scaffolds was measured, and then the scaffolds were hydrated in PBS at 37 °C overnight, followed by immersion in 5 mL of protease solution. The enzyme solution was changed every 48 hours. The samples were weight after 0.16, 0.33, 1, 7, 14, 21 and 28 days of immersion in the degradation solution at 37 °C in static conditions. The weight loss ratio was obtained using the following equation:

**Equation V-1 - Determination of weight loss ratio.**

$$\text{weight loss ratio} = \left[ \frac{(m_i - m_{d,t})}{(m_i)} \right] \times 100\%$$

where,  $m_i$  is the initial weight of the sample, and  $m_{d,t}$  is the weight of the degraded sample at each time point (n=3 per group).

#### V-2.3.5. Swelling ratio

The swelling ratio of the hierarchical scaffolds was also evaluated after immersion in PBS for time periods ranging from 3 hours to 28 days. All experiments were conducted at 37 °C in static conditions. At each time point, the samples were removed from PBS, the excess of surface water was absorbed using a filter paper, and the weight immediately determined. The swelling ratio was obtained using the following equation:

**Equation V-2 - Determination of swelling ratio.**

$$\text{swelling ratio} = \left[ \frac{(m_{w,t} - m_i)}{(m_i)} \right] \times 100\%$$

where,  $m_i$  is the initial weight of the sample, and  $m_{w,t}$  is the wet weight of the sample at each time point (n=3 per group).

#### V-2.3.6. Mechanical properties

The viscoelastic measurements were investigated using a TRITEC8000B dynamic mechanical analyzer (DMA; Triton Technology, UK) in the compressive mode. The indirect printed scaffolds were immersed in PBS overnight at 37 °C. The geometry of the indirect printed scaffolds was measured (with a micrometer of precision), clamped in the DMA apparatus and immersed in a PBS bath with the

temperature set to 37 °C. After equilibration at 37 °C, the DMA spectra were obtained during a frequency scan between 0.1 and 10 Hz. A constant strain amplitude of 50 µm was applied in each experiment.

Uniaxial compressive tests were performed using a Universal Testing Machine (Instron 4505) with a 1 kN load cell at room temperature (RT). As previously, the scaffolds were immersed in PBS overnight at 37 °C. The cross-head speed was set at 2 mm.min<sup>-1</sup> and tests were run until achieving a 60% reduction in specimen height. The elastic modulus was defined by the slope of the initial linear section of the stress–strain curve. A minimum number of 5 samples were tested per condition, with the compressive modulus values being the average of all the measurements.

#### **V-2.4. *In vitro* characterization of the indirect printed hierarchical scaffolds**

The *in vitro* characterization was performed only for the monolayers SF8, SF16, SF8/TCP and SF16/TCP, which was considered to be the easiest way to analyze the results obtained from these assays.

##### **V-2.4.1. *In vitro* bioactivity evaluation**

To evaluate the *in vitro* bioactivity of the scaffolds before cell cultures, the scaffolds were placed into polystyrene flasks containing (1.5x) simulated body fluid (SBF) with ionic concentrations (Na<sup>+</sup> 213.0, K<sup>+</sup> 7.5, Ca<sup>2+</sup> 3.75, Mg<sup>2+</sup> 2.25, Cl<sup>-</sup> 223.2, HPO<sub>4</sub><sup>-</sup> 1.5, HCO<sub>3</sub><sup>2-</sup> 6.3, SO<sub>4</sub><sup>2-</sup> 0.75 mM.L<sup>-1</sup>, pH ≈ 7.4) nearly equivalent to the human blood plasma, as reported by Tas *et al.* [24] for 7 days. The scaffolds were continuously shaken at a rate of 60 rpm, at 37 °C, and the liquid was refreshed every 2 days. Then, the scaffolds were allowed to dry at 37 °C for 1 day and analyzed by means of SEM/EDS analyses. All experiments were carried out in triplicate for each separated layer.

##### **V-2.4.2. Human meniscus cells isolation and expansion**

Human meniscus cells (hMCs) were isolated from meniscus tissue samples obtained from surgery procedures performed after patient's informed consent and using a protocol previously established with the Orthopedic department of Póvoa de Varzim Hospital (Póvoa de Varzim, Portugal). hMCs were isolated following an enzymatic digestion-based method (collagenase type II) from human meniscus



tissue obtained from patients submitted to surgery. The extracted tissue was placed in PBS solution (pH 7.4) and washed several times with PBS containing 1% (v/v) antibiotic/antimycotic mixture until total removal of blood or other bodily contaminants. Meniscus tissue was then separated from fat and vascularized tissue and after being washed several times, the meniscus was cut into small pieces. Tissue digestion was performed by incubation at 37 °C in a water bath for 24 hours in 10-20 mL of a mixture of cell medium Alpha-MEM supplemented with 10% (v/v) fetal bovine serum (FBS; Biochrom AG, Germany), 1% (v/v) antibiotic/antimycotic solution (final concentration of penicillin 100 units.mL<sup>-1</sup> and streptomycin 100 mg.mL<sup>-1</sup>; Gibco, GB) mixture and collagenase type II (1:1). The isolated hMCs were then expanded in basal medium consisting Alpha-MEM w/o nucleosides (MEM alpha medium; Life Technologies, Scotland) supplemented with 10% (v/v) FBS and 1% (v/v) antibiotic/antimycotic solution. Cells were cultured until confluence at 37 °C in an atmosphere of 5% CO<sub>2</sub> incubator, changing the culture medium every 2 days.

#### V-2.4.3. Human primary osteoblasts expansion

Human primary osteoblasts (hOBs) were cultured in non-coated T150 cell culture flasks using Human Osteoblasts Growth Medium (Sigma-Aldrich, St. Louis, MO, USA). Cells were cultured until confluence at 37 °C in an atmosphere of 5% CO<sub>2</sub> incubator, changing the culture medium every 2 days.

#### V-2.4.4. Seeding of hMCs and hOBs

The *in vitro* tests were performed using 2 different cell types. Before cell seeding, all scaffolds were sterilized overnight in ethanol and washed 3x in PBS. Then, the samples were incubated in  $\alpha$ -MEM overnight. In the following day, the scaffolds were transferred to 24-well suspension cell culture plates (Cellstar, Greiner Bio-One, Austria). Confluent hMCs (at passage 4-5) were detached with TrypLE Express (1X) (Life Technologies, Carlsbad, CA, USA) and seeded in the SF8 and SF16 scaffolds at a density of 1.5x10<sup>5</sup> cells/scaffold. The hOBs after confluence were also detached with TrypLE Express (1X) (Life Technologies, Carlsbad, CA, USA) and seeded SF8/TCP and SF16/TCP scaffolds at a density of 1.5x10<sup>5</sup> cells/scaffold. Each scaffold was kept in the CO<sub>2</sub> incubator at 37 °C for 2 hours, and then 3 mL of the respective culture medium were added to each well. Samples were retrieved at different culture times (1, 3 and 7 days) and the culture medium was changed every 2 days.

#### V-2.4.5. Cell viability and metabolic activity

Cell viability was microscopically assessed by Live/Dead assay. Briefly, cell seeded scaffolds were immersed in a calcein AM/propidium iodide (PI) solution at 1:3 ratio in culture medium for 25-30 minutes. The scaffolds were transferred for an incubator at 37 °C in an atmosphere of 5% CO<sub>2</sub>, protected from light. Viable cells metabolize calcein AM (Invitrogen, USA 1 mg.mL<sup>-1</sup>) into green fluorescent calcein (Ex/Em ≈ 495/515 nm), while dead cells find their DNA stained red by PI (Invitrogen, USA 1 mg.mL<sup>-1</sup>, Ex/Em ≈ 493/636 nm). After a washing step with PBS, samples were imaged using a Transmitted and Reflected Light Microscope (Zeiss Axio Imager.Z1m, Zeiss, Germany).

hMCs and hOBs metabolic activity was evaluated using Alamar Blue (AB). This dye yields a fluorescent signal and a colorimetric change when incubated with metabolically-active cells. Cell culture medium containing 10% AB was added to the different culture wells and incubated for 4 hours at 37 °C in an atmosphere of 5% CO<sub>2</sub>. Then, 100 µL of solution from each well were transferred to white opaque 96-well plates, in triplicates. Fluorescence was monitored at Ex/Em ≈ 530/590 nm, using a microplate reader (Synergy HT, BioTek Instruments, USA). PBS was used to wash the AB reagent and fresh medium was added. The metabolic activity values were calculated by normalization with the mean fluorescence value obtained for the controls (scaffolds without cells).

#### V-2.4.6. Cell proliferation

The quantity of double stranded DNA (dsDNA) was determined using a fluorimetric dsDNA quantification kit (PicoGreen, Molecular Probes, Invitrogen Corporation, USA). The assay was performed according to the manufacturer's instructions. This test is based on the principle that the quantity of double stranded DNA is directly proportional to cell number. After each time point, samples were washed twice with PBS solution and kept in 1 mL of ultrapure water at -80 °C until further analysis. Constructs were thawed at RT, sonicated for 1 hour to induce complete membrane lysis. After sonication, the scaffold was discarded. Solution fluorescence was measured at an excitation wavelength ( $\lambda$ ) of 485/20 nm and at an emission  $\lambda$  of 528/20 nm, in a microplate reader (Synergy HT, BioTek Instruments, USA). The quantification of dsDNA was calculated according to a standard curve prepared with concentrations ranging between 0 and 2 µg.mL<sup>-1</sup>, relating quantity of DNA and fluorescence intensity. Scaffolds without cells were used as controls.

## V-2.5. *In vivo* biocompatibility assessment of the indirect printed hierarchical scaffolds

As aforementioned, the *in vivo* studies were assayed for the monolayers SF8, SF16, SF8/TCP and SF16/TCP, which was considered to be the easiest way to analyze the results.

### V-2.5.1. Subcutaneous implantation

The maintenance and use of animals were carried out in accordance to the Ethics Committee of University of Minho and approved by the Portuguese Licensing Authority (DGV-DSSPA). Six mice Hsd:ICR (CD-1) of 5 weeks old and average weight of 25-30g (Charles River Laboratories, Massachusetts, USA) were used in this study. Each mouse was anesthetized by intraperitoneal injection of: ketamine (25 mg.Kg<sup>-1</sup>) and medetomidine (0.15 mg.Kg<sup>-1</sup>) for anesthesia; cephalexin (15 mg.Kg<sup>-1</sup>) as antibiotic; and bupivacaine, pethidine (5-10 mg.Kg<sup>-1</sup>) as analgesic. The mice hair was shaved at the implantation area, followed by disinfection with 70% ethanol and iodine. In each mouse, four skin incisions (1 cm length) were made in the dorsal midline, one close from the head (CH) and the other far from the head (FH). In the following, one specimen of each formulation (SF8, SF16, SF8/TCP and SF16/TCP) was implanted subcutaneously into the respective pocket and then the skin was sutured. Four specimens of both formulations were implanted. Eight weeks post-surgery, the mice were euthanized by injection of overdose pentobarbital sodium followed by harvesting of the implanted materials. The explants were fixed with 10% (v/v) formalin solution (Sigma-Aldrich, Germany) for 24 hours at RT and then transferred to histological cassettes. Sections were prepared by cutting the specimen into 20 µm-thick sections using a microtome (Spencer 820, American Optical Company, NY, USA). The obtained sections were stained with hematoxylin and eosin (H&E) and Masson's trichrome (MT).

### V-2.6. Statistical analysis

All the numerical results are presented as mean ± standard deviation (SD). Statistical analysis was performed using the GraphPad Prism 5.0 (GraphPad Software, La Jolla, CA, USA). First, a Shapiro-Wilk test was used to ascertain regarding data normality. For all the biological quantification assays, the differences between the experimental results were analyzed using a Kruskal-Wallis test followed by Dunn's multiple comparison test. Three independent experiments were performed for cell studies

(metabolic activity and cell proliferation), and three samples were analyzed per group in each culturing time. The significance level was set to  $*p < 0.05$ ,  $**p < 0.01$ ,  $***p < 0.001$ .

### V-3. RESULTS

As aforementioned, a meniscus model previously developed by our group [6] was herein used to produce a negative mold (**Figure V-1bi**). As it can be seen in **Figures V-1bii, biii**, the presented indirect printing strategy enabled the fabrication of hierarchical patient-specific implants with the meniscus native shape. Cube-shape molds with 36 mm<sup>2</sup> of base and 5 mm of height were designed with four properly centered cylinders with 1 mm of diameter to produce smaller scaffolds for characterization (**Figures V-2a and b**). The mold design was chosen, not only to simplify the subsequent characterization, but also to show the tuning capability of our approach in terms of mold architecture. Two different SF (8% and 16% (w/v)) solutions were used to produce the indirect printed scaffolds in order to evaluate the influence of the polymer concentration (**Figure V-2c-f**). From **Figures V-2d-f**, it is possible to observe the hierarchical indirect printed scaffolds, as well as the two well-defined layers: the top layer composed only by SF and the bottom layer composed by 80/20 (w/w) ratio of SF/TCP (*i.e.*, Hi8 and Hi16). The hierarchical structure was obtained after optimized steps (data not shown) and resulted from the use of the enzymatic-crosslinking middle step. In short, after the crosslinking reaction of the SF8/TCP and SF16/TCP solutions that occurred for 25 minutes and 15 minutes, respectively, it was possible to add a pure SF solution on the top to create a hierarchical structure. In fact, the crosslinking reaction time was optimized in order to obtain a distinct separation zone, as well as a good integration of both layers.

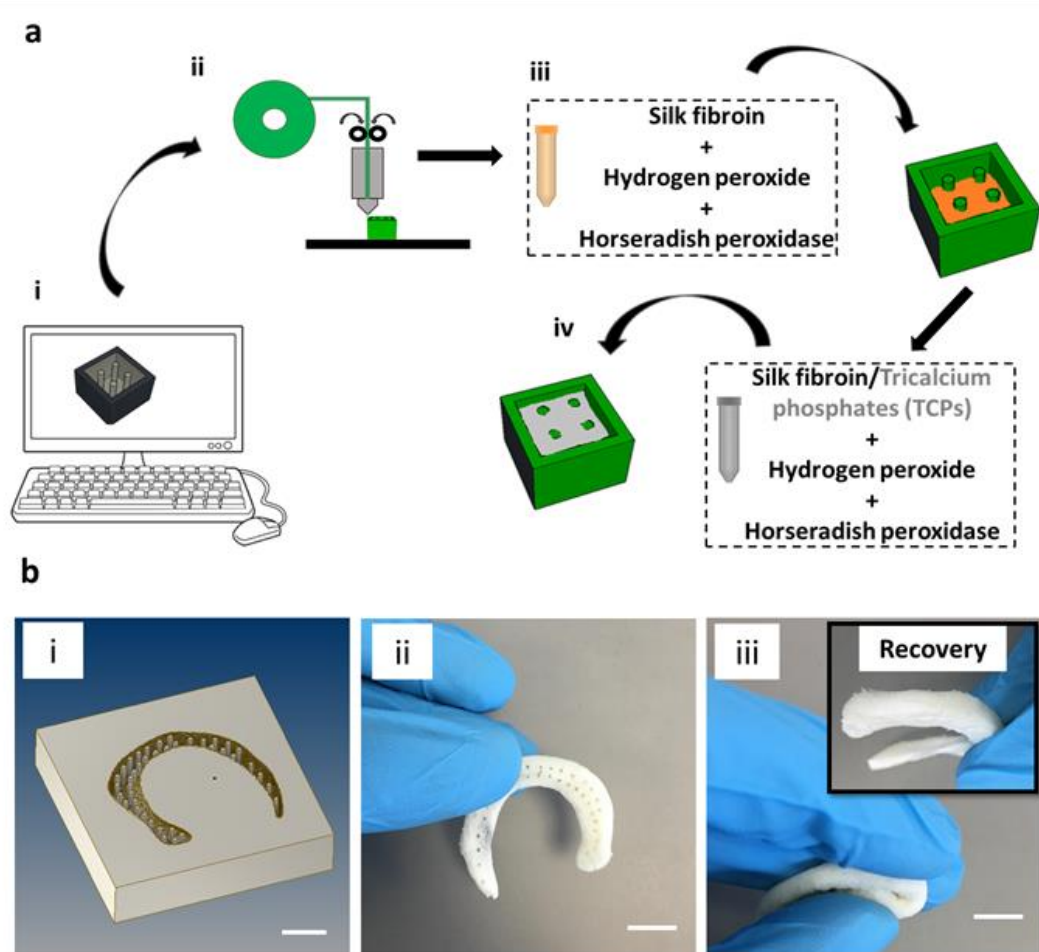


Figure V-1 - Scheme of the production of indirect printed scaffolds. (a) Different steps were required to produce indirect printed cube-shape hierarchical scaffolds: (ai) design of the negative mold, (aai) printing of the negative mold, (aiii) mold casting of the SF, and (aiv) SF blending with  $\beta$ -tricalcium phosphate. The same strategy was used to produce patient-specific indirect printed hierarchical scaffolds of human meniscus: (bi) model of the negative mold, (bii) patient-specific meniscus scaffold, and (biii) patient-specific meniscus scaffold tightly compressed and total original shape recovery. Scale bars: 1cm.

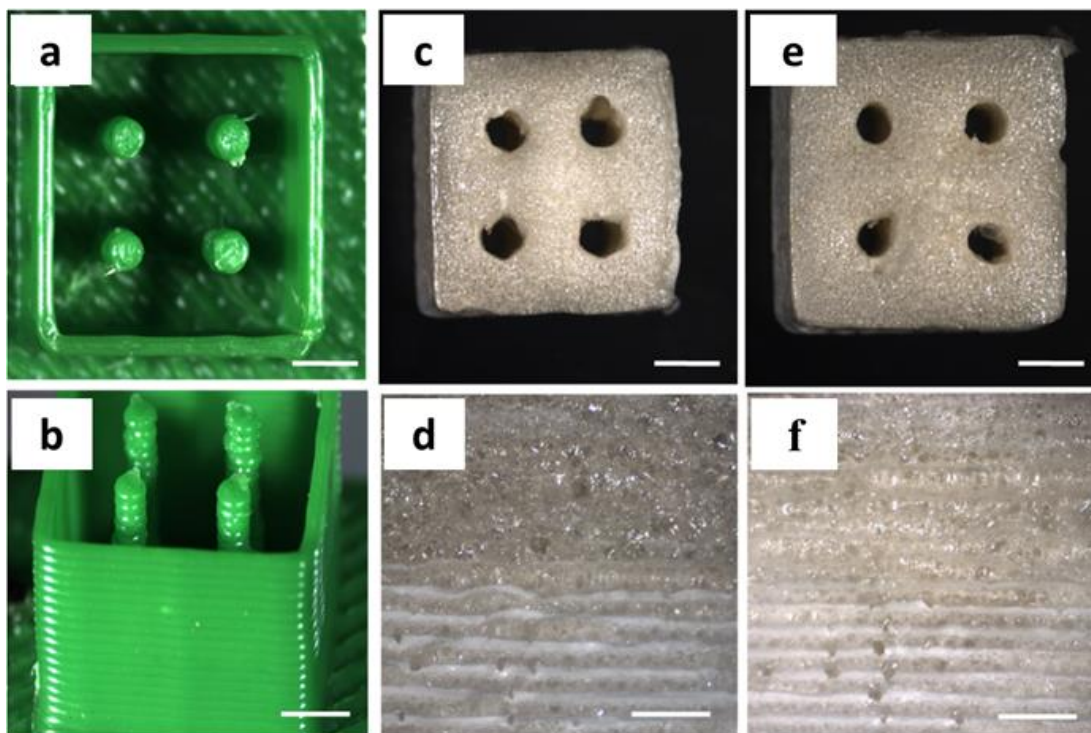


Figure V-2 - Macroscopic images of the indirect printed cube-shape scaffolds. (a-b) Macroscopic images of the negative molds, (c-d) Hi8, and (e-f) Hi16. Scale bars: 2 mm (a-c and e); and 1 mm (d and f).

### V-3.1. Morphology and microstructure

The pore morphology, and the quantitative and qualitative analysis of porosity were assessed by means of SEM and Micro-CT analyses, respectively (**Figure V-3**). From SEM images (**Figure V-3a**), it is possible to observe the pore morphology of both scaffold formulations (Hi8 and Hi16) and the presence of TCP in the bottom layer. The porosity observed was induced by the freeze-drying technique used in the production of scaffolds and it is characterized by pores with size ranging from 60  $\mu\text{m}$  to 110  $\mu\text{m}$ . Comparing both layers, larger pores were observed in the bottom layers of the hierarchical scaffolds possibly due to the higher integrity conferred by the ceramic powders. A 3D reconstruction of the Hi8 and Hi16 scaffolds was also performed by Micro-CT (**Figure V-3b**). From the 3D image, it can be observed that the scaffolds present a high degree of porosity. It can also be clearly distinguished the difference between the ceramic bottom layer and the pure silk top layer. No significant differences in terms of mean porosity, pore size and trabecular thickness were observed comparing both formulations. The morphometric analysis confirmed the similarity of both formulations in terms of mean porosity, mean pore size and mean trabecular thickness (**Table V-1**). The mean porosity of Hi8 and Hi16 was  $74.1 \pm 1.4\%$  and  $72.9 \pm 3.1\%$ , respectively. The Hi8 scaffold presented a mean pore size and

trabecular thickness of  $119.7 \pm 11.5 \mu\text{m}$  and  $32.2 \pm 3.2 \mu\text{m}$ , respectively, whereas the Hi16 scaffold revealed slightly higher values of mean pore size ( $126.9 \pm 18.9 \mu\text{m}$ ) and trabecular thickness ( $40.7 \pm 0.5 \mu\text{m}$ ). Comparing the different layers of the scaffolds, higher values of mean pore size and trabecular thickness were found in the bottom layer. The higher values of trabecular thickness can be explained by the presence of TCP. In addition, the presence of TCP enhances the structural integrity leading to more homogeneous pores in the bottom layer, which can be an explanation for the slightly high values of pore size. However, no significant differences were observed in terms of pore geometry and morphology between the Hi8 and Hi16 scaffolds.

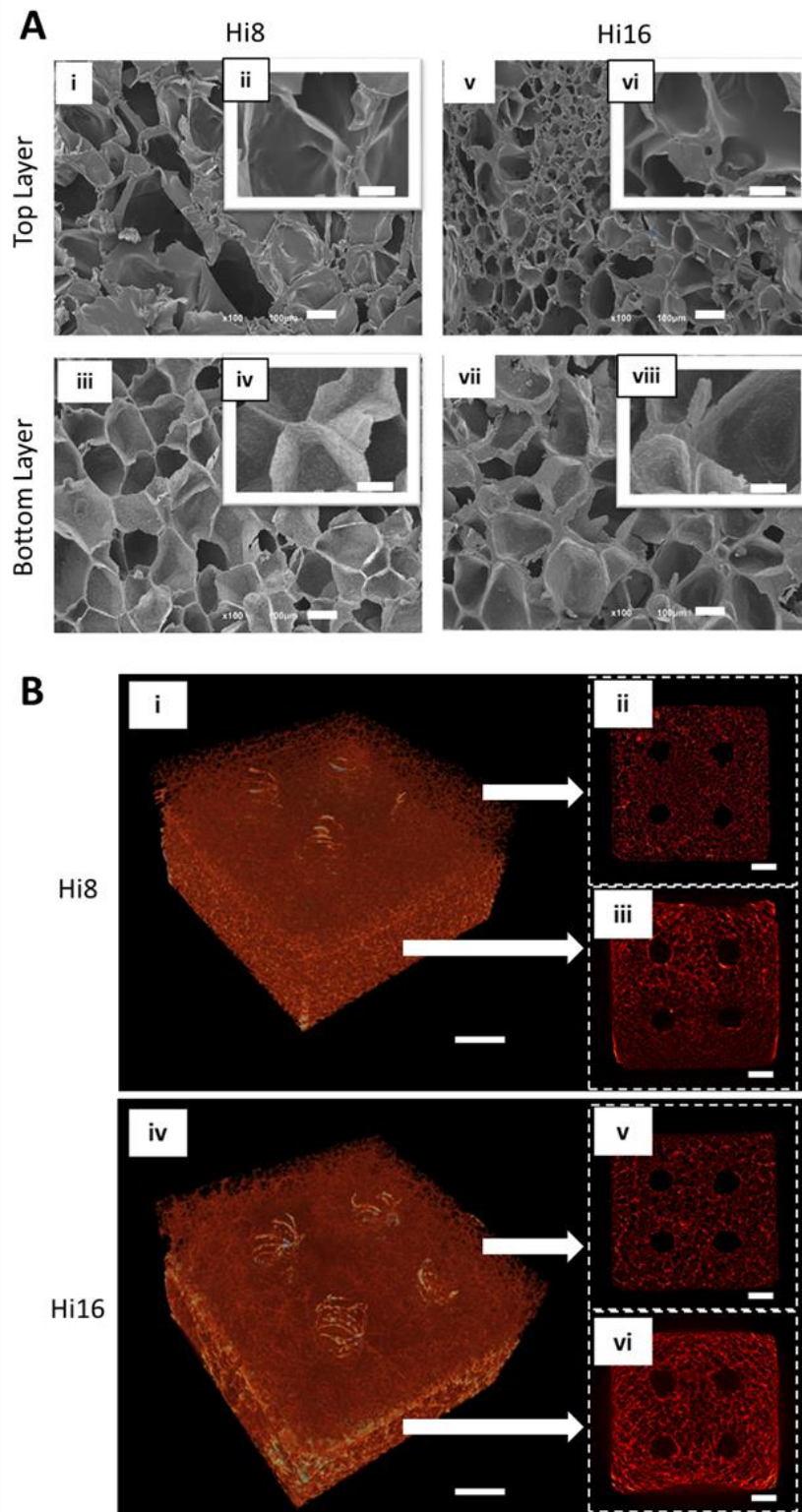


Figure V-3 - SEM images and 3D reconstruction of the indirect printed hierarchical scaffolds. (a) SEM images of Hi8 and Hi16 scaffolds at different magnifications from the top layer (ai, aii and av, avi, respectively) and bottom layer (aiii, aiv and avii, aviii, respectively). (b) 3D reconstruction by micro-CT of the Hi8 and Hi16 (bi and biv, respectively), 2-D images from the top layer (bii and bv, respectively), and bottom layer (biii and bvi, respectively). Scale bars: 500 µm (ai, iii, v and vii), 50 µm (aii, vi, iv and viii), and 1 mm (bi-vi).



Table V-1 - Microstructure of the indirect printed hierarchical scaffolds analyzed by micro-CT.

		Mean porosity (%)	Mean pore size ( $\mu\text{m}$ )	Mean trabecular thickness ( $\mu\text{m}$ )
Hi8	Top layer	75.9 $\pm$ 1.3	113.3 $\pm$ 22.9	30.7 $\pm$ 2.9
	Bottom layer	73.8 $\pm$ 1.5	125.0 $\pm$ 24.4	50.7 $\pm$ 0.5
	Total scaffold	74.1 $\pm$ 1.4	119.7 $\pm$ 11.5	32.2 $\pm$ 3.2
Hi16	Top layer	72.2 $\pm$ 1.8	117.0 $\pm$ 18.7	37.3 $\pm$ 0.5
	Bottom layer	75.9 $\pm$ 1.5	137.5 $\pm$ 22.6	55.7 $\pm$ 0.9
	Total scaffold	72.9 $\pm$ 3.1	126.9 $\pm$ 18.9	40.7 $\pm$ 0.5

### V-3.2. Chemical structure

The SF conformation and the presence of the ceramics were evaluated by ATR-FTIR analysis (**Figure V-4a**). Regarding silk conformation, the predominance of  $\beta$ -sheet conformation was confirmed by the presence of the characteristic peaks at 1623  $\text{cm}^{-1}$  and 1526  $\text{cm}^{-1}$ . Additionally, the bottom layers spectra of the Hi8 and Hi16 scaffolds showed the appearance of a main peak around 1030  $\text{cm}^{-1}$ . This new peak is related with the characteristic vibrational modes of the  $\text{PO}_4$  group in the ionic-doped TCP [21]. In another work, Yan *et al.* [25] developed silk scaffolds containing calcium phosphate powders. After ATR-FTIR analysis, a similar spectrum was obtained revealing the presence of the ceramic powders and the predominance of  $\beta$ -sheet conformation.

### V-3.3. Degradation and swelling properties

The degradation profile of the Hi8 and Hi16 scaffolds was evaluated using protease XIV (**Figure V-4b**). After 1 day, only 4.3  $\pm$  2.6% and 2.7  $\pm$  2.8% of degradation was observed for the Hi8 and Hi16 scaffolds, respectively. Nevertheless, the degradation percentage increased significantly in the following 7 days with the Hi8 and Hi16 scaffolds presenting 48.8  $\pm$  9.9% and 75.1  $\pm$  16.2% of degradation, respectively. After 21 days, the Hi8 was completely degraded whereas the Hi16 scaffold presented 64.4  $\pm$  8.4% of degradation. However, at the end of the test (28 days), the Hi16 scaffold was completely

degraded. The formulation with lower concentration of silk presented, as expected, higher degradation ratios and a faster degradation. Regarding the water uptake capacity of these scaffolds, higher values of swelling were presented by the Hi8 scaffolds in the first 5 days of immersion in PBS (**Figure V-4c**). This difference was only noted up to 5 days, when the scaffolds reached a similar pattern of swelling. Nevertheless, after 28 days Hi8 and Hi16 scaffolds revealed values of swelling of  $148.3 \pm 23.7\%$  and  $150.5 \pm 21.1\%$ , respectively. Despite the high swelling capacity demonstrated by both formulations, it is important to emphasize that they maintained their shape after 28 days in PBS solution.

#### V-3.4. Mechanical properties

The mechanical properties of both formulations were assessed by DMA and by performing a uniaxial compression test (Instron). The viscoelastic properties were analyzed by DMA in a range of frequencies from 0.1 to 10 Hz (**Figure V-4d-e**). The formulations with higher silk concentration revealed higher values of storage modulus ( $E'$ ) (**Figure V-4d**) and lower values of damping factor ( $\tan \delta$ ) (**Figure V-4e**). The storage modulus of Hi8 and Hi16 increased from  $1.03 \pm 0.08$  MPa to  $1.56 \pm 0.13$  MPa and from  $2.17 \pm 0.25$  MPa to  $3.19 \pm 0.38$  MPa, respectively. Furthermore, the damping factor values were very similar comparing Hi8 and Hi16 scaffolds, with slightly higher values in the Hi8 formulation. Thus, the scaffold with lower concentration of silk (Hi8) has a slightly higher propensity to disperse energy under a compressive force.

**Figure V-4f** shows the representative stress-strain plot of the developed hierarchical scaffolds. The values of compressive modulus were higher for Hi16 ( $0.66 \pm 0.05$  MPa) as compared with Hi8 ( $0.27 \pm 0.08$  MPa). In short, the results obtained by the uniaxial compressive test corroborate the previous data obtained by DMA analysis, showing that the polymer concentration has a critical role in the mechanical behavior.

The mechanical properties of SF8, SF16, SF8/TCP and SF16/TCP scaffolds were also assessed (**Supplementary Figures V-1-3 and Supplementary Table V-1**). It was observed that the presence of TCP provided an increase in terms of stiffness and a decrease of their damping properties.

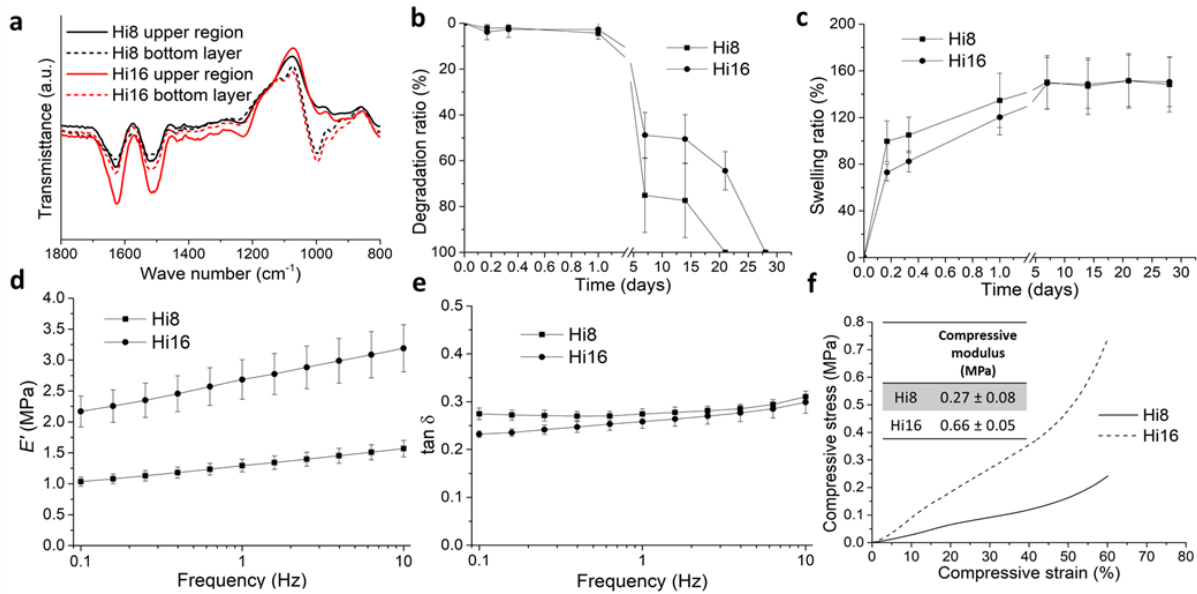


Figure V-4 - Chemical analysis, degradation and swelling behavior, and mechanical performance of the indirect printed hierarchical scaffolds. (a) ATR-FTIR spectra of the Hi8 and Hi16 top and bottom layers. (b-c) Degradation and swelling profiles of the Hi8 and Hi16, obtained in protease XIV and PBS solutions, respectively. (d-e) Storage modulus ( $E'$ ) and damping properties of the Hi8 and Hi16 obtained by DMA. (f) Stress-strain plot of the Hi8 and Hi16 and respective compressive modulus.

### V-3.5. *In vitro* bioactivity of the indirect printed scaffolds

The bioactivity of the scaffolds was evaluated on the top and bottom layers of Hi8 and Hi16 by soaking the scaffold in a SBF solution (Figure V-5). Results showed that the Hi8 and Hi16 bottom layers (Figure V-5b and V-5e, respectively) appeared partially covered with cauliflower-like of apatite crystals, while no apatite crystals were induced on the top layers of Hi8 and Hi16 (Figure V-5a and V-5c respectively), after 7 days of soaking. This apatite crystals morphology are comparable to that of hydroxyapatite (HAp) also confirmed by the quantified Ca/P ratio obtained from EDS elemental analysis (Figure V-5c and V-5f).

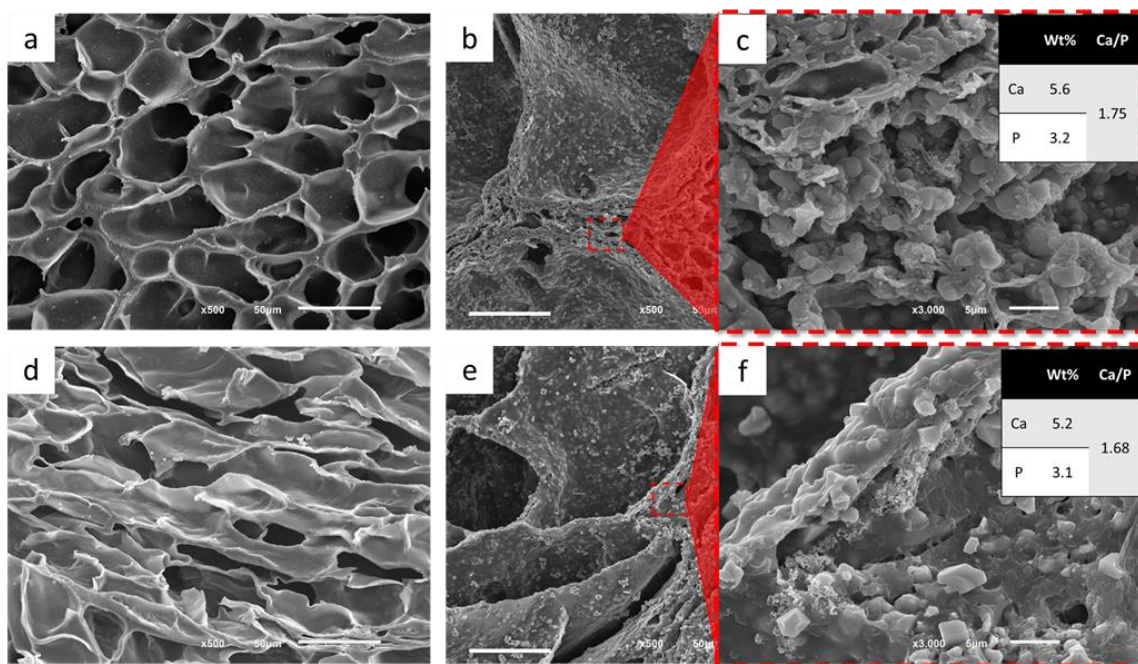


Figure V-5 - SEM micrographs of Hi8 top (a) and bottom (b) layers, and Hi16 top (d) and bottom (e) layers after 7 days of mineralization, and respective Ca and P wt.% obtained from EDS analysis after mineralization. Scale bars: 50  $\mu\text{m}$  (a, b, d and e); 5  $\mu\text{m}$  (c and f).

### V-3.6. Attachment, viability and proliferation of hMCs and hOBs on the indirect printed scaffolds

As mentioned before, scaffolds composed only by pure SF (SF8 and SF16) and SF blended with TCP (SF8/TCP and SF16/TCP) were produced in order to assess the biological performance of both layers of the hierarchical scaffolds. The SF8 and SF16 were seeded with hMCs, whereas the SF8/TCP and SF16/TCP were seeded with hOBs. From the live/dead staining, it was observed that the hMCs and hOBs were viable over the 7 days of culture (Figure V-6a). From day 1 to day 7, an increase in fluorescence was detected, indicating that cells adhered to the indirect printed scaffolds and proliferated. The cells were well dispersed in the scaffolds surface and presented the typical spreading morphology after 7 days of culturing. The cells metabolic activity and proliferation were quantified by Alamar blue assay and DNA content analysis, respectively. The results of metabolic activity were normalized with the DNA content (Figure V-6b). In the scaffolds seeded with hMCs (Figure V-6bi), a significant increase from day 1 to day 7 ( $***p < 0.001$ ) was observed for both formulations. However, no statistically significant differences were observed when comparing the SF8 with SF16 scaffolds. For both the SF8/TCP and SF16/TCP scaffolds (Figure V-6bii), the *in vitro* biological assays revealed a significant increase from day 1 to day 3 ( $**p < 0.001$ ) and from day 1 to day 7 ( $***p < 0.001$ ). As for

the pure silk scaffolds, no statistically significant differences were observed when comparing the scaffolds with different SF concentrations. These results could be explained by the lack of significant differences in terms of pore geometry and morphology between the Hi8 and Hi16, as previously shown in the SEM and micro-CT data. In short, the variation of the silk concentration does not have an effective impact in the scaffold's biological performance.

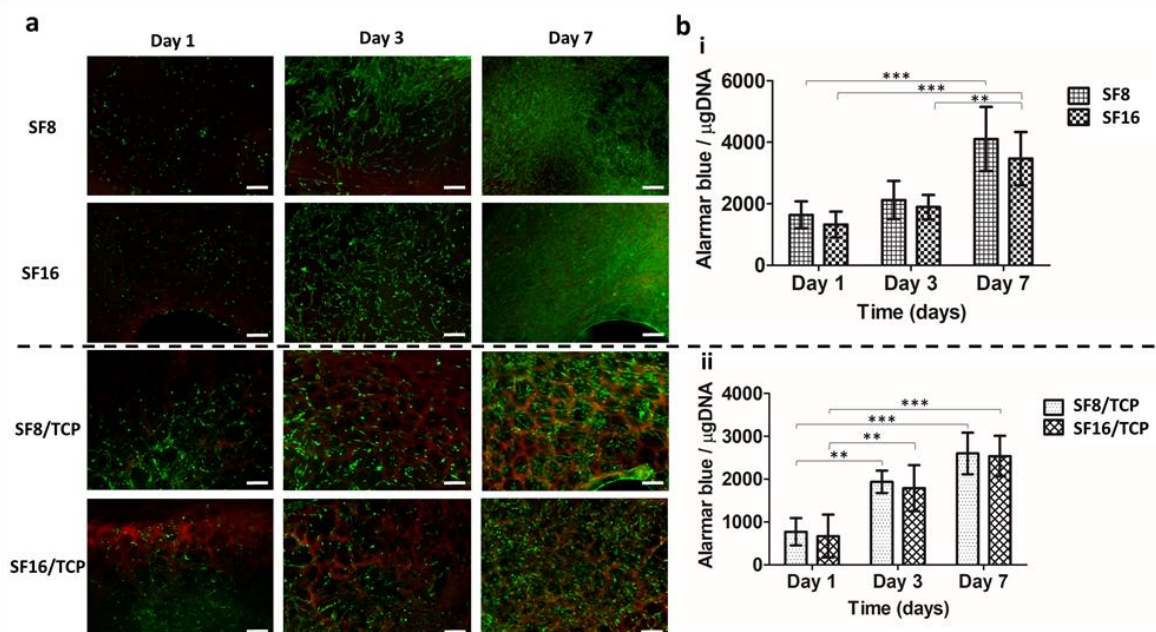


Figure V-6 - *In vitro* biological performance of the different layers of the indirect printed hierarchical scaffolds. (a) Live/dead staining of the SF8, SF16, SF8/TCP and SF16/TCP after 1, 3 and 7 days of culturing. (b) Metabolic activity by Alamar Blue assay normalized with DNA content. Results were obtained after 1, 3 and 7 days of culturing for the SF8 and SF16 (bi), and SF8/TCP and SF16/TCP (bii). Statistically significant differences were represented by \* ( $p < 0.5$ ), \*\* ( $p < 0.01$ ), and \*\*\* ( $p < 0.001$ ). Scale bars: 200  $\mu\text{m}$ .

### V-3.7. Subcutaneous implantation of the indirect printed scaffolds

The *in vivo* biocompatibility of the indirect printed scaffolds was assessed by subcutaneous implantation in CD-1 mice (Figure V-7). The macroscopic images of the explants retrieved after 8 weeks of implantation showed a good integration of the scaffolds with the host subcutaneous tissue. Nevertheless, a slightly better integration was observed in the SF8 and SF16. In addition, the scaffolds were capable of maintaining their shape and integrity over the implantation period. No signs of infection or acute inflammation were observed, with the scaffolds presenting good biocompatibility with the surrounding connective tissue. The MT staining images revealed the formation of collagenous



surrounding tissue (blue fibers). Herein, no significant differences were found when comparing all formulations.

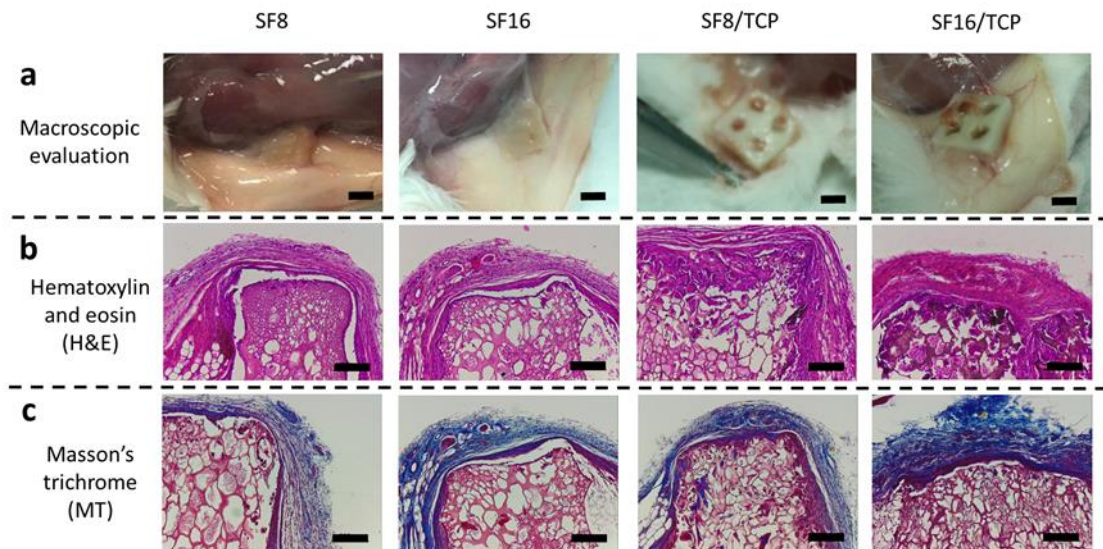


**Figure V-7** - Subcutaneous implantation of the different layers of the indirect printed hierarchical scaffolds in CD-1 mice for 8 weeks. (a) Macroscopic images of the explants after 8 weeks of implantation. (b) H&E staining, and (c) MT staining of the explants. Scale bars: 4 mm (a) and 200  $\mu$ m (b and c).

#### V-4. DISCUSSION

Meniscus, as mentioned before, has a very important biomechanical function in human knee. Meniscus limited healing capacity triggered the interest in finding new TE strategies for treating irreparable meniscus injuries. Total/partial meniscectomy has been the gold standard treatment, however its contribution for significant arthritic changes in the knee and non-satisfactory long-term outcomes has increased the use of conservative approaches [2, 26]. Nowadays, non-operative approaches and physical therapy programs have been used rather meniscectomy in some traumatic and degenerative meniscal lesions. The similarity in terms of clinical outcomes between meniscectomy and the conservative strategies has been changing the paradigm and the concept of meniscus preservation has gaining interest among the medical community. However, the conservative strategies cannot be considered a good alternative to the current available treatments. Depending on the lesions, occasionally, conservative treatments cannot be applied. Therefore, new strategies must be developed, especially TE-based approaches, in order to achieve the desired meniscus regeneration and biofunctionality. Different strategies have been investigated and there are already some commercial

available solutions (*e.g.*, Actifit®, CMI® and NUsurface®), but many issues still remain to be solved, namely related with mechanical properties, degradation behavior, biocompatibility, patient specificity and anchorage [27]. In the last few years, the use of SF has extended from the textile to the TE field, due to its well-known biocompatibility, mechanical strength and degradation behavior. In this study, it is proposed the development of hierarchical patient-specific SF scaffolds for meniscus regeneration, using an indirect printing strategy to overcome conventional processing limitations, and their characterization by *in vitro* and *in vivo* studies.

The macroscopic characterization of the indirect printed scaffolds (Hi8 and Hi16) (**Figure V-2c-f**) revealed the reproducibility of this method, from which hierarchical scaffolds were obtained with the proposed shape. The four similar vertical holes created by the proposed mold aimed to improve the interconnectivity and tissue ingrowth inside the scaffold. Previous works developed indirect printed scaffolds with higher porosity and interconnectivity [12, 13, 15, 16, 28]. However, it is well known that the increase of porosity leads to a decrease of the mechanical performance [29]. In this sense, it is essential to have a good balance between the porosity and the mechanical properties in order to ensure the mechanical functionality and chondroprotective effect of the scaffold. In addition to the macro pores, micro pores were formed by the freeze-drying technique (**Figure V-3**). Freeze-drying has been widely used for the production of porous scaffolds in the TE field [30]. This method is based on rapid cooling and subsequent solvent removal by sublimation under vacuum. Different freezing temperatures and successive freeze-thaw cycles were shown to have an impact in the scaffolds pore size and morphology [31]. In this work, the scaffolds were frozen at -80°C overnight and directly freeze-dried. The mean porosity values obtained were around 72.9-74.1%, whereas the mean pore size had around 119.7-126.9  $\mu\text{m}$  (**Table V-1**). In this sense, we believe that an adequate porosity and pore sizes were achieved, in combination with the macro porosity induced by the mold design, that are suitable for a meniscus TE approach, providing a good balance between the ability for cell invasion and the mechanical performance of the scaffold. Nevertheless, it is important to preserve the idea that is possible to tune the scaffolds' macro porosity by changing the mold design. This tuning ability can only be obtained by using a 3D printing technology. In this case, an indirect printing approach can be a faster and easier alternative when compared to direct printing. In what concerns direct printing strategies, the printing fidelity is highly dependent on the ink properties. Among these properties, the gelation time can be a huge limitation in terms of time of printing, fidelity and size of the scaffold [28, 32]. In this sense, we selected to use an indirect printing approach that allows producing patient-specific hierarchical scaffolds by printing different supporting structures.

The silk conformation and the presence of TCP in the bottom layer was assessed by ATR-FTIR (**Figure V-4a**). Comparing with previous studies [21, 25], the scaffolds maintained the chemical structure with predominance of the  $\beta$ -sheet conformation. The predominance of this type of conformation is very important in this strategy, since a previous study confirmed lower degradation ratios and higher mechanical performance in the presence of  $\beta$ -sheet conformation [25]. Moreover, the presence of TCP was also confirmed.

The degradation behavior of the scaffolds has a critical role in tissue engineering approaches [33]. It is important to tune the scaffolds degradation ratio in order to have a good balance between new tissues' formation and implant degradation. The possibility to tune the degradation behavior of SF scaffolds has already been shown and well investigated [34-36]. In this study, the capability for tuning degradation was demonstrated by changing the polymer concentration. The results revealed that scaffolds with higher silk concentration presented lower degradability (**Figure V-4b**). In a previous *in vivo* work, Wang *et al.* [37] showed that scaffolds prepared from a 10% (w/v) SF solution maintained their structural integrity for at least 8 weeks, while those prepared from a 6% (w/v) solution did not. In addition, this degradation behavior was also observed *in vitro* when enzymatic digestion of porous silk scaffolds was performed [38]. In this work, the developed scaffolds completely degraded upon contact to protease for 21 days. Compared with previous works [39, 40], the indirect printed scaffolds presented similar degradation profile, as well as an indirect proportionality between the silk concentration and the degradation ratio. Since the Hi16 scaffolds revealed a slower degradation ratio, they can be a better alternative for future applications in meniscus TE.

The mechanical properties of the scaffolds play a major role in the total restoration of the meniscus function in the knee joint. The stabilization of the knee joint through absorption and distribution of the stress loads, as well as the prevention of early degenerative joint diseases, is directly related with the implant mechanical performance [41]. In addition, a recent study demonstrated that cartilage contact pressures and implant displacement are sensitive to the implant material stiffness [42]. The values of storage modulus ( $E'$ ) obtained at 1 Hz (frequency associated to normal ambulation [43]) under dynamic conditions were  $1.29 \pm 0.10$  MPa and  $1.48 \pm 0.08$  MPa for Hi8 and Hi16 scaffolds, respectively (**Figure V-4e**). Under the same conditions, two distinct works performed by Pereira *et al.* [44] and Bursac *et al.* [45] revealed similar values using human meniscus samples. In both works,  $E'$  values ranged from 0.4-1.7 MPa. Furthermore, under static conditions, the indirect printed scaffolds presented similar values of compressive modulus comparing with the native tissue.



The results obtained from the uniaxial compression test (**Figure V-4f**) revealed a compressive modulus of  $0.27 \pm 0.08$  MPa for Hi8 scaffold and  $0.66 \pm 0.05$  MPa for Hi16 scaffold. Chia *et al.* [46] performed an unconfined compression test at the physiological strain rate in human frozen meniscus. The axial and radial compressive modulus measured at a physiological loading rate at 12% strain were 0.718 MPa and 0.605 MPa, respectively, suggesting again that the mechanical performance of the indirect printed scaffolds is suitable for meniscus TE. The indirect printed scaffolds revealed, not only similar mechanical behavior comparing with the native tissue but also mechanical properties comparable to other silk scaffolds produced using conventional techniques such as salt leaching, freeze-drying and gas foaming [22, 47, 48]. In a similar indirect printing approach using SF, Liu *et al.* [15] reported higher values of compressive modulus in scaffolds with lower concentration of silk. This might be due to the conditions used in the test, since the authors used dry scaffolds instead of wet scaffolds. However, this study also revealed a similar correlation in terms of silk concentration and mechanical performance, where the compressive modulus was found to increase with increasing SF concentrations. Besides that, the presence of TCP in the bottom layer helped to increase the stiffness of the scaffolds. This was confirmed by the mechanical tests performed in SF8, SF16, SF8/TCP and SF16/TCP scaffolds (**Supplementary Figures V-1-3 and Supplementary Table V-1, Supplementary material**), as well as in another study performed by our group [25]. Another important mechanical property, especially in meniscus TE applications, is the damping effect, which reduces the internal forces in the knee [49]. The produced indirect printed scaffolds showed damping factors at 1 Hz of  $0.27 \pm 0.01$  and  $0.25 \pm 0.01$  for Hi8 and Hi16 scaffolds respectively. Comparing with the native tissue, these values were slightly higher. Pereira *et al.* [44] reported values of damping factor ranging from 0.12 to 0.18. According to the previous results and, since the indirect printed scaffolds presented higher stiffness than the native tissue, it was already expected that the indirect printed scaffolds revealed less propensity to disperse energy. Nevertheless, the mechanical performance of the indirect printed scaffolds proved to be suitable for meniscus TE presenting an adequate stiffness and viscoelastic properties.

The *in vitro* mineralization ability of the Hi scaffolds was investigated after soaking the scaffolds in SBF solution for 7 days (**Figure V-5**). Results showed the formation of apatite crystals onto the surface of Hi8 and Hi16 bottom layers (**Figure V-5b and V-5c and Figure V-5e and V-5f, respectively**). This result was expected due to the presence of TCP powders, as well as from the Zn and Sr presence. It is well known that these trace elements are able to improve the apatite layer deposition and mineral growth [50].

The biological performance of the scaffolds is critical for any TE application, which should allow cells to adhere and proliferate. In a preliminary cell culture assay, we decide to use pure silk scaffolds (SF8 and SF16) and scaffolds blended with TCP (SF8/TCP and SF16/TCP) seeded with different cells types. The SF8 and SF16 scaffolds were seeded with hMCs, whereas the SF8/TCP and SG16/TCP were seeded with hOBs. The aim was to mimic the physiological conditions, where meniscus cells will be in contact with the pure silk layer, whereas the osteoblasts will be in contact with the bottom layer containing TCP. Both formulations presented good biocompatibility, showing cell adhesion and proliferation up to 7 days of culture (**Figure V-6**). SF has been widely exploited for TE applications [51], especially for the production of silk-based scaffolds for musculoskeletal regeneration [52]. Mandal *et al.* [47] developed a three-layered SF meniscal material system to mimic the meniscus architecture. In this work, human chondrocytes and fibroblasts were seeded in the SF scaffold. The cell culture results showed that the construct was a suitable template for meniscus-like tissue growth. On the other hand, it is well established that the presence of ceramics plays a major role in bone TE applications [53]. As mentioned before and based on the literature, we envisioned that the presence of TCP in the bottom layer of the indirect printed scaffolds would be a huge factor to enhance the scaffold anchorage. Using similar ceramic powders, Pina *et al.* [21] showed that the presence of ionic-doped TCP in silk scaffolds led to a higher osteogenic potential. These results are in line with other studies, where the presence of ceramics induced higher alkaline phosphatase activity comparing with pure silk scaffolds [25, 54]. Supported by the literature and by our results, it is expected a better interaction in the interface bone-scaffold that will possibly lead to a superior scaffold anchorage. However, further *in vivo* assays should be performed to confirm this hypothesis.

The biocompatibility between the indirect printed scaffolds and *in vivo* tissues was analyzed by subcutaneous implantation (**Figure V-7**). Like in the *in vitro* assays, only the individual SF8, SF16, SF8/TCP and SF16/TCP scaffolds were implanted. Due to the good mechanical behavior of the indirect printed scaffolds, the integrity and shape was maintained after 8 weeks of implantation. This result is in agreement with the *in vitro* mechanical analysis. Furthermore, the scaffolds were able to support tissue presenting good biocompatibility and a minimal inflammatory response. Similar results were found using SF-based scaffolds after 4 [55] and 12 [56] weeks of implantation. Herein, indirect printed SF scaffolds were shown to present a good *in vivo* biocompatibility. The good biological performance of SF-based scaffolds can be affected by the type of processing used, which is directly related with the physical and chemical properties of SF [57].

## V-5. CONCLUSIONS

In this study, novel indirect printed hierarchical scaffolds composed by a SF top layer and a SF/TCP bottom layer were developed. The use of an indirect printing approach allowed the production of scaffolds with tunable porosity and shape, as well as patient-specificity. The adequate morphology and porosity, together with superior mechanical properties and suitable integrity, make these scaffolds promising candidates for meniscus regeneration. The *in vitro* biological assays demonstrated that the top layer and the bottom layer of the scaffolds supported the viability and proliferation of human meniscus cells and human primary osteoblasts, respectively, up to 7 days. Moreover, these scaffolds induced a very weak inflammatory response when subcutaneously implanted in mice inflammatory response when subcutaneously implanted in mice. However, a complementary *in vivo* study, for example in a rabbit meniscus model, would be necessary to fully validate these indirect printing hierarchical scaffolds and confirm the hypothesis envisioned by the authors that the presence of TCP in the bottom layer of the scaffolds would enhance the anchorage properties, by improving the interaction bone-implant. Nevertheless, the *in vitro* and *in vivo* results are encouraging and confirmed the potential of the developed indirect printed hierarchical scaffolds for meniscus tissue engineering applications.

## V-6. ACKNOWLEDGMENTS

The authors thank the financial support provided by the Portuguese Foundation for Science and Technology (FCT) through the project B-FABULUS (PTDC/BBB-ECT/2690/2014). FCT/MCTES is also acknowledged for the PhD scholarship attributed to J.B.C. (PD/BD/113803/2015) and the financial support provided to J.S.C. (IF/00115/2015) and J.M.O. (IF/01285/2015) under the program “Investigador FCT”. The authors would like to also acknowledge the contribution of Teresa Oliveira for histology samples processing.

## V-7. REFERENCES

- [1] Khetia EA, McKeon BP. Meniscal allografts: biomechanics and techniques. Sports medicine and arthroscopy review 2007;15:114-20.
- [2] Mordecai SC, Al-Hadithy N, Ware HE, Gupte CM. Treatment of meniscal tears: An evidence based approach. World Journal of Orthopedics 2014;5:233-41.

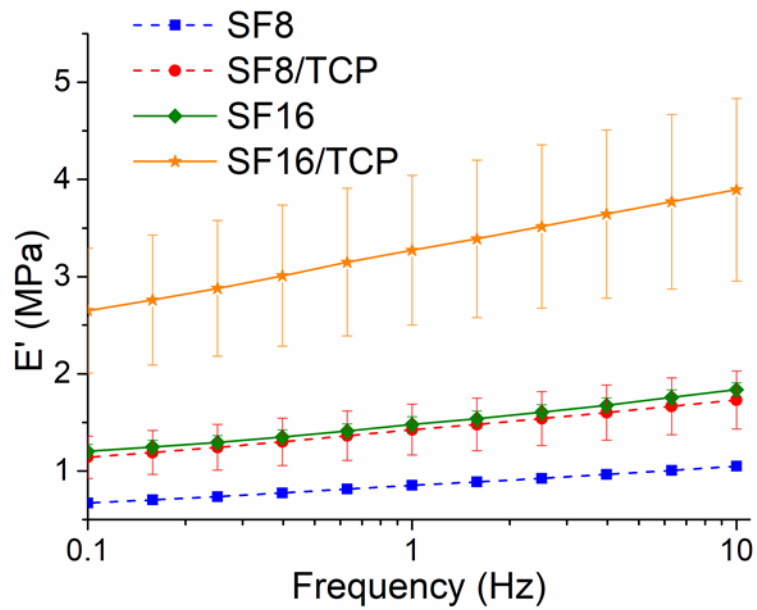
- [3] Abrams GD, Frank RM, Gupta AK, Harris JD, McCormick FM, Cole BJ. Trends in meniscus repair and meniscectomy in the United States, 2005-2011. *The American journal of sports medicine* 2013;41:2333-9.
- [4] Costa JB, Oliveira JM, Reis RL. Biomaterials in Meniscus Tissue Engineering. In: Oliveira JM, Reis RL, editors. *Regenerative Strategies for the Treatment of Knee Joint Disabilities*. Cham: Springer International Publishing; 2017. p. 249-70.
- [5] Costa JB, Pereira H, Espregueira-Mendes J, Khang G, Oliveira JM, Reis RL. Tissue engineering in orthopaedic sports medicine: current concepts. *Journal of ISAKOS: Joint Disorders & Orthopaedic Sports Medicine* 2017;2:60.
- [6] Cengiz IF, Pitikakis M, Cesario L, Parascandolo P, Vosilla L, Viano G, *et al.* Building the basis for patient-specific meniscal scaffolds: From human knee MRI to fabrication of 3D printed scaffolds. *Bioprinting* 2016;1-2:1-10.
- [7] Haglin JM, Eltorai AE, Gil JA, Marcaccio SE, Botero-Hincapie J, Daniels AH. Patient-Specific Orthopaedic Implants. *Orthopaedic surgery* 2016;8:417-24.
- [8] Houben A, Van Hoorick J, Van Erps J, Thienpont H, Van Vlierberghe S, Dubrueel P. Indirect Rapid Prototyping: Opening Up Unprecedented Opportunities in Scaffold Design and Applications. *Annals of biomedical engineering* 2017;45:58-83.
- [9] Lee M, Dunn JCY, Wu BM. Scaffold fabrication by indirect three-dimensional printing. *Biomaterials* 2005;26:4281-9.
- [10] Lee JY, Choi B, Wu B, Lee M. Customized biomimetic scaffolds created by indirect three-dimensional printing for tissue engineering. *Biofabrication* 2013;5:045003.
- [11] Park JH, Jung JW, Kang HW, Cho DW. Indirect three-dimensional printing of synthetic polymer scaffold based on thermal molding process. *Biofabrication* 2014;6:025003.
- [12] Wai-Yee Y, Chee-Kai C, Kah-Fai L, Margam C, Mun-Wai L. Indirect fabrication of collagen scaffold based on inkjet printing technique. *Rapid Prototyping Journal* 2006;12:229-37.
- [13] Liu CZ, Xia ZD, Han ZW, Hulley PA, Triffitt JT, Czernuszka JT. Novel 3D collagen scaffolds fabricated by indirect printing technique for tissue engineering. *Journal of biomedical materials research Part B, Applied biomaterials* 2008;85:519-28.
- [14] Tan JY, Chua CK, Leong KF. Indirect fabrication of gelatin scaffolds using rapid prototyping technology. *Virtual and Physical Prototyping* 2010;5:45-53.
- [15] Liu MJ, Chou SM, Chua CK, Tay BC, Ng BK. The development of silk fibroin scaffolds using an indirect rapid prototyping approach: morphological analysis and cell growth monitoring by spectral-domain optical coherence tomography. *Medical engineering & physics* 2013;35:253-62.
- [16] Chen CH, Liu J, Chua C-K, Chou S-M, Shyu V, Chen J-P. Cartilage Tissue Engineering with Silk Fibroin Scaffolds Fabricated by Indirect Additive Manufacturing Technology. *Materials* 2014;7:2104.

- [17] Yan LP, Oliveira JM, Oliveira AL, Reis RL. Core-shell silk hydrogels with spatially tuned conformations as drug-delivery system. *Journal of tissue engineering and regenerative medicine* 2017;11:3168-77.
- [18] Yan LP, Silva-Correia J, Ribeiro VP, Miranda-Goncalves V, Correia C, da Silva Morais A, *et al.* Tumor Growth Suppression Induced by Biomimetic Silk Fibroin Hydrogels. *Scientific reports* 2016;6:31037.
- [19] Buckland D. M, Sadoghi P, Wimmer MD, Vavken P, Pagenstert GI, Valderrabano V, *et al.* Meta-analysis on biomechanical properties of meniscus repairs: are devices better than sutures? *Knee surgery, sports traumatology, arthroscopy : official journal of the ESSKA* 2015;23:83-9.
- [20] Pina S, Vieira SI, Rego P, Torres PM, da Cruz e Silva OA, da Cruz e Silva EF, *et al.* Biological responses of brushite-forming Zn- and ZnSr- substituted beta-tricalcium phosphate bone cements. *European cells & materials* 2010;20:162-77.
- [21] Pina S, Canadas RF, Jimenez G, Peran M, Marchal JA, Reis RL, *et al.* Biofunctional Ionic-Doped Calcium Phosphates: Silk Fibroin Composites for Bone Tissue Engineering Scaffolding. *Cells, tissues, organs* 2017;204:150-63.
- [22] Gruchenberg K, Ignatius A, Friemert B, von Lubken F, Skaer N, Gellynck K, *et al.* *In vivo* performance of a novel silk fibroin scaffold for partial meniscal replacement in a sheep model. *Knee surgery, sports traumatology, arthroscopy : official journal of the ESSKA* 2015;23:2218-29.
- [23] Wojtyla S, Klama P, Baran T. Is 3D printing safe? Analysis of the thermal treatment of thermoplastics: ABS, PLA, PET, and nylon. *Journal of occupational and environmental hygiene* 2017;14:D80-d5.
- [24] Tas AC. Synthesis of biomimetic Ca-hydroxyapatite powders at 37 degrees C in synthetic body fluids. *Biomaterials* 2000;21:1429-38.
- [25] Yan LP, Silva-Correia J, Oliveira MB, Vilela C, Pereira H, Sousa RA, *et al.* Bilayered silk/silk-nanoCaP scaffolds for osteochondral tissue engineering: *In vitro* and *in vivo* assessment of biological performance. *Acta Biomaterialia* 2015;12:227-41.
- [26] Beaufils P, Becker R, Kopf S, Matthieu O, Pujol N. The knee meniscus: management of traumatic tears and degenerative lesions. *EFORT Open Reviews* 2017;2:195-203.
- [27] Vrancken ACT, Buma P, van Tienen TG. Synthetic meniscus replacement: a review. *International Orthopaedics* 2013;37:291-9.
- [28] Hendriks S, Kascholke C, Flath T, Schumann D, Gressenbuch M, Schulze FP, *et al.* Indirect rapid prototyping of sol-gel hybrid glass scaffolds for bone regeneration – Effects of organic crosslinker valence, content and molecular weight on mechanical properties. *Acta Biomaterialia* 2016;35:318-29.
- [29] Ahmad SN, Hashim J, Ghazali MI. The Effects of Porosity on Mechanical Properties of Cast Discontinuous Reinforced Metal–Matrix Composite. *Journal of Composite Materials* 2005;39:451-66.
- [30] Annabi N, Nichol JW, Zhong X, Ji C, Koshy S, Khademhosseini A, *et al.* Controlling the porosity and microarchitecture of hydrogels for tissue engineering. *Tissue engineering Part B, Reviews* 2010;16:371-83.

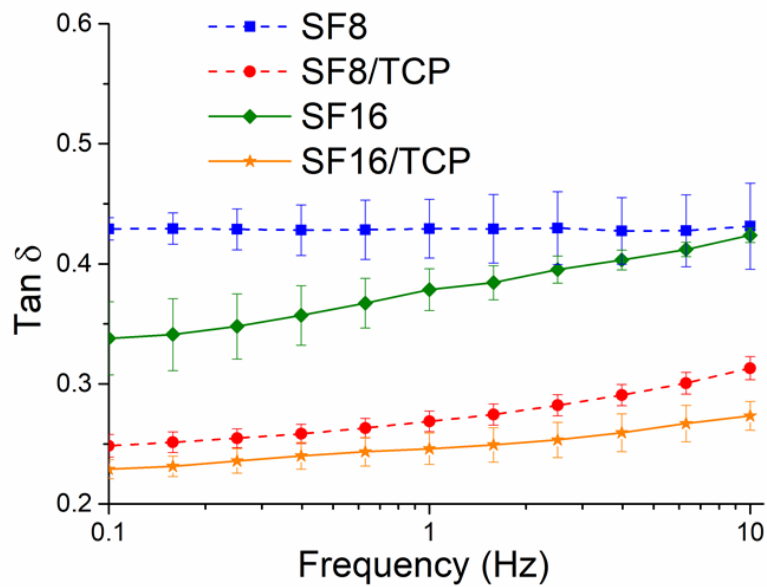
- [31] Wu X, Black L, Santacana-Laffitte G, Patrick CW, Jr. Preparation and assessment of glutaraldehyde-cross-linked collagen-chitosan hydrogels for adipose tissue engineering. *Journal of biomedical materials research Part A* 2007;81:59-65.
- [32] Critchley SE, Kelly DJ. Bioprinting functional meniscus and articular cartilage. *Journal of 3D Printing in Medicine* 2017;1:269-90.
- [33] Zhang H, Zhou L, Zhang W. Control of scaffold degradation in tissue engineering: a review. *Tissue engineering Part B, Reviews* 2014;20:492-502.
- [34] Brown J, Lu CL, Coburn J, Kaplan DL. Impact of silk biomaterial structure on proteolysis. *Acta Biomater* 2015;11:212-21.
- [35] Ghanaati S, Orth C, Unger RE, Barbeck M, Webber MJ, Motta A, *et al.* Fine-tuning scaffolds for tissue regeneration: effects of formic acid processing on tissue reaction to silk fibroin. *Journal of tissue engineering and regenerative medicine* 2010;4:464-72.
- [36] Cao Y, Wang B. Biodegradation of Silk Biomaterials. *International Journal of Molecular Sciences* 2009;10:1514-24.
- [37] Wang Y, Rudym DD, Walsh A, Abrahamsen L, Kim HJ, Kim HS, *et al.* *In vivo* degradation of three-dimensional silk fibroin scaffolds. *Biomaterials* 2008;29:3415-28.
- [38] Kim UJ, Park J, Joo Kim H, Wada M, Kaplan DL. Three-dimensional aqueous-derived biomaterial scaffolds from silk fibroin. *Biomaterials* 2005;26:2775-85.
- [39] Ribeiro VP, Pina S, Costa JB, Cengiz IF, García-Fernández L, Fernández-Gutiérrez MdM, *et al.* Enzymatically Cross-Linked Silk Fibroin-Based Hierarchical Scaffolds for Osteochondral Regeneration. *ACS Applied Materials & Interfaces* 2019;11:3781-99.
- [40] Ribeiro VP, da Silva Morais A, Maia FR, Canadas RF, Costa JB, Oliveira AL, *et al.* Combinatory approach for developing silk fibroin scaffolds for cartilage regeneration. *Acta Biomaterialia* 2018;72:167-81.
- [41] Abdelgaied A, Stanley M, Galfe M, Berry H, Ingham E, Fisher J. Comparison of the biomechanical tensile and compressive properties of decellularised and natural porcine meniscus. *Journal of Biomechanics* 2015;48:1389-96.
- [42] Shriram D, Praveen Kumar G, Cui F, Lee YHD, Subburaj K. Evaluating the effects of material properties of artificial meniscal implant in the human knee joint using finite element analysis. *Scientific reports* 2017;7:6011.
- [43] Lee JH, Kisiday J, Grodzinsky AJ. Tissue-engineered versus native cartilage: linkage between cellular mechano-transduction and biomechanical properties. *Novartis Foundation symposium* 2003;249:52-64; discussion -9, 170-4, 239-41.
- [44] Pereira H, Caridade SG, Frias AM, Silva-Correia J, Pereira DR, Cengiz IF, *et al.* Biomechanical and cellular segmental characterization of human meniscus: building the basis for Tissue Engineering therapies. *Osteoarthritis and Cartilage* 2014;22:1271-81.

- [45] Bursac P, Arnoczky S, York A. Dynamic compressive behavior of human meniscus correlates with its extra-cellular matrix composition. *Biorheology* 2009;46:227-37.
- [46] Chia HN, Hull ML. Compressive moduli of the human medial meniscus in the axial and radial directions at equilibrium and at a physiological strain rate. *Journal of Orthopaedic Research* 2008;26:951-6.
- [47] Mandal BB, Park S-H, Gil ES, Kaplan DL. Multilayered silk scaffolds for meniscus tissue engineering. *Biomaterials* 2011;32:639-51.
- [48] Nazarov R, Jin H-J, Kaplan DL. Porous 3-D Scaffolds from Regenerated Silk Fibroin. *Biomacromolecules* 2004;5:718-26.
- [49] Stoffel M, Weichert D, Müller-Rath R. Mechanical modelling and experimental validation of meniscus replacement material. *PAMM* 2008;8:10197-8.
- [50] Bose S, Fielding G, Tarafder S, Bandyopadhyay A. Understanding of dopant-induced osteogenesis and angiogenesis in calcium phosphate ceramics. *Trends in biotechnology* 2013;31:594-605.
- [51] Vepari C, Kaplan DL. Silk as a Biomaterial. *Progress in polymer science* 2007;32:991-1007.
- [52] Yao D, Liu H, Fan Y. Silk scaffolds for musculoskeletal tissue engineering. *Experimental Biology and Medicine* 2016;241:238-45.
- [53] Samavedi S, Whittington AR, Goldstein AS. Calcium phosphate ceramics in bone tissue engineering: A review of properties and their influence on cell behavior. *Acta Biomaterialia* 2013;9:8037-45.
- [54] Zhang Y, Wu C, Friis T, Xiao Y. The osteogenic properties of CaP/silk composite scaffolds. *Biomaterials* 2010;31:2848-56.
- [55] Mandal BB, Gil ES, Panilaitis B, Kaplan DL. Laminar silk scaffolds for aligned tissue fabrication. *Macromolecular bioscience* 2013;13:48-58.
- [56] Xie H, Wang J, He Y, Gu Z, Xu J, Li L, *et al.* Biocompatibility and safety evaluation of a silk fibroin-doped calcium polyphosphate scaffold copolymer *in vitro* and *in vivo*. *RSC Advances* 2017;7:46036-44.
- [57] Kundu B, Rajkhowa R, Kundu SC, Wang X. Silk fibroin biomaterials for tissue regenerations. *Advanced drug delivery reviews* 2013;65:457-70.

V-8. SUPPLEMENTARY MATERIAL

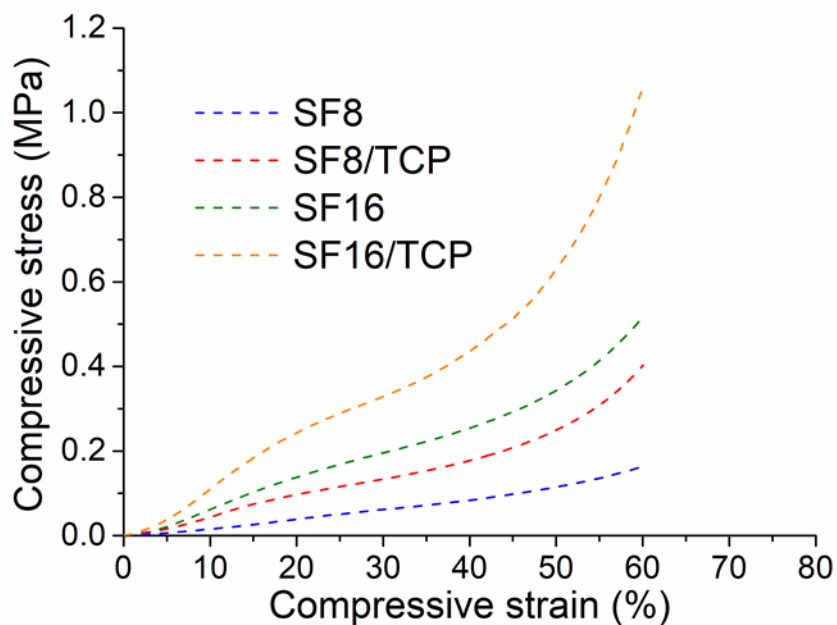


Supplementary Figure V-1 - Storage modulus of the SF8, SF16, SF8/TCP and SF16/TCP obtained by DMA.



Supplementary Figure V-2 - Damping properties of the SF8, SF16, SF8/TCP and SF16/TCP obtained by DMA.





Supplementary Figure V-3 - Stress-strain plot of the SF8, SF16, SF8/TCP and SF16/TCP obtained in the Instron apparatus.

Supplementary Table V-1 - Compressive modulus of the SF8, SF16, SF8/TCP and SF16/TCP obtained in the Instron apparatus.

Formulations	Compressive Modulus (MPa)
SF8	$0.15 \pm 0.02$
SF16	$0.48 \pm 0.03$
SF8/TCP	$0.34 \pm 0.03$
SF16/TCP	$0.79 \pm 0.30$

## Chapter VI

# PATENT - INKS FOR 3D PRINTING, METHODS OF PRODUCTION AND USES THEREOF

## Chapter VI

### Patent - INKS FOR 3D PRINTING, METHODS OF PRODUCTION AND USES THEREOF§

#### ABSTRACT

The present disclosure relates to a silk-fibroin ink suitable for 3D printing. The ink for 3D printing now disclosed may be used in chemical and pharma industries, medicine, engineering, manufacturing namely for the production of capsules, fibers, membranes, particles, scaffolds, medical devices, microfluidic devices and patient-specific implants.

---

§ This chapter is based on the following patent:

Costa J. B., Silva-Correia J., Oliveira J. M., and Reis R. L., "INKS FOR 3D PRINTING, METHODS OF PRODUCTION AND USES THEREOF", WO/2018/225049, Priority date: 10136 09.06.2017 PT, 2017.

## VI-1. DESCRIPTION

### VI-1.1. Technical field

The present disclosure relates to a silk-fibroin ink suitable for 3D printing. The ink for 3D printing now disclosed may be used in chemical and pharma industries, medicine, engineering, manufacturing namely for the production of capsules, fibers, membranes, particles, scaffolds, medical devices, microfluidic devices and patient-specific implants.

### VI-1.2. Background

3D printing, an additive manufacturing, is a technology that comprises a computer-assisted approach providing the production of 3D structures. The endless potential of this technology led to its application in many areas, such as, medicine, engineering, manufacturing, etc.

Until now, regarding tissue engineering and medicine regenerative, a large number of materials have been used in 3D Printing [1]. Among the natural and biodegradable materials (alginate and gelatin, collagen, chitosan, fibrin and hyaluronic acid, often isolated from animal or human tissues) the alginate, gelatin and hyaluronic acid, due to its properties, are the ones that have been more explored in this field [2]. The ideal properties of a bioink comprises several factors, such as, printability, biocompatibility, degradation, mechanical properties and biomimicry [1]. Silk fibroin (SF) obtained from the silk worm *Bombyx mori* has often been used as a textile material, but, in the last few years, this natural biomaterial has gained a lot of attention in the tissue engineering and regenerative medicine area. Its excellent mechanical properties along with its biocompatibility, degradation properties, water-based processing and the presence of easy accessible chemical groups for functional modifications filled almost all the parameters for and ideal material for bioprinting. However, the scientific community still not founded the best processing method in order to print silk fibroin.

These facts are disclosed in order to illustrate the technical problem addressed by the present disclosure.

### VI-1.3. Brief description

3D printing, an additive manufacturing, is a technology that comprises a computer-assisted approach providing the production of 3D structures. In the field of tissue engineering and regenerative medicine the use of this technique can be a huge advantage even more if it is used a natural material as a bioink. Silk fibroin (SF) has gained a lot of attention in the tissue engineering and regenerative medicine due to its excellent mechanical properties along with its biocompatibility, degradation properties, water-based processing and the presence of easy accessible chemical groups for functional modifications filled almost all the parameters for and ideal material for bioprinting.

The present disclosure relates to the development a methodology that comprises the use of an enzymatically cross-linked approach that provides a silk ink able to be used in 3D printing. This methodology overcomes the facts previously pointed out by referring to the development of an enzymatically cross-linked silk fibroin ink, using horseradish peroxidase and hydrogen peroxide as enzyme and substrate respectively to modify the silk fibroin water solution to be used as a bioink.

This disclosure concerns reliable 3D structures such as scaffolds, patient specific implants, microchips, among others. Besides that, the physico-chemical performances of the silk constructs can be tuned for specific uses, by means of using different processing methods after the printing of the 3D constructs as well as the tuned ability provided by the 3D printer itself (Construct Design).

An advantage of using this methodology is the capability to print the silk constructs in an amorphous state giving the opportunity to induce the  $\beta$ -sheet conformation in many different ways.

This is the first time such methodology is used for the production of silk fibroin enzymatically cross-linked inks to be used in 3D printing technology.

The process of production is depicted in **Figure VI-1** and comprises the following steps:

- preparing 10% to 20% (w/v) of an aqueous silk fibroin (SF) solution concentration to be defined according to final intended features It can be used
- by adding of horseradish peroxidase from 4% to 6% (v/v) ( $40 - 60 \mu\text{L}\cdot\text{mL}^{-1}$ ) and hydrogen peroxide from 1.5% to 3.5% (v/v) ( $15 - 35 \mu\text{L}\cdot\text{mL}^{-1}$ ) in 3D Printer cartridge;
- by incubating the whole system at 37 °C for 30-45 minutes for the complete formation of the hydrogel;
- 3D printing of architectures using a silk fibroin enzymatically cross-linked hydrogel (**Figure VI-2**).

In an embodiment, 10% (w/v) of an aqueous silk fibroin may be used for soft tissues/cartilage.

In an embodiment, 15% (w/v) of an aqueous silk fibroin may be used for hard cartilage or tissues that will be subjected to high mechanical forces.

In an embodiment, 20% (w/v) of an aqueous silk fibroin may be used for bone repair.

As described before, SF inks is produced using a peroxidase mediated cross-linking method. The horseradish peroxidase (HRP)/hydrogen peroxide (H<sub>2</sub>O<sub>2</sub>) cross-linking approach is used in polymers containing or functionalized with phenol group-containing molecules, including tyrosine, tyramine or aminophenol [3]. Considering that SF contains these groups, it was explored this feature in order to develop a bioink. SF ink was combined with horseradish peroxidase solution (HRP type VI, 0.84 mg.mL<sup>-1</sup>) and hydrogen peroxide solution (H<sub>2</sub>O<sub>2</sub>, 0.36% (v/v); Panreac, Barcelona, Spain).

In an embodiment, the physico-chemical performances of the silk constructs can be tuned for specific uses, by means of using different processing methods after the printing of the 3D constructs as well as the tuned ability provided by the 3D printer itself (Construct Design). One big advantage of using this methodology is the capability to print the silk constructs in an amorphous state giving the opportunity to induce the  $\beta$ -sheet conformation in many different ways.

This is the first time such methodology is used for the production of silk fibroin enzymatically cross-linked inks to be used in 3D printing technology.

The present disclosure relates to an ink comprising a silk fibroin enzymatically cross-linked hydrogel comprising an aqueous solution of silk fibroin.

In an embodiment, the ink may comprise 7-20% (w/v) of the aqueous solution of silk fibroin, preferably 8-18% (w/v), more preferably 11-15% (w/v), in particular wherein the molecular weight of the silk fibroin is 300-350 kDa.

In an embodiment, the ink may also comprise 10-20% (w/v) of the aqueous solution of silk fibroin.

In an embodiment, the ink may comprise a partial  $\beta$ -sheet conformation.

In an embodiment, the ink may comprise 0.1-10% (w/v) of keratin, preferably 0.5-5% (w/v), more preferably 1-3% (w/v), in particular wherein the molecular weight of the keratin is 40-60 kDa.

In an embodiment, the ink may comprise 0.1-10% (w/v) of elastin, preferably 0.5-5% (w/v), more preferably 1-3% (w/v), in particular wherein the molecular weight of the elastin is 40-60 kDa. The advantage of using elastin is that it helps to mimetic, for example, the intervertebral disc.

In an embodiment, the ink now disclosed may have a viscosity of  $100 \text{ kPa}\cdot\text{s}^{-1} - 0.1 \text{ Pa}\cdot\text{s}^{-1}$  as function as shear rate at  $25 \text{ }^\circ\text{C}$ . The viscosity was measured by a Kinexus pro+ rheometer (Malvern Instruments, UK) and using the acquisition software rSpace (Malvern Instruments, UK) at  $25 \text{ }^\circ\text{C}$ .

In an embodiment, the ink may have a loss modulus ( $G'$ ) of 50-1500 Pa at  $25 \text{ }^\circ\text{C}$ .

In an embodiment, the ink may have a storage modulus ( $G''$ ) of 10-100 Pa at  $25 \text{ }^\circ\text{C}$ . The oscillatory tests was measured by a Kinexus pro+ rheometer (Malvern Instruments, UK) and using the acquisition software rSpace (Malvern Instruments, UK) at  $25 \text{ }^\circ\text{C}$ .

In an embodiment, the hydrogel may be a capsule, fiber, coating, membrane, particle, scaffold, medical device, microfluidic device or patient-specific implant.

The present disclosure also relates to a method to prepare the ink comprising a silk fibroin enzymatically cross-linked hydrogel, wherein said method comprises the following steps:

- preparing 7-20% (w/v) of the aqueous solution of silk fibroin, preferably 8-18% (w/v), more preferably 11-15% (w/v) of an aqueous solution of silk fibroin;
- adding 4%-6% (v/v) of horseradish peroxidase and 1.5%-3.5% (v/v) of hydrogen peroxide to the aqueous silk fibroin solution;
- incubating the mixture at  $37 \text{ }^\circ\text{C}$  for 30-45 minutes for the complete formation of the hydrogel;
- freeze-drying at  $-80 \text{ }^\circ\text{C}$  for 3 days.

In an embodiment, the horseradish peroxidase is horseradish peroxidase type VI.

In an embodiment, the method now disclosed may further comprise a step of adding 1-3 % (w/v) of keratin.

In an embodiment, the method now disclosed may further comprise a step of adding 1-3 % (w/v) of elastin.

This disclosure also relates to the use of the ink now disclosed for 3D printing.

#### **VI-1.4. Brief description of the drawings**

The following figures provide preferred embodiments for illustrating the description and should not be seen as limiting the scope of disclosure.

**Figure VI-1** – Schematic representation of the preparation of SF ink for 3D printing.

**Figure VI-2** – 3D Printing of 3D structures a) 2-layer cube shape structure before freeze-drying and b) after freeze-drying. c) 6 layer cube shape (30x30mm) 3D structure. d) 6 layer cube shape (5x5 mm) structure after freeze-drying. e) Human meniscus implant before freeze drying and f) after freeze-drying. Scale bars: 500  $\mu\text{m}$  (a and b); 1 mm (d, e and f); 10 mm (c).

**Figure VI-3** – Steady-Shear rheological measurements (frequency 1 Hz) for enzymatically cross-linked silk inks at different concentration (8% (w/v) and 16% (w/v) of silk solution).

**Figure VI-4** – Oscillatory rheological measurements (frequency 1 Hz) for enzymatically cross-linked silk inks at different concentration (8% (w/v) and 16% (w/v) of silk solution).

**Figure VI-5** – Printed structures using S16 ink. (a) 1 layer, (b) 2 layers, (c) 4 layers, and (d) 5 layers cube shape printed structure. e), f) stereomicroscope images from 2 layers structures. g) 8 layers cube shape structure (30x30x4mm).

**Figure VI-6** – 3D printed structures before (a and c) and after freeze-drying (b and d).

**Figure VI-7** – ATR-FTIR spectra for the 3D structures after printing (day 0), after 7 days immersed in PBS (day 7), and after freeze drying (Freeze dry).

**Figure VI-8** – Loss moduli ( $\tan \delta$ ) of the 3D structures obtained by DMA, tested at 37 °C in PBS.

**Figure VI-9** – Storage modulus ( $E'$ ) of the 3D structures obtained by DMA, tested at 37 °C in PBS.

**Figure VI- 10** – SEM images of the 3D structures after freeze-drying. Scale bars: 500  $\mu\text{m}$  (a and b), and 100  $\mu\text{m}$  (c).

### VI-1.5. Detailed description

The present disclosure relates to a silk-fibroin ink suitable for 3D printing. The ink for 3D printing now disclosed may be used in chemical and pharma industries, medicine, engineering, manufacturing namely for the production of capsules, fibers, membranes, particles, scaffolds, medical devices, microfluidic devices and patient-specific implants.

In an embodiment, the rheological properties of silk inks were determined as follows.

In an embodiment, the enzymatically cross-linked silk inks is subjected to high shear forces when used in 3D direct printing. The inks should have a shear-thinning behavior in order to, not only ensure the filament shape during the printing process but also the correct flow through the nozzle.



In an embodiment, two different concentrations of silk were used for these tests 16% (w/v) and 8% (w/v).

**Figure VI-3 and VI-4** shows that both silk inks present shear thinning properties. However, regarding **Figure VI-3**, it is observed a high decrease of viscosity as the shear rate increases. The SF 8% (w/v) ink presents higher viscosity at higher shear rates.

For both inks, the oscillatory measurements reveal an elastic behavior at low shear rates ( $G' > G''$ ). The dynamic yield stress can also be observed ( $G' = G''$ ).

Concerning the yield stress, the S16 ink presents a higher value, endorsing the previous results.

In an embodiment, the S16 ink was used in a 3D Bioplotter (Envisiotec) in order to print 3D Silk structures. The cartridge was previous prepared with S16 ink and further printed using a 22G nozzle. Square shape structures were printed (**Figure VI-5**). The structures have between 1 and 8 layers with a distance between strands of 1.5 mm.

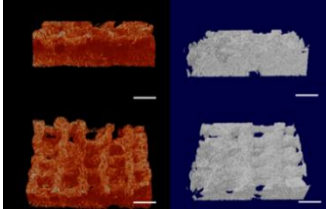
In an embodiment, after printed, the structures were frozen at -80 °C and freeze-dried (**Figure VI-6**).

In an embodiment, the characterization of 3D structures was carried out as follows. Since, the silk ink can be used for many different applications, it was chosen to define two different strategies that will allow developing cellular and acellular 3D structures, in a near future. As described above, one strategy consists in freeze dry the 3D structures (acellular strategy) and the other consists in the immersion directly in PBS (cellular strategy).

In an embodiment, ATR-FTIR analysis are presented to understand the conformation of the 3D structures, Dynamic mechanical analysis to access the mechanical properties, Scanning electronic microscopy and Micro-CT to understand the structures architecture after freeze-drying.

With these results, a new strategy to use silk as a bioink for 3D printing is disclosed.

Table VI-1 - Micro-CT results of a 3D structures after freeze dry. Scale bar: 500  $\mu\text{m}$ .

3D reconstructions	Mean Porosity (%)			Mean pore size ( $\mu\text{m}$ )	Mean trabecular thickness ( $\mu\text{m}$ )
	Microporosity	Macroporosity	Total porosity		
	$26.1 \pm 3.2$	$33.1 \pm 6.3$	$59.1 \pm 3.4$	$224.4 \pm 29.2$	$47.8 \pm 2.8$

In an embodiment, the mean porosity is defined as the percentage of pores of the structure. This was determined by micro-CT.

In an embodiment, the mean porosity of the microporosity is defined as  $26.1 \pm 3.2\%$ . This was determined by micro-CT.

In an embodiment, the mean porosity of the macroporosity is defined as  $33.1 \pm 6.3\%$ . This was determined by micro-CT.

In an embodiment, the mean porosity of the total porosity is defined as  $59.1 \pm 3.4\%$ . This was determined by micro-CT.

In an embodiment, the mean pore size is defined as  $224.4 \pm 29. \mu\text{m}$ . This was determined by micro-CT.

In an embodiment, the mean trabecular thickness is defined as  $47.8 \pm 2.8 \mu\text{m}$ . This was determined by micro-CT.

In an embodiment, dynamic mechanical analyses (DMA) were conducted as follows: the viscoelastic measurements were performed using a TRITEC8000B dynamic mechanical analyzer (Triton Technology, UK) in the compressive mode. The measurements were carried out at  $37 \text{ }^\circ\text{C}$ . The geometry of the samples was measured (measured each sample accurately with a micrometer) and the samples were clamped in the DMA apparatus and immersed in PBS solution. After equilibration at  $37 \text{ }^\circ\text{C}$ , the DMA spectra were obtained during a scan between 0.1 and 10 Hz.

In an embodiment, **Figure VI-8**, the damping properties ( $\tan \delta$ ) are represented. The damping properties represents the ability to disperse energy, ie, softer structures have more damping properties

than harder structures. That is what has been confirmed, as the material after printing (day 0) have higher values than after 7 days or after freeze drying.

In an embodiment, **Figure VI-9**, the storage modulus is represented. The storage modulus is related to the hardness of the material. Higher results of the hardness of the material may be obtained for freeze-drying material, in contrast with the material at day 0 or day 7.

The term "comprising" whenever used in this document is intended to indicate the presence of stated features, integers, steps, components, but not to preclude the presence or addition of one or more other features, integers, steps, components or groups thereof.

It will be appreciated by those of ordinary skill in the art that unless otherwise indicated herein, the particular sequence of steps described is illustrative only and can be varied without departing from the disclosure. Thus, unless otherwise stated the steps described are so unordered meaning that, when possible, the steps can be performed in any convenient or desirable order.

The disclosure should not be seen in any way restricted to the embodiments described and a person with ordinary skill in the art will foresee many possibilities to modifications thereof.

The above described embodiments are combinable.

The following claims further set out particular embodiments of the disclosure.

## VI-2. CLAIMS

1. Ink comprising a silk fibroin enzymatically cross-linked hydrogel comprising an aqueous solution of silk fibroin.
2. Ink according to the previous claim comprising 7-20% (w/v) of the aqueous solution of silk fibroin, preferably 8-18% (w/v), more preferably 11-15% (w/v).
3. Ink according to any one of the previous claims comprising a partial  $\beta$ -sheet conformation.
4. Ink according to any one of the previous claims comprising 0.1-10% (w/v) of keratin, preferably 0.5-5% (w/v), more preferably 1-3% (w/v).
5. Ink according to any one of the previous claims comprising 0.1-10% (w/v) of elastin, preferably 0.5-5% (w/v), more preferably 1-3% (w/v).

6. Ink according to any one of the previous claims, wherein the ink has a viscosity of  $100 \text{ kPa}\cdot\text{s}^{-1}$  –  $0.1 \text{ Pa}\cdot\text{s}^{-1}$  as function as shear rate at  $25 \text{ }^\circ\text{C}$ .
7. Ink according to any one of the previous claims, wherein the ink has a loss modulus ( $G''$ ) of 50-1500 Pa at  $25 \text{ }^\circ\text{C}$ .
8. Ink according to any one of the previous claims, wherein the ink has a storage modulus ( $G'$ ) of 10-100 Pa at  $25 \text{ }^\circ\text{C}$ .
9. Ink according to any one of the previous claims, wherein the molecular weight of the silk fibroin is 300-350 kDa.
10. Ink according to any one of the previous claims, wherein the molecular weight of the keratin is 40-60 kDa.
11. Ink according to any one of the previous claims, wherein the molecular weight of the elastin is 40-60 kDa.
12. Ink according to any one of the previous claims, wherein the hydrogel is a capsule, fiber, coating, membrane, particle, scaffold, medical device, microfluidic device or patient-specific implant.
13. Method to prepare the ink comprising a silk fibroin enzymatically cross-linked hydrogel any one of the previous claims comprising the following steps:
  - preparing 7%-20% (w/v) of an aqueous solution of silk fibroin;
  - adding 4%-6% (v/v) of horseradish peroxidase and 1.5%-3.5% (v/v) of hydrogen peroxide to the aqueous silk fibroin solution;
  - incubating the mixture at  $37 \text{ }^\circ\text{C}$  for 30-45 minutes for the complete formation of the hydrogel;
  - freeze-drying at  $-80 \text{ }^\circ\text{C}$  for 3 days.
14. Method according to the previous claim wherein the horseradish peroxidase is horseradish peroxidase type VI.
15. Method according to the previous claims 13-14 comprising a step of adding 1-3 % (w/v) of keratin.
16. Method according to the previous claims 13-15 comprising a step of adding 1-3 % (w/v) of elastin.
17. Use of the ink of any of the previous claims 1-12 for 3D printing.

VI-3. DRAWINGS

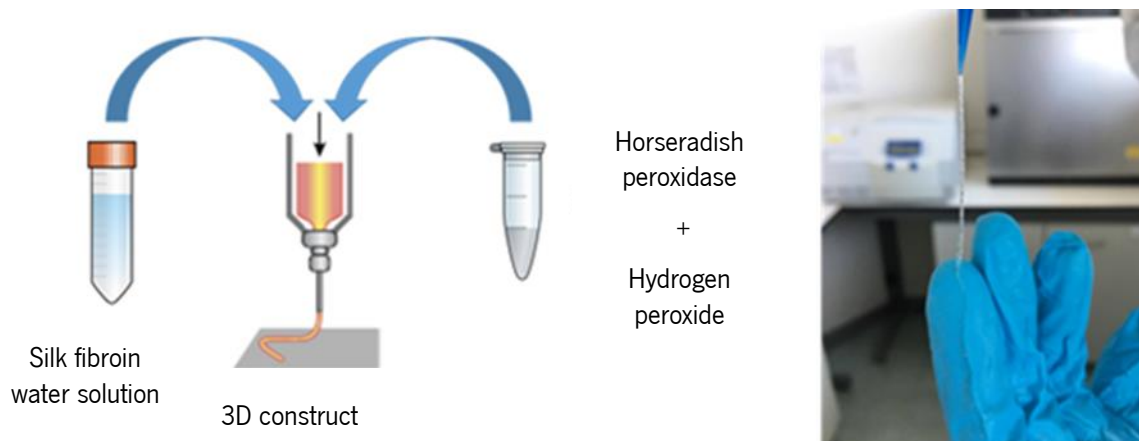


Figure VI-1 - Schematic representation of the preparation of SF ink for 3D printing.

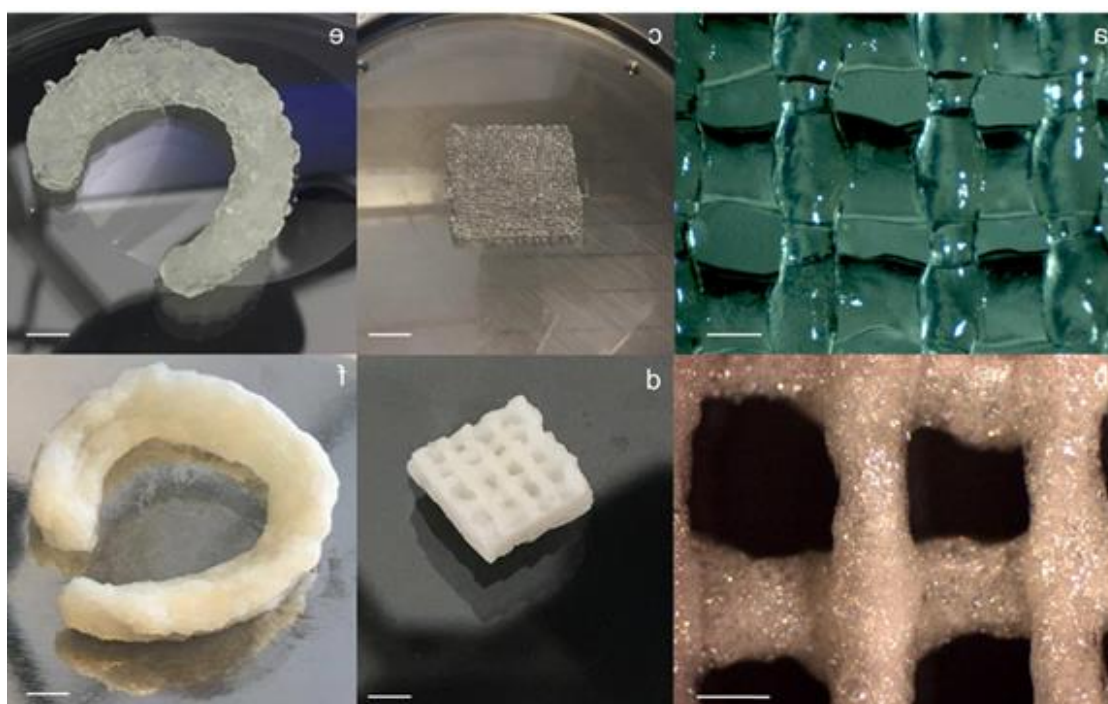


Figure VI-2 - 3D Printing of 3D structures a) 2-layer cube shape structure before freeze-drying and b) after freeze-drying. c) 6 layer cube shape (30x30mm) 3D structure. d) 6 layer cube shape (5x5 mm) structure after freeze-drying. e) human meniscus implant before freeze drying and f) after freeze-drying. Scale bars: 500  $\mu$ m (a and b); 1 mm (d, e and f); 10 mm (c).

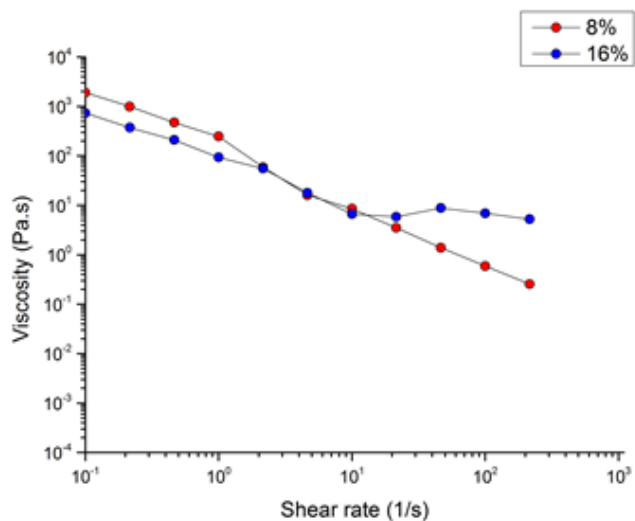


Figure VI-3 - Steady-Shear rheological measurements (frequency 1 Hz) for enzymatically cross-linked silk inks at different concentration (8% (w/v) and 16% (w/v) of silk solution).

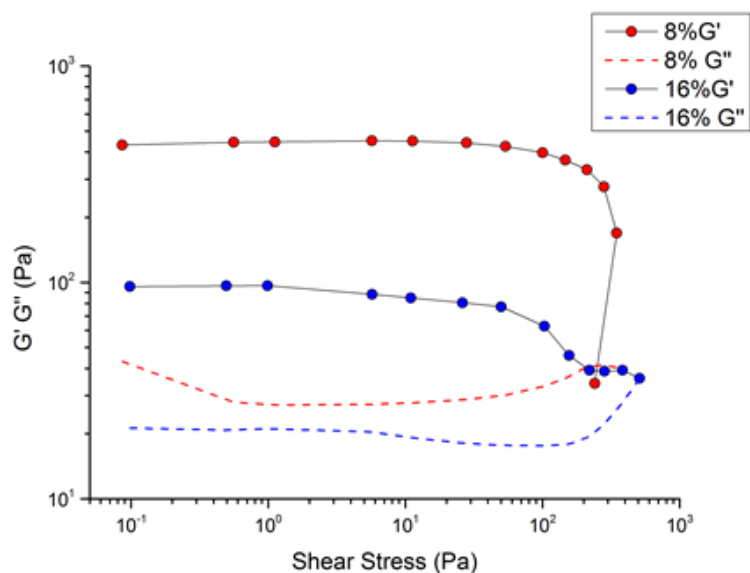


Figure VI-4 - Oscillatory rheological measurements (frequency 1 Hz) for enzymatically cross-linked silk inks at different concentration (8% (w/v) and 16% (w/v) of silk solution).

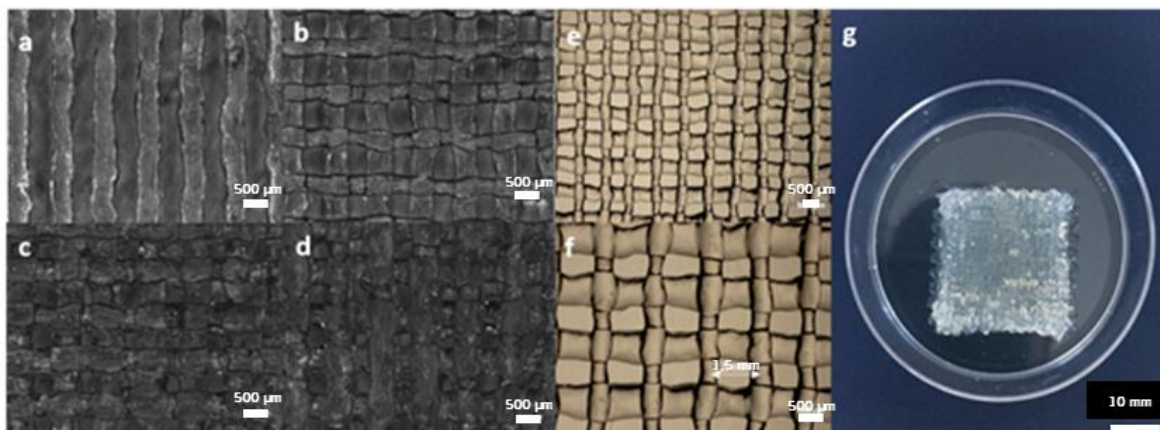


Figure VI-5 - Printed structures using S16 ink. (a) 1 layer, (b) 2 layers, (c) 4 layers, and (d) 5 layers cube shape printed structure. e), f) stereomicroscope images from 2 layers structures. g) 8 layers cube shape structure (30x30x4mm).

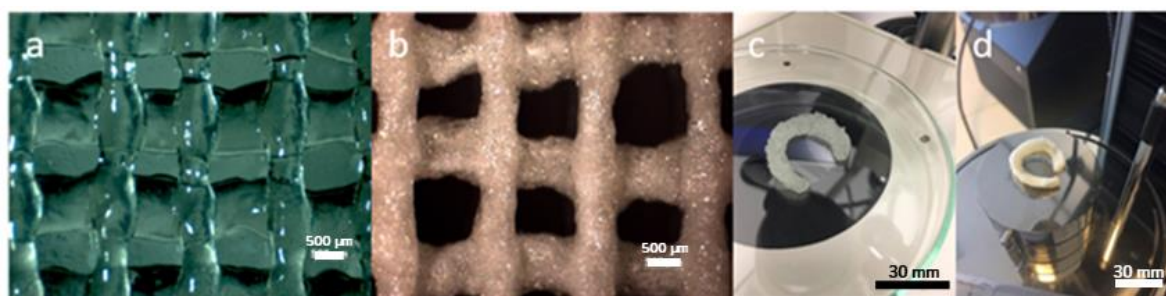


Figure VI-6 - 3D printed structures before (a and c) and after freeze-drying (b and d).

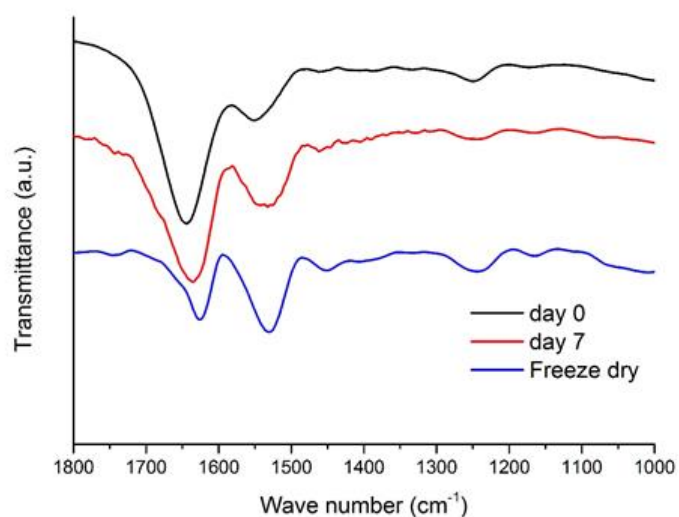


Figure VI-7 - ATR-FTIR spectra for the 3D structures after printing (day 0), after 7 days immersed in PBS (day 7), and after freeze drying (Freeze dry).

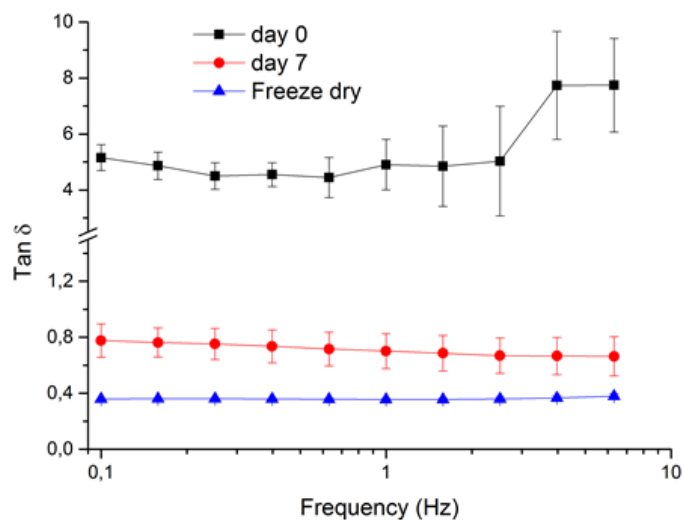


Figure VI-8 - Loss moduli ( $\tan \delta$ ) of the 3D structures obtained by DMA, tested at 37 °C in PBS.

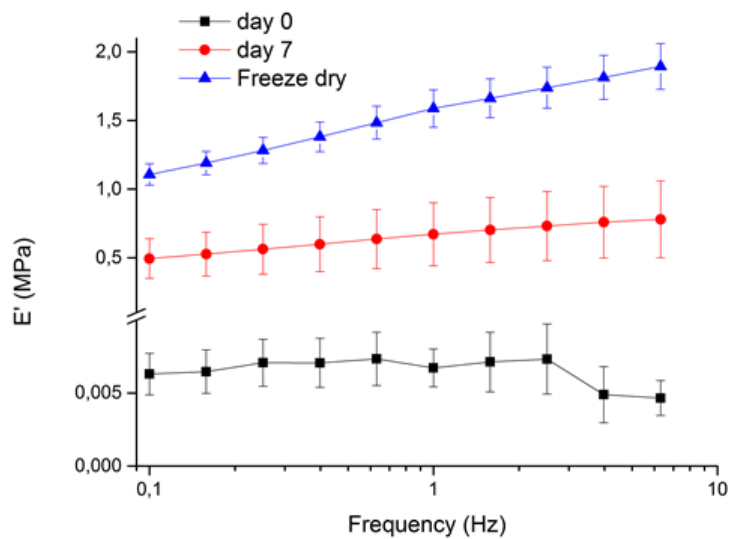


Figure VI-9 - Storage modulus ( $E'$ ) of the 3D structures obtained by DMA, tested at 37 °C in PBS.



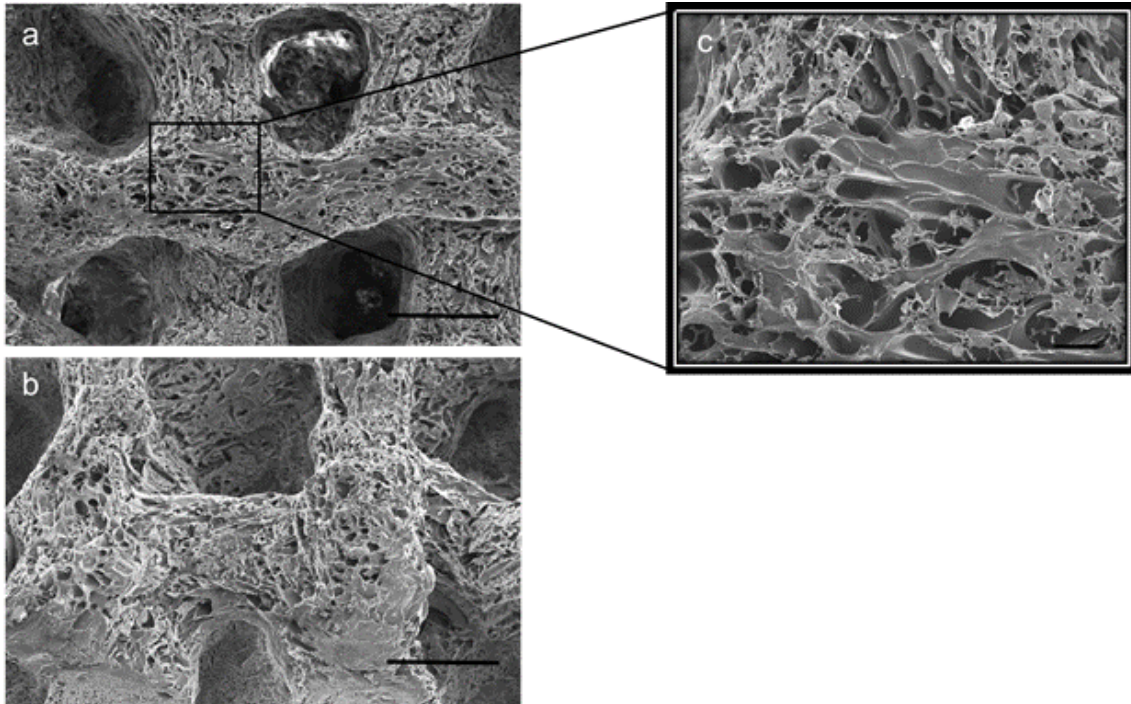


Figure VI-10 - SEM images of the 3D structures after freeze-drying. Scale bars: 500  $\mu\text{m}$  (a and b), and 100  $\mu\text{m}$  (c).

#### VI-4. REFERENCES

- [1] Murphy SV, Atala A. 3D bioprinting of tissues and organs. *Nature Biotechnology* 2014;32:773.
- [2] Kang HW, Lee SJ. A 3D bioprinting system to produce human-scale tissue constructs with structural integrity. 2016;34:312-9.
- [3] Teixeira LS, Feijen J, van Blitterswijk CA, Dijkstra PJ, Karperien M. Enzyme-catalyzed crosslinkable hydrogels: emerging strategies for tissue engineering. *Biomaterials* 2012;33:1281-90.

## Chapter VII

# Fast Setting Silk Fibroin Bioink for Bioprinting of Patient-Specific Memory- Shape Implants

Fast Setting Silk Fibroin Bioink for Bioprinting  
of Patient-Specific Memory-Shape Implants\*\*

**ABSTRACT**

The pursuit for the “perfect” biomimetic and personalized implant for musculoskeletal tissue regeneration remains a big challenge. 3D printing technology that makes use of a novel and promising biomaterials can be part of the solution. In this study, a fast setting enzymatic-cross-linked silk fibroin (SF) bioink for 3D bioprinting was developed. Their properties are fine-tuned and different structures with good resolution, reproducibility and reliability can be fabricated. Many potential applications exist for the SF bioinks including 3D bioprinted scaffolds and patient-specific implants exhibiting unique characteristics such as good mechanical properties, memory-shape feature, suitable degradation and tunable pore architecture and morphology.

---

\*\* This chapter is based on the following publication:

Costa J. B., Silva-Correia J., Oliveira J. M., and Reis R. L., "Fast Setting Silk Fibroin Bioink for Bioprinting of Patient-Specific Memory-Shape Implants", *Advanced Healthcare Materials*, vol. 6, issue 22, doi:10.1002/adhm.201701021, 2017.

Images from this publication resulted in the cover of the journal *Advanced Healthcare Materials*, vol. 6, issue 22 published in 22 November 2017.

## VII-1. INTRODUCTION

The regeneration or substitution of different tissues of the human body using artificially designed scaffolds and implants respecting the patient's unique anatomy is still a big challenge [1]. The "perfect" biomimetic implant should possess certain advantageous features similar to those observed in natural tissues to facilitate cell recruiting/seeding, adhesion, proliferation, differentiation and neo tissue genesis [2]. One way of achieving a highly precise biomimetic implant is to use 3D printing, an additive manufacturing technology that comprises a computer-assisted approach combined with the production of 3D structures. The endless potential of this technology led to its application in many areas, such as, medicine, engineering, manufacturing, etc. In Tissue Engineering (TE) field, 3D printing brings several advantages since it can provide reproducibility of the produced implants. Also, it allows the production of patient-specific implants that closely mimic the native tissue to regenerate in terms of size, shape, mechanical performance, and biodegradability, which can help to improve patient recovery time and to restore biofunctionality [3, 4]. In addition, 3D printing can improve biomimetism of the produced implants, that has been shown to be tremendously relevant for their biomechanical and biofunctional performance [5]. Until now, a large number of materials have been used in 3D printing for producing tissue engineered implants [6]. Nevertheless, the absence of suitable hydrogel bioinks for the 3D biofabrication process has been identified as a major barrier for a more rapid and successful progress in the field [7]. Natural biomaterials present similar features as compared to native tissues, and among the natural and biodegradable materials, alginate [8], gelatin [9] and hyaluronic acid [10] are the ones that have been more used in 3D Printing applications [6]. An ideal bioink should comprise several properties, such as, printability, biocompatibility, degradation, mechanical properties and biomimicry [5]. Silk fibroin (SF) from the silkworm *Bombyx mori* has been gaining a lot of attention in TE scaffolding for the last 30 years [11, 12]. Its excellent mechanical properties along with its biocompatibility, degradation properties, water-based processing and the presence of easily accessible chemical groups for functional modifications, filled almost all the required parameters for an ideal material for bioprinting. Ghosh *et al.* [13] reported one possibility of printing silk scaffolds using direct-write assembly, however the use of harsh conditions by employing organic solvents in the processing, such as a methanol bath, do not allow both achieving a stable and biocompatible construction of scaffolds in height and to print them with cells. Different approaches using enzymatically cross-linkable hydrogels have been developed in TE [14]. Our research group has been exploring the presence of tyrosine groups in silk to obtain hydrogel formation of silk solutions through enzymatic cross-link, by using

horseradish peroxidase (HRP) as enzyme and hydrogen peroxide (H<sub>2</sub>O<sub>2</sub>) as substrate [15, 16]. Taking this into account, it was hypothesized to use this enzymatic mediated cross-link method to develop a silk fibroin bioink for bioprinting of patient-specific memory-shape implants. Up to now, no literature has reported on using silk fibroin enzymatically cross-linked hydrogel as bioink for bioprinting. The development of this bioink would allow the production of scaffolds with tuned properties for specific uses, by simply applying different processing methods after the printing stage and the 3D printer settings. One big advantage of using our methodology is the possibility to mimic natural silk extrusion of spiders (**Figure VII-1a**), *i.e.* by bioprinting silk fibroin scaffolds in an amorphous state and allow inducing  $\beta$ -sheet conformation afterwards in many different ways. This advantage would allow using SF bioink in different printing strategies, either in cellular approaches, where the bioink is printed in combination with cells allowing the development of constructs, or in acellular approaches, creating scaffolds and patient-specific memory-shape implants.

## VII-2. MATERIALS AND METHODS

### VII-2.1. Materials

Silk derived from the silkworm *Bombyx mori* in the form of cocoons was provided by the Portuguese Association of Parents and Friends of Mentally Disabled Citizens (APPACDM, Castelo Branco, Portugal). All reagents were purchased from Sigma-Aldrich (St. Louis, MO, USA) unless otherwise stated.

### VII-2.2. Preparation of silk fibroin (SF) bioink

Purified silk fibroin (SF) was prepared by removing the glue-like protein sericine from the cocoons in a 0.02 M boiling sodium carbonate solution for 1 hour, followed by rinsing with distilled water in order to fully remove the degumming solution [17]. A 9.3 M lithium bromide solution was used to dissolve the purified SF for 1 hour at 70 °C, and dialyzed in distilled water for 48 hours using the benzoylated dialysis tubing (MWCO: 2 kDa). SF was concentrated against a 20 (w/v) poly(ethylene glycol) solution for at least 6 hours. The final concentration of SF was determined by measuring the dry weight of the SF solution placed in the oven at 70 °C overnight. Meanwhile, the prepared SF solution was stored at 4 °C until further use. SF solution was diluted to 16% (w/v) in distilled water and

combined with horseradish peroxidase solution (HRP type VI, 0.84 mg.mL<sup>-1</sup>) and hydrogen peroxide solution (H<sub>2</sub>O<sub>2</sub>, 0.36% (v/v); Panreac, Barcelona, Spain). A mixture of SF ink, 5% (v/v) HRP solution and H<sub>2</sub>O<sub>2</sub> solution at three different concentrations, 1.5% (SI15), 2.5% (SI25) and 3.5% (SI35) (v/v) was prepared and incubated at 37 °C for 30 minutes.

### VII-2.3. Rheological properties of silk fibroin bioinks

The rheological analyses of the developed silk fibroin bioinks were performed using a Kinexus pro+ rheometer (Malvern Instruments, UK) and using the acquisition software rSpace (Malvern Instruments, UK). For the oscillatory experiments the measuring system was equipped with stainless steel (316 grade) parallel plates using an upper measurement geometry plate of 20 mm diameter. Frequency-sweep and strain sweep experiments were performed using SF inks prepared as described above. For the rotational experiments, the measuring system was equipped with an upper measurement geometry cone (40 mm diameter and 4° angle). In addition, a tack adhesion test was performed with a Peltier plate cartridge using a 20 mm upper plate and 65-mm lower plate (stainless steel). Following a contact period of 2 seconds, the gap was increased linearly at 0.01 mm.s<sup>-1</sup> and the normal force recorded as a function of time. These experiments were performed at room temperature and all plots represent the average of at least 3 samples.

### VII-2.4. 3D printing of scaffolds

As described before, the SI25 was prepared directly in the cartridge and incubated at 37°C for 30 minutes. Using a 4<sup>th</sup> generation Envisiontec 3D Bioplotter, the silk fibroin bioink was extruded pneumatically. The nozzle size had 400 µm of diameter and the 3D scaffolds were constructed using pressures ranging from 250 to 350 kPa at a speed of 5 to 8 mm.s<sup>-1</sup>. The SF patient-specific memory-shape implants of human meniscus were printed through a reverse engineering approach using a semi-automatic methodology of segmenting meniscus tissue from volumetric MRI datasets and reconstruction of 3D models with an advanced segmentation software [3]. The scaffolds and implants were further frozen at -80°C for 2 days and freeze-dried for 3 days (Telstar-Cryodos-80, Spain). In order to access the changing of conformation to β-sheet over time, SF scaffolds and implants were both immersed directly in PBS after printing. Before any characterization test the freeze-dried scaffolds were immersed in ethanol 70% for 3 hours and then in PBS overnight.

### VII-2.5. Fourier transform infrared spectroscopy

The chemical composition and structural conformation of the SF 3D scaffolds were analyzed by Fourier transform infrared (FTIR) spectroscopy (Perkin-Elmer 1600 series equipment, CA, USA) under an attenuated total reflectance (ATR) model (IRPrestige-21, Shimadzu, Japan). All spectra were obtained between 4600 and 800  $\text{cm}^{-1}$ , at a 4  $\text{cm}^{-1}$  resolution with 50 scans. PBS was used as background.

### VII-2.6. Dynamic mechanical analysis

The viscoelastic measurements were performed using a TRITEC8000B dynamic mechanical analyzer (Triton Technology, UK) in the compressive mode. The measurements were carried out at 37 °C. The geometry of the samples was measured (each sample was accurately measured with a micrometer) and the samples were clamped in the DMA apparatus and immersed in PBS solution. After equilibration at 37 °C, the DMA spectra were obtained during a frequency scan between 0.1 and 10 Hz. The experiments were performed under a constant strain amplitude (50  $\mu\text{m}$ ).

### VII-2.7. Cyclic uniaxial compression test

Compressive tests were performed by using a Universal Testing Machine (Instron 4505) with a 1 kN load cell at room temperature (RT). As previously, the scaffolds were immersed in PBS overnight at 37 °C. The cross-head speed was set at 2  $\text{mm}\cdot\text{min}^{-1}$  and tests were run until achieving 80% reduction in specimen height. The test was repeated over 5 cycles. The compressive modulus (E) was defined by the slope of the initial linear section of the stress–strain curve. A minimum number of 3 samples were tested.

### VII-2.8. *In vitro* weight loss

The stability of the SF bioprinted scaffolds was evaluated by enzymatic degradation test. Protease XIV solution (0.5  $\text{U}\cdot\text{mL}^{-1}$ ) was prepared by dissolving the enzyme in distilled water. The initial weight of the 3D scaffold was measured, and then the scaffolds were hydrated in PBS at 37 °C overnight, followed by immersion in 5 mL of protease solution. The enzyme solution was changed every 48 hours.

The samples were weighed after 0.16, 0.33, 1, 7, 14, 21 and 28 days of soaking in the degradation solution.

The weight loss ratio was obtained using the following equation:

**Equation VII-1 - Determination of weight loss ratio.**

$$\text{weight loss ratio} = \left[ \frac{(m_i - m_{d,t})}{(m_i)} \right] \times 100\%$$

where,  $m_i$  is the initial weight of the sample, and  $m_{d,t}$  is the weight of the degraded sample at each time point. Three specimens per group were used for each time point.

### VII-2.9. Scanning electron microscopy

The morphology of the 3D scaffolds after freeze-drying was observed by scanning electron microscopy (SEM) (Nova NanoSEM 200; FEI, Hillsboro, OR, USA). Before the observation, the scaffolds were coated with one layer of Au/Pd (SC502–314B) in a E6700 coater (Quorum Technologies, East Grinstead, UK).

### VII-2.10. Micro-computed tomography

The architecture of the 3D scaffolds was evaluated using a high-resolution Micro-CT Skyscan 1072 scanner (Skyscan, Kontich, Belgium) with a pixel size of 10  $\mu\text{m}$ . Data sets were reconstructed using standardized cone-beam reconstruction software (NRecon v1.4.3, SkyScan). Representative dataset of the slices was segmented into binary images with a dynamic threshold of 22-40 (grey values). Then, the binary images were used for morphometric analysis (CT Analyser, v1.5.1.5, SkyScan) and to build the three-dimensional models (ANT 3D creator, v2.4, SkyScan).

### VII-2.11. hASCs isolation and expansion

Human adipose-derived stem cells (hASCs) were isolated from abdominal subcutaneous adipose tissue samples obtained from liposuction procedures on healthy male and female donors with ages between 18 and 57 years, after informed consent, under established cooperative agreements between



Hospital da Senhora da Oliveira (Guimarães, Portugal) and 3B's Research Group. After the liposuction procedure, the samples were processed within 24 hours and hASCs were enzymatically isolated. The expansion procedure occurred in basal medium consisting of Alpha-MEM ( $\alpha$ -MEM; Life Technologies, Scotland) supplemented with 10% fetal bovine serum (FBS; Biochrom AG, Germany) and 1% antibiotic/antimycotic solution (final concentration of penicillin 100 units.mL<sup>-1</sup> and streptomycin 100 mg.mL<sup>-1</sup>; Gibco, GB). Cells were cultured until confluence, at 37 °C in an atmosphere of 5% CO<sub>2</sub> incubator, by changing the culture medium every 2 days.

#### VII-2.12. Seeding of hASCs in the 3D bioprinted scaffolds after freeze-drying

The *in vitro* tests were performed in 3D bioprinted scaffolds in the form of a cylinder with 4 mm of diameter and 2 mm of height. The samples were immersed in ethanol 70% (6 hours) for sterilization. Before cell seeding, all samples were washed 3x in PBS and then left in  $\alpha$ -MEM overnight. The scaffolds were transferred to 48-well suspension cell culture plates (Cellstar, Greiner Bio-One, Austria). Confluent hASCs (at passage 3) were detached with TrypLE Express (1X) (Life Technologies, Carlsbad, CA, USA) and seeded at a density of 8x10<sup>4</sup> cells/scaffold. The 48-well suspension cell culture plates were kept in the CO<sub>2</sub> incubator at 37 °C for 2 hours, and then 1 mL of  $\alpha$ -MEM culture medium were added to each well. Culture medium was changed every 2 days and samples were removed at different culture times (1, 3 and 7 days).

#### VII-2.13. Cell viability and metabolic activity

Live/Dead assay was performed in order to microscopically assess cell viability. Cell seeded scaffolds were immersed in a calcein AM/propidium iodide (PI) solution at 1:3 ratio in PBS, for 30-40 minutes, at 37 °C in an atmosphere of 5% CO<sub>2</sub> incubator, and protected from light. Viable cells metabolize calcein AM (Invitrogen, USA 1 mg.mL<sup>-1</sup>) into green fluorescent calcein (Ex/Em  $\approx$  495/515 nm), while dead cells presenting damaged cell membrane find their DNA stained red by PI (Invitrogen, USA 1mg.mL<sup>-1</sup>; Ex/Em  $\approx$  493/636 nm). The samples were washed 2x with PBS and imaged using a Transmitted and Reflected Light Microscope (Zeiss Axio Imager.Z1m, Zeiss, Germany).

In other hand, hASCs metabolic activity was evaluated using Alamar Blue (AB). AB is a dye that yields a colorimetric change and subsequently a fluorescent signal when incubated with metabolically-active cells. Cell culture medium mixture with 10% AB was added to the different culture wells and

incubated for 4 hours at 37 °C. Then, 100 µl of each solution were removed to white opaque 96-well plates, in triplicates. Fluorescence was monitored at Ex/Em  $\approx$  530/590 nm, using a microplate reader (Synergy HT, BioTek Instruments, USA). The culture well plates were washed with PBS and fresh medium was added. After 2 hours, the culture medium was replaced by fresh medium to avoid any reminiscence of AB. The metabolic activity values were calculated by normalization with the mean fluorescence value obtained for the controls (scaffolds without cells).

#### VII-2.14. Cell proliferation:

The quantity of double stranded DNA (dsDNA) was determined using a fluorimetric dsDNA quantification kit (PicoGreen, Molecular Probes, Invitrogen Corporation, USA), according to the manufacturer's instructions. This assay is based on the principle that the quantity of dsDNA is directly proportional to cell number. At each time point, samples were washed twice with PBS solution and kept in 1 mL of ultrapure water at  $-80$  °C until further analysis. Constructs were thawed at RT, sonicated for 1 hour to induce complete membrane lysis, and centrifuged at 300 *g* for 5 min to spin down all non-genomic materials. After centrifugation, the scaffold was discarded and the supernatant collected to new 1.5 mL sterile Eppendorf tubes. Supernatant fluorescence was measured at an excitation wavelength ( $\lambda$ ) of 485/20 nm and at an emission  $\lambda$  of 528/20 nm, in a microplate reader (Synergy HT, BioTek Instruments, USA). The quantification of dsDNA was calculated according to a standard curve prepared with concentrations ranging between 0 and 2  $\mu\text{g}\cdot\text{mL}^{-1}$ , relating quantity of DNA and fluorescence intensity. Scaffolds without cells were used as controls.

#### VII-2.15. Statistical analysis

The results from mechanical analysis, degradation ratio, mean porosity, mean pores size and mean trabecular thickness were presented as mean  $\pm$  standard deviation. At least 3 specimens were used in each condition. Statistical analysis was performed using the GraphPad Prism 5.0 (GraphPad Software, La Jolla, CA, USA). First, a Shapiro-Wilk test was used to ascertain about the data normality. For DMA assay and tack adhesion test, the differences between the experimental results at 1 Hz as well as the differences in the adhesion values, respectively, were analyzed using a Kruskal-Wallis test followed by Dunn's multiple comparison test. For all the biological quantification assay the differences between experimental results were also analyzed by the same method. Three independent experiments

were performed for cell studies (Metabolic activity and cell proliferation), and three samples were analyzed per group in each culturing time. Statistical significant differences were represented by \* ( $p < 0.5$ ), \*\* ( $p < 0.01$ ) and \*\*\* ( $p < 0.001$ ).

### VII-3. RESULTS AND DISCUSSION

The SF bioinks should have a shear-thinning behavior in order to, not only ensure the filament shape during the printing process but also the correct flow through the nozzle [18, 19]. In this study, we developed SF bioinks with 3 different conformations (SI15, SI25 and SI35) and assessed their rheological properties. Oscillatory frequency measurements in **Figure VII-1bi** showed that storage modulus  $G'$  and loss modulus  $G''$  increased as higher volumes of hydrogen peroxide were used. All the formulations presented gel-like characteristics ( $G' > G''$ ). The predominant SI25 and SI35 elastic behavior was also confirmed when oscillatory measurements were performed at low strains (**Figure VII-1bii**). It was demonstrated that at a certain shear stress (0.1 Pa), the viscoelastic behavior of SI15 becomes similar to a viscous liquid. Shear-thinning behavior can be observed in **Figure VII-1biii**, where viscosity decreases as the shear rates increases. SI25 exhibited higher viscosity at shear rates ranging from 0.01 to 50  $s^{-1}$ , that are the typical values of shear rates that are applied in these type of printing [19]. The evaluation of adhesion is also critical when considering the use of a biomaterial as bioink for 3D printing applications. The inks should have a degree of adhesion high enough to stick the first layer to the printer platform and to ensure that each layer of ink connects to the other adjacent layers. Thus, the SF bioinks with 3 different conformations were subjected to adhesion tests. In **Figure VII-1biv**, adhesion values for the three inks are presented, where the area under force time curve represents the adhesive strength. SI25 clearly demonstrated higher adhesion properties than SI15 and SI35, however only significant differences were observed when comparing values of SI15 and SI25 ( $p < 0.01$ ). Considering the results obtained in the rheology measurements, and after performing some basic extrusion tests (data not shown), it was decided that the formulation showing the best performance to be used as a bioink was the SI25 (**Figure VII-1c**).

In order to demonstrate the reliability of the selected bioink (SI25), different scaffolds were produced (**Figure VII-1d**). Cube shaped 3D scaffolds with different number of layers ( $n=2-6$ ) were printed, with filamentary features arrayed with a center-to-center distance of around 1.5 mm (**Figures VII-1di-iv**). The filamentous composing the SF scaffolds have around 500  $\mu m$  of diameter. In **Figures VII-**

**1dv-vi**, the printing of a patient-specific memory-shape human meniscus implant is also shown. For printing this type of personalized implants, a 3D model of human meniscus was previously obtained by our group through an advanced segmentation method from knee MRI [3]. Considering the bioprinting needs for a hydrogel, we believe that a very good spatial resolution of the printed objects was achieved, with a consistent resolution and fidelity comparing with previous results [8, 20-22]. For further characterization, a 6-layer cube shaped scaffold was selected (**Figure VII-1div**).

As described above, and envisioning the future application of this bioink in cellular and acellular strategies, the scaffolds studied in this work comprised 3D bioprinted scaffolds just after printing or directly immersed in PBS after printing and freeze-dried 3D bioprinted scaffolds.

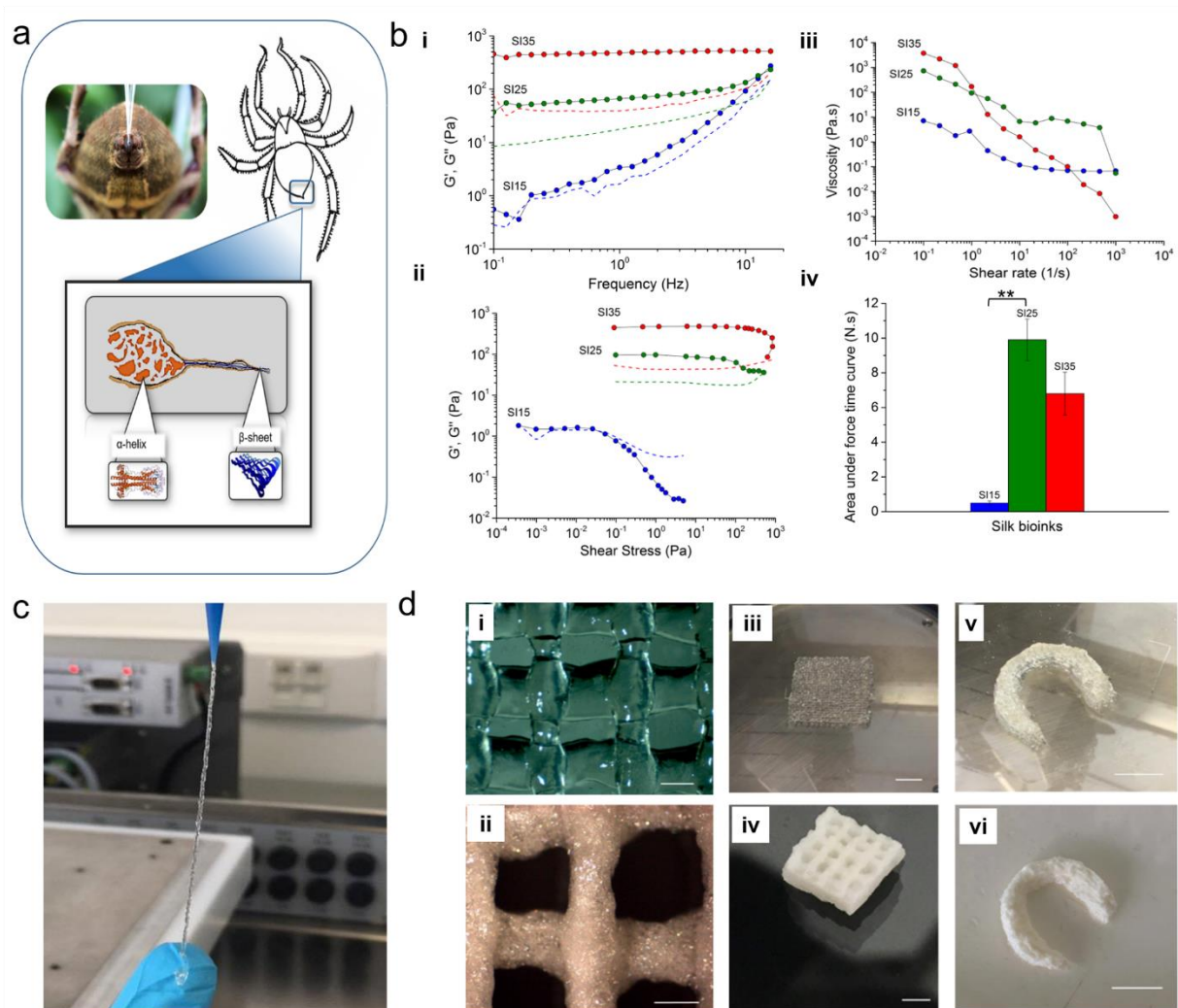


**Figure VII-1 - Rheological behavior of silk fibroin (SF) bioinks and 3D Printing of 3D scaffolds. (a)** Extrusion of silk by spider. **(b)** (i) Oscillatory rheological measurements as function of frequency ( $n=3$ ), (ii) oscillatory rheological as function of shear stress ( $n=3$ ), (iii) steady shear measurements at frequency of 1 Hz ( $n=3$ ), and (iv) tack adhesion measurements ( $n=3$ ). **(c)** Extrusion of SI25 bioink. **(d)** (i) SF with amorphous scaffold (conformation

before freeze-drying), (ii) SF with crystalline scaffold ( $\beta$ -sheet conformation) after freeze-drying, (iii) 6-layer cube shape 3D scaffold, (iv) 6 layer cube shape 3D scaffold after freeze-drying, (v) patient-specific memory-shape meniscus implant before freeze-drying, and (vi) after freeze-drying. Statistical significant differences were represented by \* ( $p < 0.5$ ), \*\* ( $p < 0.01$ ) and \*\*\* ( $p < 0.001$ ). Scale bars: 500  $\mu\text{m}$  (di and dii); 1 mm (div); 10 mm (diii, dv and dvi).

Previous results already showed evidence that enzymatically cross-linked silk hydrogels undergo from a random coil conformation (transparent appearance) into a  $\beta$ -sheet conformation (opaque appearance) over time [15]. Since the proposed SF bioinks are prepared by enzymatic cross-link, the conformational changes of the 3D scaffolds were studied by attenuated total reflectance Fourier transform infrared spectroscopy (ATR-FTIR) (**Figure VII-2a**). The main absorbance peaks of the 3D silk scaffolds just after printing (day 0) were observed at 1650  $\text{cm}^{-1}$  and 1538  $\text{cm}^{-1}$ . These peaks are associated to random coil conformation [15]. After 7 days in PBS (day 7), it was observed a slight deflection of the peaks to the right, confirming the conformation change from random coil to  $\beta$ -sheet. In the 3D scaffolds immersed in PBS for 7 days, as well as in freeze-dried scaffolds, the peaks were located at 1627 $\text{cm}^{-1}$  and 1535  $\text{cm}^{-1}$ , suggesting a predominance in  $\beta$ -sheet conformation [23]. The degradation profile of the 3D scaffolds was accessed both after printing (day 0) and after freeze-drying (**Figure VII-2b**). As expected, the scaffolds directly immersed in PBS after printing revealed a faster degradation profile, achieving complete degradation after 21 days. Yan *et al.* [15] reported a higher degradation ratio of SF hydrogels, when random coil is the predominant conformation (amorphous state). In the case of the freeze-dried scaffolds, the degradation ratio was 22.5% after 28 days in the degradation solution. The reported data confirmed that the 3D scaffolds present lower degradation when  $\beta$ -sheet conformation is predominant [24]. The freeze-dried scaffolds showed appropriate degradation behavior for cartilage regeneration, since in this tissue long-term mechanical support is needed. In addition, it was previously reported that silk fibroin is able to degrade in the presence of protease XIV and the degradation products are not cytotoxic to cells [25].

The mechanical performance of the 3D printed scaffolds was assessed using dynamic mechanical analysis (**Figures VII-2c and VII-2d**). Since the scaffolds are intended to use in a hydrated environment, the three formulations were tested in a PBS bath at 37 °C. The freeze-dried scaffolds and the scaffolds maintained in PBS (day 7) exhibited a substantially higher storage modulus than the scaffolds in an amorphous state (day 0). Regarding the frequency that can be found during normal ambulation (1Hz), the freeze-dried scaffolds and the day 7 scaffolds revealed a storage modulus of  $1.59 \pm 0.14$  MPa and  $0.67 \pm 0.23$  MPa, respectively. However, only significant differences were observed comparing values for freeze-dried scaffolds with the day 0 scaffolds at the frequency of 1 Hz ( $p < 0.01$ ). In addition, the

values of storage modulus for freeze-dried scaffolds and day 7 scaffolds increased from  $1.11 \pm 0.08$  MPa to  $1.89 \pm 0.17$  MPa and  $0.49 \pm 0.14$  MPa to  $0.78 \pm 0.28$  MPa, respectively, as frequency increased from 0.1 to 10 Hz. Concerning the damping properties ( $\tan \delta$ ), day 0 scaffolds presented higher values than day 7 and freeze-dried scaffolds, as expected. Again, only significant differences were observed comparing values for freeze-dried scaffolds with the day 0 scaffolds at the frequency of 1 Hz ( $p < 0.01$ ). These values corroborate the results obtained in the storage modulus data, where day 0 scaffolds exhibited higher propensity to dissipate energy due to its lower stiffness. At the frequency of 1 Hz, the freeze-dried scaffolds and the day 7 scaffolds presented damping factor values of  $0.36 \pm 0.01$  and  $0.7 \pm 0.12$ , respectively. Under dynamic conditions, a central body segment of a medial human meniscus presented a storage modulus of 0.87 MPa and a damping factor of 0.13, revealing very similar values as compared with the 3D printed scaffolds [26]. Overall, the mechanical behavior of the 3D freeze-dried scaffolds and day 7 scaffolds is very similar to articular cartilage [24, 27] or meniscus native tissue [26]. **Figure VII-2e** shows a printed patient-specific memory-shape meniscus implant that was submitted to 80% compressive strain. Memory-shape or shape memory materials (SMMs) are featured by the capability to recover their original shape when a particular stimulus is applied [28]. In **figure VIII-2e**, total shape recovery of the 3D silk scaffold is exhibited, demonstrating its memory-shape properties, which outstand the good mechanical performance of these scaffolds. In addition, a cyclic uniaxial compression test was made, revealing similar mechanical behaviors over 5 cycles. The results obtained in the stress-strain plot (**Figure VII-2f**) and the values of compressive stress for 25%, 50% and 80% of strain (**Figure VII-2g**) confirm the memory-shape properties stated before. Depending on test type and conditions, the reported compressive modulus for human meniscus ranged between 0.09 and 0.23 MPa [29] which is very similar to the range obtained for the 3D bioprinted scaffolds after freeze-drying (0.15 – 0.32 MPa) (**Supplementary Table VII-1, Supplementary material**). We hypothesize that the scaffolds memory-shape feature observed can be related to both scaffolds architecture (micro- and macro-porosity) and molecular changes resulting from enzymatic polymerization of tyrosine residues, which promote an increase in crosslinking density and ultimately led to an increase of the scaffolds elasticity. McGill *et al.* [30] reinforced the benefits and the tuning possibility of this HRP-mediated crosslinking mechanism by modulating the silk and hydrogen peroxide concentration. The authors concluded that silk hydrogels have tunable matrices and by changing the reaction conditions, is possible to adjust not only the mechanical properties but also the diffusion behavior. This promising mechanism based on unique patterns at the molecular level can be a preponderant tool in fibrocartilage

regeneration approaches, allowing us to envision the modulation of blood vessels ingrowth, where vascularized hierarchic native tissues should be mimicked.

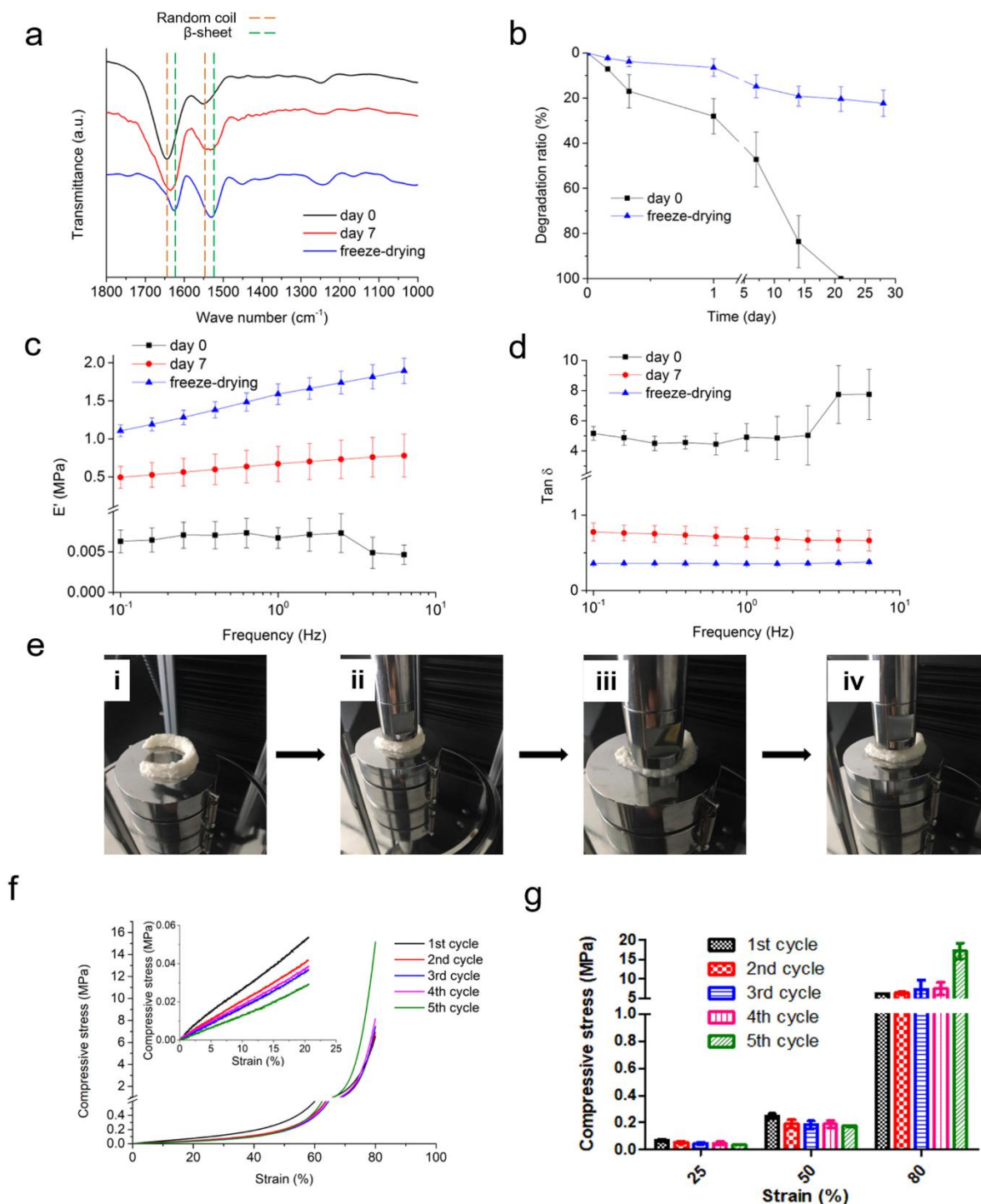


Figure VII-2 - Characterization of 3D silk scaffolds. (a) Chemical characterization of 3D scaffolds. FTIR spectra of the 3D scaffolds (day 0, day 7 and after freeze-drying) (n=3). (b) *In vitro* degradation test. Degradation profile using 0.5 U.mL<sup>-1</sup> of protease XIV solution for the 3D scaffolds (day 0 and freeze-drying) (n=3). (c) Storage modulus and (d) loss modulus of 3D scaffolds as function of frequency (0.1 to 10 Hz) (n=3). (e) (i) Patient-specific memory-shape meniscus implant into Instron platform, (ii) initial appearance before compression, (iii)

implant under a compressive strain of 80%, (iv) returning to original shape. (f) Stress-strain plot of cyclic uniaxial compression test (5 cycles) (n=3). (g) Compressive stress of cyclic uniaxial compression test as function of strain (25%, 50% and 80%) (n=3).

The pore architecture and morphology of the 3D silk scaffold was investigated using SEM and Micro-CT. Freeze-drying methodologies in silk scaffolds already proved to induce porosity in different ways [31-33]. It is known that specific cells require different pore sizes for optimal attachment, growth and motility and a porous surface improves the implant anchorage to the natural tissue [34]. SEM images and the 3D reconstruction obtained from Micro-CT analysis provided details of the surface morphology of the 3D scaffolds and the patient-specific meniscus implant (**Figure VII-3**). SEM analysis of the freeze-dried bioprinted scaffolds revealed the presence of both macro porosity (**Figure VII-3a**) and micro porosity (**Figure VII-3b**). The ability to control the macro porosity of the 3D scaffolds is one of the biggest advantages of using 3D printing technologies. From the qualitative and quantitative analysis of porosity by Micro-CT (**Figure VII-3c and Supplementary Table VII-2, Supplementary material**), it can be observed that the 3D scaffolds exhibited a total porosity of  $59.1 \pm 3.4\%$ , of which  $26.1 \pm 3.2\%$  relates with micro porosity and  $33.1 \pm 6.3\%$  reports to macro porosity. Combining the macro and micro porosity, the mean pore size and pore thickness of the entire 3D freeze-dried scaffolds are  $224.4 \pm 29.2 \mu\text{m}$  and  $47.8 \pm 2.8 \mu\text{m}$ , respectively. Zhang *et al.* [35] reported that scaffolds with a mean pore size of around  $215 \mu\text{m}$  presented superior results in biological assays.

The biocompatibility of the bioprinted SF scaffolds was also evaluated with a 7 days-period biological assay. Human adipose-derived stem cells (hASCs) were seeded onto the scaffolds and cell adhesion and proliferation were assessed. The live/dead assay showed living cells attached on the surface of the scaffolds (**Figure VII-3e**) during culturing time. This qualitative assay showed an evolution in terms of cell proliferation, presenting some adhered cells at day 1 that evolved to a higher number of well spread cells at day 7. In addition, **Figure VII-3f** showed cells attached to the surface of the bioprinted SF scaffold, demonstrating good cell adhesion and proliferation. Quantitative analysis comprised the assessment of cells metabolic activity by Alamar Blue assay and cells proliferation by DNA content up to 7 days of culturing. The results of metabolic activity were normalized with the DNA content (**Figure VII-3e**). A significant increase was observed after 7 days of culturing, as compared to day 1 and day 3 ( $***p < 0.001$ ). These results confirmed the previous qualitative data indicating cells proliferation throughout the culturing period. Silk-based scaffolds presented good biological performance when seeded with hASCs. In a work performed by Ribeiro *et al.* [17], SF biotextiles also showed good



hASCs adhesion and proliferation, as well as the ability of these type of cells to differentiate in an osteogenic lineage.

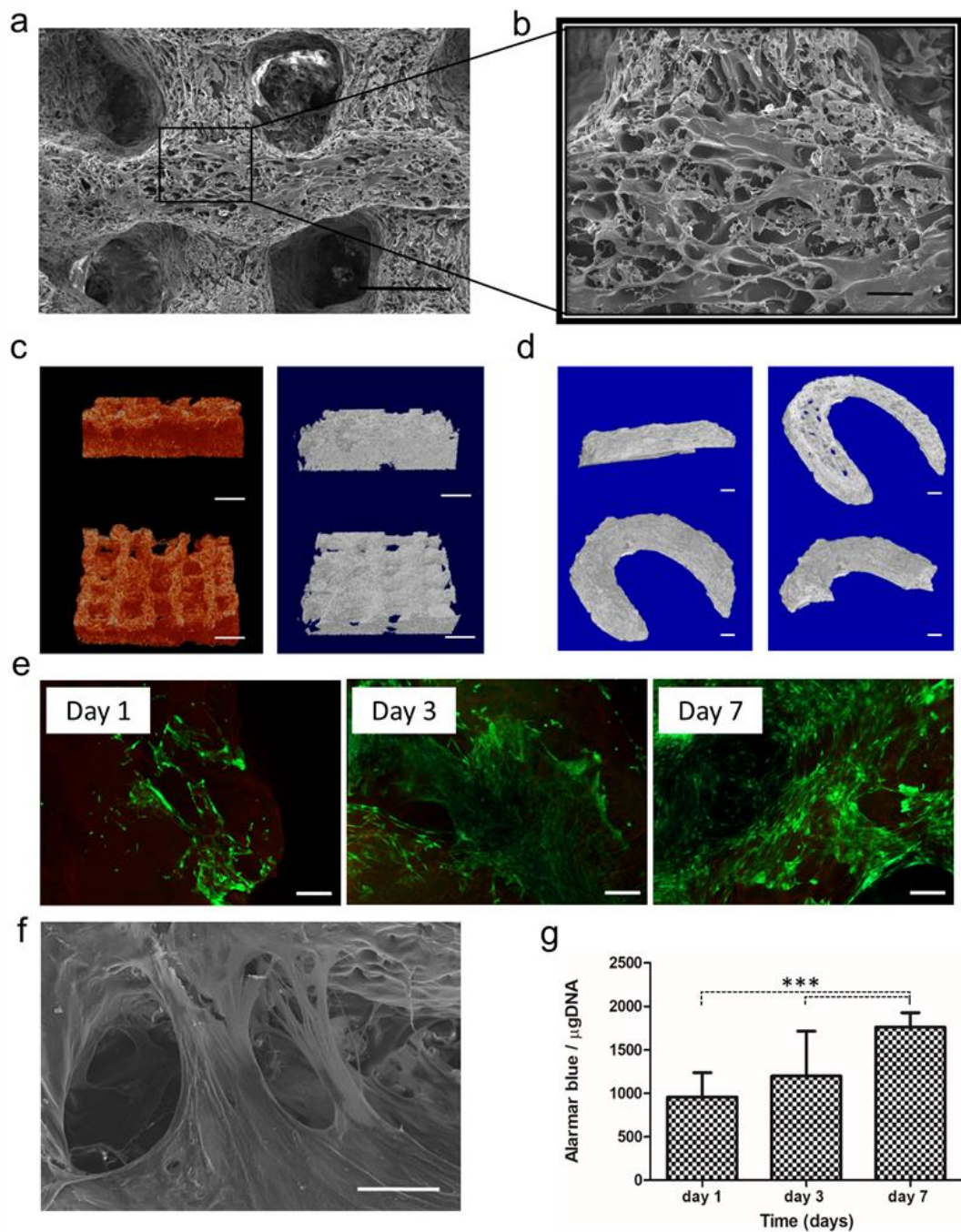


Figure VII-3 - Morphology and *in vitro* biological evaluation of bioprinted SF scaffolds after freeze-drying. Evaluation was performed after 1, 3 and 7 days of culturing in scaffolds seeded hASCs. (a) SEM image of freeze-dried scaffolds. (b) SEM image of freeze-dried scaffolds at higher magnification. (c) 3D reconstruction by Micro-CT. (d) 3D reconstruction of patient-specific human meniscus implant. (e) Calcein AM and propidium iodide staining. (f) SEM image of the bioprinted scaffolds seeded with hASCs after culture for 7 days. (g) Metabolic activity by Alamar Blue assay normalized with DNA content. Statistical significant differences were

represented by \* ( $p < 0.5$ ), \*\* ( $p < 0.01$ ) and \*\*\* ( $p < 0.001$ ). Scale bars: 500  $\mu\text{m}$  (a); 100  $\mu\text{m}$  (b); 1 mm (c); 2.5 mm (d); 200  $\mu\text{m}$  (e) and 50  $\mu\text{m}$  (f).

#### VII-4. CONCLUSIONS

In this work, we demonstrated for the first time the development of a fast-setting SF bioink with potential to be used in different applications in 3D printing. The developed SF bioink has unique properties such as elasticity and adhesion and is capable to be printed in an amorphous state giving the possibility to follow different strategies. Furthermore, the *in vitro* cellular assays demonstrated that the constructs obtained from this SF bioink are biocompatible, supporting hASCs proliferation and viability up to 7 days of culturing. This versatile fast enzymatic setting and biomimetic method opens up new horizons for the use of SF bioinks, not only concerning the development of tissue substitutes using TE approaches but also regarding all type of applications where the printing of an implantable biomaterial is relevant, and in particular for the biofabrication of patient-specific memory-shape implants.

#### VII-5. ACKNOWLEDGMENTS

J.B.C., J.S-C., J.M.O. and R.L.R. contributed equally to this work. The work was supported by Portuguese Foundation for Science and Technology (FCT) through the project B-FABULUS (PTDC/BBB-ECT/2690/2014). FCT/MCTES is also acknowledged for the PhD scholarship attributed to J.B.C. (PD/BD/113803/2015) and the financial support provided to J.S-C. (IF/00115/2015) and J.M.O. (IF/00423/2012 and IF/01285/2015) under the program “Investigador FCT”.

#### VII-6. REFERENCES

- [1] Li J, Connell S, Shi R. Biomimetic Architectures for Tissue Engineering. In: Mukherjee A, editor. Biomimetics Learning from Nature. Rijeka: InTech; 2010. p. Ch. 24.
- [2] Ma PX. Biomimetic Materials for Tissue Engineering. *Advanced drug delivery reviews* 2008;60:184-98.
- [3] Cengiz IF, Pitikakis M, Cesario L, Parascandolo P, Vosilla L, Viano G, *et al.* Building the basis for patient-specific meniscal scaffolds: From human knee MRI to fabrication of 3D printed scaffolds. *Bioprinting* 2016;1-2:1-10.

- [4] Mok S-W, Nizak R, Fu S-C, Ho K-WK, Qin L, Saris DBF, *et al.* From the printer: Potential of three-dimensional printing for orthopaedic applications. *Journal of Orthopaedic Translation* 2016;6:42-9.
- [5] Kang H-W, Lee SJ, Ko IK, Kengla C, Yoo JJ, Atala A. A 3D bioprinting system to produce human-scale tissue constructs with structural integrity. *Nat Biotech* 2016;34:312-9.
- [6] Murphy SV, Atala A. 3D bioprinting of tissues and organs. *Nature biotechnology* 2014;32:773-85.
- [7] Malda J, Visser J, Melchels FP, Jüngst T, Hennink WE, Dhert WJA, *et al.* 25th Anniversary Article: Engineering Hydrogels for Biofabrication. *Advanced Materials* 2013;25:5011-28.
- [8] Markstedt K, Mantas A, Tournier I, Martinez Avila H, Hagg D, Gatenholm P. 3D Bioprinting Human Chondrocytes with Nanocellulose-Alginate Bioink for Cartilage Tissue Engineering Applications. *Biomacromolecules* 2015;16:1489-96.
- [9] He Y, Yang F, Zhao H, Gao Q, Xia B, Fu J. Research on the printability of hydrogels in 3D bioprinting. *Scientific Reports* 2016;6:29977.
- [10] Ouyang L, Highley CB, Rodell CB, Sun W, Burdick JA. 3D Printing of Shear-Thinning Hyaluronic Acid Hydrogels with Secondary Cross-Linking. *ACS Biomaterials Science & Engineering* 2016;2:1743-51.
- [11] Zhang W, Chen L, Chen J, Wang L, Gui X, Ran J, *et al.* Silk Fibroin Biomaterial Shows Safe and Effective Wound Healing in Animal Models and a Randomized Controlled Clinical Trial. *Advanced healthcare materials* 2017.
- [12] Das S, Bora U, Borthakur BB. 2 - Applications of silk biomaterials in tissue engineering and regenerative medicine In: Kundu SC, editor. *Silk Biomaterials for Tissue Engineering and Regenerative Medicine*: Woodhead Publishing; 2014. p. 41-77.
- [13] Ghosh S, Parker ST, Wang X, Kaplan DL, Lewis JA. Direct-Write Assembly of Microperiodic Silk Fibroin Scaffolds for Tissue Engineering Applications. *Advanced Functional Materials* 2008;18:1883-9.
- [14] Teixeira LS, Feijen J, van Blitterswijk CA, Dijkstra PJ, Karperien M. Enzyme-catalyzed crosslinkable hydrogels: emerging strategies for tissue engineering. *Biomaterials* 2012;33:1281-90.
- [15] Yan L-P, Oliveira JM, Oliveira AL, Reis RL. Core-shell silk hydrogels with spatially tuned conformations as drug-delivery system. *Journal of Tissue Engineering and Regenerative Medicine* 2016:n/a-n/a.
- [16] Yan LP, Silva-Correia J, Ribeiro VP, Miranda-Goncalves V, Correia C, da Silva Morais A, *et al.* Tumor Growth Suppression Induced by Biomimetic Silk Fibroin Hydrogels. *Sci Rep* 2016;6:31037.
- [17] Ribeiro VP, Silva-Correia J, Nascimento AI, da Silva Morais A, Marques AP, Ribeiro AS, *et al.* Silk-based anisotropical 3D biotextiles for bone regeneration. *Biomaterials* 2017;123:92-106.
- [18] Lewis JA. Direct Ink Writing of 3D Functional Materials. *Advanced Functional Materials* 2006;16:2193-204.

- [19] Siqueira G, Kokkinis D, Libanori R, Hausmann MK, Gladman AS, Neels A, *et al.* Cellulose Nanocrystal Inks for 3D Printing of Textured Cellular Architectures. *Advanced Functional Materials* 2017;27:1604619-n/a.
- [20] Ouyang L, Highley CB, Sun W, Burdick JA. A Generalizable Strategy for the 3D Bioprinting of Hydrogels from Nonviscous Photo-crosslinkable Inks. *Advanced Materials* 2017;29:1604983-n/a.
- [21] Censi R, Schuurman W, Malda J, di Dato G, Burgisser PE, Dhert WJA, *et al.* A Printable Photopolymerizable Thermosensitive p(HPMAM-lactate)-PEG Hydrogel for Tissue Engineering. *Advanced Functional Materials* 2011;21:1833-42.
- [22] Hong S, Sycks D, Chan HF, Lin S, Lopez GP, Guilak F, *et al.* 3D Printing of Highly Stretchable and Tough Hydrogels into Complex, Cellularized Structures. *Advanced Materials* 2015;27:4035-40.
- [23] Cho SY, Yun YS, Lee S, Jang D, Park K-Y, Kim JK, *et al.* Carbonization of a stable  $\beta$ -sheet-rich silk protein into a pseudographitic pyroprotein. *Nature Communications* 2015;6:7145.
- [24] Yan L-P, Silva-Correia J, Oliveira MB, Vilela C, Pereira H, Sousa RA, *et al.* Bilayered silk/silk-nanoCaP scaffolds for osteochondral tissue engineering: *In vitro* and *in vivo* assessment of biological performance. *Acta Biomater* 2015;12:227-41.
- [25] Numata K, Cebe P, Kaplan DL. Mechanism of enzymatic degradation of beta-sheet crystals. *Biomaterials* 2010;31:2926-33.
- [26] Pereira H, Caridade SG, Frias AM, Silva-Correia J, Pereira DR, Cengiz IF, *et al.* Biomechanical and cellular segmental characterization of human meniscus: building the basis for Tissue Engineering therapies. *Osteoarthritis and cartilage* 2014;22:1271-81.
- [27] McMahon LA, O'Brien FJ, Prendergast PJ. Biomechanics and mechanobiology in osteochondral tissues. *Regenerative medicine* 2008;3:743-59.
- [28] Huang WM, Ding Z, Wang CC, Wei J, Zhao Y, Purnawali H. Shape memory materials. *Materials Today* 2010;13:54-61.
- [29] Abdelgaied A, Stanley M, Galfe M, Berry H, Ingham E, Fisher J. Comparison of the biomechanical tensile and compressive properties of decellularised and natural porcine meniscus. *Journal of biomechanics* 2015;48:1389-96.
- [30] McGill M, Coburn JM, Partlow BP, Mu X, Kaplan DL. Molecular and macro-scale analysis of enzyme-cross-linked silk hydrogels for rational biomaterial design. *Acta biomaterialia* 2017.
- [31] Yan LP, Oliveira JM, Oliveira AL, Caridade SG, Mano JF, Reis RL. Macro/microporous silk fibroin scaffolds with potential for articular cartilage and meniscus tissue engineering applications. *Acta biomaterialia* 2012;8:289-301.
- [32] Bhardwaj N, Chakraborty S, Kundu SC. Freeze-gelled silk fibroin protein scaffolds for potential applications in soft tissue engineering. *International Journal of Biological Macromolecules* 2011;49:260-7.

[33] Luo Z, Zhang Q, Shi M, Zhang Y, Tao W, Li M. Effect of Pore Size on the Biodegradation Rate of Silk Fibroin Scaffolds. *Advances in Materials Science and Engineering* 2015;2015:7.

[34] Chang H-I, Wang Y. Cell Responses to Surface and Architecture of Tissue Engineering Scaffolds. In: Eberli D, editor. *Regenerative Medicine and Tissue Engineering - Cells and Biomaterials*. Rijeka: InTech; 2011. p. Ch. 27.

[35] Zhang ZZ, Jiang D, Ding JX, Wang SJ, Zhang L, Zhang JY, *et al.* Role of scaffold mean pore size in meniscus regeneration. *Acta biomaterialia* 2016;43:314-26.

## VII-7. SUPPLEMENTARY MATERIAL

Cyclic uniaxial compression test of the 3D bioprinted scaffolds after freeze-drying. The scaffolds were submitted to a 5 cycles compression test that is represented in a stress-strain plot (**Figure VII-2f**). From this plot, the compressive modulus (E) was calculated by the slope of the initial linear section and presented in the following table (**Supplementary table VII-1**).

**Supplementary Table VII-1 - Compressive modulus of the 3D Bioprinted scaffolds after freeze-drying over 5 cycles.**

	Compressive modulus (MPa)
1 <sup>st</sup> cycle	0.32 ± 0.04
2 <sup>nd</sup> cycle	0.24 ± 0.03
3 <sup>rd</sup> cycle	0.17 ± 0.03
4 <sup>th</sup> cycle	0.21 ± 0.04
5 <sup>th</sup> cycle	0.15 ± 0.01

The micro and macro porosity of the scaffolds was also analyzed individually (**Supplementary Table VII-2**) since the induction of each kind of porosity was made by different techniques. The micro porosity was induced by freeze-drying, whereas the macro porosity was induced by the construct architecture.

Supplementary Table VII-2 - Pore architecture evaluation of freeze-dried 3D scaffolds using Micro-CT. Values of mean porosity (%), mean pore size ( $\mu\text{m}$ ), and mean trabecular size ( $\mu\text{m}$ ) for micro and macro porosity in the freeze-dried 3D scaffolds.

	Microporosity	Macroporosity	Total porosity
Mean porosity (%)	26.1 $\pm$ 3.2	33.1 $\pm$ 6.3	59.1 $\pm$ 3.4
Mean pore size ( $\mu\text{m}$ )	40.3 $\pm$ 3.3	427.7 $\pm$ 12.7	224.4 $\pm$ 29.2
Mean trabecular thickness ( $\mu\text{m}$ )	38.5 $\pm$ 1.6	611.4 $\pm$ 8.5	47.8 $\pm$ 2.8

This chapter includes 3 supplementary movies that are described below and can be displayed using the following links.

**Supplementary Movie 1.** This movie shows the 3D printing of a human meniscus patient-specific memory-shape implant.

<https://onlinelibrary.wiley.com/action/downloadSupplement?doi=10.1002%2Fadhm.201701021&file=adhm201701021-sup-0001-S1.mov>

**Supplementary Movie 2.** This movie reveals the recovery of a 3D printed patient-specific memory-shape implant of human meniscus compression test. After 80% compressive strain the implant shows its memory-shape characteristics recovering almost its original shape.

<https://onlinelibrary.wiley.com/action/downloadSupplement?doi=10.1002%2Fadhm.201701021&file=adhm201701021-sup-0002-S2.mov>

**Supplementary Movie 3.** This movie shows the 3D reconstruction of a 3D printed patient-specific human meniscus implant by micro-CT.

<https://onlinelibrary.wiley.com/action/downloadSupplement?doi=10.1002%2Fadhm.201701021&file=adhm201701021-sup-0003-S3.mov>

## Chapter VIII

# Engineering Patient-Specific Bioprinted Constructs for Treatment of Degenerated Intervertebral Disc

## Engineering Patient-Specific Bioprinted Constructs for Treatment of Degenerated Intervertebral Disc<sup>††</sup>

### ABSTRACT

Lower back pain (LBP), which is strongly associated with intervertebral disc (IVD) degeneration, is one of the most frequently reported age- and work-related disorders in actual society, leading to a huge socio-economic impact worldwide. The current treatments have poor clinical outcomes and do not consider each patient needs. Thus, there is a growing interest in the potential of personalized cell-based tissue engineering (TE) approaches aimed to regenerate the damaged IVD and efficiently restore full disc function. In this work, a bioink composed by silk fibroin (SF) hydrogel combined with elastin was used to bioprint patient-specific substitutes mimicking IVD ultrastructure, and particularly for the outer region of the IVD, *i.e.* annulus fibrosus (AF). Following a reverse engineering approach, the proposed strategy makes use of a 3D model of AF obtained by semi-automatic morphological segmentation from magnetic resonance imaging dataset of human IVD. SF/elastin bioprinted scaffolds were characterized thoroughly *in vitro*, in terms of physico-chemical and biological performance. The bioprinted SF/elastin scaffolds were shown to possess structural and mechanical properties similar to the native AF and supports cell attachment and growth. Human adipose-derived stem cell cultured onto the SF/elastin bioprinted scaffolds were shown to adhere, proliferate and maintain metabolic activity and viability up to 21 days of culturing. The implantation of custom-made SF/elastin implants that best emulate a patient AF anatomy can potentially open up new personalized treatments for tackling IVD disorders by means of improving recovery time after surgery and help to restore spine biofunctionality.

---

<sup>††</sup> This chapter is based on the following publication:

Costa J. B., Silva-Correia J., Ribeiro V. P., da Silva Morais A., Oliveira J. M., and Reis R. L., "Engineering patient-specific bioprinted constructs for treatment of degenerated intervertebral disc", *Materials Today Communications*, vol. 19, issue 2019, pp. 506-512, doi:10.1016/j.mtcomm.2018.01.011, 2019.



## VIII-1. INTRODUCTION

Degeneration of the intervertebral disc (IVD) is indicated as one of the main causes of lower back pain (LBP), a work-incapacitating painful condition estimated to affect up to 80% of the population at some time in their lives [1, 2]. The IVD lies between two adjacent vertebrae and is composed by a fibrous ring (annulus fibrosus, AF) that surrounds a fluid viscoelastic region (nucleus pulposus, NP) [3]. This specialized fibrocartilaginous structure provides flexibility to the spine, allowing limited movements, and supports compressive loads arising from body weight and muscle tension. The avascular and relatively acellular environment of IVD translates into limited endogenous repair capacity.

Existing conservative and surgical treatments are focused on pain relief and do not adequately reestablish each patient's disc structure and mechanical function [4]. The demand for new personalized therapies that address IVD degeneration and stimulate regeneration has led to an increasing interest in novel biological and tissue engineering (TE) strategies [4-6]. Several TE strategies for NP, AF or total IVD regeneration have been described in the literature [6]. However, there are several challenges that are currently limiting its clinical translation, namely the selection of suitable scaffolds and efficient fixation of the substitute materials. Despite the several promising studies to fully regenerate the IVD [7], none until now has achieved a precise replication of a customized IVD scaffold to prepare a tissue engineered total disc replacement implant.

Personalized approaches by means of using reverse engineering, *i.e.* combining imaging techniques (*e.g.* MRI and/or Micro-CT) and 3D bioprinting technology are now being envisioned [6]. The clinical use of custom-made implants mimicking native IVD and possessing an appropriate size, shape, porosity, mechanical performance, and biodegradability can improve recovery time after surgery and help to restore spine biofunctionality. Rapid prototyping (RP) technologies, including 3D printing, are interesting processing technologies that are becoming more widely used to precisely tune the architecture of tissue engineered scaffolds [8, 9]. This technology enables to produce scaffolds, in a reproducible manner, personalized to the patient and with high structural complexity, and to have a fast on-demand manufacture at low-cost. One limitation that is currently hindering the progress of 3D printing in biofabrication is the absence of biomaterial-based inks that can be adequately used to produce patient-specific implants. Hydrogels have become especially attractive as matrices for developing a wide variety of tissue engineered tissues and organs using different processing technologies, including 3D printing [4, 10]. Nevertheless, one of the main disadvantages of processing hydrogels is the difficulty to shape them in predesigned geometries even when RP technologies are

used. The difficulties are mostly related with the difficulty in controlling the gelation event. Our group has recently developed a novel bioink based on enzymatically cross-linked silk fibroin (SF) hydrogel that allows to bioprint different structures with high resolution, reproducibility and reliability [11]. The crosslinking process of silk fibroin hydrogels occurs between tyrosine groups and is mediated by the presence of the enzyme peroxidase and the oxidizer hydrogen peroxide [12]. The SF bioink can be printed in its amorphous state, and an irreversible beta-sheet transition obtained through different post-printing processing methods allows tailoring the final scaffolds' physico-chemical and biofunctional properties. Silk fibroin scaffolds [13, 14] have been shown to possess promising features for both acellular and cell-seeded strategies of AF, once scaffold architecture and porosity are important considerations in controlling tissue formation. Our hypothesis is that silk fibroin hydrogels combined with elastin are a step forward as it enable mimicking the lamellar structure of AF, which comprises collagens, proteoglycans and co-localization of microfibrils and elastin fibers [15, 16], creating a more favorable environment for ECM deposition. Moreover, they present bioadhesive and biological properties that can help modulate the regeneration process driven by patient own cells, achieving a better implant integration, thus reducing the risk of displacement and implant failure. Moreover, the conversion of SF hydrogels to beta-sheet conformation could be explored using different methodologies in order to match the mechanical stability of the implant to that of native AF.

In this work, SF bioink was blended with elastin to bioprint 3D patient-specific implants that emulate AF ultrastructure. The AF substitute was printed by using a 3D model of AF obtained by semi-automatic morphological segmentation from magnetic resonance imaging dataset of human IVD [17]. The SF/elastin bioprinted scaffolds structure and architecture was investigated under a Fourier transform infrared spectroscopy, and scanning electron microscope and micro-computed tomography, respectively. *In vitro* assays comprised the evaluation of SF/elastin scaffolds' degradation and water uptake profile, and biological performance. Cell viability, metabolic activity and proliferation were investigated up to 21 days of culturing.

## VIII-2. MATERIALS AND METHODS

### VIII-2.1. Materials

Silk, derived from the silkworm *Bombyx mori* cocoons, was provided by the Portuguese Association of Parents and Friends of Mentally Disabled Citizens (APPACDM, Castelo Branco, Portugal). A soluble elastin powder from bovine neck ligament with a molecular weight of 60 kDa was purchased from Sigma-Aldrich. All reagents were purchased from Sigma-Aldrich (St. Louis, MO, USA) unless otherwise stated.

### VIII-2.2. Bioprinting of silk fibroin/elastin scaffolds

#### VIII-2.2.1. Preparation of silk fibroin/elastin scaffolds

Purified silk fibroin (SF) solution was prepared by removing the glue-like protein sericin from the cocoons in a 0.02 M boiling sodium carbonate solution for 1 hour, followed by rinsing with distilled water. Then, the purified SF was dissolved in a 9.3 M lithium bromide solution for 1 hour at 70 °C and dialyzed in distilled water for 48 hours using the benzoylated dialysis tubing (MWCO: 2 kDa). The obtained SF aqueous solution was concentrated against a 20 (w/v) poly(ethylene glycol) solution for at least 6 hours. The final concentration of SF was determined by assessing the dry weight of the SF solution placed overnight in the oven at 70 °C. Temporarily, the prepared SF solution was stored at 4 °C until use. The SF was diluted to 16% (w/v) distilled water and an elastin solution was prepared at 16% (w/v) also in distilled water. A silk/elastin solution was obtained through the mixture of both solutions at a ratio of 90:10 respectively. SF/elastin ink was produced combining with horseradish peroxidase solution (HRP type VI, 0.84 mg.mL<sup>-1</sup>) and hydrogen peroxide solution (H<sub>2</sub>O<sub>2</sub>, 0.36% (v/v); Panreac, Barcelona, Spain). A mixture of SF/elastin, 5% (v/v) HRP solution and 2.5% (v/v) H<sub>2</sub>O<sub>2</sub> was prepared inside the cartridge and incubated at 37 °C for 30 minutes.

#### VIII-2.2.2. 3D Printing of silk fibroin/elastin scaffolds and patient-specific AF implants

Using a 4<sup>th</sup> generation Envisiontec 3D Bioplotter, the previously prepared SF/elastin bioink was extruded pneumatically through a nozzle diameter of 400 µm, pressures ranging from 250 to 350 kPa

and at a speed of 5 to 8 mm.s<sup>-1</sup>. Furthermore, and in order to fully characterize the produced scaffolds, cube-shape structures with 4 layers were printed. The scaffolds and implants were further frozen at -80 °C for 48 hours and freeze-dried for 72 hours (Telstar-Cryodos-80, Spain). Before any characterization assay the freeze-dried scaffolds were immersed in ethanol 70% for 3 hours and then in Phosphate-buffered saline (PBS) overnight.

The patient-specific SF/elastin AF substitute was printed using a model previously developed in our group [17]. In brief, a 47-year-old male patient underwent an MRI scan in head-first supine position using a 3.0-T scanner (Siemens MAGNETOM Spectra, Munich, Germany). Thereafter, a three-stage reconstruction (image segmentation, manual corrections and 3D reconstruction) was performed to obtain a 3D model of the L1-L2 IVD of the patient. The patient-specific implant mimicking the patient AF anatomy was produced using the same printing parameters as described for printing the SF/elastin scaffolds.

### VIII-2.3. Physico-chemical characterization of the bioprinted silk fibroin/elastin scaffolds

#### VIII-2.3.1. Fourier transform infrared (FTIR) spectroscopy

The chemical composition and structural conformation of the SF/elastin 3D scaffolds were evaluated by FTIR spectroscopy (Perkin-Elmer 1600 series equipment, CA, USA) under an attenuated total reflectance (ATR) model (IRPrestige-21, Shimadzu, Japan). All spectra were obtained between 4600 to 800 cm<sup>-1</sup> at a 4 cm<sup>-1</sup> resolution with 50 scans.

#### VIII-2.3.2. *In vitro* degradation

The stability of the SF/elastin scaffolds was assessed by enzymatic degradation assay. Protease XIV solution (0.5 U.mL<sup>-1</sup>) was prepared by dissolving the enzyme in distilled water. The initial weight of the scaffolds was measured, and then the scaffolds were hydrated in PBS at 37 °C overnight, followed by immersion in 5 mL of protease solution. The enzyme solution was changed every 48 hours. The samples were weight after 0.16, 0.33, 1, 7, 14, 21 and 28 days of immersion in the degradation solution at 37 °C in static conditions.

The weight loss ratio was obtained using the following equation:

**Equation VIII-1 - Determination of weight loss ratio.**

$$\text{weight loss ratio} = \left[ \frac{(m_i - m_{d,t})}{(m_i)} \right] \times 100\%$$

where,  $m_i$  is the initial weight of the sample, and  $m_{d,t}$  is the weight of the degraded sample at each time point (n=3 per group).

### VIII-2.3.3. Swelling tests

The swelling of the SF/elastin scaffolds was evaluated after immersion in PBS for time periods ranging from 3 hours to 28 days. All experiments were conducted at 37 °C in static conditions. At each time point, the samples were removed from PBS, the excess of surface water was absorbed using a filter paper, and the weight immediately determined. The swelling was obtained using the following equation:

**Equation VIII-2 - Determination of swelling ratio.**

$$\text{swelling ratio (\%)} = \left[ \frac{(m_{w,t} - m_i)}{(m_i)} \right] \times 100\%$$

where,  $m_i$  is the initial weight of the sample, and  $m_{w,t}$  is the wet weight of the sample at each time point (n=3 per group).

### VIII-2.3.4. Mechanical properties

Compressive tests were performed by using a Universal Testing Machine (Instron 4505) with a 1 kN load cell at room temperature (RT). As previously, the scaffolds were immersed in PBS overnight at 37 °C. The cross-head speed was set at 2 mm.min<sup>-1</sup> and tests were run until achieving a 60% reduction in specimen height. The elastic modulus was defined by the slope of the initial linear section of the stress–strain curve. A minimum number of 5 samples were tested, with the compressive modulus values being the average of all the measurements.

The viscoelastic measurements were performed using a TRITEC8000B dynamic mechanical analyzer (Triton Technology, UK) in the compressive mode. The SF/elastin scaffolds were immersed in

PBS overnight at 37 °C. The measurements were carried out at 37 °C. The geometry of the SF/elastin scaffolds was measured (with a micrometer of precision), clamped in the DMA apparatus and immersed in PBS. After equilibration at 37 °C, the DMA spectra were obtained during a frequency scan between 0.1 and 10 Hz. The experiments were performed under a constant strain amplitude of 50 µm.

#### **VIII-2.3.5. Scanning Electron Microscopy (SEM)**

The morphology of the SF/elastin scaffolds was observed by scanning electron microscopy (SEM) (Nova NanoSEM 200; FEI, Hillsboro, OR, USA). Before the observation, the scaffolds were coated with one layer of Gold/Palladium (Au/Pd) (SC502–314B) in a coater (E6700; Quorum Technologies, East Grinstead, UK).

#### **VIII-2.3.6. Micro-computed tomography (Micro-CT)**

The architecture of the SF/elastin scaffolds was determined using a high-resolution Micro-CT Skyscan 1072 scanner (Skyscan, Kontich, Belgium) with a pixel size of 10 µm. Data sets were reconstructed using standardized cone-beam reconstruction software (NRecon v1.4.3, SkyScan). Representative data set of the slices was segmented into binary images with a dynamic threshold of 22–40 (grey values). Then, the binary images obtained were used for morphometric analysis (CT Analyser, v1.5.1.5, SkyScan) and construction of three-dimensional models (ANT 3D creator, v2.4, SkyScan)

### ***VIII-2.4. In vitro biological characterization of the bioprinted silk fibroin/elastin scaffolds***

#### **VIII-2.4.1. hASCs isolation and expansion**

Human adipose-derived stem cells (hASCs) were isolated from subcutaneous adipose tissue samples obtained from liposuction procedures performed after patient's informed consent and using a protocol previously established with the Department of Plastic Surgery of Hospital da Prelada (Porto, Portugal). All the samples were processed within 24 hours after the liposuction procedure and hASCs were enzymatically isolated from the subcutaneous adipose tissue, as previously described [18]. The isolated hASCs were then expanded in basal medium consisting of Dulbecco's Modified Eagle Medium/Nutrient Mixture F-12 with Glutamax medium (DMEM:F12; Life Technologies, Scotland)

supplemented with 10% fetal bovine serum (FBS; Biochrom AG, Germany) and 1% antibiotic/antimycotic solution (final concentration of penicillin 100 units.mL<sup>-1</sup> and streptomycin 100 mg.mL<sup>-1</sup>; Gibco, GB). Cells were cultured until confluence at 37 °C in an atmosphere of 5% CO<sub>2</sub> incubator, changing the culture medium every 2 days.

#### VIII-2.4.2. Seeding of hASCs in the silk fibroin/elastin scaffolds

For performing the *in vitro* tests, 3D SF/elastin scaffolds were produced in the form of a cube (5x5x4 mm). Before cell seeding, all samples were removed from ethanol and washed 3x in PBS. Then, the samples were incubated in DMEM:F12 overnight. In the following day, the scaffolds were transferred to 24-well suspension cell culture plates (Cellstar, Greiner Bio-One, Austria). Confluent hASCs (at passage 2) were detached with TrypLE Express (1X) (Life Technologies, Carlsbad, CA, USA) and seeded at a density of 2x10<sup>5</sup> cells/scaffold to develop the SF/elastin constructs. Each scaffold was kept in the CO<sub>2</sub> incubator at 37 °C for 2 hours, and then 2 mL of DMEM:F12 culture medium were added to each well. SF/elastin constructs were retrieved at different culture times (0, 1, 7, 14 and 21 days) and the culture medium was changed every 2 days.

#### VIII-2.4.3. Cell viability and metabolic activity

Cell viability was microscopically assessed by Live/Dead assay. Briefly, SF/elastin constructs were immersed in a calcein AM/propidium iodide (PI) solution at 1:3 ratio in PBS, for 5-10 minutes at 37 °C in an atmosphere of 5% CO<sub>2</sub> incubator, protected from light. Viable cells metabolize calcein AM (Invitrogen, USA 1 mg.mL<sup>-1</sup>) into green fluorescent calcein (Ex/Em ≈ 495/515 nm), while dead cells presenting damaged cell membrane find their DNA stained red by PI (Invitrogen, USA 1mg.mL<sup>-1</sup>; Ex/Em ≈ 493/636 nm). After a washing step with PBS, samples were imaged using a Transmitted and Reflected Light Microscope (Zeiss Axio Imager.Z1m, Zeiss, Germany).

hASCs metabolic activity was evaluated using Alamar Blue (AB), a dye that yields a fluorescent signal and a colorimetric change when incubated with metabolically-active cells. Cell culture medium containing 10% AB was added to the different culture wells and the plates were incubated for 4 hours, after which 100 µL of each solution were transferred to white opaque 96-well plates, in triplicates. Fluorescence was monitored at Ex/Em ≈ 530/590 nm, using a microplate reader (Synergy HT, BioTek Instruments, USA). PBS was used for removing the AB reagent and fresh medium was added in its

place after each AB determination. The metabolic activity values were calculated by normalization with the mean fluorescence value obtained for the controls (scaffolds without cells).

#### VIII-2.4.4. Cell proliferation

The quantity of double stranded DNA (dsDNA), directly proportional to cell number, was determined using a fluorometric dsDNA quantification kit (PicoGreen, Molecular Probes, Invitrogen Corporation, USA), according to the manufacturer's instructions. After each time point, the SF/elastin constructs were washed twice with PBS solution and kept in 1 mL of ultrapure water at  $-80\text{ }^{\circ}\text{C}$  until further analysis. Constructs were thawed at RT, sonicated for 1 hour to induce complete membrane lysis, and centrifuged at  $300\text{ }g$  for 5 min to spin down all non-genomic materials. After centrifugation, the scaffold was discarded and the supernatant collected to new 1.5 mL sterile Eppendorf tubes. Supernatant fluorescence was measured at an excitation wavelength ( $\lambda$ ) of 485/20 nm and at an emission  $\lambda$  of 528/20 nm, in a microplate reader (Synergy HT, BioTek Instruments, USA). The quantification of dsDNA was calculated according to a standard curve prepared with concentrations ranging between 0 and  $2\text{ }\mu\text{g}\cdot\text{mL}^{-1}$ , relating quantity of DNA and fluorescence intensity. Scaffolds without cells were used as controls.

#### VIII-2.5. Statistical analysis

All the numerical results are presented as mean  $\pm$  standard deviation (SD). Statistical analysis was performed using the GraphPad Prism 5.0 (GraphPad Software, La Jolla, CA, USA). First, a Shapiro-Wilk test was used to ascertain regarding data normality. For all the biological quantification assays, the differences between the experimental results were analyzed using a Kruskal-Wallis test followed by Dunn's multiple comparison test. Three independent experiments were performed for cell studies (metabolic activity and cell proliferation), and three samples were analyzed per group in each culturing time. The significance level was set to  $*p < 0.05$ ,  $**p < 0.01$ ,  $***p < 0.001$ .

### VIII-3. RESULTS AND DISCUSSION

SF protein exists in three different conformations, namely random coil and  $\beta$ -sheet conformation. The conformational changes of the scaffolds were studied by attenuated total reflectance Fourier



transform infrared spectroscopy (ATR-FTIR) (**Figure VIII-1a**). The scaffolds just after printing presented a spectrum with bands around  $1640\text{ cm}^{-1}$  and  $1538\text{ cm}^{-1}$  indicating the predominance of random coil conformation. After freeze-drying, the conformation transition from random coil to  $\beta$ -sheet was confirmed by the shift of the bands to  $1620\text{ cm}^{-1}$  and  $1514\text{ cm}^{-1}$ , respectively. Vasconcelos *et al.* already described this typical shift in FTIR bands characteristic of the conformation transition from random coil to  $\beta$ -sheet in SF/elastin scaffolds [19].

The weight loss and water uptake ratios of the SF/elastin 3D scaffolds were accessed (**Figure VIII-1b and VIII-c**). IVD tissue engineered scaffolds should not only restore the IVD functions but also should degrade over time, ideally matching the formation of new native tissue [20]. After 28 days in contact with a protease XIV solution, the scaffolds presented a weight loss percentage of  $30.3 \pm 2.2\%$ . This result suggests a suitable degradation profile of the 3D scaffolds intended for IVD regeneration, since it was observed a low degradation ratio. Regarding the swelling capacity of the scaffolds, the values for water uptake increased in the first 24 hours up to  $375 \pm 22\%$ , and remained within these percentages after 28 days.

The mechanical properties of the SF/elastin scaffolds were investigated by a uniaxial compression test (Instron) and by DMA. The compressive modulus and the stress-strain plot are represented in **Figure VIII-1d**. Either the stress-strain curve or the compressive modulus value ( $0.44 \pm 0.02\text{ MPa}$ ) revealed to be similar to fibrocartilage ( $0.45$  to  $0.80\text{ MPa}$ ) [21] and human AF ( $0.56 \pm 0.21\text{ MPa}$ ) [22] mechanical properties. In what concerns the viscoelastic properties, the values of storage modulus ( $E'$ ) for printed scaffolds increased from  $0.56 \pm 0.06\text{ MPa}$  to  $0.86 \pm 0.07\text{ MPa}$ , as frequency increased from  $0.1$  to  $10\text{ Hz}$  (**Figure VIII-1e**). The loss factor ( $\tan \delta$ ) values revealed a similar behavior, increasing from  $0.33 \pm 0.01$  to  $0.38 \pm 0.01$ , as frequency increased from  $0.1$  to  $10\text{ Hz}$  (**Figure VIII-1f**). Based on the higher storage modulus and loss factor values of the 3D scaffolds, when compared to those reported in the literature [23, 24], it can be concluded that the scaffolds revealed higher stiffness and higher propensity to dissipate energy, making them suitable for cartilage and fibrocartilage tissue regeneration.

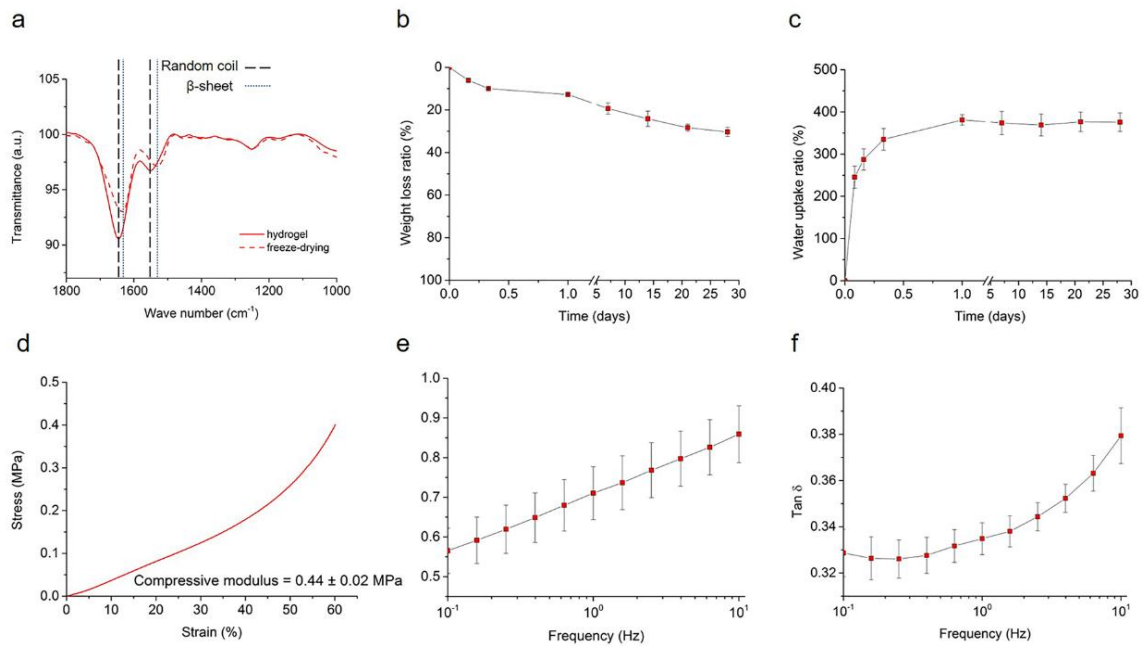


**Figure VIII-1 - Physico-chemical characterization of 3D SF/elastin scaffolds. (a) FTIR spectra. (b) Degradation profile in 0.5 U.ml-1 of protease XIV solution. (c) Swelling profile in PBS solution. (d) Stress-strain plot and compressive modulus. (e) Storage modulus, and (f) loss modulus as function of frequency (0.1 to 10 Hz).**

In this study, the pores morphology of the 3D scaffolds was investigated by SEM analysis (**Figure VIII-2a**). Two types of porosity can be observed in SEM images of the SF/elastin scaffolds. The microporosity, that was induced by freeze-drying, and the macroporosity that was tuned by 3D printing. In **Figure VIII-2ai-ii**, it can be observed macropores with a size of around 400-500  $\mu\text{m}$  and, on the other hand, in **Figure VIII-2aiii** the microporosity is characterized by pores with a size of around 70-100  $\mu\text{m}$ . The qualitative and quantitative analysis of porosity was also assessed by Micro-CT (**Figure VIII-2b and Supplementary Table VIII-1, Supplementary material**). The 3D SF/elastin scaffolds exhibited a total porosity of  $49.34 \pm 3.7\%$  and a mean pore size and pore thickness of  $131.3 \pm 5.6 \mu\text{m}$  and  $49.0 \pm 2.16 \mu\text{m}$ , respectively. Regarding these results and comparing to literature reports on scaffolds' microarchitecture for IVD regeneration, it can be concluded that the proposed bioprinted 3D SF/elastin scaffolds gather the required structural properties for providing a suitable microenvironment for cell adhesion and proliferation [25, 26].

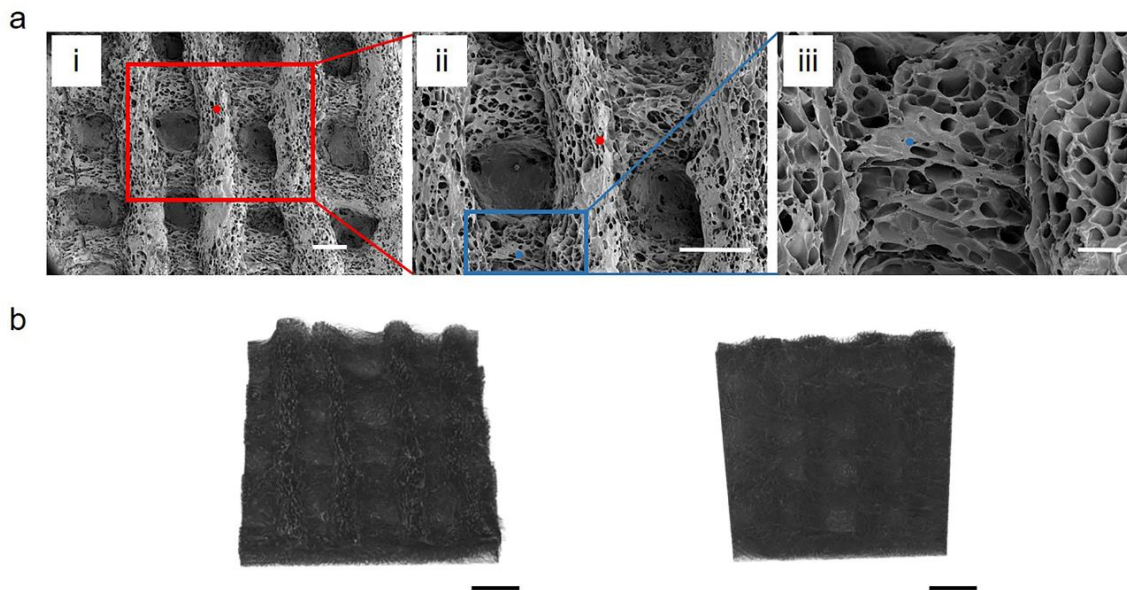


**Figure VIII-2 - Morphology of 3D SF/elastin scaffolds. (a) SEM image at different magnifications. (b) 3D reconstruction of the 3D scaffolds by Micro-CT. Scale bars: a) 500  $\mu\text{m}$  (i and ii) and 100  $\mu\text{m}$  (iii), and b) 1 mm.**

Human adipose-derived stem cells (hASCs) have shown promising results for future IVD regeneration treatments [27]. After isolation, the hASCs were seeded into the 3D scaffolds to perform a preliminary evaluation of the biological performance of these scaffolds. The live/dead assay showed living cells attached on the surface of the 3D constructs (**Figure VIII-3a**), after 1 day of culturing. After 7 days, the cells were already dispersed throughout the bioprinted scaffolds and presented a spread morphology, which indicates that cells are metabolically active. The observation of a layer of cells on the surface of the SF/elastin constructs after 21 days of culturing, indicates that the scaffolds supported hASCs proliferation from 1 up to 21 days. Quantitative analysis of cells metabolic activity was determined by Alamar Blue assay up to 21 days of culturing (**Figure VIII-3b**). A significant increase of metabolic activity was observed after 7 days of culturing, as compared to day 1 (\*\* $p < 0.01$ ). From day 14 and day 21 results, it was observed significantly higher activity levels as compared to day 1 (\*\* $p < 0.001$ ). The DNA content was also investigated (**Figure VIII-3c**), confirming the previous data indicating cells proliferation throughout the culturing period. After 14 and 21 days of culturing, the concentration of DNA significantly increased (\*\* $p < 0.001$ ) as compared to day 1. However, no significant differences were found between day 14 and day 21, possibly due to cell confluency. A previous study performed by our group already showed good biological performance of ASCs when seeded in macro/microporous silk scaffolds produced by salt leaching and freeze drying technique [28]. The *in vitro* evaluation evidenced that the produced bioprinted SF/elastin constructs supported hASCs proliferation, thus

corroborating the idea that the proposed strategy is promising when personalized cell-based IVD tissue engineering strategies are envisioned.

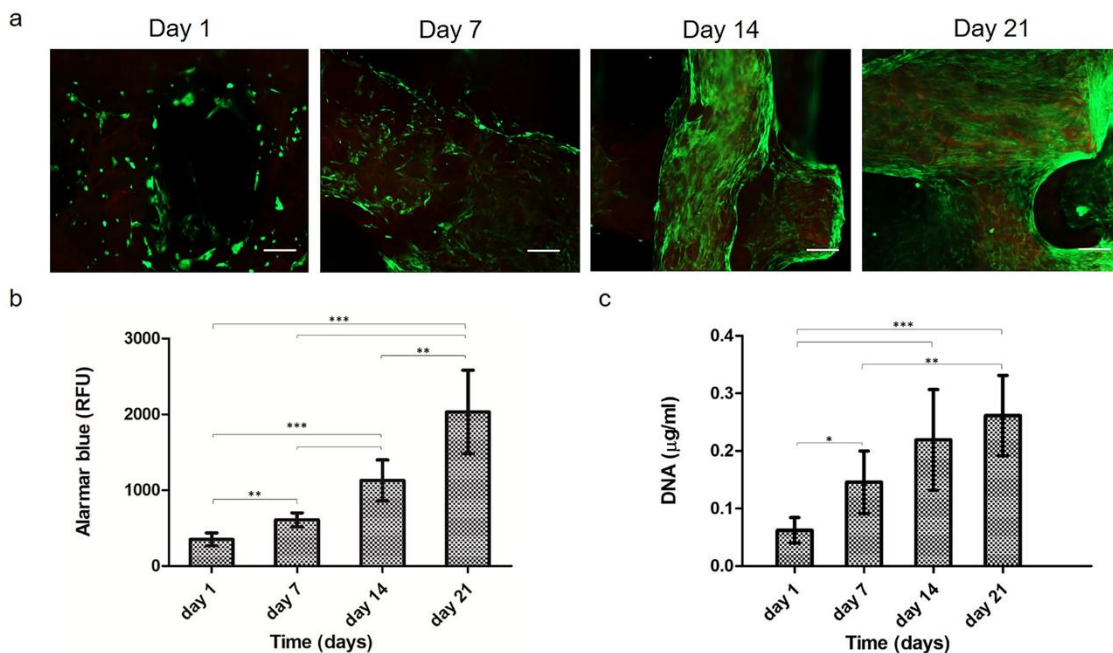
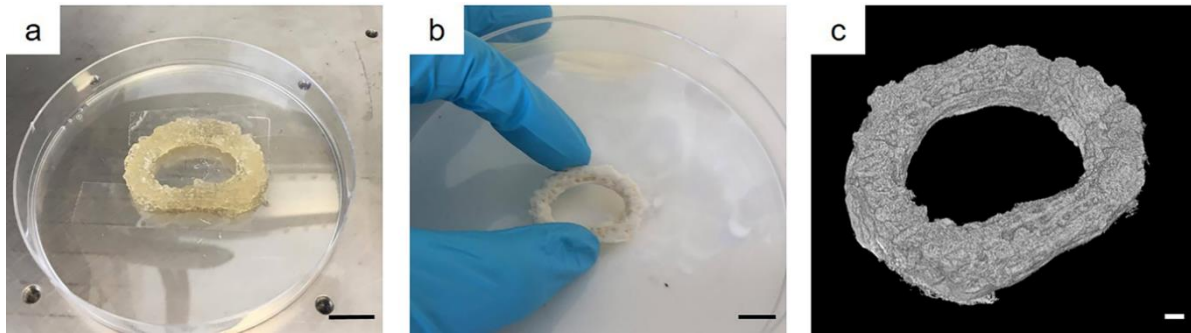


Figure VIII-3 - *In vitro* biological performance of the bioprinted SF/elastin scaffolds seeded with hASCs. Evaluation was performed after 1, 7, 14 and 21 days of culturing. (a) Calcein AM and propidium iodide staining. (b) Metabolic activity by Alamar Blue assay. (c) DNA content. Statistical significant differences were represented by \* ( $p < 0.5$ ), \*\* ( $p < 0.01$ ) and \*\*\* ( $p < 0.001$ ). Scale bar: a) 200  $\mu\text{m}$ .

Finally, as proof-of-concept an SF/elastin AF implant respecting the patient anatomy was printed (Figure VIII-4). In this section, a semi-automated methodology of a geometry reconstruction pipeline from volumetric medical image data that was demonstrated in a previous work [17], was used to produce a patient-specific IVD model. This reverse engineering approach has the aim to improve the current outcomes in IVD tissue engineering application, especially in terms of anchorage, given the opportunity to produce an implant with the size and shape suitable to the patient. On the other hand, this novel approach can be the first step for the use of silk fibroin combined with different molecules as a bioink for 3D printing strategies. The versatility and the possibility to include different molecules in the bioink can be an interesting feature to fabricate patient-specific implants that best emulate the native ECM of different tissues.



**Figure VIII-4 - Production of a patient-specific AF substitute. (a) AF-like implant before freeze-drying and (b) after freeze-drying. (c) 3D reconstruction of AF substitute by Micro-CT. Scale bars: a-b) 10 mm, and c) 1 mm.**

By means of applying a reverse engineering approach, we successfully produce an AF implant with promising physico-chemical and biological properties, by bioprinting enzymatically cross-linked SF/elastin hydrogels with the size and shape of the patient AF. It is envisioned to combine this AF-like implant with ionic-cross-linked methacrylated gellan gum (iGG-MA) hydrogels [11, 29] in the central part of the implant, for mimicking the NP component and create a total IVD implant. The iGGMA hydrogels were previously developed with appropriate mechanical and biological properties that closely resemble natural NP tissue [30, 31]. Further *in vitro* studies are required to assess the biological performance of both AF and NP substitutes, namely regarding the capacity to induce AF- and NP-specific phenotypes and efficiency in formation/replacement by new tissue.

#### VIII-4. CONCLUSIONS

This study provided proof-of-concept on the use of reverse engineering and 3D printing to produce patient-specific AF implants and constructs using an enzymatically cross-linked silk fibroin/elastin bioink. The 3D bioprinted SF/elastin scaffolds can be tuned for their degradation profile, mechanical properties and architecture by varying the bioink formulation and conformation, and bioprinting parameters. In addition, the *in vitro* biological assays demonstrated that the SF/elastin scaffolds supported hASCs proliferation and viability up to 21 days of culturing. The proposed low-cost bioink and approach is a step forward for the development of future IVD personalized treatments, as it opens up the possibility to produce patient-specific SF/elastin constructs, respecting the AF patient anatomy.

## VIII-5. ACKNOWLEDGMENTS

The authors would like to acknowledge the financial support provided by the Portuguese Foundation for Science and Technology (FCT) through the project EPIDisc (UTAP-EXPL/BBBECT/0050/2014), funded in the Framework of the “International Collaboratory for Emerging Technologies, CoLab”, UT Austin|Portugal Program. FCT is also greatly acknowledged for the distinctions attributed to J. Silva-Correia (IF/00115/2015) and J. M. Oliveira (IF/00423/2012 and IF/01285/2015) under the Investigator FCT program. V. P. Ribeiro was awarded a PhD scholarship (PD/BD/113806/2015) under the financial support from FCT/MCTES and FSE/POCH, PD/59/2013. FCT/MCTES is also acknowledged for the PhD scholarship attributed to J. B. Costa (PD/BD/113803/2015).

## VIII-6. REFERENCES

- [1] Diamond S, Borenstein D. Chronic low back pain in a working-age adult. *Best Pract Res Clin Rheumatol* 2006;20:707-20.
- [2] Zhao C-Q, Wang L-M, Jiang L-S, Dai L-Y. The cell biology of intervertebral disc aging and degeneration. *Ageing Res Rev* 2007;6:247-61.
- [3] Roberts S, Evans H, Trivedi J, Menage J. Histology and pathology of the human intervertebral disc. *J Bone Joint Surg Am* 2006;88:10-4.
- [4] Kalson NS, Richardson S, Hoyland JA. Strategies for regeneration of the intervertebral disc. *Regen Med* 2008;3:717-29.
- [5] Richardson SM, Mobasher A, Freemont AJ, Hoyland JA. Intervertebral disc biology, degeneration and novel tissue engineering and regenerative medicine therapies. *Histol Histopathol* 2007;22:1033-41.
- [6] Silva-Correia J, Correia SI, Oliveira JM, Reis RL. Tissue engineering strategies applied in the regeneration of the human intervertebral disc. *Biotechnol Adv* 2013;31:1514-31.
- [7] Mizuno H, Roy AK, Vacanti CA, Kojima K, Ueda M, Bonassar LJ. Tissue-engineered composites of annulus fibrosus and nucleus pulposus for intervertebral disc replacement. *Spine* 2004;29:1290-7.
- [8] Guvendiren M, Molde J, Soares RMD, Kohn J. Designing Biomaterials for 3D Printing. *ACS Biomater Sci Eng* 2016;2:1679-93.
- [9] Murphy SV, Atala A. 3D bioprinting of tissues and organs. *Nat Biotechnol* 2014;32:773-85.

- [10] Pereira DR, Silva-Correia J, Oliveira JM, Reis RL. Hydrogels in acellular and cellular strategies for intervertebral disc regeneration. *J Tissue Eng Regen Med* 2013;7:85-98.
- [11] Costa JB, Silva-Correia J, Oliveira JM, Reis RL. Inks for 3D Printing, Methods of Production and Uses Thereof. P5141 PP, Priority date: 09062017 PT 2017.
- [12] Ying G-L, Jiang N, Maharjan S, Yin Y-X, Chai R-R, Cao X, *et al.* Aqueous Two-Phase Emulsion Bioink-Enabled 3D Bioprinting of Porous Hydrogels. *Advanced Materials* 2018;30:1805460.
- [13] Chang G, Kim HJ, Kaplan D, Vunjak-Novakovic G, Kandel RA. Porous silk scaffolds can be used for tissue engineering annulus fibrosus. *Eur Spine J* 2007;16:1848-57.
- [14] Chang G, Kim HJ, Vunjak-Novakovic G, Kaplan DL, Kandel R. Enhancing annulus fibrosus tissue formation in porous silk scaffolds. *J Biomed Mater Res A* 2010;92A:43-51.
- [15] Park S-H, Gil ES, Mandal BB, Cho H, Kluge JA, Min B-H, *et al.* Annulus fibrosus tissue engineering using lamellar silk scaffolds. *J Tissue Eng Regen Med* 2012;6:s24-s33.
- [16] Yu J, Tirlapur U, Fairbank J, Handford P, Roberts S, Winlove CP, *et al.* Microfibrils, elastin fibres and collagen fibres in the human intervertebral disc and bovine tail disc. *J Anat* 2007;210:460-71.
- [17] Oner T, Cengiz IF, Pitikakis M, Cesario L, Parascandolo P, Vosilla L, *et al.* 3D segmentation of intervertebral discs: from concept to the fabrication of patient-specific scaffolds. *J 3D Printing Med* 2017;1:91-101.
- [18] Cerqueira MT, Pirraco RP, Santos TC, Rodrigues DB, Frias AM, Martins AR, *et al.* Human adipose stem cells cell sheet constructs impact epidermal morphogenesis in full-thickness excisional wounds. *Biomacromolecules* 2013;14:3997-4008.
- [19] Vasconcelos A, Gomes AC, Cavaco-Paulo A. Novel silk fibroin/elastin wound dressings. *Acta Biomater* 2012;8:3049-60.
- [20] Park SH, Gil ES, Cho H, Mandal BB, Tien LW, Min BH, *et al.* Intervertebral disk tissue engineering using biphasic silk composite scaffolds. *Tissue Eng Part A* 2012;18:447-58.
- [21] Mansour JM. Biomechanics of cartilage. *Kinesiology: The Mechanics and Pathomechanics of Human Movement: Second Edition* 2013. p. 69-83.
- [22] Iatridis JC, Setton LA, Foster RJ, Rawlins BA, Weidenbaum M, Mow VC. Degeneration affects the anisotropic and nonlinear behaviors of human anulus fibrosus in compression. *J Biomech* 1998;31:535-44.
- [23] Yan L-P, Silva-Correia J, Oliveira MB, Vilela C, Pereira H, Sousa RA, *et al.* Bilayered silk/silk-nanoCaP scaffolds for osteochondral tissue engineering: *In vitro* and *in vivo* assessment of biological performance. *Acta Biomater* 2015;12:227-41.
- [24] Yan LP, Oliveira JM, Oliveira AL, Caridade SG, Mano JF, Reis RL. Macro/microporous silk fibroin scaffolds with potential for articular cartilage and meniscus tissue engineering applications. *Acta Biomater* 2012;8:289-301.

- [25] Xu B, Xu H, Wu Y, Li X, Zhang Y, Ma X, *et al.* Intervertebral Disc Tissue Engineering with Natural Extracellular Matrix-Derived Biphasic Composite Scaffolds. *PLoS one* 2015;10:e0124774.
- [26] Park SH, Gil ES, Mandal BB, Cho H, Kluge JA, Min BH, *et al.* Annulus fibrosus tissue engineering using lamellar silk scaffolds. *J Tissue Eng Regen Med* 2012;6 Suppl 3:s24-33.
- [27] Sakai D, Andersson GB. Stem cell therapy for intervertebral disc regeneration: obstacles and solutions. *Nat Rev Rheumatol* 2015;11:243-56.
- [28] Yan LP, Oliveira JM, Oliveira AL, Reis RL. *In vitro* evaluation of the biological performance of macro/micro-porous silk fibroin and silk-nano calcium phosphate scaffolds. *J Biomed Mater Res B Appl Biomater* 2015;103:888-98.
- [29] Silva-Correia J, Oliveira JM, Caridade SG, Oliveira JT, Sousa RA, Mano JF, *et al.* Gellan gum-based hydrogels for intervertebral disc tissue-engineering applications. *J Tissue Eng Regen Med* 2011;5:e97-e107.
- [30] Silva-Correia J, Zavan B, Vindigni V, Silva TH, Oliveira JM, Abatangelo G, *et al.* Biocompatibility Evaluation of Ionic- and Photo-Cross-linked Methacrylated Gellan Gum Hydrogels: *In Vitro* and *In Vivo* Study. *Adv Healthc Mater* 2013;2:568-75.
- [31] Silva-Correia J, Miranda-Gonçalves V, Salgado A, Sousa N, Oliveira J, Reis R, *et al.* Angiogenic potential of gellan gum-based hydrogels for application in nucleus pulposus regeneration: *In vivo* study. *Tissue Eng Part A* 2012 18:1203-12.

#### VIII-7. SUPPLEMENTARY MATERIAL

Supplementary Table VIII-1 - Pore architecture evaluation of the 3D silk fibroin/elastin scaffolds using Micro-CT. Values of mean porosity (%), mean pore size ( $\mu\text{m}$ ), and mean trabecular size ( $\mu\text{m}$ ) in the 3D scaffolds.

<b>Mean porosity (%)</b>	49.34 $\pm$ 3.7
<b>Mean pore size (<math>\mu\text{m}</math>)</b>	131.3 $\pm$ 5.6
<b>Mean trabecular thickness (<math>\mu\text{m}</math>)</b>	49.0 $\pm$ 2.16



## Chapter IX

# 3D Bioprinting of a Mechanically Reinforced Hybrid Tissue Construct for Advanced Fibrocartilaginous Regeneration

3D Bioprinting of a Mechanically Reinforced  
Hybrid Tissue Construct for Advanced Fibrocartilaginous  
Regeneration<sup>##</sup>

**ABSTRACT**

Meniscus fibrocartilaginous tissue has a poor regenerative capacity, and, eventually, the damaged meniscus can lead to osteoarthritis. Therefore, strategies to bioengineer a fibrocartilaginous tissue to restore the function of the meniscus are needed. To address this currently unmet medical needs, three-dimensional (3D) bioprinting technologies have shown the potential to produce patient-specific and customizable complex structures. Despite these technologies offer a remarkable perspective in the bioengineering of personalized implants, there are still critical challenges to be addressed. Herein, we developed a novel hybrid tissue construct that could provide a biological microenvironment to accommodate cells with structural integrity for fibrocartilaginous tissue regeneration. This hybrid construct was fabricated by printing a cell-laden gellan gum/fibrinogen (GG/FB) bioink together with a silk methacrylate (SiI-MA) bioink in integrated patterns. Furthermore, *in vivo* study demonstrated that the hybrid system supported fibrocartilaginous tissue formation in the bioprinted construct without dimensional change. The proposed 3D bioprinted mechanically reinforced hybrid tissue construct is believed to offer a versatile and promising alternative for the production of patient-specific fibrocartilaginous tissue constructs.

---

<sup>##</sup> This chapter is based on the following publication:

Costa J. B., Park J. H., Silva-Correia J., Reis R. L., Oliveira J. M., Atala A., Yoo J. and Lee S. J., "3D Bioprinting of a Mechanically Reinforced Hybrid Tissue Construct for Advanced Fibrocartilaginous ", (Submitted), 2019.

## IX-1. INTRODUCTION

Fibrocartilage is a type of cartilages that can be found in the meniscus in the knee, temporomandibular joint (TMJ), and annulus fibrosus of the intervertebral disc (IVD). Because avascular meniscus has the poor intrinsic regenerative capacity, the number of patients affected by the degeneration of this tissue has been significantly increased [1]. In addition, the lack of efficiency presented by the currently available treatments together with the difficulty to mimic its unique combination of tensile strength, compressive strength, deformability, and complex microarchitecture has led to the pursuit of novel approaches [2]. The 3D bioprinting technologies have provided a promising and versatile processing pathway for the biofabrication of precisely biomimetic tissue constructs that resemble the anatomical, biomechanical, and biological properties of native tissues [3, 4]. The capability of 3D bioprinting is to precisely deposit multiple components, including cells and biomaterials, in a single tissue construct, and, especially, cells can be positioned by using cell-laden hydrogel-based bioinks.

Bioinks should create suitable 3D networks capable to mimic *in vivo* microenvironment in order to support cell adhesion, proliferation, and differentiation. Nevertheless, the pursue for the “perfect” bioink to allow the cell’s spatial distribution and an efficient and homogenous seeding in a 3D structure is still ongoing [5]. The functional and mechanical features of an ideal bioink should be tuned according to the tissue that is to replace. In this sense, different tissues require different mechanical properties and microenvironments in order to ensure implant integrity and post-printing cell phenotype. In addition, the compromise between the printability, the capability to encapsulate cells and maintain their viability, the control of the implant behavior post printing (degradation, shape maintenance, shrinkage...) and the mechanical performance of the entire implant has to be considered to achieve the desired result.

More advanced bioinks are now being designed to overcome the current challenges [6]; however, regardless of the noteworthy improvements in the 3D bioprinting technologies challenges still remain. Numerous natural and synthetic materials, such as fibrin [4, 7-10], gelatin [11], alginate [12], hyaluronic acid (HA) [13], collagen [14], poly( $\epsilon$ -caprolactone) (PCL) [15] and poly(ethylene glycol) (PEG) [16], have been exploited in the biofabrication of 3D constructs and, in some cases, used together to produce hybrid constructs [4, 15, 17-20]. The use of hybrid structures in 3D Bioprinting aims to produce biologically and mechanically suitable implants by means of using two bioinks: (i) one to give the biological functionality by carrying cells and biological factors and (ii) other to impart the proper mechanical strength. In most cases, natural hydrogels are elected as cell-laden bioinks and synthetic

materials as support materials. However, hydrogels have some limitations in terms of shape integrity, rapid degradation, mechanical stability, and printability [21, 22]. In addition, the synthetic polymers are well known for their poor biological properties due to its high hydrophobicity. This leads to a reduced cell adhesion capacity and subsequently a weak implant integration. Furthermore, these polymers present a slow degradation and, in some cases, inappropriate stiffness [23, 24].

In this study, we aimed to develop a novel 3D hybrid tissue construct by sequentially printing a cell-laden gellan gum/fibrinogen (GG/FB) bioink and a silk methacrylate (Sil-MA) bioink for fibrocartilaginous tissue regeneration (**Figure IX-1**). We hypothesized that the cell-laden GG/FB bioink could impart the biological microenvironment needed for cell proliferation and tissue formation, while the Sil-MA bioink could provide the mechanical support and stability required for the 3D printing process. Evaluation of the histological characteristics and function of the fibrocartilaginous tissue in the bioprinted hybrid constructs *in vitro* and *in vivo* showed tissue maturation and organization as well as dimensional maintenance over time.

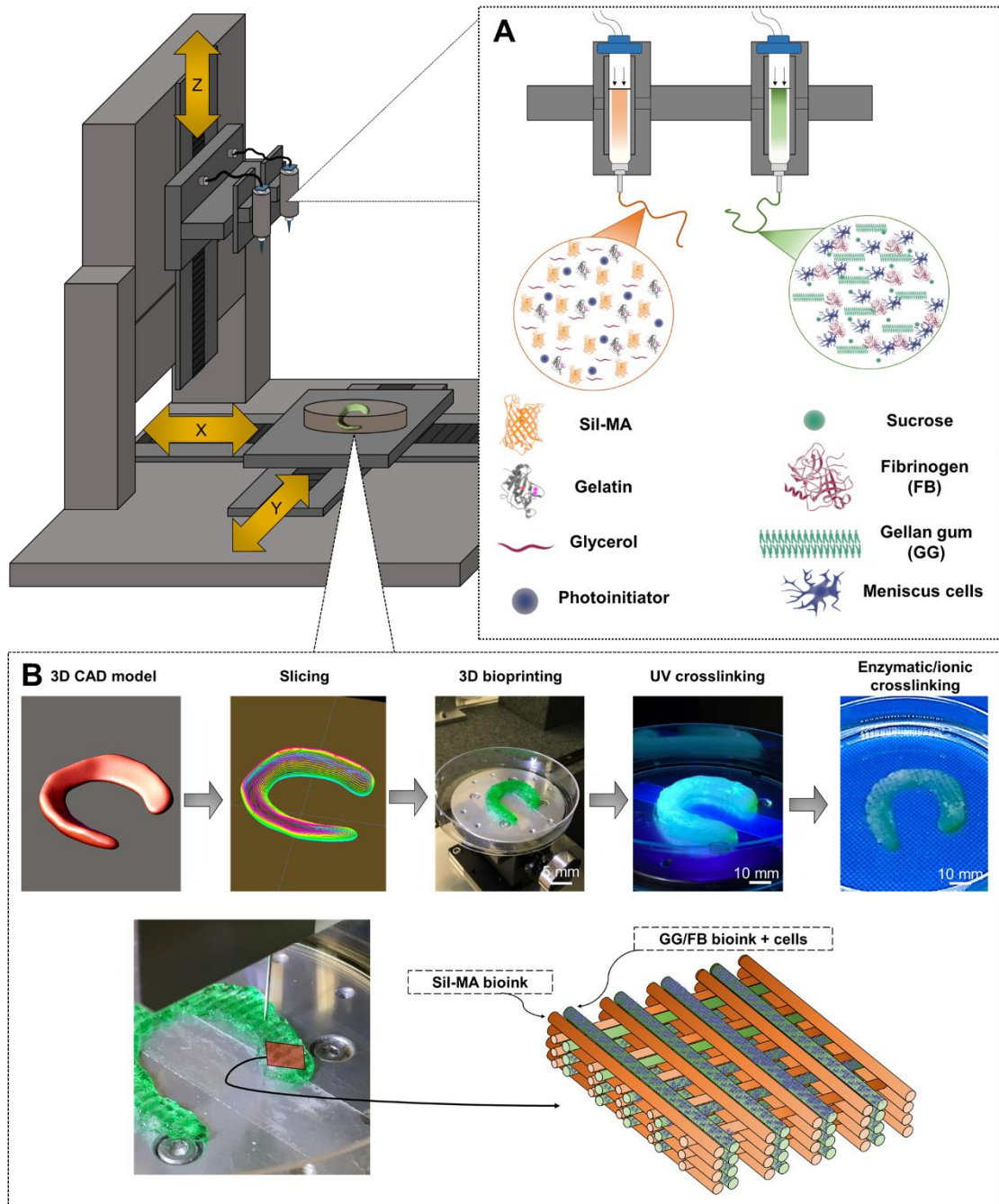


Figure IX-1 - Scheme of the 3D bioprinting of cell-laden hybrid scaffolds: (A) printing of hybrid 3D constructs using a Sil-MA bioink and a cell-laden GG/FB bioink. (B) 3D bioprinting and post-printing processes for the production of 3D hybrid constructs and respective patterning. (UV: Ultraviolet light).

## IX-2. MATERIALS AND METHODS

### IX-2.1. Materials

Low-acyl gellan gum (GG) powder and Fibrinogen (FB) were purchased from Sigma Aldrich (St Louis, MO, USA). Silk fibroin (SF) derived from the silkworm *Bombyx mori* in the form of cocoons was provided by the Portuguese Association of Parents and Friends of Mentally Disabled Citizens (APPACDM, Castelo Branco, Portugal). All reagents were purchased from Sigma-Aldrich (St. Louis, MO, USA) unless otherwise stated.

### IX-2.2. Bioink preparation

Different concentrations of fibrinogen were tested in the preparation of the GG/FB bioink. Briefly, different concentrations (25, 50, 75, 100, 125, and 150 mg.mL<sup>-1</sup>) of a FB solution were prepared by mixing in PBS at 37 °C for 2 hours. The fibrinogen was previously sterilized by UV radiation for 30 minutes. A solution of GG at 12 mg.mL<sup>-1</sup> was mixed with sucrose in distilled water at room temperature (RT) under constant stirring. The final concentration of sucrose was 0.25 M. The solution was progressively heated to 84 °C in an oil bath and kept at this temperature for 20 minutes under constant stirring. In addition, the solution was filtered using a 0.45 µm syringe filter and kept at 37 °C until further use. The GG solution was mixed with each of the FB solutions in a final ratio of 1:25. In the end, it was obtained GG/FB bioinks with different concentrations of FB (1, 2, 3, 4, 5, and 6 mg.mL<sup>-1</sup>). In the following table are represented the nomenclatures of the bioinks formulations.

Table IX-1 – Nomenclatures of the GG/FB bioinks.

Starting solutions	Mixing ratio	Bioink formulations	Nomenclatures
GG 12 mg.mL <sup>-1</sup>	1:25	GG	GG
GG 12 mg.mL <sup>-1</sup> + FB 25 mg.mL <sup>-1</sup>	1:25	GG + FB 1 mg.mL <sup>-1</sup>	GG/FB1
GG 12 mg.mL <sup>-1</sup> + FB 50 mg.mL <sup>-1</sup>	1:25	GG + FB 2 mg.mL <sup>-1</sup>	GG/FB2
GG 12 mg.mL <sup>-1</sup> + FB 75 mg.mL <sup>-1</sup>	1:25	GG + FB 3 mg.mL <sup>-1</sup>	GG/FB3
GG 12 mg.mL <sup>-1</sup> + FB 100 mg.mL <sup>-1</sup>	1:25	GG + FB 4 mg.mL <sup>-1</sup>	GG/FB4

GG 12 mg.mL <sup>-1</sup> + FB 125 mg.mL <sup>-1</sup>	1:25	GG + FB 5 mg.mL <sup>-1</sup>	GG/FB5
GG 12 mg.mL <sup>-1</sup> + FB 150 mg.mL <sup>-1</sup>	1:25	GG + FB 6 mg.mL <sup>-1</sup>	GG/FB6

Regarding the Sil-MA bioink preparation, purified silk fibroin (SF) was prepared by removing the glue-like protein sericin from the cocoons in a 0.02 M boiling sodium carbonate solution for 1 hour, followed by rinsing with distilled water in order to fully remove the degumming solution. A 9.3 M lithium bromide solution was used to dissolve the purified SF for 1 hour at 70 °C. After dissolution, 1, 2, and 3 mL of glycidyl methacrylate solution was added to 50 mL of silk solution. The reaction occurred under stirring at 55 °C for 3 hours. From this process, a high (Sil-MA (H)), a medium (Sil-MA (M)) and a low (Sil-MA (L)) methacrylate silk solutions were obtained. Then, the solutions were dialyzed in distilled water for 7 days using the benzoylated dialysis tubing (MWCO: 2 kDa). Sil-MA solutions were concentrated against poly (ethylene glycol) for at least 6 hours. The final concentration of the solutions was determined by measuring the dry weight in the oven at 70 °C overnight. In order to print the Sil-MA solutions gelatin and glycerol were used as printing support materials. The Sil-MA solutions at a final concentration of 16% (w/v) were mixed with glycerol and gelatin at a final concentration of 8% (w/v) and 4.5% (w/v), respectively. The solutions were incubated for 45 minutes at 65 °C. Then, the addition of Irgacure 2959 at a final concentration of 0.2 % (w/v) was the final step in the Sil-MA bioinks production. The support materials were washed out after printing.

### IX-2.3. Rheology

The rheological analyses of the developed bioinks were performed using a Discovery HR-2 (TA Instruments, US) and the acquisition software TRIOS (TA Instruments, US). For the oscillatory experiments, the measuring system was equipped with stainless steel parallel plates using an upper measurement geometry plate of 12 mm diameter. Frequency-sweep and strain sweep experiments were performed. For the rotational experiments, the measuring system was equipped with an upper measurement cone geometry (40 mm diameter and 1° angle). These experiments were performed at 20°C and all plots represent the average of at least three samples.

## IX-2.4. Printing process

The printing process was conducted in the house-made 3D ITOP system [4]. The system includes an XYZ stage/controller, multiple dispensing modules, a pneumatic pressure controller, and a closed chamber with a temperature controller. Printed constructs were designed with 3D computer-aided design (CAD) modeling using our customized software. The created models were converted to a motion program containing the path information and printing speed and air pressure were controlled. The environmental temperature was kept at 20 °C. Regarding the GG/FB bioinks, a microscale nozzle (240 µm of diameter, TECDIA, Inc., Tokyo, Japan) was used to print 3D constructs at a speed of 250 mm.min<sup>-1</sup> and air pressures ranging 45 to 65 kPa. After printing, the constructs were cross-linked using a PBS/Thrombin solution (20 U.mL<sup>-1</sup>) for 30 minutes at RT.

Regarding the SiI-MA bioinks, a microscale nozzle (300 µm of diameter, TECDIA, Inc., Tokyo, Japan) was used to print 3D constructs at a speed of 250 mm.min<sup>-1</sup> and air pressures ranging 450 to 550 kPa. After printing, the constructs were UV cross-linked by a BlueWave® MX<sup>1</sup>50 LED Spot-Curing System (Dymax, USA) for 120 seconds at an intensity of 400 mw.cm<sup>2</sup>.

## IX-2.5. Physico-chemical characterization

### IX-2.5.1. Proton nuclear magnetic resonance (<sup>1</sup>H-NMR) spectroscopy

The different degrees of methacrylation were measured through <sup>1</sup>H-NMR at a frequency of 400 MHz using a Bruker NMR Spectrometer (Bruker, Billerica, MA). SiI-MA solutions were frozen in -80 °C for 12 hours and freeze-dried for 48 hours. A 9.3M lithium bromide solution was prepared in deuterium oxide (D<sub>2</sub>O, Sigma-Aldrich). Using this solution, lyophilized SiI-MA powders were re-dissolved at a final concentration of 50 mg.mL<sup>-1</sup>. SF solution was used as control. The degree of methacrylation was defined according to the percentage of ε-amino groups of lysine in SF that are modified in SiI-MA. Therefore, the lysine methylene signals (2.4–2.6 ppm) of samples were integrated to obtain the areas. The degree of methacrylation was obtained by the equation:

Equation IX-1 - Determination of methacrylation degree.

$$\text{Methacrylation degree (\%)} = 1 - \left[ \frac{L_i^{\text{SMA}}}{L_i^{\text{SF}}} \right] \times 100\%$$



where,  $L_iSMA$  is the lysine integration signal of Sil-MA and  $L_iSF$  is the lysine integration signal of SF.

#### IX-2.5.2. Swelling tests

The swelling ratio of the constructs was evaluated after immersion in PBS for time periods ranging from 1 hour to 14 days. All experiments were conducted at 37 °C in static conditions. At each time point, the samples were removed from PBS, the excess of surface water was absorbed using a filter paper, and the weight immediately determined. In the end, the samples were dried at 60 °C and weight. The water uptake was obtained using the following equation:

Equation IX-2 - Determination of swelling ratio.

$$\text{swelling ratio (\%)} = \left[ \frac{(m_{w,t} - m_i)}{m_i} \right] \times 100\%$$

where,  $m_i$  is the initial weight of the sample, and  $m_{w,t}$  is the wet weight of the sample at each time point. A minimum number of three samples were tested.

#### IX-2.5.3. Mechanical properties

Uniaxial compressive tests were performed using a Universal Testing Machine (Instron5544) with a 100 N cell load at RT. The cross-head speed was set at 2 mm min<sup>-1</sup> and tests were run until achieving 60% reduction in specimen height. From the stress-strain curve, the secant modulus was calculated at 3%, 6% and 12% of strain. A minimum number of three samples was tested. Under the same operating conditions, a cyclic stress-relaxation compression test was performed. The samples were subjected to 5 cycles of compression with a strain of 60%.

#### IX-2.5.4. Diffusion tests

Diffusion tests were performed in the GG/FB bioinks using fluorescein isothiocyanate dextrans (FITC dextrans, Sigma-Aldrich, St. Louis, USA) with two different molecular weights (4 and 70 kDa). FITC dextrans were dissolved in 1 mL of a 12 mg.mL<sup>-1</sup> GG solution and kept at 37 °C. The GG/FITC dextran solutions were posteriorly mixed with the FB solutions obtaining a final concentration of FITC of

0.2 mg.mL<sup>-1</sup>. Then, 100 µL of the mixture was added to a 2 mL Eppendorf tube. The samples were incubated at 37 °C and 1 mL of PBS buffer, pH 7.4, was added to each tube. After 1, 3, 6, and 24 hours of incubation, the amount of dye present in the release medium (PBS) was determined by measuring fluorescence intensity ( $\lambda_{\text{ex}}$  490 nm,  $\lambda_{\text{em}}$  525 nm) using a plate reader (SpectraMax M5, Molecular Devices, USA). A minimum number of three samples were tested.

#### **IX-2.5.5. Scanning electron microscopy**

The morphology of the constructs was observed by SEM (FlexSEM 1000 VP-SEM, Hitachi, Japan). Before observation, the constructs were dried by critical point drying (Leica EM CPD300, Leica, USA) and coated with one layer of 4 nm of Au/Pd in a Leica EM ACE600 coater (Leica, USA). The same process was used for the Sil-MA constructs, however, a freeze-drying process was used.

#### **IX-2.6. In vitro biological evaluation of 3D constructs**

##### **IX-2.6.1. Pig meniscus cells (PMCs) isolation and expansion**

Pig meniscus cells (PMCs) were isolated from meniscus tissue samples obtained from euthanized pigs. PMCs were isolated following an enzymatic digestion-based method (collagenase type II and pronase). The extracted tissue underwent 3 washing steps: (1) povidone iodine, (2) PBS containing 10% (v/v) antibiotic/antimycotic mixture and (3) PBS containing 2% (v/v) antibiotic/antimycotic mixture. The washing steps were performed until the total removal of blood or other bodily contaminants. Meniscus tissue was then separated from the fat and vascularized tissue and was cut into small pieces. Tissue digestion was performed by incubation at 37 °C in an orbital stirring for 24 hours in 10-20 mL of a mixture of cell medium Alpha-MEM ( $\alpha$ -MEM, Life Technologies, Carlsbad, CA) supplemented with 10% (v/v) fetal bovine serum (FBS), 1% (v/v) antibiotic/antimycotic solution, 0.3% (w/v) collagenase type II and 0.5 mg.mL<sup>-1</sup> of pronase. The isolated PMCs were then expanded in basal medium consisting Alpha-MEM w/o nucleosides (MEM alpha medium; Life Technologies, Scotland) supplemented with 10% (v/v) FBS and 1% (v/v) antibiotic/antimycotic solution. Cells were cultured until confluence at 37 °C in an atmosphere of 5% CO<sub>2</sub> incubator, changing the culture medium every 2 days.

### IX-2.6.2. Encapsulation of PMCs on the GG and GG/FB4 3D constructs

In the following *in vitro* biological experiments, only the GG and GG/FB4 were used.

3D printed cell-laden constructs were produced. Using the previous developed bioink formulations (GG and GG/FB4), cube shape constructs were printed using the 3D ITOP system. Confluent PMCs (Passage 4-5) were detached with trypsin and encapsulated in the bioinks at a density of  $1.5 \times 10^7$  cells.mL<sup>-1</sup>. The constructs were posteriorly cross-linked with a PBS/thrombin solution for 30 minutes at RT. Then, fresh  $\alpha$ -MEM was added. The medium was changed every 2-3 days. The samples were removed at different time points. The timepoints 1, 3, 7, and 14 days were used for live/dead and viability tests and the time points 14 and 28 days were used for total collagen quantification, glycosaminoglycans (GAGs) quantification, and histology analysis.

### IX-2.6.3. Surface seeding of PMCs on the Sil-MA 3D constructs

In a 48 well plate, 200  $\mu$ L of each formulation was added to each well and posteriorly UV cross-linked for 120 seconds at an intensity of 400 mw.cm<sup>2</sup>. Confluent PMCs (Passage 4 -5) were detached with trypsin and seeded at a density of  $2.5 \times 10^4$  cells per well. Culture medium was changed every 2-3 days and samples were removed at different culture times (1, 3, and 7 days) to perform live/dead and viability tests.

### IX-2.6.4. Live/Dead staining

Cell viability of the PMCs in both tests (seeding and encapsulation) was confirmed by performing a calcein-AM (Life Technologies, Carlsbad, CA, USA) and propidium 269 iodide (PI; Life Technologies, Carlsbad, CA, USA) staining. At the end of each time point, two samples of each formulation were incubated in 1  $\mu$ g.mL<sup>-1</sup> calcein-AM and 5  $\mu$ g.mL<sup>-1</sup> PI prepared in PBS, for 30 minutes in the dark at 37 °C in the CO<sub>2</sub> incubator. After washing in PBS, samples were immediately examined under fluorescence microscopy (Calcein-AM in green: ex/em 495/515 nm; PI in red: ex/em 495/635 nm) in a transmitted and reflected light microscope Olympus IX83 (Olympus, Japan) for the surface seeding assays and a transmitted and reflected light Leica TCS LSI macro Confocal (Leica Microsystems Inc., Germany) for the cell encapsulation assays.

#### IX-2.6.5. Cell proliferation assay

Cell proliferation assay was performed to assess the metabolic activity of PMCs after seeding and encapsulation. Following the manufacturer's instructions, after each time point, a solution of 10% (v/v) AlamarBlue® (DAL1100; Life Technologies, Carlsbad, CA, USA) prepared in  $\alpha$ -MEM medium, was transferred to the culture plates in 500  $\mu$ L/scaffold. In the encapsulation assay, the 3D printed cell-laden constructs were transferred to a new culture plate before the addition of the reagent. After 3 hours of reaction with cells at 37 °C in the CO<sub>2</sub> incubator, 100  $\mu$ L of AlamarBlue solution was taken from each well and placed in a 96-well white opaque plate in triplicate. The absorbance was measured in a microplate reader (SpectraMax M5, Molecular Devices, USA) at 2 different wavelengths (570 nm and at 600 nm). The calculations were made according to the manufacturer's instructions. The culture well plates were washed with PBS and fresh medium was added. After 2 hours, the culture medium was replaced by fresh medium to avoid any reminiscence of the assay solution.

#### IX-2.6.6. Quantitative glycosaminoglycans and collagen assays in the 3D printed cell-laden constructs.

A dimethyl methylene blue (DMB) based-kit (Blyscan, Biocolor Ltd, UK) was used for sulfated glycosaminoglycans (GAGs) quantification, according to the manufacturer's instructions. After each time point, the constructs were washed with PBS solution and frozen at -80 °C until further analysis. Samples were digested overnight at 65 °C in 1 mL papain digestion solution, prepared by adding to each 50 mL of digestion buffer, 25 mg of papain and 48 mg of n-acetyl cysteine. Digestion buffer was composed of 200 mM of phosphate buffer (sodium phosphate monobasic) containing 1 mM ethylenediaminetetraacetic acid (EDTA) (pH 6.8). Then, samples were centrifuged at 10,000 rpm for 10 minutes and the supernatants collected. Furthermore, the GAGs content was determined according to the manufacturer's instructions by adding the DMB dye. The absorbance was measured in a microplate reader with a wavelength of 656 nm. A chondroitin sulphate stock solution was used to make a standard curve with concentrations ranging from 0 to 5  $\mu$ g.mL<sup>-1</sup>. All the results were normalized against the day 1 obtained values.

The amount of collagen was determined using a total collagen assay kit (Biovision, USA). The assay is based on the acid hydrolysis of samples to form hydrolysates and hydroxyproline. The oxidation of the hydroxyproline leads to the production of an intermediate that forms a chromophore (Abs 560

nm). After each time point, the constructs were washed with PBS solution and frozen at -80 °C until further analysis. Following the manufacturer's instructions, the samples were hydrolyzed at 75 °C overnight using an HCl solution ( $\approx 12$  M). Then, the samples were vortexed and centrifuged at 10,000 rpm for 3 minutes and 25  $\mu$ L of each hydrolyzed sample were transferred in triplicate to 96-well plate. The plate was posteriorly placed in an oven in order to evaporate. A standard curve was obtained by using the same procedure with a Collagen type I Standard. After drying, 100  $\mu$ L of the Chloramine T reagent was added to each well and incubate at RT for 5 minutes. Then, 100  $\mu$ L of the DMAB reagent was added to each well and incubate for 90 minutes at 60 °C. The absorbance was measured in a microplate reader with a wavelength of 560 nm. All the results were normalized against day 1 obtained values.

#### IX-2.6.7. Histology staining of the 3D printed cell-laden GG and GG/FB constructs (*in vitro*)

After 14 and 28 days of culture, the 3D printed cell-laden constructs were fixed overnight in 10% buffered formalin at RT. Then, after paraffin-embedding, the samples were serially sectioned with 7.5  $\mu$ m thick using a microtome. Sections of the constructs were stained with Hematoxylin and eosin staining, Safranin-O staining, Alcian Blue/Sirius Red staining and Picrosirius Red staining. Representative pictures of each sample were obtained using a transmitted and reflected light microscope Olympus BX63 (Olympus, Japan).

### IX-2.7. *In vivo* biological evaluation of 3D printed constructs

#### IX-2.7.1. Subcutaneous implantation

For the *in vivo* animal studies 3D constructs were implanted in dorsal subcutaneous pockets in athymic nude mice. All animal studies were conducted in accordance with Wake Forest University Animal Care and Use Committee (ACUC) regulations. General anesthesia was induced using an anesthesia machine that mixed isoflurane with oxygen. Isoflurane was used with a dose between 0-5% (up to 5% induction, 1-3% maintenance). Before the surgery, Ketoprofen (for analgesic purposes, 3-5 mg.kg<sup>-1</sup>) were administered subcutaneously. After shaving the surgical site on the left limb, local anesthesia (Bupivacaine, diluted to 0.25%, 2.5 mg.kg<sup>-1</sup>) was also administered. The shaved area was then cleaned by scrubbing three pairs of alternating applications of chlorhexidine followed by 70%

isopropyl alcohol in circular motions. Under general anesthesia, the dorsal surface was cleaned and sterilized with betadine and wiped with 70% alcohol. All surgical procedures were performed aseptically. A dorsal or paramedian longitudinal incision of approximately 2 cm long was made and two subcutaneous pockets (left and right sides) were created. Two bioprinted constructs were placed in the subcutaneous space and the wound was closed in a routine fashion way using a single layer interrupted non-absorbable sutures or staples. Sutures were removed within 14 days of placement. In this study, four groups (Sil-MA (H), GG/FB4 with and without cells and hybrid constructs) were tested and a total of 10 constructs from each group were used for implantation. The implanted constructs were harvested after 2 weeks, 5 weeks and 10 weeks.

### IX-2.7.2. Dimensional changes

The dimensional changes of the constructs were assessed after subcutaneous implantation. The volume of the constructs was measure using a displacement method.

The calculation of the percentage by volume was obtained using the following equation:

Equation IX-3 - Determination of the volume by the displacement method.

$$\text{Volume percentage} = \frac{v_{f,t} - v_i}{v_{0,t} - v_i} \times 100$$

where,  $v_{0,t}$  is the initial volume of the sample before implantation,  $v_{f,t}$  is the volume of the sample at each time point and  $v_i$  is the initial volume before immersion of the construct. A minimum number of three samples were tested.

### IX-2.7.3. Mechanical analysis

The mechanical performance of the constructs was assessed after subcutaneous implantation. The assay was performed according with the protocol described in the sub-section IX-2.5.3.

#### **IX-2.7.4. Histological evaluation**

Explants were collected and processed for histological analysis following the standard procedures. The collected explants were sectioned with 7.5  $\mu\text{m}$  thick in a microtome.

Representative samples were stained with H&E, Safranin O, Masson's trichrome and Alcian Blue/Picosirius red according to the manufacturer's instructions.

#### **IX-2.7.5. Quantitative glycosaminoglycans and collagen assays**

Total collagen and glycosaminoglycan quantification assays were performed according with protocol described in the sub-section IX-2.6.6.

#### **IX-2.7.6. Alcian Blue/Sirius Red polarized image analysis with MatLab, CT-FIRE, and CurveAlign**

Captured Alcian Blue/Sirius red polarized images were analyzed with a CurveAlign program (Laboratory for Optical and Computational Instrumentation, University of Wisconsin-Madison) and the output data were analyzed and graphed using MATLAB. Each collagen fiber was overlaid and converted into a direction heat map to quantify the alignment coefficient; with zero being no alignment and one being complete alignment. About 300 fibers per image were analyzed (3 images per sample; 3 samples per group). The alignment coefficient and collagen fiber color were both quantified using a custom MatLab code. The color threshold for the image was used to isolate the four main colors (red, yellow, orange, and green) seen in picosirius red stained samples under polarized light. The relative percentage of each color was quantified by dividing the pixel count of each color by the total pixel count in each image.

#### **IX-2.8. Statistical analysis**

All the numerical results are presented as mean  $\pm$  standard deviation (SD). Statistical analysis was performed using the GraphPad Prism 5.0 (GraphPad Software, La Jolla, CA, USA). First, a Shapiro-Wilk test was used to ascertain regarding data normality. For the compressive elastic modulus results and all the biological quantification assays, the differences between the experimental results were analyzed using a Kruskal-Wallis test followed by Dunn's multiple comparison test. Two independent experiments

were performed for cell studies, and at least three samples were analyzed per group in each culturing time. Statistical significant differences were represented by \* ( $p < 0.5$ ), \*\* ( $p < 0.01$ ) and \*\*\* ( $p < 0.001$ ).

### IX-3. RESULTS

#### IX-3.1. Preparation and characterization of gellan gum/fibrinogen (GG/FB) bioink

The material selection during the development of a novel bioink is a crucial step for successful bioprinting of cell-laden constructs [25]. Fibrin is a protein that has been widely used as a hydrogel in the biofabrication of cell-laden 3D constructs, mainly owing to its simple gelation properties and inherent cell-adhesion capability [4, 7, 8, 10, 26-30]. However, fibrin has some limitations, such as shape maintenance (shrinkage) after some culture time, rapid degradation and non-suitable mechanical properties. In opposite, GG is a commercial available anionic polysaccharide commonly used in the food and pharmaceutical industry that has been explored as a hydrogel [31, 32] and as a bioink [32-36] due to its good biocompatibility and ability to withstand compressive loads. It is imperative to notice that polysaccharides have been extensively used because of the advantage of effectively mimic the biological microenvironment of the native tissues [37]. However, we believe that the enhancement of cell-adhesion capability and mechanical stability by the insertion of FB in GG bioinks can be a great upgrade in terms of polysaccharides-based bioinks used in 3D bioprinting applications. Furthermore, it was envisioned that the double crosslinking step by means of an ionic (PBS) and enzymatic (thrombin) crosslink of the bioink could play a critical role in the integrity enhancement of the bioink.

The rheological properties assessment of a newly developed bioink is a critical step to understand the system printability, in particular for extrusion-based bioprinting approaches. GG is a temperature-sensitive material, which is more viscous at lower temperatures than at higher temperatures due to its reversible physical crosslinking [38].

Six different concentrations of FB between  $1 \text{ mg.mL}^{-1}$  and  $6 \text{ mg.mL}^{-1}$  (GG/FB1, GG/FB2, GG/FB3, GG/FB4, GG/FB5 and GG/FB6) were tested and GG bioink was used as control. Furthermore, the assessment of bioinks rheological behavior was performed using different methodologies (**Figure IX-2A and Supplementary Figure IX-1A and IX-1B, Supplementary material**). Oscillatory measurements at different frequencies (**Supplementary Figure IX-1A**) and at low strains (**Supplementary Figure IX-1B**)



revealed that no significant differences were found between all formulations. An elastic behavior ( $G' > G''$ ) was mainly exhibited by the bioinks. Regarding the viscosity test, all the formulations presented a shear-thinning behavior which is crucial in extrusion-based systems (**Figure IX-2A**) [39].

The fluidic exchanges and the nutrient diffusion of cell-laden hydrogels are two key features in the fabrication of 3D bioprinted constructs [40, 41]. Depending on different factors, such as the size of the model, the complexity of the design, the printing velocity and the number of bioinks used during the printing process, variation on printing times can occur. In this sense, is important to develop highly permeable hydrogels for a fast nutrient diffusion during the post-printing process. Swelling and diffusion tests with two different molecular weight molecules were performed. Regarding the diffusion tests, the different concentrations of fibrin did not affect the permeability of the constructs. After 1 hour, occurred a release of around 60% and 40% of the lower molecular weight molecule and higher molecular weight molecule, respectively (**Supplementary Figure IX-1C and IX-1D, Supplementary material**). All the formulations reached equilibrium after 1 hour of immersion in phosphate-buffered saline (PBS) solution ( $\approx 2800\%$ ), maintaining their weights up to 24 hours (**Supplementary Figure IX-1E, Supplementary material**). Overall, no significant differences were found in terms of swelling ratio and permeability.

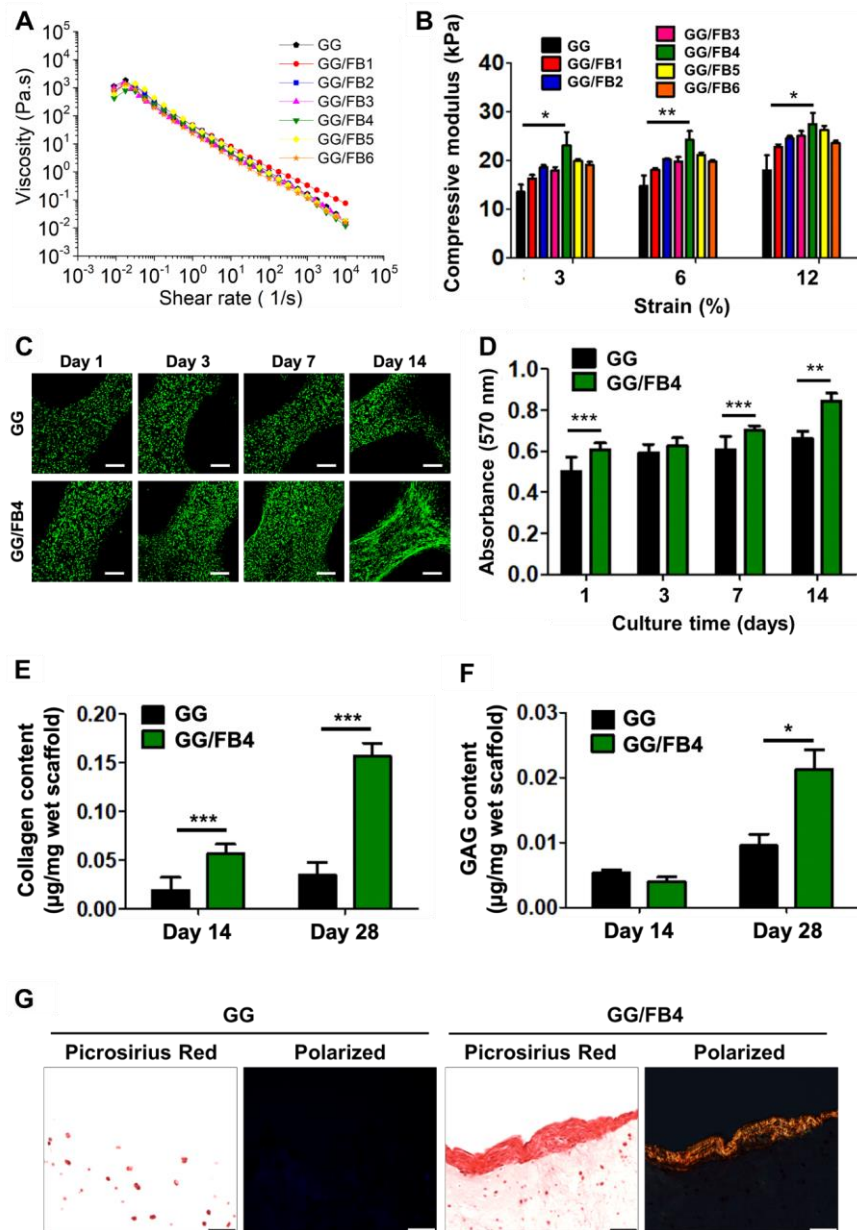


Figure IX-2 - Physico-chemical and *in vitro* biological characterization of the GG/FB cell-laden bioinks. A GG group without FB was used as control. (A) Viscosity of GG/FB bioinks as function of shear rate. (B) Compressive elastic modulus of 3D GG/FB constructs (cylinders, 12 mm in diameter and 4 mm in thickness) at 3%, 6% and 12% of strain after enzymatic/ionic crosslink. (C) Fluorescence micrographs of encapsulate PMCs in GG and GG/FB4 3D bioprinted constructs showing viability on Day 1, Day 3, Day 7 and Day 14, where live cells were stained in green and dead cells in red. (D) Quantification of metabolic activity of PMCs encapsulated in GG and GG/FB4 3D bioprinted constructs on Day 1, Day 3, Day 7 and Day 14 using the Alamar Blue assay. (E) Quantification of collagen amount produced by the PMCs encapsulated in GG and GG/FB4 3D bioprinted constructs on Day 14 and Day 28. (F) Quantification of glycosaminoglycans amount produced by the PMCs encapsulated in GG and GG/FB4 3D bioprinted constructs on Day 14 and Day 28. (G) Non-polarized (i and iii) and polarized (ii and iv) histological images of GG and GG/FB4 3D cell-laden bioprinted constructs stained with a picosirius red staining after 28 days of culture. Statistical significant differences were represented by \* ( $p < 0.5$ ), \*\* ( $p < 0.01$ ), and \*\*\* ( $p < 0.001$ ). Scale bars: 50  $\mu\text{m}$  (G); 200  $\mu\text{m}$  (C).

Mechanical performance of the crosslinked hydrogels was further evaluated through a uniaxial compression test (**Figure IX-2B and Supplementary Figure IX-1F, Supplementary material**). The inclusion of FB enhanced the constructs mechanical behavior and higher values of compressive elastic modulus were observed. Compared with the control group, the compressive elastic modulus of the GG/FB4 hydrogel increased from  $13.6 \pm 1.5$  kPa to  $23.1 \pm 2.7$  kPa,  $14.8 \pm 2.1$  kPa to  $24.3 \pm 1.8$  kPa and from  $17.9 \pm 3.2$  to  $27.5 \pm 2.3$  kPa at 3%, 6% and 12% of strain, respectively. In addition, statistical analysis revealed significant differences at 3% (\* $p < 0.1$ ), 6% (\*\* $p < 0.01$ ) and 12% (\* $p < 0.1$ ) of strain when these two formulations were compared. The double crosslinking mechanism is a plausible explanation for this improvement in terms of mechanical behavior. However, the increase in the amount of FB is not directly proportional to the increase of the compressive elastic modulus values. The formulations GG/FB5 and GG/FB6 presented lower modulus values when compared with the GG/FB4. A possible explanation is the existence of a crosslink “competition” between the ionic and the enzymatic crosslink leading to less stable constructs. In this sense, to ensure an appropriate mechanical behavior GG/FB4 was selected to be used as bioink in further assays.

To assess the *in vitro* biological properties of the GG/FB4 bioink, cell-laden 3D constructs were bioprinted and subsequently crosslinked with a PBS/Thrombin solution. Isolated pig meniscus cells (PMCs) were used for cell-encapsulation in the GG/FB4 bioink. The cells were cultured for 14 days and their viability and metabolic activity were characterized by Live/Dead (**Figure IX-2C**) and Alamar Blue (**Figure IX-2D**), respectively. The GG bioink was used as control. The metabolic activity of the PMCs encapsulated in the GG/FB4 bioink was significantly higher compared with the control group. Significant differences were found at day 1 ( $p^{***} < 0.001$ ), day 7 ( $p^{***} < 0.001$ ) and day 14 ( $p^{**} < 0.001$ ), endorsing that the presence of fibrin was a key factor to improve the bioink biological properties. Extracellular matrix (ECM) deposition is also an important feature to be addressed in order to assess the bioink biological performance. Fibrocartilage is an avascular and aneural tissue highly embedded in a readily visible ECM [42, 43]. Thus, the presence of ECM deposition could be a good indicator of cell adhesion, spreading and phenotype maintenance. When encapsulated in the GG/FB4 bioink, PMCs revealed a higher deposition of collagen (**Figure IX-2E**) and glycosaminoglycans (GAGs) (**Figure IX-2F**) when compared with control. Significant differences were found in terms of collagen ( $p^{***} < 0.001$ ) and GAGs ( $p^* < 0.05$ ) production after 28 days of *in vitro* culture. In addition, histological images (**Figure IX-2G and Supplementary Figure IX-2, Supplementary material**) corroborated the previous results, revealing ECM deposition mostly in the surface of the GG/FB4 bioink.

### IX-3.2. Preparation and characterization of mechanically reinforced silk fibroin methacrylate (Sil-MA) bioink

Fibrocartilaginous tissues are characterized to be present in zones of the human body that are subjected to great compressive and tensile loads [44, 45]. Despite the good mechanical behavior and structural integrity maintenance of GG/FB4 bioink, better mechanical performance is needed for fibrocartilage applications. Herein, a Sil-MA bioink was developed to be printed side by side with the GG/FB4 bioink in a hybrid system.

Silk fibroin (SF) from the silkworm *Bombyx mori* has been widely used in several biotechnological applications in the regenerative medicine field [46-48]. SF has been increasingly recognized as a promising material for scaffold fabrication mainly due to its excellent biocompatibility, remarkable mechanical properties, memory-shape capability, and tailorable degradability [46, 49]. These promising features have increased the scientific community awareness and different silk-based bioinks have been developed for 3D bioprinting applications [49-54]. Moreover, SF potential can be enhanced through a variety of chemical modifications including the addition of methacrylate groups to the amine-containing groups of the SF. This functionalization creates a light polymerizable hydrogel that can be used as an advantage in terms of *in situ* or post-processing crosslink [55]. The potential of this functionalization was confirmed by Kim *et al.* [53], where an SF-based bioink was developed by a methacrylation process using glycidyl methacrylate. This bioink was posteriorly used in a digital light processing (DLP) bioprinting process revealing good structure stability and biocompatibility. Despite the promising results, the use of a DLP bioprinting methodology can be restrictive in terms of cell spatial distribution, cell density, and multi-material printing. In contrast, extrusion-based bioprinting technologies have a lower cost, are simpler and with the capability to print multiple materials and high cell densities. In this sense, the use of Sil-MA bioink in an extrusion-based technology may allow the production of implants that better mimic the human native tissues, especially the fibrocartilaginous tissues [56, 57].

Therefore, Sil-MA-based bioinks with three different degrees of methacrylation were developed. The degree of methacrylation was evaluated and calculated based on the proton nuclear magnetic resonance (<sup>1</sup>H-NMR) spectroscopy results (**Supplementary Figure IX-3, Supplementary material**). Depending on the amount of glycidyl methacrylate used during the methacrylation reaction different degrees were obtained. In this work, Sil-MA solutions with 63.5% (Sil-MA (H)), 57.2% (Sil-MA (M)) and 44.5% (Sil-MA (L)) of methacrylate were produced and used in further characterization tests. Based on previous studies [4, 54] and preliminary extrusion tests (data not shown), Sil-MA solutions were used at

a final concentration of 16% (w/v) and posteriorly mixed with glycerol and gelatin at a final concentration of 8% (w/v) and 4.5 % (w/v), respectively. Aware that a controllable and fast phase transition material is needed, gelatin and glycerol were used as bulking agents in the bioprinting process. In a rational manner, the addition of gelatin and glycerol allowed the creation of a thermo-responsive bioink and endorsed the shear-thinning behavior of the bioink [54]. Rheological tests (**Figure IX-3A and Supplementary Figure IX-4A and IX-4B, Supplementary material**) revealed, as expected, that the chemical modification of the bioinks did not affect the rheological behavior. Furthermore, the bioinks presented the desired elastic ( $G' > G''$ ) and shear-thinning behavior. These results suggest that the rheological behavior is totally related to the bulking materials (glycerol and gelatin) allowing to maintain the printing parameters despite the degree of methacrylation used during the bioprinting process. Moreover, the developed system allowed to print 3D constructs with good printing fidelity and easy to handle.

The conformation change over time of the SF hydrogels was investigated. SF hydrogels are characterized by the occurrence of a spontaneous conformation change overtime from random coil to  $\beta$ -sheet [58, 59]. In previous studies, enzymatically crosslinked SF hydrogels presented a spontaneous change to a crystalline conformation ( $\beta$ -sheet) that was responsible for the enhancement of the hydrogels stiffness and mechanical performance. In this work, the spontaneous conformation change was also confirmed after a photo-crosslinking process using ultraviolet light (UV). In addition, by playing with different methacrylation degrees, the results showed the possibility to tune the conformation change speed as well as the mechanical properties over time (**Figure IX-3B and IX-3C and Supplementary Figure IX-4C, Supplementary material**). As it can be seen in optical images of **Figure IX-3B** after printing (day 0) the hydrogels presented a predominance of random coil conformation that is characterized by their transparent appearance. Then, the hydrogels were incubated in PBS for 14 days at 37 °C. After 1 day of soaking, the Sil-MA (H) hydrogels maintained a transparent appearance. In opposite, Sil-MA (M) hydrogels started to present a whitish color and the Sil-MA (L) hydrogels were completely white. This color change is also indicative of a conformation change from random coil to  $\beta$ -sheet as previously reported elsewhere [58, 59]. After 7 days, all the hydrogels were completely white indicating the predominance of  $\beta$ -sheet conformation. These results were endorsed by the results obtained in mechanical properties assays. As before, a uniaxial compression test was performed. After printing (day 0), the compressive elastic modulus of the hydrogels were  $24.4 \pm 2.8$  kPa,  $11.6 \pm 1.2$  kPa and  $5.4 \pm 0.3$  kPa for Sil-MA (H), Sil-MA (M) and Sil-MA (L), respectively. As expected, after 1 day the value of compressive elastic modulus remained similar for the Sil-MA (H) hydrogel ( $23.3 \pm 5.2$  kPa) and

increased from  $5.4 \pm 0.3$  kPa to  $62.2 \pm 10.6$  kPa for the Sil-MA (L) hydrogel. After total conformation change (day 7), the Sil-MA (H) revealed a higher value of compressive elastic modulus ( $510 \pm 92.4$  kPa) compared with the other two formulations. In addition, the Sil-MA (M) hydrogels showed an intermediate value ( $298 \pm 87.8$  kPa) with the Sil-MA (L) hydrogel presenting the lowest value ( $151.1 \pm 44.7$  kPa). In the next following 7 days, a slight decrease in the mechanical properties was observed that is possibly related to hydrogels degradation. As a conclusion, a higher degree of methacrylation (Sil-MA (H)) leads to higher mechanical stability post-printing (Day 0), a higher mechanical performance after total conformation change (Day 7 and Day 14) and a lower conformation change speed. These results may be associated with the higher number of chain-chain linkages obtained in the Sil-MA (H) bioinks after the photo-crosslinking process. Herein, these results indicate that using our 3D hybrid bioprinting system, is possible to tune the mechanical properties of the bioprinted implants only by changing the Sil-MA methacrylation degree. The hydrogels pore size and swelling ratio were also affected by the different degrees of crosslinking. The scanning electron microscope images (Figure IX-3D), revealed that Sil-MA (H) presented smaller pores compared with Sil-MA (M) and Sil-MA (L). Furthermore, the swelling ratio was also lower for bioinks with higher degrees of methacrylation (Supplementary Figure IX-4D, Supplementary material). The swelling results are highly related to the hydrogels pore size where hydrogels with small pores allow less water uptake. In addition, these results are in concordance with the mechanical performance of the hydrogels where higher compressive modulus was found for hydrogels with smaller pores and lower swelling ratio.

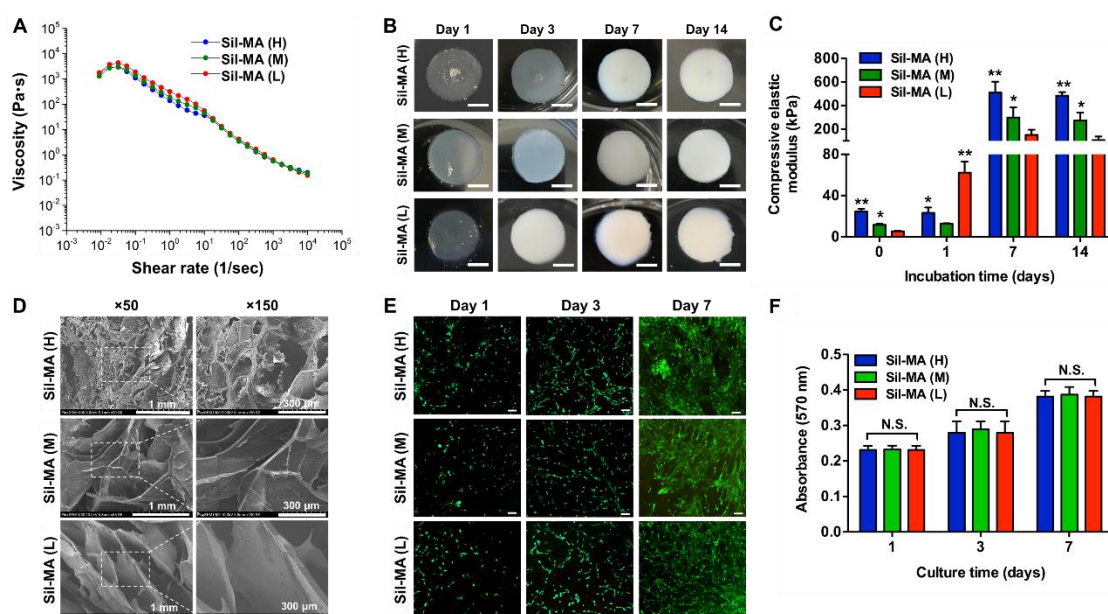


Figure IX-3 - Physico-chemical and *in vitro* biological characterization of the Sil-MA bioinks. (A) Viscosity of Sil-MA bioinks as function of shear rate. (B) Photographs of 3D Sil-MA constructs (cylinders, 12 mm in diameter and 4 mm in

thickness) showing the change of conformation overtime. (C) Compressive elastic modulus of 3D Sil-MA constructs (cylinders, 12 mm in diameter and 4 mm in thickness) at 12% of strain on Day 0, Day1, Day 7 and Day 14. (D) Scanning electron microscope images of 3D Sil-MA constructs produced using Sil-MA (H) bioink (i and ii), Sil-MA (M) bioink (iii and iv) and Sil-MA (L) bioink (v and vi) at different magnifications. (E) Fluorescence micrographs of seeded PMCs Sil-MA 3D constructs showing viability on Day 1, Day 3 and Day 7, where live cells were stained in green and dead cells in red. (F) Quantification of metabolic activity of PMCs seeded in Sil-MA 3D constructs on Day 1, Day 3 and Day 7 using the Alamar Blue assay. Statistical significant differences: (C) \* ( $p < 0.05$ ) compared with Sil-MA (L) at 0, 7, and 14 days; \*  $p < 0.05$  compared with Sil-MA (M) at 1 day and \*\* ( $p < 0.05$ ) compared with others. (F) N.S.: no significant. Scale bars: 5 mm (B); 200  $\mu\text{m}$  (E).

In spite of the fact that Sil-MA bioink was developed with the main purpose of providing mechanical stability, the choice of SF as supporting was also to guarantee an enhanced biological performance of the hybrid implant. It is important to emphasize that a support bioink in a hybrid system should not only provide implant mechanical stability but suitable biological properties for good implant integration and anchorage. In this sense, to assess the Sil-MA bioinks *in vitro* biological properties PMCs were seeded on their surface. The viability (**Figure IX-3E**) and metabolic activity (**Figure IX-3F**) assays showed that all Sil-MA bioinks not only supported cell adhesion but also maintained PMCs metabolically active for 7 days of culture. No significant differences were found comparing the three formulations.

### IX-3.3. 3D Bioprinting of a Mechanically Reinforced Hybrid Tissue Construct

Finally, based on previous results, GG/FB4 and Sil-MA (H) were chosen for the bioprinting of 3D hybrid constructs. In this final characterization section, GG/FB4 and Sil-MA (H) 3D bioprinted constructs were used as controls. Mechanical uniaxial compression tests (**Figure IX-4**) and an *in vivo* subcutaneous implantation (**Figure IX-5, IX-6 and IX-7**) were performed. As expected, massive differences were observed in the compressive elastic modulus values of the Sil-MA (H) and hybrid constructs compared with the GG/FB4 constructs after 14 days submerged in PBS at 37 °C (**Figure IX-4A and IX-4B**). The compressive modulus values increase from  $14.7 \pm 2.1$  kPa to  $352.4 \pm 19.2$  kPa and from  $23.9 \pm 5.7$  kPa to  $306.5 \pm 43.7$  kPa for the Sil-MA (H) and hybrid constructs, respectively. As expected, after conformation change from random coil to  $\beta$ -sheet, the Sil-MA (H) bioink granted excellent mechanical properties to the 3D constructs. In addition, the Sil-MA (H) bioink confers memory-shape properties to the hybrid construct by maintaining their original shape immediately after compression release (**Figure IX-4C**). This memory-shape behavior was confirmed by a cyclic stress-relaxation compressive test (**Figure IX-4D and IX-4E**). The 3D printed constructs were tested up to 60% strain to examine their mechanical recovery. Five identical stress-strain plots were obtained from the

five sequential stress-relaxation cycles, confirming a fully shape recovery of the 3D printed constructs. Furthermore, this test evidenced the presence of the memory-shape behavior conferred by the silk-based bioink [49, 60]. Comparing with previously developed PCL/collagen hybrid constructs, lower values of compressive elastic modulus were obtained [17]. However, regarding the native tissue, the mechanical behavior of the produced 3D hybrid constructs revealed to be suitable for the biofabrication of 3D bioprinted patient-specific implants for cartilage/fibrocartilage regeneration [45, 61, 62]. In addition, it is important to emphasize that the target mechanical properties could be tuned using different degrees of methacrylation and different concentrations of SF [53].

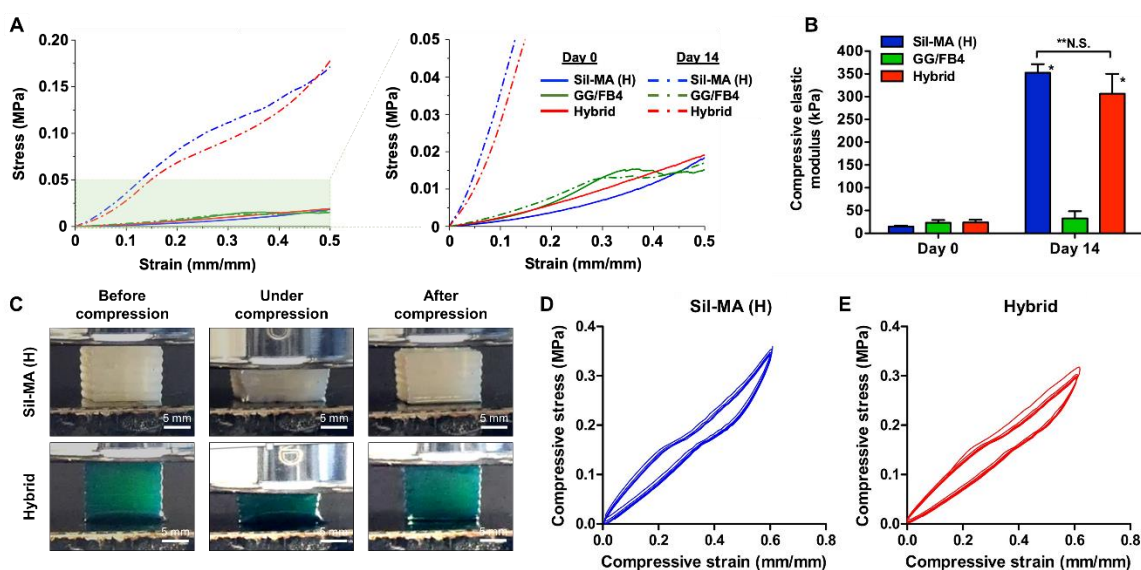


**Figure IX-4** - Physical characterization of 3D bioprinted constructs. (A) Stress-strain plot of compressive uniaxial compression test performed in 3D bioprinted constructs. (B) Compressive elastic modulus of 3D bioprinted constructs at 12% of strain on Day 0 and Day 14. (C) Macroscopic images of the 3D bioprinted constructs (Sil-MA (H) and Hybrid) before, under and after compression. (D) Stress-strain plot of the compressive uniaxial cyclic stress-relaxation test performed in the Sil-MA (H) 3D bioprinted constructs. (E) Stress-strain plot of the compressive uniaxial cyclic stress-relaxation test performed in the Hybrid 3D bioprinted constructs. Statistical significant differences: (B) \* ( $p < 0.05$ ) compared with GG/FB4, \*\*N.S.: no significant.

To evaluate the *in vivo* maturation of the 3D bioprinted constructs implantation in the subcutaneous space of athymic nude mice was performed. The constructs were retrieved 2 weeks, 5 weeks and 10 weeks after implantation. The macroscopic assessment revealed that the hybrid constructs maintained their shape during the entire assay and vascularization was observed in the Sil-MA (H) and hybrid constructs (Figure IX-5A and IX-5B). In contrast, a reduction in terms of size was observed in the GG/FB4 constructs. Biomechanical analysis (Figure IX-5C) showed that after 2 weeks of implantation the Sil-Ma (H) ( $333.1 \pm 109.9$  kPa) and hybrid ( $220.0 \pm 99.0$  kPa) constructs presented



higher compressive modulus compared with the GG/FB4 ( $18.9 \pm 6.1$  kPa). However, a decrease in terms of mechanical behavior was observed from week 2 to week 5 and significant differences ( $p^* < 0.05$ ) were observed comparing the Sil-Ma (H) ( $154.8 \pm 38.5$  kPa) with the hybrid ( $64.2 \pm 9.5$  kPa) constructs. Despite tissue formation, a possible degradation and deterioration of the Sil-MA (H) resulted in lower values of compressive modulus. Nevertheless, the constructs mechanical performance seems to stabilize from week 5 to week 10. The mechanical properties of the GG/FB4 constructs remained stable during the entire assay. Histological analysis revealed the formation of chondrocyte-like tissue in the GG/FB4 and hybrid constructs after 5 weeks and 10 weeks of implantation (**Figure IX-6A and Figure IX-6B**). In both samples, an increase in terms of GAGs deposition and collagenous tissue formation seems to occur over time. Quantification assays of collagen (**Figure IX-6C**) and GAGs (**Figure IX-6D**) were performed. The results revealed that the hybrid construct presented a considerable higher amount of collagen ( $4.71 \pm 0.15 \mu\text{g}.\text{mg}^{-1}$ ) and GAGs ( $0.4 \pm 0.01 \mu\text{g}.\text{mg}^{-1}$ ) deposition comparing with the others formulations after 10 weeks of implantation. As expected, GG/FB4 3D bioprinted without cells presented less collagen and GAGs deposition and histological analysis only revealed host tissue infiltration (**Supplementary Figure IX-5, Supplementary material**).

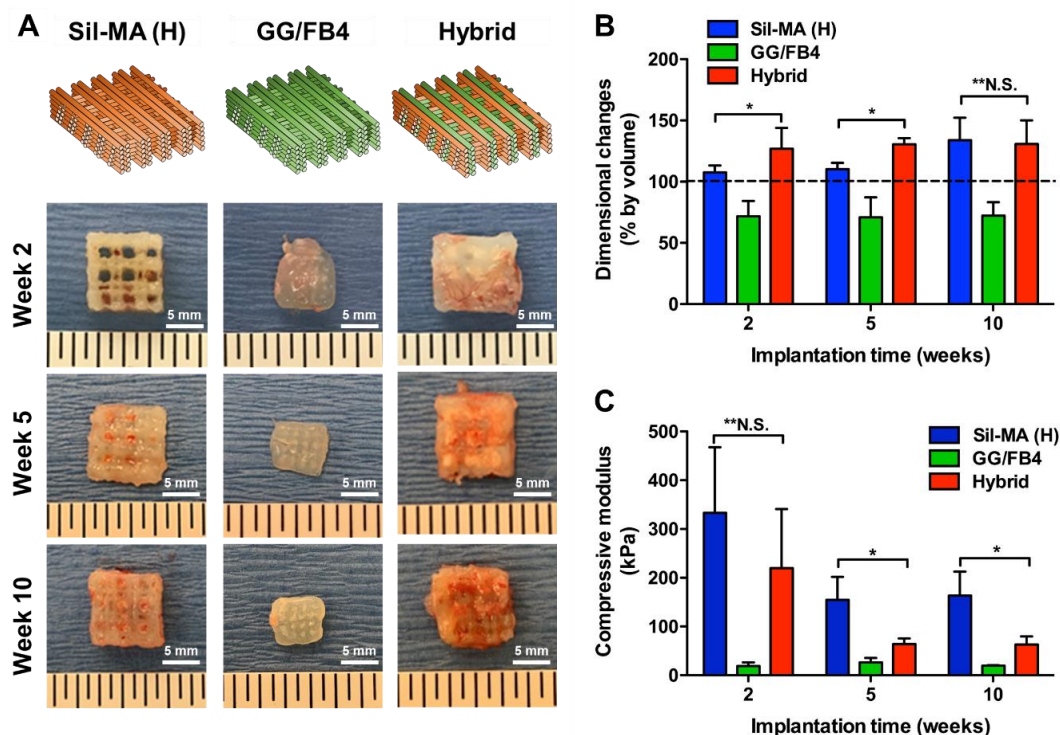


Figure IX-5 - *In vivo* biological characterization of 3D bioprinted constructs. (A) Scheme of the patterning used for the production of 3D bioprinted constructs and macroscopic images of the explants, 2 weeks, 5 weeks and 10 weeks after subcutaneous implantation. (B) Dimensional changes of the 3D bioprinted constructs after 2 weeks, 5 weeks and 10 weeks of subcutaneous implantation. (C) Compressive elastic modulus of 3D

bioprinted constructs at 12% of strain after 2 weeks, 5 weeks and 10 weeks of subcutaneous implantation. Statistical significant differences: (B) and (C) \* ( $p < 0.05$ ), \*\*N.S.: no significant.

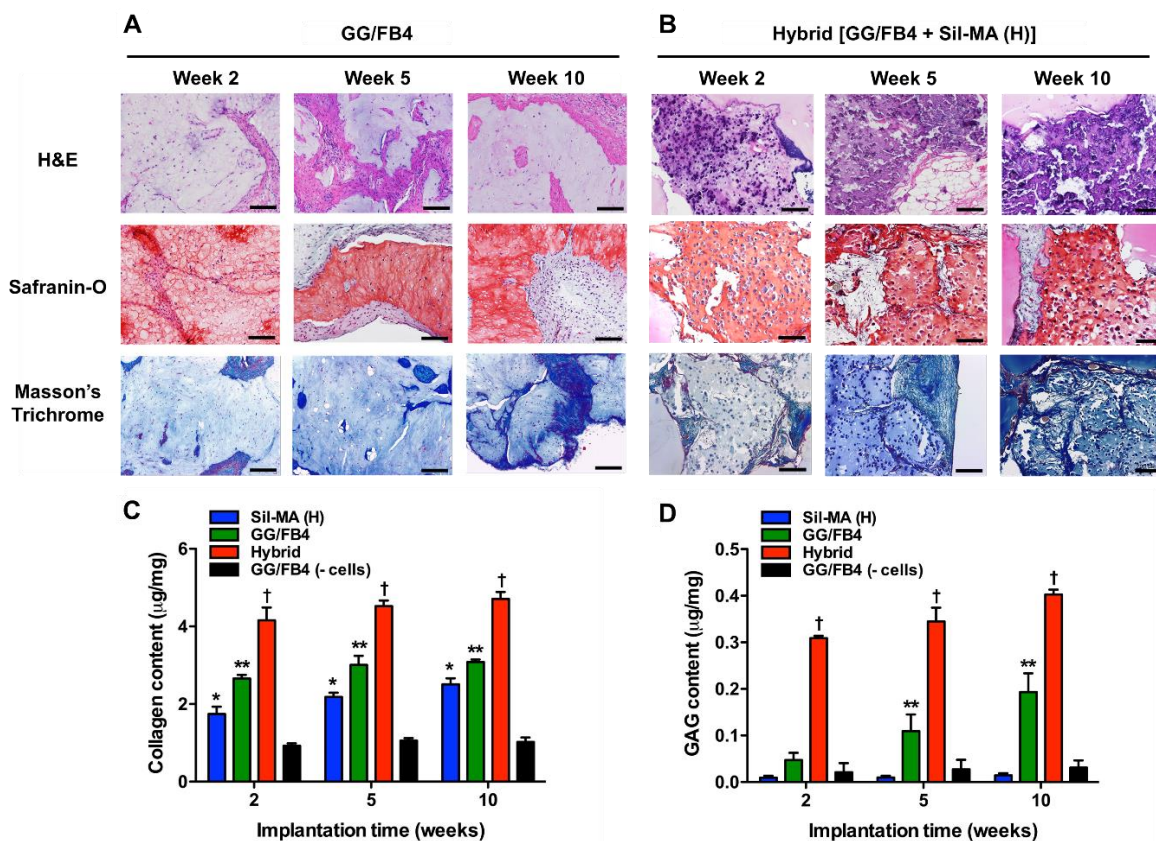
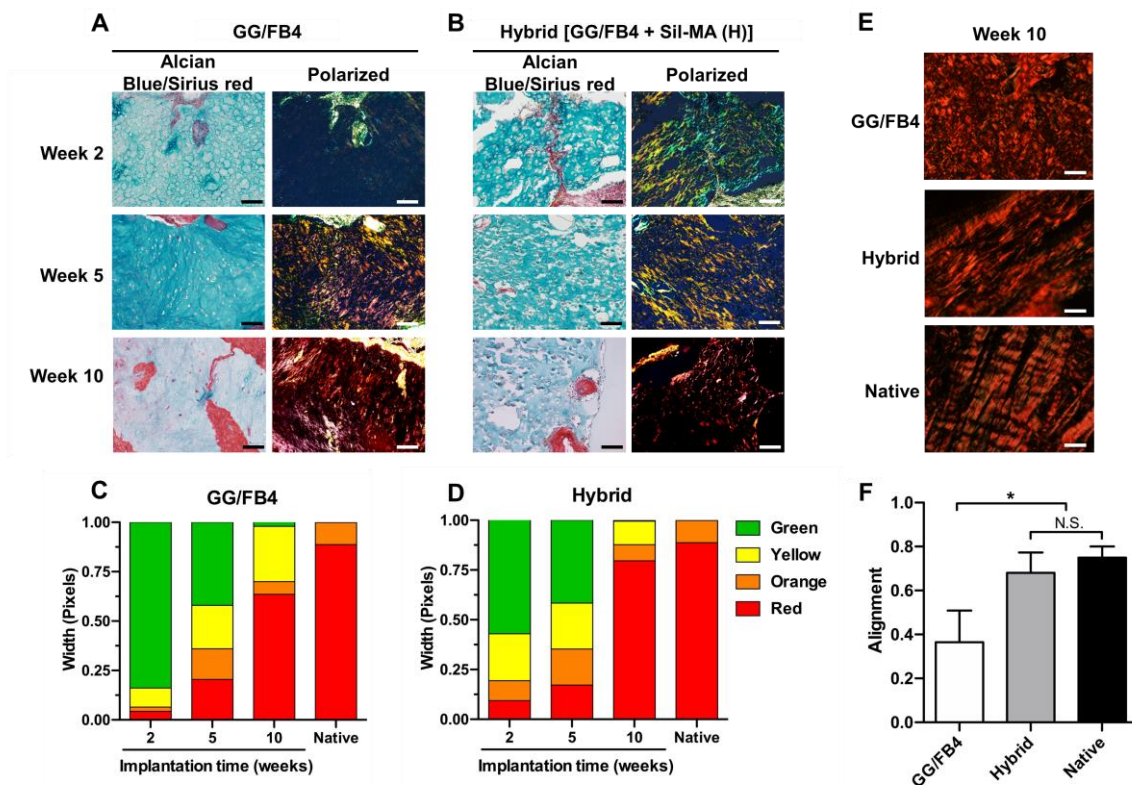


Figure IX-6 - Histological analysis and quantification assays of the 3D bioprinted constructs after 2 weeks, 5 weeks and 10 weeks of subcutaneous implantation. (A) Histological images of GG/FB4 3D bioprinted cell-laden constructs stained with a Hematoxylin & Eosin, Safranin-O, Masson's trichrome. (B) Histological images of hybrid 3D bioprinted cell-laden constructs stained with a Hematoxylin & Eosin, Safranin-O, Masson's trichrome (C) Quantification of collagen deposition of the Sil-MA (H), GG/FB4, hybrid and GG/F4 without cells 3D bioprinted constructs. (D) Quantification of glycosaminoglycans deposition of the Sil-MA (H), GG/FB4, hybrid and GG/F4 without cells 3D bioprinted constructs. Statistical significant differences: \* ( $p < 0.05$ ) compared with GG/FB4 (-cells), \*\* ( $p < 0.05$ ) compared with Sil-MA (H), † ( $p < 0.05$ ) compared with others. Scale bars: 200  $\mu\text{m}$ .

Furthermore, histological analysis using an Alcian Blue/Picrosirius red staining was performed and the stained samples were observed under polarized light (Figure IX-7A and Figure IX-7B). Previous studies revealed that, in the picrosirius red-polarization detection method, collagen type I fibers are assigned to a yellow-red birefringence while collagen type III fibers display weak birefringent and are associated to a greenish color [63-65]. Taking this into account, the histological analysis under polarized light suggested that tissue maturation occurred for both samples over the 10 weeks of

implantation. **Figure IX-7C** and **Figure IX-7D** depicts the average percentage of each collagen fiber color in the GG/FB4 and Hybrid constructs, respectively. This image analysis was performed using a custom MATLAB code and allowed to quantify the collagen fiber maturity based on the abovementioned principle. The results confirmed the change from green color to red color over the 10 weeks of implantation for both formulations, suggesting once more tissue maturation and presence of mature collagen fibers. After 10 weeks of implantation, the hybrid construct revealed a higher presence of red fibers ( $0.79 \pm 0.01$  pixels) resembling the results obtained in the native tissue ( $0.88 \pm 0.04$  pixels). In addition, CurvAlign software was used to determine the coefficient of alignment of collagen fibers in each formulation (**Figure IX-7E** and **Figure IX-7F**). The coefficient of alignment is considered zero when there is no alignment and one when the fibers are completely aligned. No significant differences were found between the hybrid constructs ( $0.68 \pm 0.08$ ) and the meniscus native tissue ( $0.75 \pm 0.04$ ). These results suggest that the produced tissue resembles the ECM native tissue composition and architecture [44, 66].



**Figure IX-7** - Histological analysis and image analysis using MatLab, CT-FIRE, and CurveAlign of the 3D bioprinted constructs after 2 weeks, 5 weeks and 10 weeks of subcutaneous implantation. (A) Histological images of GG/FB4 3D bioprinted cell-laden constructs stained with Alcian Blue/Sirius red (not polarized and polarized images). (B) Histological images of hybrid 3D bioprinted cell-laden constructs stained with Alcian Blue/Sirius red (not polarized and polarized images). (C) Measured average percentage of each collagen fiber color in GG/FB4 3D bioprinted cell-laden constructs using a custom MATLAB code. (D) Measured average percentage of each

collagen fiber color in hybrid bioprinted cell-laden constructs using a custom MATLAB code. (E) Representative polarized images of the GG/FB4 and hybrid 3D bioprinted cell-laden constructs (10 weeks after implantation) and Pig meniscus (native) at higher magnification that were used in the alignment analysis. (F) Alignment analysis of the fibers using a CruveAlign software (Laboratory for Optical and Computational Instrumentation, University of Wisconsin-Madison) where each fiber was overlaid and converted into a direction heat map to quantify the alignment coefficient; with zero being no alignment and one being complete alignment. Statistical significant differences: (F) \*  $p < 0.05$  compared with GG/FB4, N.S.: no significant. Scale bars: 100  $\mu\text{m}$  (A) and (B); 20  $\mu\text{m}$  (E).

#### IX-4. DISCUSSION

The presented results provided a proof of concept strategy that used two natural-based bioinks for the bioprinting of mechanically reinforced hybrid tissue constructs. This novel approach was focused on the production of patient-specific implants for fibrocartilage regeneration. For this purpose, the authors aimed to use a GG/FB cell-laden bioink and a Sil-MA bioink that were directed deposited side by side using a previously developed integrated tissue–organ printer (ITOP) [4]. First, the rheological properties, mechanical performance, printability and biological properties of different formulations of GG/FB cell-laden bioink and Sil-MA bioinks were properly characterized in order to achieve a suitable combination for cartilage/fibrocartilage applications. In the end, this hybrid approach incorporated a GG/FB4 bioink with suitable biological and mechanical performance as well as a Sil-MA (H) bioink that allowed to confer great stability and the mechanical properties needed for fibrocartilage regeneration. Furthermore, *in vivo* maturation of the 3D bioprinted constructs revealed shape maintenance and chondrocyte-like tissue maturation up to 10 weeks of implantation. Moreover, the versatility and tunability of the developed bioinks suggest the possible use of this system in different tissue engineering applications that require mechanically reinforced patient-specific implants.

The development of two natural-based bioinks as novel and broadly applicable alternative for the production of patient-specific hybrid constructs is what differs from the conventional methods. The use of only natural-based biomaterials allows the possibility to tailor the final scaffold's properties as well as impart guaranteed biocompatibility to the scaffold. In clinical orthopedic applications, the engineered implant should be highly biocompatible in order to ensure the integration of the implant with the adjacent tissue [67]. In addition, the mechanical performance of the produced implants should also be tailored to match the adjacent tissue providing an immediate and short-term mechanical function [68]. Previous research using the combination of a natural biomaterial with a synthetic biomaterial in hybrid approaches [4, 15, 69, 70] showed promising results. However, some of these strategies revealed

inadequate stiffness and lack of tunability. To overcome this limitation, it is the author's belief that the use of two only natural-based bioinks presents great versatility and capability to produce patient-specific scaffolds with better biocompatibility and suitable mechanical performance. The natural-based biomaterials can better mimic the native tissue microenvironment and enhance the attachment and migration of cells from the surrounding tissue resulting in a better implant integration and tissue repair [71]. In addition, the memory-shape properties evidenced their potential to be used in a minimally invasive surgery, *i.e.* arthroscopy surgery [72].

Owing to these features, the proposed natural-based bioinks can grant a more effective alternative in the production of hybrid tissue constructs. *In vivo* studies confirmed that the produced hybrid constructs are capable to maintain their shape and suitable mechanical performance up to 10 weeks of implantation and more importantly to allow tissue maturation and ECM deposition that resembles the native tissue.

## IX-5. CONCLUSIONS

In this study novel bioinks with suitable integrity and biocompatibility were for the first time designed and produced using two natural-based hydrogels. Looking at the available literature, bioinks for 3D Bioprinting aims to produce biologically and mechanically suitable implants. This generally requires two different bioinks: (i) one to give the biological functionality by carrying cells and biological factors and (ii) other to impart the proper mechanical strength. In this sense, it was used for the first time a gellan gum/fibrinogen cell-laden bioink combined with a silk fibroin methacrylate bioink) in an extrusion-based 3D printing hybrid system. 3D bioprinted constructs presented good mechanical properties allowing producing hybrid constructs that resemble cartilage mechanical performance. Furthermore, pig meniscus cells encapsulated and seeded on the bioinks revealed a good adhesion, proliferation and extracellular matrix deposition. *In vivo* maturation of the 3D bioprinted constructs was also performed and evaluated, where the constructs presented shape maintenance and formation of mature cartilaginous tissue up to 10 weeks of implantation.

Herein, these results anticipate that our 3D bioprinting approach, applying a GG/FB4 bioink and a SiI-MA (H) bioink in a hybrid system, could be a great alternative to be used either in future patient-specific fibrocartilage applications or in tissue engineered personalized treatments that required a mechanically stable and biocompatible scaffold.



## IX-6. REFERENCES

- [1] Lowe J, Almarza AJ. A review of in-vitro fibrocartilage tissue engineered therapies with a focus on the temporomandibular joint. *Archives of Oral Biology* 2017;83:193-201.
- [2] Costa JB, Silva-Correia J, Reis RL, Oliveira JM. Recent advances on 3D printing of patient-specific implants for fibrocartilage tissue regeneration. *Journal of 3D Printing in Medicine* 2018;2:129-40.
- [3] Vijayavenkataraman S, Yan W-C, Lu WF, Wang C-H, Fuh JYH. 3D bioprinting of tissues and organs for regenerative medicine. *Advanced Drug Delivery Reviews* 2018;132:296-332.
- [4] Kang H-W, Lee SJ, Ko IK, Kengla C, Yoo JJ, Atala A. A 3D bioprinting system to produce human-scale tissue constructs with structural integrity. *Nature Biotechnology* 2016;34:312.
- [5] Gungor-Ozkerim PS, Inci I, Zhang YS, Khademhosseini A, Dokmeci MR. Bioinks for 3D bioprinting: an overview. *Biomaterials science* 2018;6:915-46.
- [6] Kyle S, Jessop ZM, Al-Sabah A, Whitaker IS. 'Printability' of Candidate Biomaterials for Extrusion Based 3D Printing: State-of-the-Art. *Advanced healthcare materials* 2017;6.
- [7] Hinton TJ, Jallerat Q, Palchesko RN, Park JH, Grodzicki MS, Shue H-J, *et al.* Three-dimensional printing of complex biological structures by freeform reversible embedding of suspended hydrogels. *Science Advances* 2015;1:e1500758.
- [8] Kolesky DB, Homan KA, Skylar-Scott MA, Lewis JA. Three-dimensional bioprinting of thick vascularized tissues. *Proceedings of the National Academy of Sciences* 2016;113:3179-84.
- [9] Rajangam T, An SSA. Fibrinogen and fibrin based micro and nano scaffolds incorporated with drugs, proteins, cells and genes for therapeutic biomedical applications. *International journal of nanomedicine* 2013;8:3641-62.
- [10] Kim JH, Seol Y-J, Ko IK, Kang H-W, Lee YK, Yoo JJ, *et al.* 3D Bioprinted Human Skeletal Muscle Constructs for Muscle Function Restoration. *Scientific Reports* 2018;8:12307.
- [11] Ying G-L, Jiang N, Maharjan S, Yin Y-X, Chai R-R, Cao X, *et al.* Aqueous Two-Phase Emulsion Bioink-Enabled 3D Bioprinting of Porous Hydrogels. *Advanced Materials* 2018;30:1805460.
- [12] Romanazzo S, Vedicherla S, Moran C, Kelly DJ. Meniscus ECM-functionalised hydrogels containing infrapatellar fat pad-derived stem cells for bioprinting of regionally defined meniscal tissue. 2018;12:e1826-e35.
- [13] Groen WM, Diloksumpan P, van Weeren PR, Levato R, Malda J. From intricate to integrated: Biofabrication of articulating joints. *Journal of orthopaedic research : official publication of the Orthopaedic Research Society* 2017;35:2089-97.
- [14] Yang X, Lu Z, Wu H, Li W, Zheng L, Zhao J. Collagen-alginate as bioink for three-dimensional (3D) cell printing based cartilage tissue engineering. *Materials Science and Engineering: C* 2018;83:195-201.

- [15] Dong L, Wang SJ, Zhao XR, Zhu YF, Yu JK. 3D- Printed Poly(epsilon-caprolactone) Scaffold Integrated with Cell-laden Chitosan Hydrogels for Bone Tissue Engineering. *Sci Rep* 2017;7:13412.
- [16] Hong S, Sycks D, Chan HF, Lin S, Lopez GP, Guilak F, *et al.* 3D Printing of Highly Stretchable and Tough Hydrogels into Complex, Cellularized Structures. *Advanced materials (Deerfield Beach, Fla)* 2015;27:4035-40.
- [17] Koo Y, Choi E-J, Lee J, Kim H-J, Kim G, Do SH. 3D printed cell-laden collagen and hybrid scaffolds for *in vivo* articular cartilage tissue regeneration. *Journal of Industrial and Engineering Chemistry* 2018;66:343-55.
- [18] Aisenbrey EA, Tomaschke A, Kleinjan E, Muralidharan A, Pascual-Garrido C, McLeod RR, *et al.* A Stereolithography-Based 3D Printed Hybrid Scaffold for In Situ Cartilage Defect Repair. 2018;18.
- [19] Schuurman W, Khristov V, Pot MW, van Weeren PR, Dhert WJA, Malda J. Bioprinting of hybrid tissue constructs with tailorable mechanical properties. *Biofabrication* 2011;3:021001.
- [20] Xu T, Binder KW, Albanna MZ, Dice D, Zhao W, Yoo JJ, *et al.* Hybrid printing of mechanically and biologically improved constructs for cartilage tissue engineering applications. *Biofabrication* 2012;5:015001.
- [21] Wang X, Yan Y, Zhang R. Recent trends and challenges in complex organ manufacturing. *Tissue engineering Part B, Reviews* 2010;16:189-97.
- [22] Hoffman AS. Hydrogels for biomedical applications. *Advanced Drug Delivery Reviews* 2012;64:18-23.
- [23] Coenen AMJ, Bernaerts KV, Harings JAW, Jockenhoevel S, Ghazanfari S. Elastic materials for tissue engineering applications: Natural, synthetic, and hybrid polymers. *Acta Biomaterialia* 2018;79:60-82.
- [24] Krishnan UM, Sethuraman S. Electrospun Nanofibers as Scaffolds for Skin Tissue Engineering AU - Sundaramurthi, Dhakshinamoorthy. *Polymer Reviews* 2014;54:348-76.
- [25] Murphy SV, Atala A. 3D bioprinting of tissues and organs. *Nature Biotechnology* 2014;32:773.
- [26] Abelseth E, Abelseth L, De la Vega L, Beyer ST, Wadsworth SJ, Willerth SM. 3D Printing of Neural Tissues Derived from Human Induced Pluripotent Stem Cells Using a Fibrin-Based Bioink. *ACS Biomaterials Science & Engineering* 2019;5:234-43.
- [27] Thomas M, Willerth SM. 3-D Bioprinting of Neural Tissue for Applications in Cell Therapy and Drug Screening. *Frontiers in bioengineering and biotechnology* 2017;5:69-.
- [28] Cui X, Boland T. Human microvasculature fabrication using thermal inkjet printing technology. *Biomaterials* 2009;30:6221-7.
- [29] Zhang K, Fu Q, Yoo J, Chen X, Chandra P, Mo X, *et al.* 3D bioprinting of urethra with PCL/PLCL blend and dual autologous cells in fibrin hydrogel: An *in vitro* evaluation of biomimetic mechanical property and cell growth environment. *Acta Biomaterialia* 2017;50:154-64.

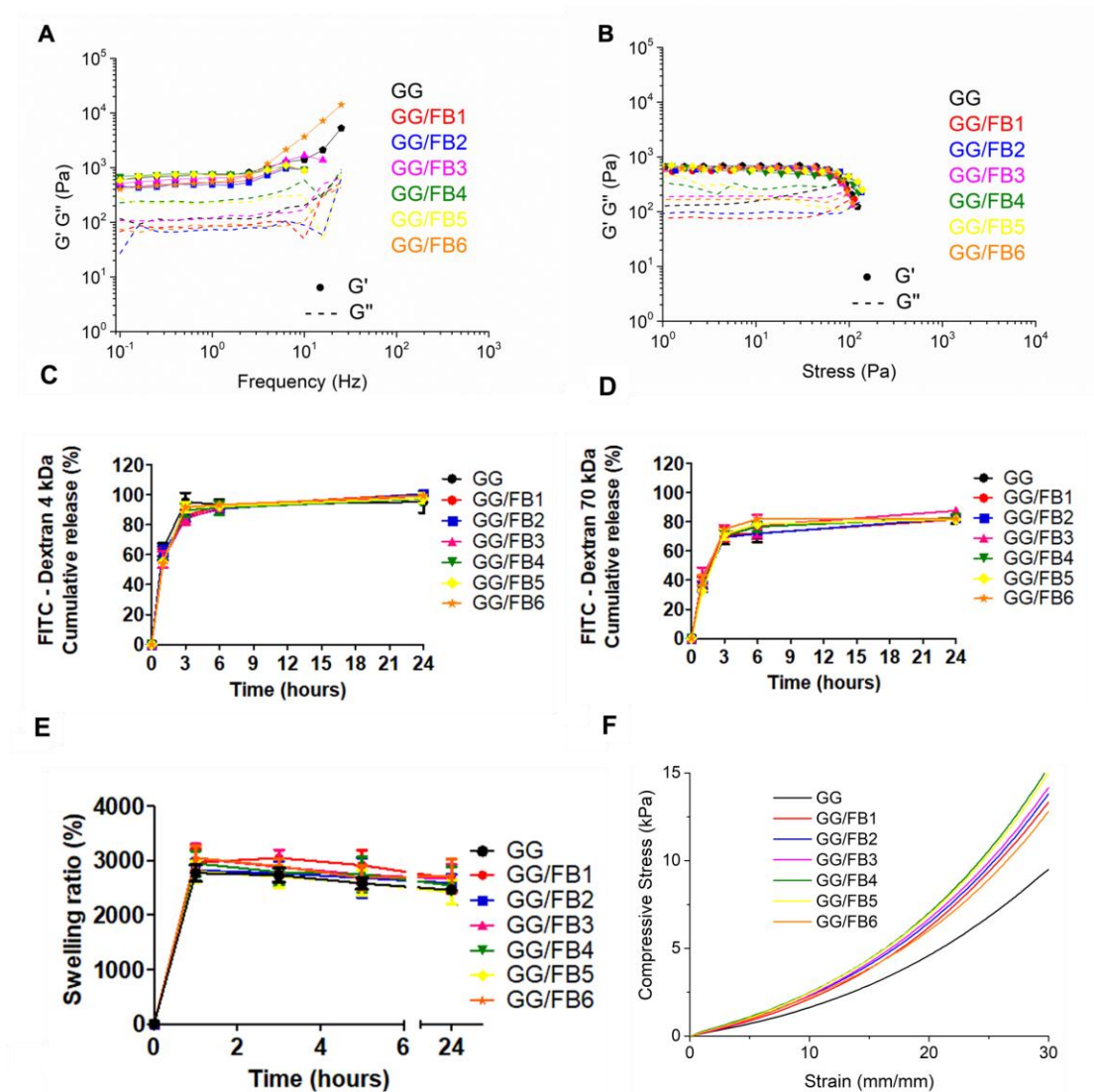
- [30] England S, Rajaram A, Schreyer DJ, Chen X. Bioprinted fibrin-factor XIII-hyaluronate hydrogel scaffolds with encapsulated Schwann cells and their *in vitro* characterization for use in nerve regeneration. *Bioprinting* 2017;5:1-9.
- [31] Xu Z, Li Z, Jiang S, Bratlie KM. Chemically Modified Gellan Gum Hydrogels with Tunable Properties for Use as Tissue Engineering Scaffolds. *ACS Omega* 2018;3:6998-7007.
- [32] Silva-Correia J, Oliveira JM, Caridade SG, Oliveira JT, Sousa RA, Mano JF, *et al.* Gellan gum-based hydrogels for intervertebral disc tissue-engineering applications. *Journal of tissue engineering and regenerative medicine* 2011;5:e97-107.
- [33] Sworn G. 9 - Gellan gum. In: Phillips GO, Williams PA, editors. *Handbook of Hydrocolloids* (Second Edition): Woodhead Publishing; 2009. p. 204-27.
- [34] Oliveira JT, Santos TC, Martins L, Picciochi R, Marques AP, Castro AG, *et al.* Gellan gum injectable hydrogels for cartilage tissue engineering applications: *in vitro* studies and preliminary *in vivo* evaluation. *Tissue engineering Part A* 2010;16:343-53.
- [35] Visser J, Peters B, Burger TJ, Boomstra J, Dhert WJ, Melchels FP, *et al.* Biofabrication of multi-material anatomically shaped tissue constructs. *Biofabrication* 2013;5:035007.
- [36] Levato R, Visser J, Planell JA, Engel E, Malda J, Mateos-Timoneda MA. Biofabrication of tissue constructs by 3D bioprinting of cell-laden microcarriers. *Biofabrication* 2014;6:035020.
- [37] Skardal A, Atala A. Biomaterials for integration with 3-D bioprinting. *Annals of biomedical engineering* 2015;43:730-46.
- [38] Coutinho DF, Sant SV, Shin H, Oliveira JT, Gomes ME, Neves NM, *et al.* Modified Gellan Gum hydrogels with tunable physical and mechanical properties. *Biomaterials* 2010;31:7494-502.
- [39] Paxton N, Smolan W, Bock T, Melchels F, Groll J, Jungst T. Proposal to assess printability of bioinks for extrusion-based bioprinting and evaluation of rheological properties governing bioprintability. *Biofabrication* 2017;9:044107.
- [40] Figueiredo L, Pace R, D'Arros C, Réthoré G, Guicheux J, Le Visage C, *et al.* Assessing glucose and oxygen diffusion in hydrogels for the rational design of 3D stem cell scaffolds in regenerative medicine. *Journal of tissue engineering and regenerative medicine* 2018;12:1238-46.
- [41] Zhu J, Marchant RE. Design properties of hydrogel tissue-engineering scaffolds. *Expert review of medical devices* 2011;8:607-26.
- [42] Benjamin M, Ralphs JR. Biology of fibrocartilage cells. *International review of cytology* 2004;233:1-45.
- [43] Verdonk PC, Forsyth RG, Wang J, Almqvist KF, Verdonk R, Veys EM, *et al.* Characterisation of human knee meniscus cell phenotype. *Osteoarthritis and cartilage* 2005;13:548-60.
- [44] Fox AJS, Bedi A, Rodeo SA. The basic science of human knee menisci: structure, composition, and function. *Sports health* 2012;4:340-51.



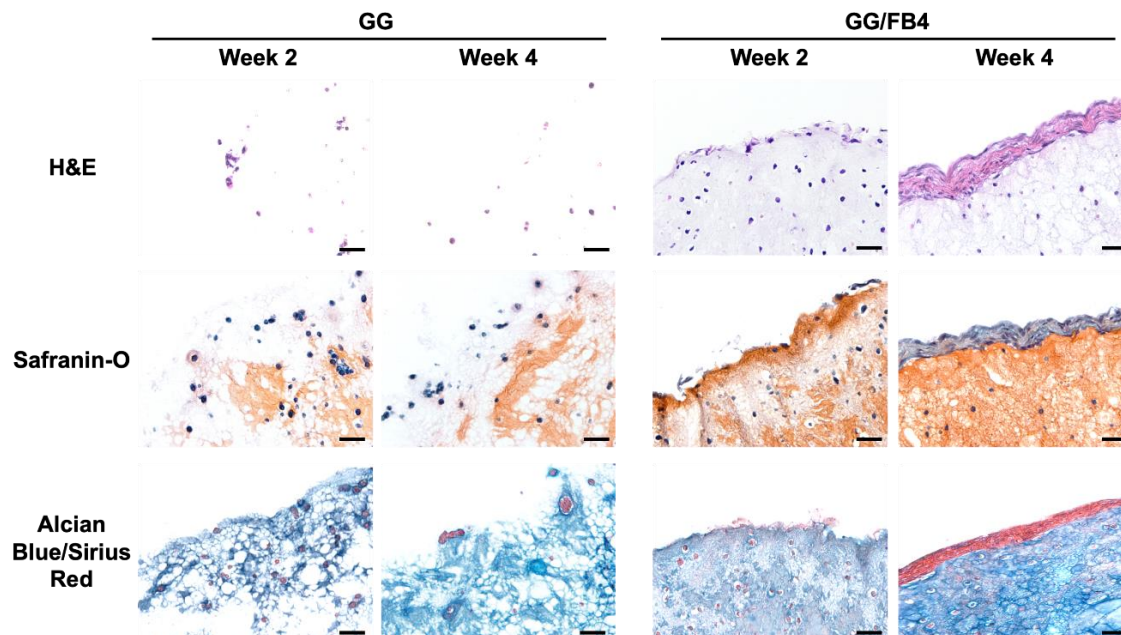
- [45] Newell N, Little JP, Christou A, Adams MA, Adam CJ, Masouros SD. Biomechanics of the human intervertebral disc: A review of testing techniques and results. *Journal of the mechanical behavior of biomedical materials* 2017;69:420-34.
- [46] Kasoju N, Bora U. Silk Fibroin in Tissue Engineering. *Advanced healthcare materials* 2012;1:393-412.
- [47] Ma D, Wang Y, Dai W. Silk fibroin-based biomaterials for musculoskeletal tissue engineering. *Materials Science and Engineering: C* 2018;89:456-69.
- [48] Li Z-H, Ji S-C, Wang Y-Z, Shen X-C, Liang H. Silk fibroin-based scaffolds for tissue engineering. *Frontiers of Materials Science* 2013;7:237-47.
- [49] Costa JB, Silva-Correia J, Oliveira JM, Reis RL. Fast Setting Silk Fibroin Bioink for Bioprinting of Patient-Specific Memory-Shape Implants. *Advanced healthcare materials* 2017;6:1701021.
- [50] Rodriguez MJ, Dixon TA, Cohen E, Huang W, Omenetto FG, Kaplan DL. 3D freeform printing of silk fibroin. *Acta Biomaterialia* 2018;71:379-87.
- [51] Sommer MR, Schaffner M, Carnelli D, Studart AR. 3D Printing of Hierarchical Silk Fibroin Structures. *ACS Applied Materials & Interfaces* 2016;8:34677-85.
- [52] Costa JB, Silva-Correia J, Ribeiro VP, da Silva Morais A, Oliveira JM, Reis RL. Engineering patient-specific bioprinted constructs for treatment of degenerated intervertebral disc. *Materials Today Communications* 2018.
- [53] Kim SH, Yeon YK, Lee JM, Chao JR, Lee YJ, Seo YB, *et al.* Precisely printable and biocompatible silk fibroin bioink for digital light processing 3D printing. *Nature Communications* 2018;9:1620.
- [54] Rodriguez MJ, Brown J, Giordano J, Lin SJ, Omenetto FG, Kaplan DL. Silk based bioinks for soft tissue reconstruction using 3-dimensional (3D) printing with *in vitro* and *in vivo* assessments. *Biomaterials* 2017;117:105-15.
- [55] Murphy AR, Kaplan DL. Biomedical applications of chemically-modified silk fibroin. *Journal of materials chemistry* 2009;19:6443-50.
- [56] Derakhshanfar S, Mbeleck R, Xu K, Zhang X, Zhong W, Xing M. 3D bioprinting for biomedical devices and tissue engineering: A review of recent trends and advances. *Bioactive materials* 2018;3:144-56.
- [57] Bishop ES, Mostafa S, Pakvasa M, Luu HH, Lee MJ, Wolf JM, *et al.* 3-D bioprinting technologies in tissue engineering and regenerative medicine: Current and future trends. *Genes & Diseases* 2017;4:185-95.
- [58] Yan L-P, Silva-Correia J, Ribeiro VP, Miranda-Gonçalves V, Correia C, da Silva Morais A, *et al.* Tumor Growth Suppression Induced by Biomimetic Silk Fibroin Hydrogels. *Scientific Reports* 2016;6:31037.

- [59] Ribeiro VP, Silva-Correia J, Gonçalves C, Pina S, Radhouani H, Montonen T, *et al.* Rapidly responsive silk fibroin hydrogels as an artificial matrix for the programmed tumor cells death. PLOS ONE 2018;13:e0194441.
- [60] Bencherif SA, Sands RW, Bhatta D, Arany P, Verbeke CS, Edwards DA, *et al.* Injectable preformed scaffolds with shape-memory properties. Proc Natl Acad Sci U S A 2012;109:19590-5.
- [61] Beck EC, Barragan M, Tadros MH, Gehrke SH, Detamore MS. Approaching the compressive modulus of articular cartilage with a decellularized cartilage-based hydrogel. Acta Biomaterialia 2016;38:94-105.
- [62] Chia HN, Hull ML. Compressive moduli of the human medial meniscus in the axial and radial directions at equilibrium and at a physiological strain rate. J Orthop Res 2008;26:951-6.
- [63] Lattouf R, Younes R, Lutomski D, Naaman N, Godeau G, Senni K, *et al.* Picrosirius Red Staining: A Useful Tool to Appraise Collagen Networks in Normal and Pathological Tissues. Journal of Histochemistry & Cytochemistry 2014;62:751-8.
- [64] Gowda BC, Kokila G, Gopinathan PA, Praveen KS. Picrosirius Red and Polarization Microscopy - A Tool for Gender Differentiation. Journal of clinical and diagnostic research : JCDR 2017;11:ZC107-ZC9.
- [65] Rittie L. Method for Picrosirius Red-Polarization Detection of Collagen Fibers in Tissue Sections. Methods in molecular biology (Clifton, NJ) 2017;1627:395-407.
- [66] Makris EA, Hadidi P, Athanasiou KA. The knee meniscus: structure-function, pathophysiology, current repair techniques, and prospects for regeneration. Biomaterials 2011;32:7411-31.
- [67] Makris EA, Gomoll AH, Malizos KN, Hu JC, Athanasiou KA. Repair and tissue engineering techniques for articular cartilage. Nature Reviews Rheumatology 2014;11:21.
- [68] Daly AC, Freeman FE, Gonzalez-Fernandez T, Critchley SE, Nulty J, Kelly DJ. 3D Bioprinting for Cartilage and Osteochondral Tissue Engineering. Advanced healthcare materials 2017;6:1700298.
- [69] Schuurman W, Khristov V, Pot MW, van Weeren PR, Dhert WJ, Malda J. Bioprinting of hybrid tissue constructs with tailorable mechanical properties. Biofabrication 2011;3:021001.
- [70] Xu T, Binder KW, Albanna MZ, Dice D, Zhao W, Yoo JJ, *et al.* Hybrid printing of mechanically and biologically improved constructs for cartilage tissue engineering applications. Biofabrication 2013;5:015001.
- [71] O'Brien FJ. Biomaterials & scaffolds for tissue engineering. Materials Today 2011;14:88-95.
- [72] Montgomery M, Ahadian S, Davenport Huyer L, Lo Rito M, Civitarese RA, Vanderlaan RD, *et al.* Flexible shape-memory scaffold for minimally invasive delivery of functional tissues. Nature Materials 2017;16:1038.

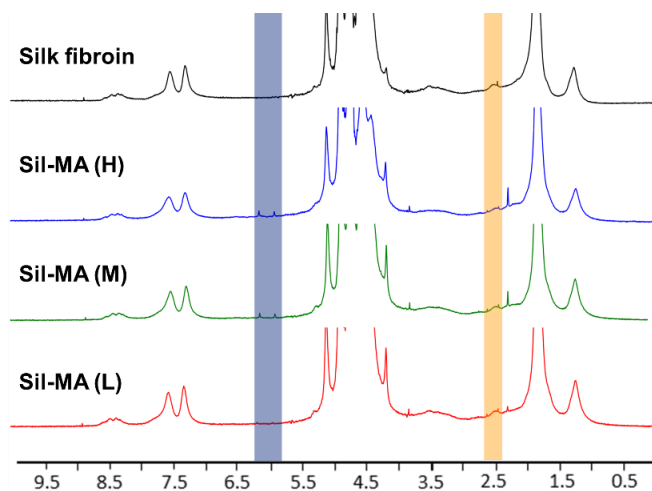
## IX-7. SUPPLEMENTARY MATERIAL



Supplementary Figure IX-1 - (A) Oscillatory rheological measurements of the GG/FB bioinks as function of frequency. (B) Steady shear measurements at frequency of 1 Hz of GG/FB bioinks. Cumulative release of FITC dextrans with different molecular weights of 4 kDa (C) and 70 kDa (D) from the GG/FB bioinks. (E) Swelling ratio of 3D GG/FB constructs (cylinders, 12 mm in diameter and 4 mm in thickness) in PBS after 24 hours of immersion. (F) Stress-strain plot of compressive uniaxial compression test performed in 3D GG/FB constructs (cylinders, 12 mm in diameter and 4 mm in thickness) after enzymatic/ionic crosslinking.

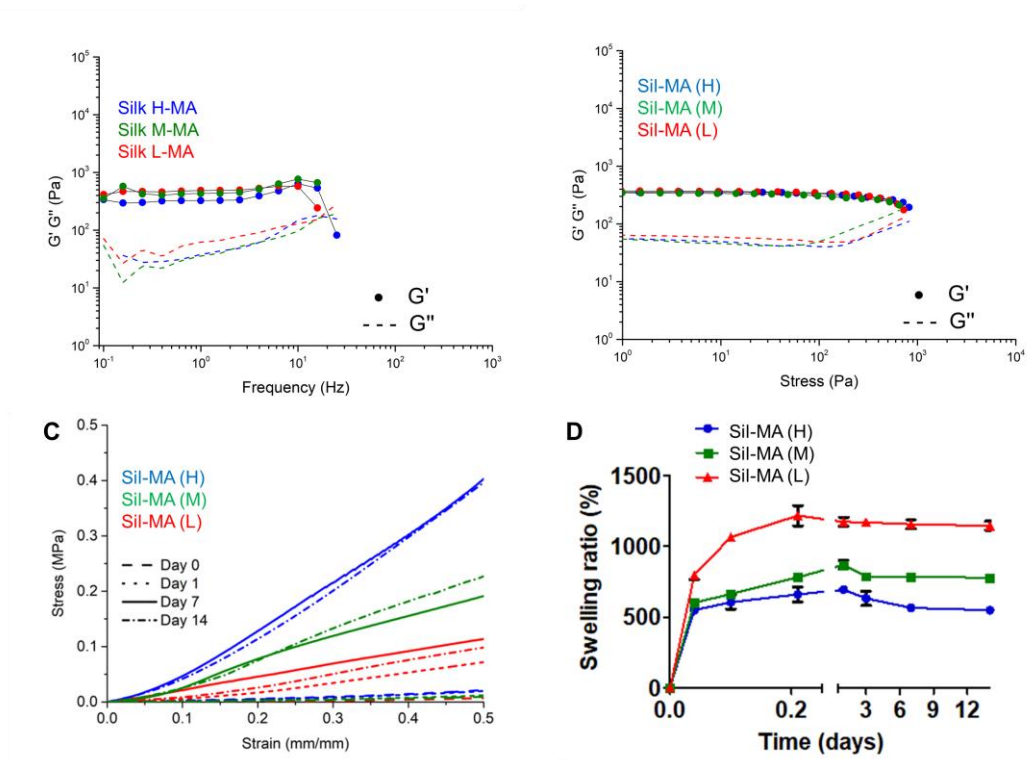


Supplementary Figure IX-2 - Histological images of GG and GG/FB4 3D cell-laden bioprinted constructs stained with a Hematoxylin & Eosin, Safranin-O and Alcian Blue/Sirius red after 14 days (2 weeks) and 28 days (4 weeks) of culture. Scale bars: 50  $\mu$ m.

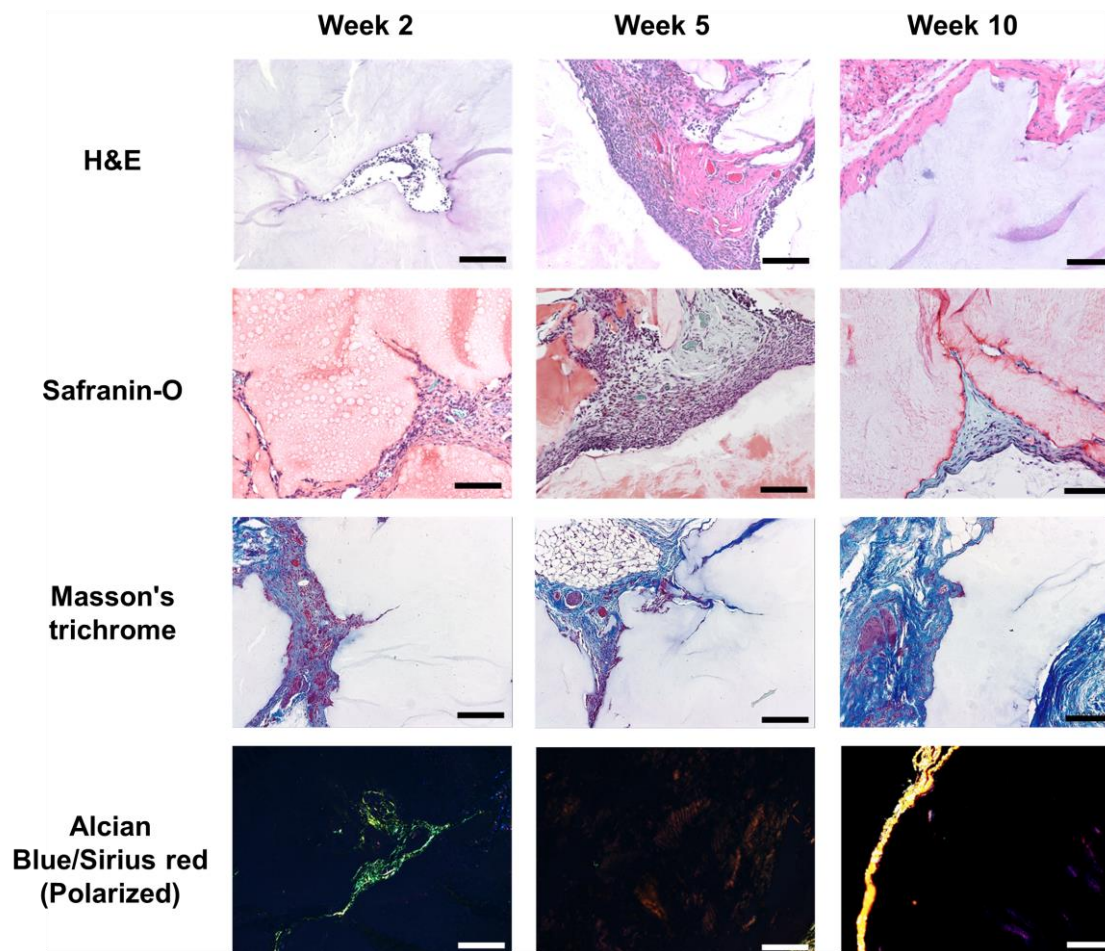


Formulations	Methacrylation degree (%)
Silk fibroin	0
SiI-MA (H)	63.5
SiI-MA (M)	57.2
SiI-MA (L)	44.5

Supplementary Figure IX-3 - <sup>1</sup>H-NMR spectra and methacrylation degree values of SiI-MA (H), SiI-MA (M) and SiI-MA (L) solutions. Silk solution was used as control.



Supplementary Figure IX-4 - (A) Oscillatory rheological measurements of the Sil-MA bioinks as function of frequency. (B) steady shear measurements at frequency of 1 Hz of Sil-MA bioinks. (C) Stress–strain plot of compressive uniaxial compression test performed in 3D Sil-MA constructs (cylinders, 12 mm in diameter and 4 mm in thickness) after UV crosslinking. (D) Swelling ratio of 3D Sil-MA constructs (cylinders, 12 mm in diameter and 4 mm in thickness) in PBS after 14 days of immersion.



Supplementary Figure IX-5 - Histological images of GG/FB4 3D bioprinted constructs without cells stained with a Hematoxylin & Eosin, Safranin-O, Masson's trichrome and Alcian Blue/Sirius red after 2 weeks, 5 weeks and 10 weeks of subcutaneous implantation. Scale bars: 200  $\mu$ m.

## **SECTION 4**

### **GENERAL CONCLUSIONS**

# Chapter X

## General Conclusions and Future Perspectives.



## General Conclusions and Future Perspectives.

### X-1. GENERAL CONCLUSIONS

The paradigm in patient care has been revolutionized by regenerative medicine and tissue engineering fields towards the development of suitable implants from the lab to the clinical setting. Tissue engineers have been making huge efforts to overcome organ shortage producing effective alternatives capable to mimic the native tissue and induce a proper tissue regeneration.

Cartilaginous tissues possess a poor intrinsic regeneration leading to a high number of clinical interventions and medical visits related with the degeneration of these tissues. In addition, the current available treatments have been shown early arthritic changes, poor implant integration and implant displacement. In this sense, the scientific community has been moving to a trend of personalized and patient-specific treatments. In other words, scientists have been combining reverse engineering with 3D printing to achieve and apply the concept of “Precision Medicine”. This concept comprises personalized treatments where each patient receives a particular medical intervention according to their injury and medical past.

The performed work under the scope of this thesis aimed to develop new bioinks and strategies for the production of patient-specific cartilage implants. Technologically advanced novel implants based only on natural origin polymers were developed in order to enhance the current state of the art. The proposed approaches intended to overcome the main downsides recognized in the current available treatments using pioneering and personalized strategies.

In chapter V, taking in consideration the state of art related to meniscus repair, it is noticeable that more effective approaches are needed, as there is still space for improvements of the current used techniques. Several strategies have already been proposed, but only few of them have been shown to be effective. In an attempt to tackle that, in this work, novel indirect printed hierarchical scaffolds composed by a silk fibroin top layer and a silk fibroin/ionic-doped  $\beta$ -tricalcium phosphate bottom layer were developed. The use of an indirect printing approach allowed the production of scaffolds with tunable porosity and shape, as well as patient-specificity. After characterization, it was found that the

adequate morphology and porosity, together with superior mechanical properties and suitable integrity, make these scaffolds promising candidates for meniscus regeneration. The *in vitro* biological assays demonstrated that the top layer and the bottom layer of the scaffolds supported the viability and proliferation of human meniscus cells and human primary osteoblasts, respectively. Moreover, when *in vivo* subcutaneously implanted in mice, the scaffolds induced a very weak inflammatory response. However, in the light of obtained results, a complementary *in vivo* study in a rabbit meniscus defect model, would be necessary to fully validate these indirect printing hierarchical scaffolds and confirm the hypothesis envisioned by the authors. This is an indispensable step to prove that the presence of ceramics in the bottom layer of the scaffolds would enhance the anchorage properties, by improving the interaction bone-implant. Nevertheless, the *in vitro* and *in vivo* results are encouraging and confirmed the potential of the developed indirect printed hierarchical scaffolds for meniscus tissue engineering applications.

In chapter VI, a new technology was developed and internationally patented. A silk-fibroin ink suitable for 3D printing was developed for the first time, and its application envisioned for chemical and pharma industries, medicine, engineering and manufacturing, namely for the production of capsules, fibers, membranes, particles, scaffolds, medical devices, microfluidic devices and patient-specific implants. In fact, the development of such ink was only possible due to the enzymatically cross-link process, where horseradish peroxidase and hydrogen peroxide are used as enzyme and substrate, respectively. This process modifies the silk fibroin water solution, covalently crosslinking the tyrosine groups in silk structure, allowing it to be used as a bioink. After process optimization, reliable 3D structures such as scaffolds, patient-specific implants, microchips, among others can be produced resorting to this technology. Furthermore, the physico-chemical performances of the silk constructs can be tuned for specific uses, by means of using different processing methods after the printing of the 3D constructs as well as the tuned ability provided by the printing process itself. One of the main benefits of this methodology is the capability to print the silk constructs in an amorphous state, giving the opportunity to induce the  $\beta$ -sheet conformation in many different ways. This confers a tremendous versatility to our in-house developed technology.

In Chapter VII, the developed and patented technology mentioned in the previous chapter was further explored. Scaffolds were produced for the first time using a fast-setting silk fibroin bioink with potential to be used in different applications in 3D printing. Through the mechanical properties assay, it was possible to see that the developed silk fibroin bioink has unique properties such as elasticity and

memory-shape as well as capability to be printed in an amorphous state giving the possibility to follow different strategies. The *in vitro* biological characterization assays demonstrated that the constructs obtained from this silk fibroin bioink are biocompatible, supporting human adipose stem cells proliferation and viability up to 7 days of culturing. This extremely versatile fast-setting approach is able to quickly prepare and print biomimetic materials. This promising strategy opens up new horizons for the use of SF bioinks, not only concerning the development of tissue substitutes using tissue engineering approaches, but also regarding all type of applications where the printing of an implantable biomaterial is relevant. This has a particular interest for the biofabrication of patient-specific memory-shape implants.

The motivation for developing the work described in Chapter VIII arose from the fact that intervertebral disc degeneration is one of the most frequently reported age- and work-related disorders in modern societies. Furthermore, the current used treatments have poor clinical outcomes and does not consider each patient needs. With the knowledge obtained from the previous works related to the bioink composed by silk fibroin hydrogel, we hypothesized that combining elastin in this respective ink could enhance in terms of mimicking the bioprinted patient-specific substitutes. With elastin, the scaffolds should be able to mimic intervertebral disc ultrastructure, in particular the outer region of the IVD, *i.e.* annulus fibrosus. For that, a 3D model of annulus fibrosus obtained by semi-automatic morphological segmentation from magnetic resonance imaging dataset of human intervertebral disc was used, in a reverse engineering process. Scaffolds were produced and fully characterized in terms of its microstructure, mechanical properties, degradation and swelling, as well as biological properties. Overall, the results indicated that the 3D bioprinted silk fibroin/elastin scaffolds can be tuned for their degradation profile, mechanical properties, and architecture by means of varying the bioink formulation and conformation, and bioprinting parameters. In addition, the *in vitro* biological assays demonstrated that the silk fibroin/elastin scaffolds supported human adipose stem cells proliferation and viability up to 21 days of culturing. The major conclusion from this experimental work is related to the fact that we could provide a real proof-of-concept on the use of reverse engineering and 3D printing to produce patient-specific annulus fibrosus implants. More specifically, this technology allowed producing constructs using an enzymatically cross-linked silk fibroin/elastin bioink. The proposed low-cost bioink and approach is a step forward for the development of future intervertebral disc personalized treatments, as it opens up the possibility to produce patient-specific silk fibroin/elastin constructs respecting the annulus fibrosus each patient's anatomy.

In sum, the acellular implants developed in the first 4 chapters of this thesis were capable to overcome some challenges present in the clinics. Using fast-setting advanced strategies, we were capable to produce biomimetic memory-shape implants respecting each patient's anatomy. Their remarkable mechanical properties, biocompatibility, patient-specificity and suturability make them a great alternative to the current available treatments.

In Chapter IX, novel bioinks with suitable integrity and biocompatibility were for the first time designed and produced using two natural-based hydrogels. Looking at the available literature, bioinks for 3D Bioprinting aims to produce biologically and mechanically suitable implants. This generally requires two different bioinks: (i) one to give the biological functionality by carrying cells and biological factors and (ii) other to impart the proper mechanical strength. In this last one, a synthetic polymer is usually used. However, we aimed at innovating at this specific point and using solely natural-origin biomaterials to develop a novel hybrid 3D bioprinted construct. Two natural-based hydrogels were then used with capability to grant a better alternative in terms of hybrid bioprinting processes for cartilage regeneration. In this sense, it was used for the first time a gellan gum/fibrinogen cell-laden bioink combined with a silk fibroin methacrylate bioink) in an extrusion-based 3D printing hybrid system. We hypothesized that this could be an exceptional combination where the produced patient-specific implants were subsequently cross-linked using an ionic/enzymatic and photo-crosslinking mediated-system. After all the characterization, we could confirm that the two natural-based biomaterials allowed to produce 3D hybrid implants with great and tunable mechanical properties as well as exceptional biological properties providing a 3D bioprinting hybrid system capable to overcome challenges found in previous systems. Despite the versatility of the developed system, the rheological properties, mechanical performance, printability and biological properties of both bioinks were properly tuned, to achieve a suitable combination for cartilage/fibrocartilage applications. As a matter of fact, the 3D bioprinted constructs presented good mechanical properties allowing producing hybrid constructs that resemble cartilage mechanical performance. Furthermore, pig meniscus cells encapsulated and seeded on the bioinks revealed a good adhesion, proliferation and extracellular matrix deposition. *In vivo* maturation of the 3D bioprinted constructs was also performed and evaluated, where the constructs presented shape maintenance and formation of mature cartilaginous tissue up to 10 weeks of implantation. Results anticipate that our 3D bioprinting approach, applying a gellan gum/fibrinogen bioink and a silk methacrylated bioink in a hybrid system, could be a great alternative to be used either in future patient-specific cartilage applications or in tissue engineered personalized treatments that required a mechanically stable and biocompatible scaffold.

Comparing with the previous approaches, the developed hybrid system allowed the production of cell-laden implants by means of using two bioinks. Maintaining the memory-shape properties and remarkable mechanical performance by using a silk-based bioink, this system allows the biofabrication of patient-specific implants that better mimic the native tissue's architecture, cell's spatial distribution and vascularization. In addition, the idea of using a cell-laden implant that can be pre-matured using a bioreactor can play a critical role in terms of a faster and proper tissue regeneration and better implant anchorage.

As a general conclusion, the work developed in this thesis is a step forward when compared with the state of the art, giving promising alternatives for bioprinting of personalized implants for cartilage tissues regeneration.

## X-2. FUTURE PERSPECTIVES

In this section, some future perspectives in the field of cartilage regeneration will be discussed and some future studies related with the work developed in this thesis will be suggested.

TE is a powerful tool that essentially attempts to mimic what nature has already achieved. However, the reality is that we do not have a thorough comprehension of how to form cartilage in order to be able to reproduce it with great fidelity. In this sense, 3 key areas should be properly addressed to accomplish the well-desired translation to humans.

First, fundamental studies that can allow unveil cartilage formation and how cartilage injuries are formed should be performed. A superior guidance in foreseeing innovative regeneration strategies and design new therapeutic approaches for cartilage repair and regeneration is a critical step to move forward in this field. The vital question where fundamental biologists should put efforts is how chondrocytes form stable cartilage. Different fundamental studies have been performed and answers have been given in terms of gene expression, cartilage maturation processes (rate and state), induction of mechanical stimuli and molecular pathways. However, questions still remain and a fully understand of cartilage formation mechanisms is yet to be unveiled. In the future, the better understanding of the *in vivo* complex molecular pathways through targeting a selection of them in high-throughput *in vitro* models could be an effective strategy to faster comprehend and acquire the necessary knowledge in this topic.

Second, the translation of novel technologies from bench to bedside are extremely dependent on the pre-clinical animal models and a better judgment and foresight must be used in the selection of the right animal model. Many factors affect the cartilage repair mechanisms in animal models including the nature of the defect, animal species, age and genetics. Furthermore, the standardization of the animal model selection for each type of cartilage injury could give a better understand of how the scaffolds performed *in vivo*. Ultimately, precise *ex vivo* models using human tissue should be used. In future, non-destructive technologies, such as cartilage *in vitro* 3D models, to reinforce the *in vitro/ex vivo* research should be highlighted in order to reduce the required animal sample size.

Lastly and the one that was extensively explored under the scope of this thesis, is the use of advanced personalized tissue engineering strategies for customization of cartilage-like substitutes. 3D printing technology allowed tissue engineers to precisely control the structure of the implants, better mimic the architecture of cartilage by controlling the cell spatial distribution and reduce the cost and time of rapid prototyping. In this sense, biofabrication uses ‘bioinks’ to print living cells within a material construct or only the material itself. Despite some promising results achieved so far, there is still a lot of work to be done before obtaining the “ideal” bioink for cartilage regeneration. The bioink should comprise printable rheological properties, suitable mechanical performance and biological properties that allow cell survival, adhesion and tissue-specific function. In a short period of time is envisioned that 3D biofabrication technologies could progress into more sophisticated tools, novel bioinks could be developed and an enhancement in terms of imaging techniques (MRI and Micro-CT) could be achieved. Furthermore, is expected that this type of technology may become available in surgical rooms to help in the implantation of patient-specific 3D implants for cartilage regeneration.

Regarding the work developed in this thesis, further *in vitro* and *in vivo* characterization assays should be performed. The innovative approaches described above revealed promising proof-of-concept results that need to be confirmed in *in vivo* orthotopic models such as pig for the intervertebral disc and sheep for meniscus. Only after the *in vivo* assays, it will be possible to confirm the effectiveness of the developed implants and personalized approaches.

Nevertheless, the potential of the developed and patented technologies, specially the silk-based bioinks, should be further explored by means of bioink functionalization (*e.g.* RGD and other peptides), the use of different silk sources (different silkworm species or spider silk) and application of the bioinks in different fields such as tendon regeneration, bone regeneration, microchips and cancer models.